New Synthetic Approaches and Structural Models of the Oxygen-Evolving Complex in Photosystem II from the Use of Oximato-Based Ligands

Alysha A. Alaimo

A thesis submitted to the Department of Chemistry in partial fulfillment of the

requirements for the Degree of Doctor of Philosophy

Supervised by

Professor Theocharis C. Stamatatos

Brock University

St. Catharines Ontario, Canada

April 2018

Abstract

The employment of the chelating/bridging ligands salicylhydroxime ($shiH_3$), quinoline-2-aldoxime (qaoH) and 2,6-diacetylpyridine dioxime ($dapdoH_2$) in heterometallic Mn–Ca chemistry has afforded various compounds with diverse topologies, metal stoichiometries and Mn oxidation state descriptions.

Chapter 1 provides a general introduction to the oxygen-evolving complex (OEC) of Photosystem II (PSII) including discussions of fundamental aspects such as composition, structural proposals, mechanism of O–O bond formation and synthetic approaches. My research results are reported in Chapter 2, 3 and 4. In the first project (Chapter 2), one-pot reactions between $Mn(ClO_4)_2{\cdot}6H_2O$, $Ca(ClO_4)_2{\cdot}4H_2O$ and the potentially tetradentate chelating/bridging ligand salicylhydroxime ($shiH_3$), resulting from the in situ metal ion-assisted amide-iminol tautomerism of salicylhydroxamic acid ($shaH_2$), in the presence of various fluorescence carboxylate groups (2-naphthoic acid = L1-H; 9-anthracenecarboxylic acid = L2-H; 1-pyrenecarboxylic acid = L3-H) and base NEt_3 has led to a family of structurally similar $\{Mn^{III}_4Ca\}$ clusters (**1**–**4**) with distorted square pyramidal topologies. The combined results demonstrate the ability of $shiH_3$ and fluorescence carboxylates to yield new heterometallic Mn–Ca clusters with (i) the same Mn–Ca ratio as the OEC of PSII, (ii) structural stability in solution, (iii) a pronounced redox and optical activity and (iv) predominant antiferromagnetic exchange interactions with $S = 0$ spin ground states. These complexes may be relevant to lower oxidation level species of the catalytic cycle of the OEC.

The second project of this thesis, discussed in Chapter 3, involved one-pot reactions between the $[Mn_3O(O_2CPh)_6(py)_x]^{+/0}$ triangular precursors and either $CaBr_2{\cdot}xH_2O$ or $CaCl_2{\cdot}6H_2O$ in the presence of $shaH_2$. This afforded the heterometallic complexes

$[Mn^{III}_4Ca_2(O_2CPh)_4(shi)_4(H_2O)_3(Me_2CO)]$ (**5**) and $(pyH)[Mn^{II}_2Mn^{III}_4Ca_2Cl_2(O_2CPh)_7(shi)_4(py)_4]$ (**6**), respectively, in good yields. Further reactions but using a more flexible synthetic scheme comprising the $Mn(NO_3)_2{\cdot}4H_2O/Ca(NO_3)_2{\cdot}4H_2O$ and $Mn(O_2CPh)_2{\cdot}2H_2O/Ca(ClO_4)_2{\cdot}4H_2O$ "metal blends" and $shaH_2$ in the presence of external base NEt_3, led to the new complexes $(NHEt_3)[Mn^{III}_4Mn^{IV}_4Ca_2(OEt)_2(shi)_{10}(EtOH)_2]$ (**7**) and $(NHEt_3)_4[Mn^{III}_8Ca_2(CO_3)_4(shi)_8]$ (**8**), respectively. Solid-state *dc* magnetic susceptibility studies of **5**–**8** revealed the presence of predominant antiferromagnetic exchange interactions between the Mn centers, leading to $S = 0$ spin ground state values. From a bioinorganic chemistry perspective, these compounds may demonstrate some relevance to both the high-valent scheme (**7**) and lower oxidation level species (**5**, **6** and **8**) of the catalytic cycle of the OEC.

In the last chapter of this thesis (Chapter 4), the ligands quinoline-2-aldoxime (qaoH) and 2,6-diacetylpyridine dioxime ($dapdoH_2$) were introduced for a first time in heterometallic Mn–Ca chemistry. This afforded a mixed-valence $\{Mn^{II/III}_{22}Ca_2\}$ (**9**) cluster containing several $\{Mn_4CaO_x\}$ subunits and a butterfly-like $\{Mn^{IV}_2Ca_2\}$ (**10**) complex, respectively. These compounds demonstrate structural and magnetic relevance to both the low- and high-valent states of the OEC.

All research-based Chapters (Chapter 2–4) are divided into subsections in order to facilitate the understanding of the research concepts by the familiar and non-familiar readers and contextualize the messages, goals and conclusions of each individual project. I felt it was appropriate to begin each Chapter with a short preface of the work that summarizes the most important aspects of the specific project, followed by the complete experimental work and discussion of the results, and end with conclusions and some future perspectives.

Acknowledgments

First and foremost, I would like to express my sincere gratitude and appreciation to my supervisor Professor Theocharis C. Stamatatos. I cannot convey how much I appreciate his time, continuous support and patience for me throughout my development as a scientist over the past four years. I am truly grateful to have had the opportunity to work and learn from him and, as a result, I will carry everything I have learned throughout my career. Thank you! Besides my supervisor I would also like to thank the other members of my thesis advisory committee: Professor Melanie Pilkington and Professor Travis Dudding. They have generously offered me valuable insight towards improving and expanding my research; their support is also much appreciated.

I would also like to thank my research collaborators for their valuable contributions to the successful completion of the present thesis. In particular, my sincere thanks go to Dr. Luís Cunha-Silva, Dr. Simon J. Teat, Dr. Catherine Raptopoulou, Dr. Vassilis Psycharis and Professor Christos Lampropoulos for solving and refining the structures of all the reported complexes. Futhermore, I am grateful to Professor George Christou and all his group members, Professor Albert Escuer and Dr. Dimitris Alexandropoulos who acquired the magnetic data of all synthesized compounds.

I would like to thank Brock University and the Queen Elizabeth II-Graduate Scholarship in Science and Technology for the financial support of my Ph.D. research over the last four years.

To my current labmate, Anne, thank you so much for your encouragement, support and all the laughs this past year. To Dimitris, Angie, Penny, Paul and Eleni, thank you all for your

continuous support throughout my four years at Brock, even after all of you have graduated. It is truly the end of an era for the original TS group; what a journey it has been!

Lastly, I would like to thank my best friends, Christina and Emily, and my family: my parents, Angelo and Lisa, and my sister, Kayla, for keeping me sane the last four years and supporting me in all that I do. I love you guys! ♥

Table of Contents

Chapter 1: **Introduction**

Chapter 2: Emissive {Mn^{III}_4Ca} Clusters with Square Pyramidal Topologies: Syntheses and Structural, Spectroscopic and Physicochemical Characterization

Chapter 3: Structural Diversities in Heterometallic Mn–Ca Cluster Chemistry from the Use of Salicylhydroxamic Acid: $\{Mn^{III}_4Ca_2\}$, $\{Mn^{II/III}_6Ca_2\}$, $\{Mn^{III/IV}_8Ca\}$ and $\{Mn^{III}_8Ca_2\}$ Complexes with Relevance to Both High- and Low-Valent States of the Oxygen- Evolving Complex

Chapter 4: **New Insights in Mn–Ca Chemistry from the Use of Oximate-Based Ligands: $\{Mn^{II/III}_{22}Ca_2\}$ and $\{Mn^{IV}_{2}Ca_2\}$ Complexes with Relevance to Both Low- and High-Valent States of the Oxygen-Evolving Complex**

List of Schemes

List of Figures

List of Tables

List of Publications

Chapter 2

A. A. Alaimo, D. Takahashi, L. Cunha-Silva, G. Christou and T. C. Stamatatos. "Emissive $\{Mn^{III}_4Ca\}$ Clusters with Square Pyramidal Topologies: Syntheses and Structural, Spectroscopic, and Physicochemical Characterization", *Inorganic Chemistry*, **2015**, 54, 2137 (Front Cover).

Chapter 3

A. A. Alaimo, E. S. Koumousi, L. Cunha-Silva, L. J. McCormick, S. J. Teat, V. Psycharis, C. P. Raptopoulou, S. Mukerjee, C. Li, S. Das Gupta, A. Escuer, G. Christou and T. C. Stamatatos. "Structural Diversities in Heterometallic Mn–Ca Cluster Chemistry from the Use of Salicylhydroxamic Acid: $\{Mn^{III}_4Ca_2\}$, $\{Mn^{II/III}_6Ca_2\}$, $\{Mn^{III/IV}_8Ca\}$, and $\{Mn^{III}_8Ca_2\}$ Complexes with Relevance to both High and Low-Valent States of the Oxygen-Evolving Complex", *Inorganic Chemistry*, **2017**, *56*, 10760.

Chapter 4

A. A. Alaimo, D. I. Alexandropoulos, C. Lampropoulos, and T. C. Stamatatos. "New insights in Mn–Ca chemistry from the use of oximate-based ligands: $\{Mn^{II/III}_{22}Ca_2\}$ and $\{Mn^{IV}_2Ca_2\}$ complexes with relevance to both low- and high-valent states of the oxygen-evolving complex", *Polyhedron*, **2018**, in press.

List of Abbreviations

Å	Angstrom
A/Ala	Alanine
AAS	Atomic absorption spectroscopy
ac	Alternating current
ATR	Attenuated total reflection
a.u.	Arbitrary units
BVS	Bond Valence Sum
C_6H_{14}	Hexane
CH_2Cl_2	Dichloromethane
$CHCl_3$	Chloroform
CIP	Cahn-Ingold-Prelog
cm^{-1}	Wavenumbers
CP	Chlorophyll protein
CShM	Continuous Shape Measurement
CV	Cyclic voltammogram
D	Zero-field splitting parameter
D/Asp	Aspartic acid
$dapdoH_2$	2,6-diacetylpyridine dioxime
dc	direct current
DMF	Dimethylformamide
DMSO	Dimethylsulfoxide
e^-	Electron

E/*anti*	Entgegen or opposite
E/Glu	Glutamic acid
EDNMR	Electron Nuclear Double Resonance detected NMR
ENDOR	Electron Nuclear Double Resonance
EPR	Electron Paramagnetic Resonance
ESI-MS	Electrospray Ionization Mass Spectroscopy
Et_2O	Diethyl ether
EtOH	Ethanol
EXAFS	Extended X-ray Absorption Fine Structure
Fc/Fc^+	Ferrocene/ferrocenium
g	Landé factor
H^+	Proton
H/His	Histidine
IM_1	First light-induced intermediate
IM_2	Second light-induced intermediate
IR	Infrared
J	Magnetic exchange coupling constant
JT	Jahn-Teller
K	Kelvin
K/Lys	Lysine
kDa	Kilodalton
kG	Kilogauss
L1-H	2-naphthoic acid

L2-H	9-anthracenecarboxylic acid
L3-H	1-pyrenecarboxylic acid
LMCT	Ligand-to-metal charge transfer
M	Metal
m/*z*	Mass to charge ratio
MC	Metallacrown
MeCN	Acetonitrile
MeOH	Methanol
Me_2CO	Acetone
Me_4NOH	Tetramethylammonium hydroxide
mpkoH	Methyl 2-pyridyl ketoxime
mV/s	Millivolts per second
N/Asn	Asparagine
N_2H_4	Hydrazine
NBu^n_3	Tributylamine
$NBu^n_4PF_6$	Tetrabutylammonium hexafluorophosphate
NEt_3	Triethylamine
NH_2OH	Hydroxylamine
nm	Nanometer
NMe_3	Trimethylamine
NMR	Nuclear Magnetic Resonance
o	Ortho position
OEC	Oxygen-Evolving Complex

P	Pigment
paoH	2-pyridinealdoxime
Phe	Pheophytin *a*
ppkoH	Phenyl 2-pyridyl ketoxime
PQ	Plastoquinone
PSII	Photosystem II
Psb	Protein subunit
py	Pyridine
Q_A	Quinone A
Q_B	Quinone B
qaoH	Quinoline-2-aldoxime
QM/MM	Quantum Mechanics/Molecular Mechanics
S	Ground-state spin
$shaH_2$	Salicylhydroxamic acid
$shiH_3$	Salicylhydroxime
SQUID	Superconducting quantum interference device
T	Temperature
T	Tesla
THF	Tetrahydrofuran
TIP	Temperature Independent Paramagnetism
UV	Ultraviolet
V	Volts
Vis	Visible

W	Water molecule
W_f	Fast exchanging substrate water molecule
W_s	Slow exchanging substrate water molecule
WOC	Water-Oxidizing Complex
X	Bridging group in cubane motif
XANES	X-ray Absorption Near Edge Structure
XAS	X-ray Absorption Spectroscopy
XES	X-ray Emission Spectroscopy
XFEL	X-ray Free-Electron Laser
XRD	X-ray Diffraction
Y_Z	Tyrosine residue
Z/syn	Zusammen or together
η^1, η^2, η^3	Coordination modes of ligands
λ	Wavelength
μ, μ_3, μ_4	Bridging modes of ligands
μA	Microampere
ν	Stretching frequency
τ	Trigonality index
χ	Magnetic susceptibility
χ'	real or in-phase susceptibility

Chapter 1

Introduction

1.1 ***Photosynthesis and Photosystem II***

Photosynthesis is the process by which plants, some bacteria and some protistans use the energy from sunlight to convert it into chemical or photochemical energy.[1] In this conversion process, the solar energy is transformed into the reducing equivalents necessary to power carbon dioxide fixation as well as other processes of life,[1a,d] producing molecular dioxygen as a byproduct. This process can be described simply as follows:

$$CO_2 + H_2O \xrightarrow[\text{chloroplasts}]{\text{light}} O_2 + [CH_2O]$$

where $[CH_2O]$ represents an organic material (i.e., sugar). The Oxygen-Evolving Complex (OEC) of Photosystem II (PSII) is responsible for catalyzing this thermodynamically demanding and important reaction. PSII has been studied in great detail and has been a topic of research interest for more than 50 years, by which progress has been made in understanding the catalytic center, the OEC. This area of research is multidisciplinary and has depended on the advances in several fields, including coordination chemistry, inorganic chemistry, biochemistry, spectroscopy, biophysics and computational chemistry. There are, however, many aspects of the OEC that remain up for debate with researchers still trying to produce conclusive results.

Photosystem II is a membrane-protein complex embedded in the thylakoid membrane of plants, algae and cyanobacteria that uses light energy to oxidize water and reduce plastoquinone. PSII is composed of 20 subunits and several cofactors with a total molecular weight of 350 kDa

(Figure 1.1).[2] This biological catalyst has a pseudo-symmetric dimeric structure with two homologous proteins, D1 and D2, being the core of the reaction center. The structure of PSII has been solved at resolutions from 3.8 to 1.9 Å in two closely related thermophilic cyanobacteria, *Thermosynechococcus elongatus*[3] and *Thermosynechococcus vulcanus*.[2,4]

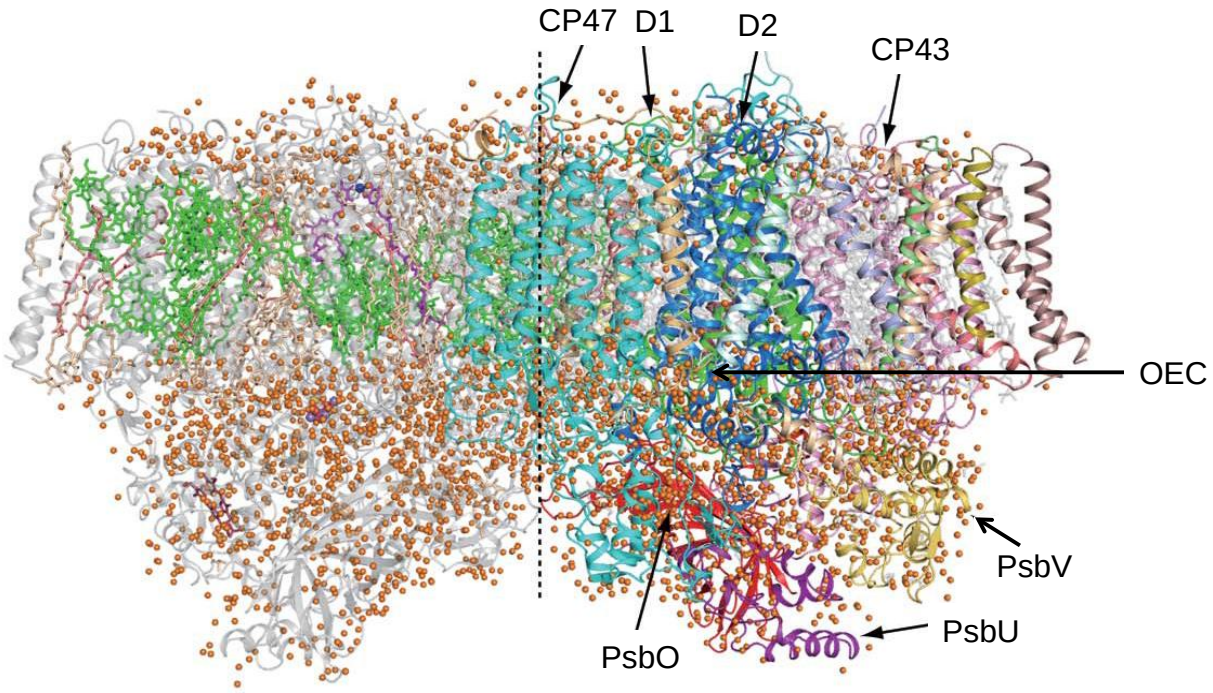

Figure 1.1. Overall structure of PSII dimer from *T. vulcanus* at a resolution of 1.9 Å. The central broken line is the non-crystallographic two-fold axis relating the two monomers. The protein subunits are coloured individually in the right-hand monomer and the cofactors are coloured in the left-hand monomer. The orange spheres represent the water molecules. Reproduced from Ref. 2.

PSII absorbs photons through the many associated chlorophylls and other pigment molecules. The energy absorbed is then transferred to the reaction center composed of the D1

and D2 proteins with the majority of the electron transfer pathways occurring in D1. Together these reaction center proteins bind and are transferred through all the redox active cofactors in the following sequence: (1) absorption of light by peripheral antennae (CP43 and CP47); (2) trapping of excitation energy in the antenna by chlorophyll *a* (P680); (3) ejection and transfer of an electron to a pheophytin *a* molecule (Phe); and (4) stabilization of the separation of charge through the reducing side, where the electron proceeds to plastoquinone molecules, quinone A (Q_A) and quinone B (Q_B). Alternatively, the separation of charge could be stabilized through the oxidizing side, in this case an electron is supplied to P680 from a water molecule via a tyrosine residue (Y_Z) from the function of the active site (OEC) (Figure 1.2).[5] The preeminent electron donor is water as four electrons and four protons are extracted from two molecules to form one molecule of dioxygen. This process can be described by the following equation:

$$2\,H_2O \xrightarrow{\text{OEC}} O_2 + 4\,H^+ + 4\,e^-$$

There are also extrinsic subunits, PsbV (Cyt *c*550), PsbU (12 kDa), and PsbO (33 kDa), involved in the retention of Ca^{II} and Cl^- at the active site essential for the reconstitution and regulation of oxygen evolution.[6]

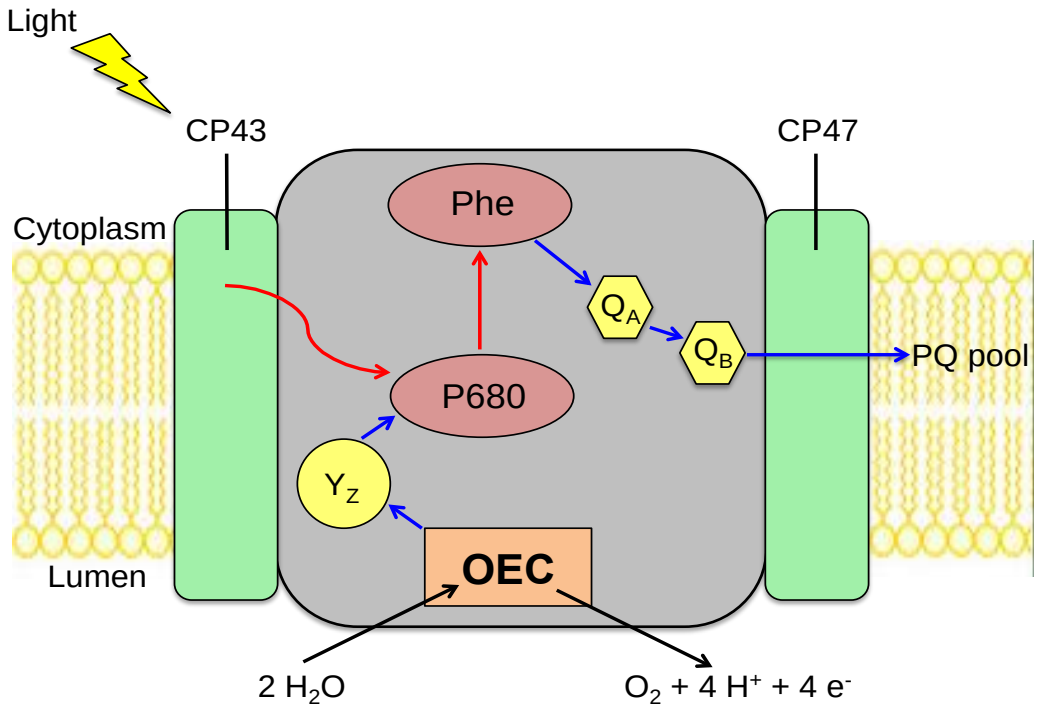

Figure 1.2. Schematic diagram of the PSII antenna system and reaction center in the thylakoid membrane of plants, algae and cyanobacteria. Y_z, Phe and Q_B, and the OEC are all located on the D1 protein, Q_A is located on the D2 protein and P680 is shared between the two proteins. The arrows represent the electron transport in PSII. Reproduced from Ref. 5.

1.2 ***Oxygen-Evolving Complex (OEC): Composition and Kok Cycle***

The OEC is located on the lumenal side of PSII and its composition has been determined through the collective efforts and results of decades of intense research. Manganese, calcium and chloride have been rendered essential for the oxygen-evolving process of PSII. X-ray absorption spectroscopy,[3a, 7] including extended X-ray absorption fine structure (EXAFS) and X-ray absorption near edge structure (XANES), quantitative electron paramagnetic resonance (EPR)[8] and atomic absorption spectroscopy (AAS)[9] have all been valuable tools in assessing the metal

stoichiometry and topology of the OEC. Experiments have established that nature's catalyst for biological photosynthesis consists of four Mn and one Ca^{II} atoms. The OEC has been known to contain Mn since the 1950s and this metal is unique in that it directly influences oxygenic photosynthesis.[10,11] Studies have shown that the inhibition of oxygenic photosynthesis is a direct result of a manganese deficiency, resembling the similar effects of hydroxylamine, hydrazine and nitric oxide, which are known to be inhibitors of oxygen evolution and reducing agents.[12] The presence of the Ca^{II} is also of specific importance for the activity of the OEC; without its presence the catalytic activity is stopped at intermediate states and electron transfer is affected.[13] Other metal ions have been substituted into synthetic models for Ca^{II} to see whether oxygen-evolution could be activated; apart from Sr^{II}, which partially recovers the catalytic activity, the others have no effect or are competitive inhibitors.[2,14] Despite this, the role of Ca^{II} in the OEC remains under debate. The first atomic-resolution (1.9 Å) model of the OEC revealed two Cl^{-} atoms in the vicinity of the $\{Mn_4Ca\}$ cluster (Figure 1.3).[2] Cl–1 and Cl–2 are the chloride binding sites found in PSII. They are located on opposite sides of the OEC and have a distance of 6–7 Å away from the $\{Mn_4Ca\}$ cluster.[15] Cl–1 is surrounded by D2–K317, D1–E333 and two water molecules, whereas Cl–2 is surrounded by CP43–E354, D1–N338 and two water molecules. These Cl^{-} anions have mainly a structural role and are found to lie at the entrance of hydrogen-bonded networks. These networks involve a number of bound water molecules and hydrophilic amino acid residues, allowing the Cl^{-} anions to potentially function as either proton exit or water inlet channels.

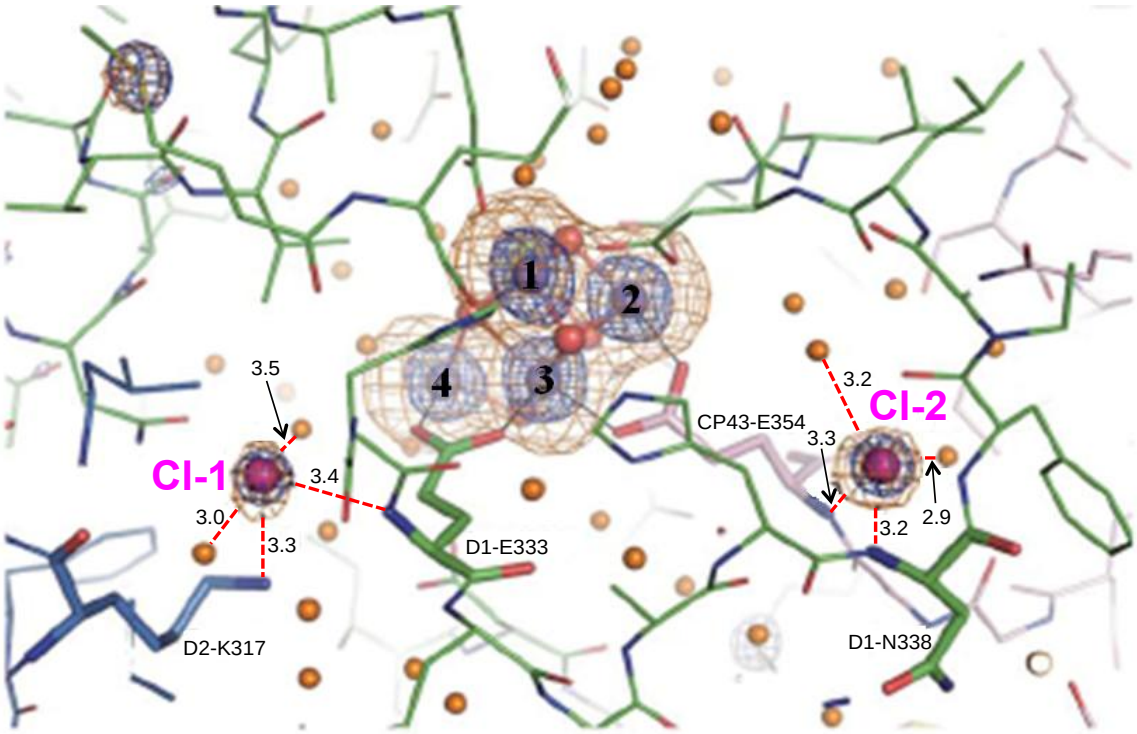

Figure 1.3. Location of Cl–1 and Cl–2 confirmed by the anomalous difference Fourier map calculated with data collected at a wavelength of 1.75 Å. The four Mn atoms found in the OEC are represented numerically. The segmented red lines indicate the distances between the Cl^- ions and their closest neighbouring molecules. The distances are expressed in Å. Abbreviations: K = Lys; E = Glu; N = Asn. The orange spheres represent the water molecules. Reproduced from Ref. 2.

The OEC must be regenerated frequently due to photo-oxidative damage.[16] The process by which the OEC is assembled is called photoactivation and requires Mn^{II}, Ca^{II}, Cl^-, bicarbonate, H_2O and oxidizing equivalents resulted from light absorption.[11,17] A mechanism for this process has been proposed based on spectroscopic and kinetic data. First Mn^{II} binds at the high affinity Mn-binding site of PSII, which is believed to contain D1–Asp170, and is photoxidized to form Mn^{III} and the first light-induced intermediate (IM_1).[18] This initial oxidation

is dependent on Ca^{II}, which can bind either before or after the Mn^{II}.[19] Data have revealed that a single proton is released upon this photoxidation in the presence of Ca^{II}. If the proton is assumed to originate from the ionization of a H_2O ligand, then IM_1 can be formulated as $\{Mn^{III}(O^{2-})Ca^{II}\}$ or $\{Mn^{III}(OH^{-})_2Ca^{II}\}$.[20] Before the next photolytic step, one Ca^{II} must be bound at its effector site so that a photoxidation of a second Mn^{II} atom can occur, resulting in the second light-induced intermediate (IM_2). IM_2 is quickly transformed into the OEC in the presence of additional equivalents of Mn^{II} through kinetically unresolved steps.[21] Bicarbonate has been shown to stimulate the rate of formation and yield of IM_1,[3c] as well as control the ligand field strength and symmetry around the initial high affinity Mn^{III}.[22] The role of the Cl^- in photoactivation is not as clear as its influence only occurs following the rate-limiting step and affects the O_2 activity of the entirely assembled cluster. However, Cl^- is an essential cofactor for both O_2 activity and photoactivation yield. The substitution of Cl^- with other anions, such as nitrate, inhibits the recovery of O_2 activity of the native enzyme.[20]

Based on a widely accepted theory originated by Bessel Kok and coworkers[23] in 1970, during catalysis the dependence of O_2 production relies on the period-four oscillation of short flashes of light on the chloroplasts, upon which four oxidizing equivalents are accumulated from the oxidation of H_2O to O_2. In regards to the mechanism of catalysis, the $\{Mn_4Ca\}$ cluster passes through five oxidation states of an S_n state (S_n, where n = 0–4) cycle, where the subscript indicates the number of stored oxidizing equivalents (Scheme 1.1, top).[23c] The S_2 and S_3 states are metastable and eventually decay to the dark and stable S_1 state, whereas the S_4 state is the transient state that releases O_2 and decays to the S_0 state. Although the catalytic cycle rationalizes the process of oxygen evolution, it does not place restrictions on the Mn oxidation states or the protonation states of the oxygen ligands of the inorganic cluster.[24] After decades of intense

research, these states have remained contentious. Two possible schemes have been developed in order to describe the sequence of Mn oxidation events: the high-valent and low-valent (Scheme 1.1, bottom). The low-valent scheme has the Mn atoms in lower oxidation states (i.e., Mn^{II} and Mn^{III}) than that of the desirable, high-valent scheme. The lower oxidation species do not require the presence of oxido groups in the inorganic core,[18,20] resulting in the S_n (n = 0, –1, –2, –3) states, known as the reduced OEC states. During the catalytic turnover, lower oxidation state species with lower oxygen-atom content must be generated upon loss of O_2.[25] The high oxidation state pathway has been supported by EPR,[26] ^{55}Mn electron nuclear double resonance (ENDOR),[27] XAS,[28] and Kβ X-ray emission spectroscopy (XES).[29] However, biochemical, spectroscopic and computational data have also been interpreted to support the existence of the lower oxidation state cycle.[24,30]

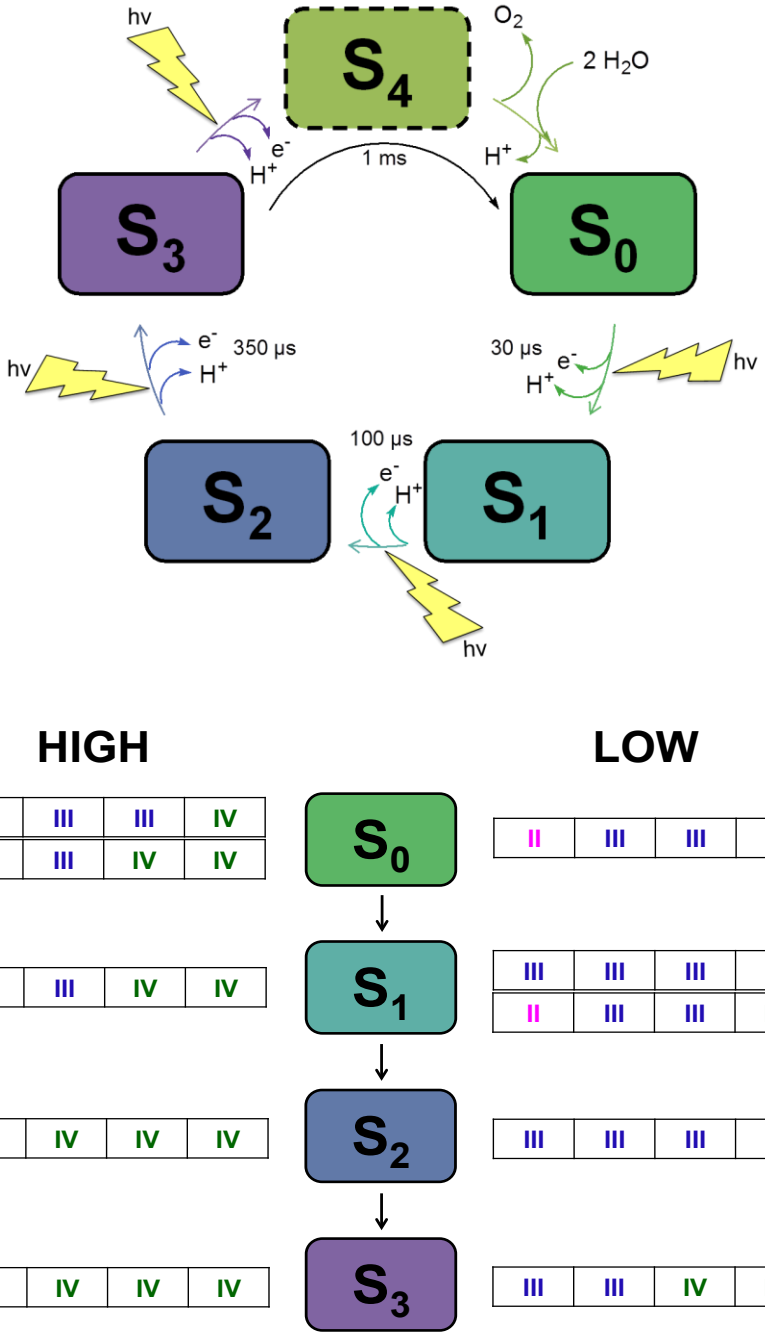

Scheme 1.1. The Kok cycle of the photoinduced S_n states for oxygen evolution. The oxidation and proton release events are indicated between each step of the cycle as well as the rate of each transition (top). The proposed formal oxidation states of the four Mn atoms of the OEC in the S_0–S_3 states based on the high-valent and low-valent schemes (bottom). Reproduced from Refs. 1d and 24.

The first evidence for direct water ligation to the {Mn_4Ca} cluster came from kinetic studies.[31,32,33] By using time-resolved mass spectrometry to study the kinetics of substrate water binding to the OEC throughout the S_n state cycle, it became evident that water is exchangeable through the S_3 state.[32] For every S_n state there are distinct fast (W_f) and slow (W_s) exchanging substrate water molecules, consistent with the water binding sites to the OEC.[32, 34] A Sr^{II} substitution gave an increase in the rate for the slow exchange process suggesting the water is bound to Ca^{II}.[35] The protonation states of the oxygen atoms, the Mn and Ca coordination and terminal or bridging ligation can explain the rate of exchanging water molecules; therefore, these studies are important to consider in terms of mechanistic proposals for O–O bond formation (see Section 1.4).

1.3 ***Structural Proposals for the OEC: A Historical Background***

The elemental composition and the fact that the Mn ions should be close enough to one another to interact magnetically was the only available information about the structure of the OEC until the early 2000s. The topology of the complex and number of oxygen and/or carboxylate bridges was uncertain. Due to the absence of a specific targeted structural motif, hypotheses regarding the structure of the OEC were prompted by molecules that were synthesized and spectroscopically characterized through XAS and EPR techniques. A survey of the literature from the 1980s and 1990s affirms that any molecule possessing more than one Mn atom was considered a potential mimic of the OEC. The results of this serendipitous chemistry have yielded a vast library of Mn complexes possessing novel and aesthetically-pleasing

structures with interesting physical and spectroscopic properties. Early synthetic endeavours encompassed various mixed-valent Mn-oxo complexes of varying nuclearity, composition and arrangement.[36,37,38,39] Specifically, tetranuclear Mn complexes have been historically significant in biomimetic synthetic chemistry, as it is a tetramanganese cluster that resides at the active site of PSII, albeit most of these complexes would not be identified today as direct mimics of the OEC. Various tetranuclear systems with metal oxidation states ranging from $\{Mn^{II}_4\}$ to $\{Mn^{IV}_4\}$ are present throughout the literature.[36,37,39] The most frequently observed and structurally distinct patterns of the tetranuclear Mn-oxo clusters are shown in Scheme 1.2.[36,37,39,40]

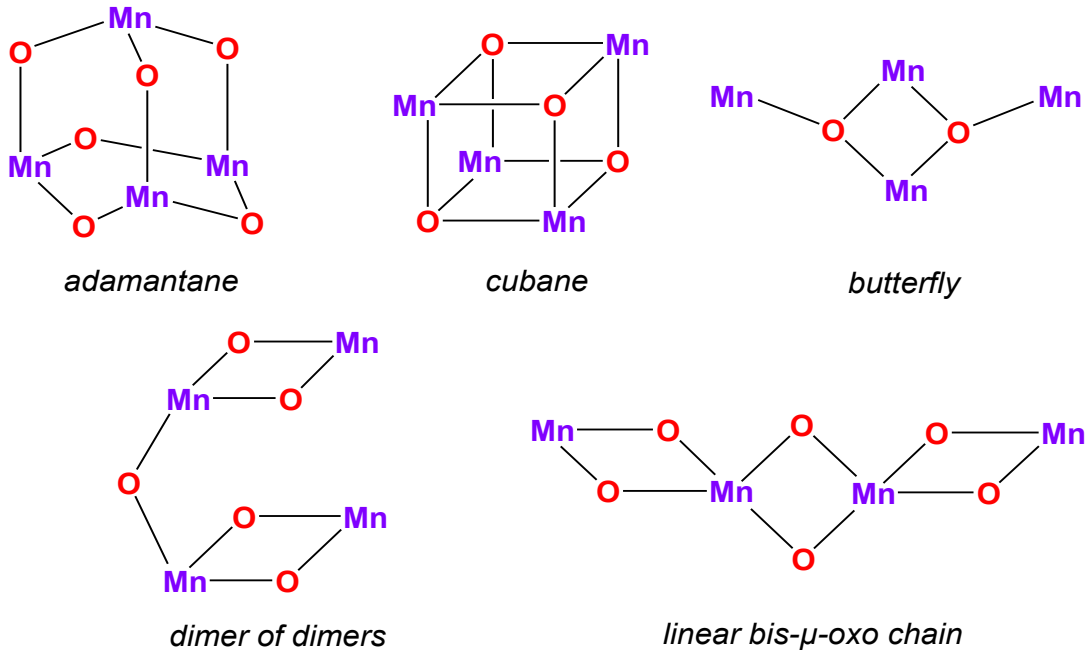

Scheme 1.2. Schematic diagram of the most frequently observed and structurally distinct topologies of oxo-bridged tetramanganese clusters. Reproduced from Ref. 39.

One of the earliest models comprising a tetramanganese motif was the $[Mn^{IV}_4(\mu\text{-}O)_6]^{4+}$ adamantane-like complex stabilized by four chelating 1,4,7-triazacyclononane ligands (Figure

1.4). [41] This adamantane-shaped core has been suggested as a reaction intermediate in photosynthetic water oxidation, proposed by Brudvig and Crabtree.[42] This complex exhibits weak ferromagnetic interactions between the Mn^{IV} centers that changes to weak antiferromagnetic upon protonation of the bridging oxides. This is analogous to what is observed for the $S_1 \rightarrow S_2$ transition in PSII.[43]

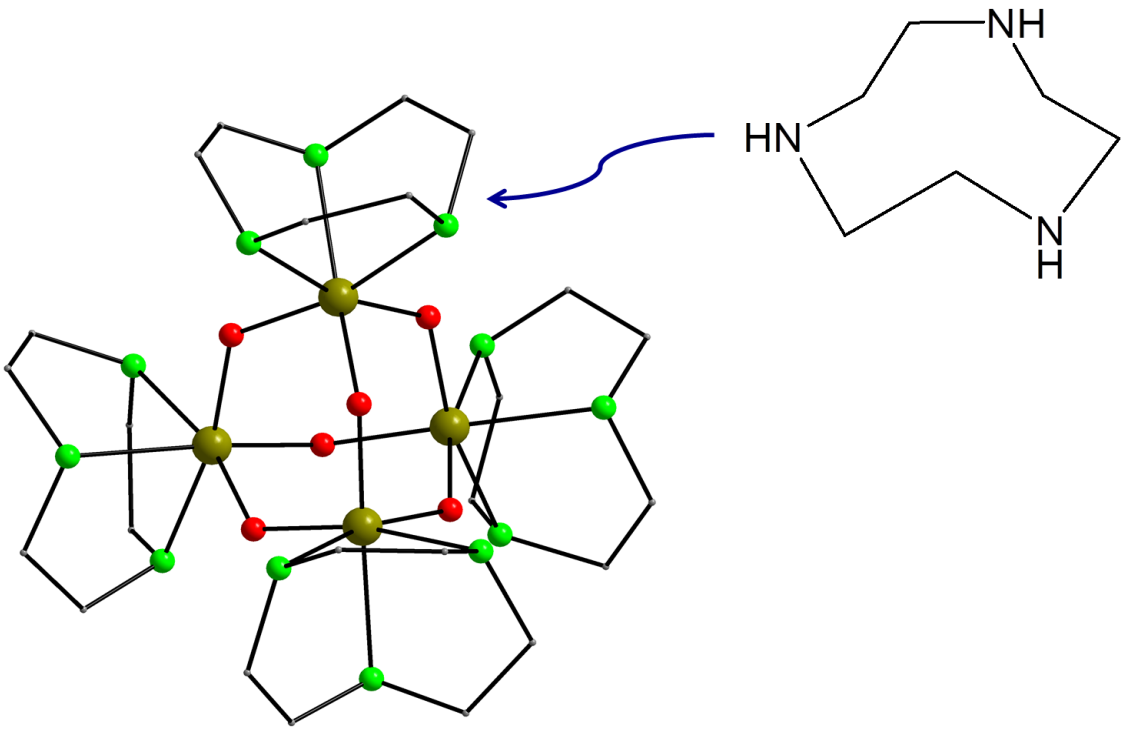

Figure 1.4. Molecular structure of the $[Mn^{IV}_4(\mu\text{-}O_6)]^{4+}$ adamantane-like structural model with four chelating 1,4,7-triazacyclononane ligands synthesized by Wieghardt and coworkers. H atoms are omitted for clarity. Colour scheme: Mn^{IV}, olive green; O, red; N, green; C, gray. Reproduced from Ref. 41.

The $[Mn_4(\mu_3\text{-}O)_4]^{n+}$ cubane core is another example of an early model for the structure of the OEC at different S_n states of the catalytic cycle.[42,44] This cubane core was achieved by

Christou and coworkers[45] in the mixed-valent $[Mn^{III}_3Mn^{IV}(\mu_3\text{-}O)_3X]^{6+}$ (X^- = Cl or Br) compound bearing additional bridging carboxylate groups (Figure 1.5, top left). In terms of biological relevance, this complex shows two sets of signals in the EPR spectra, a 16-line hyperfine-structured signal at $g \sim 2$ and a broad peak at $g \sim 6$.[46] Although this is not identical with the EPR spectrum of the S_2 state (i.e, signals at $g = 2$ and $g \geq 4.1$),[47] this complex reproduces some of the defining features. This complex also contains a μ_3-bridging Cl^- atom. Remembering the Cl^- requirement for oxygen evolution, it can be theorized that a μ_3-Cl^- within a Mn aggregate may be needed to stabilize the S_2 oxidation level.[44,48] Slightly different from the cubane core of Christou and coworkers, a $[Mn^{III}_2Mn^{IV}_2(\mu_3\text{-}O)_4]^{6+}$ cubane complex with exclusively μ_3-O^{2-} bridges was synthesized by Dismukes and coworkers (Figure 1.5, top right).[49] Despite being a mixed-valent species, no large JT (Jahn-Teller) distortions were observed for the Mn^{III}-O bond lengths, attributed to valence delocalization. This complex is a rare example of a class-III delocalized, mixed-valence Mn(III/IV) compound. This conclusion has been further supported by ^{1}H NMR data.[49] Another exciting characteristic of this cubane is that it can undergo photo-rearrangement to yield O_2 and a diarylphosphinate ligand and consequently decay to a butterfly-shaped complex (Figure 1.5, bottom). A reversible cubane/butterfly transformation has also been proposed as a mechanism for photosynthetic water oxidation and the butterfly-shaped complex has been suggested as a structural model for the lower S_n states of the catalytic cycle.[44,50]

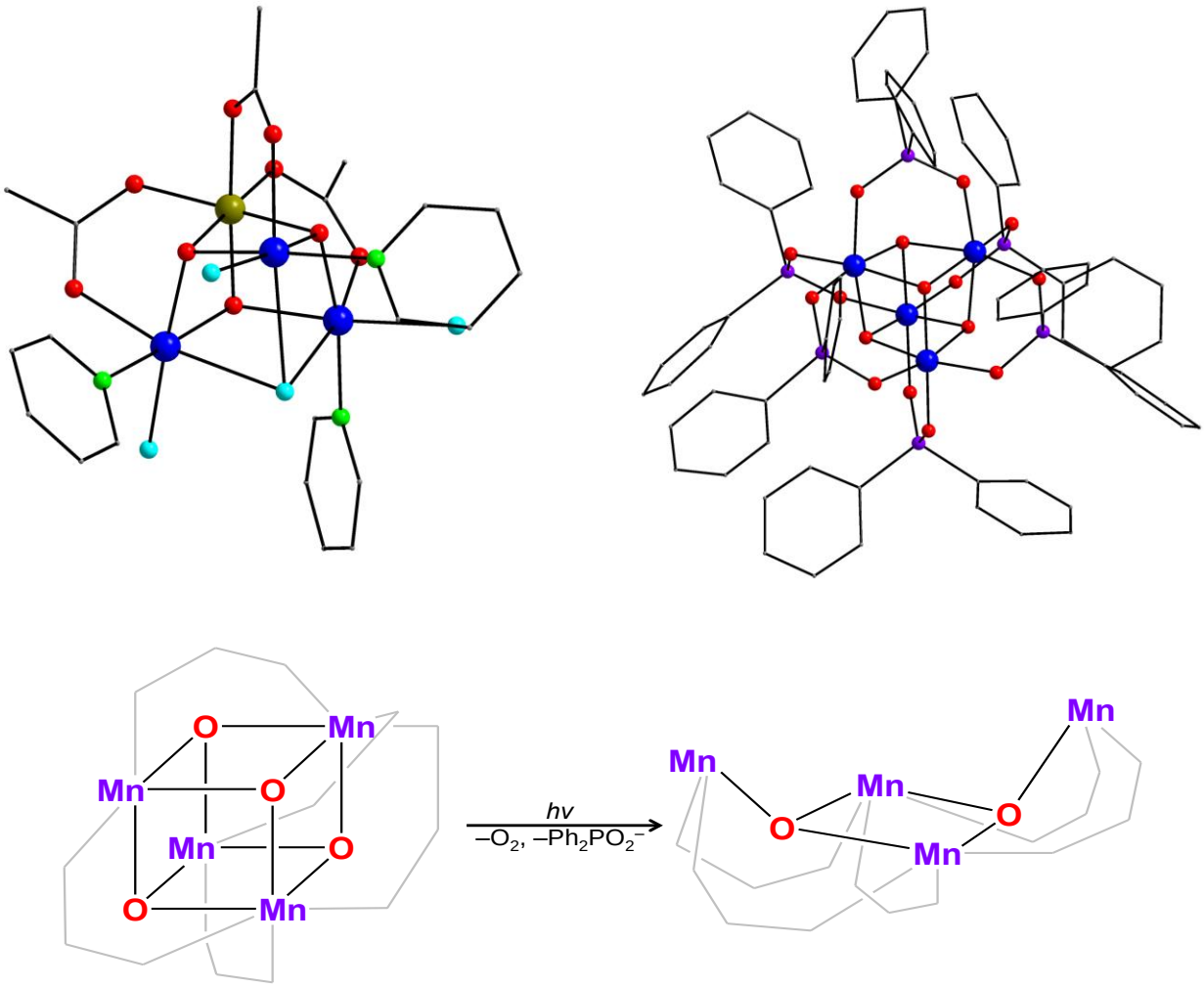

Figure 1.5. Molecular structure of the $[Mn^{III}_3Mn^{IV}(\mu_3\text{-}O)_3X]^{6+}$ (X^- = Cl or Br) cubane core reported by Christou and coworkers (top, left) and the molecular structure of the $[Mn^{III}_2Mn^{IV}_2(\mu_3\text{-}O)_4]^{6+}$ cubane core with exclusively $\mu_3\text{-}O^{2-}$ bridges synthesized by Dismukes and coworkers (top, right). Schematic diagram of the photo-rearrangement of the Dismukes cubane to a butterfly-shaped core (bottom). H atoms are omitted for clarity. The Mn atoms of the Dismukes cubane have all been identified as the same colour, as the exact oxidation states could not be assigned. Colour scheme: Mn^{III}, blue; Mn^{IV}, olive green (Christou cubane); Mn, blue (Dismukes cubane); O, red; N, green; Cl, cyan; P, purple; C, gray. Reproduced from Refs. 39, 46 and 49.

Several butterfly-type complexes have been reported in the literature;[51,52,53,54] however, none of these contain at least one Mn^{IV}. Therefore, these complexes do not correspond to any of the physiological states of the OEC but they may be relevant to the low-valent scheme of the catalytic cycle.[24]

The "dimer of dimers" topology was another possible model proposed for the structure of the Mn atoms in the OEC. Several complexes of this type have been reported with a variety of symmetric and asymmetric bridging ligands between the two $[Mn_2(\mu\text{-}O)_2]^{n+}$ units, with the Mn ions in various oxidation states.[55,56,57,58,59] An example of this type of inorganic core is depicted in Figure 1.6, left.[59] This complex reported by Brudvig, Crabtree and coworkers features two $[Mn^{IV}{}_2(\mu\text{-}O)_2]^{4+}$ units with a terpyridine ligand coordinating to each Mn atom. Similar to this topology is the bis-μ-oxo chain reported by Girerd and coworkers (Figure 1.6, right).[60] This $\{Mn^{IV}{}_4\}$ complex comprises a chain of bis-μ-oxo units with terminal-chelating bipyridine ligands. In relevance to the native OEC, under γ-ray irradiation this complex is reduced to a $\{Mn^{III}Mn^{IV}{}_3\}$ form and exhibits an 18-line hyperfine-structured EPR signal similar to the multiline signal of the S_2 state,[57] making it a spectroscopic mimic for understanding the EPR signal at this state of the OEC.[61]

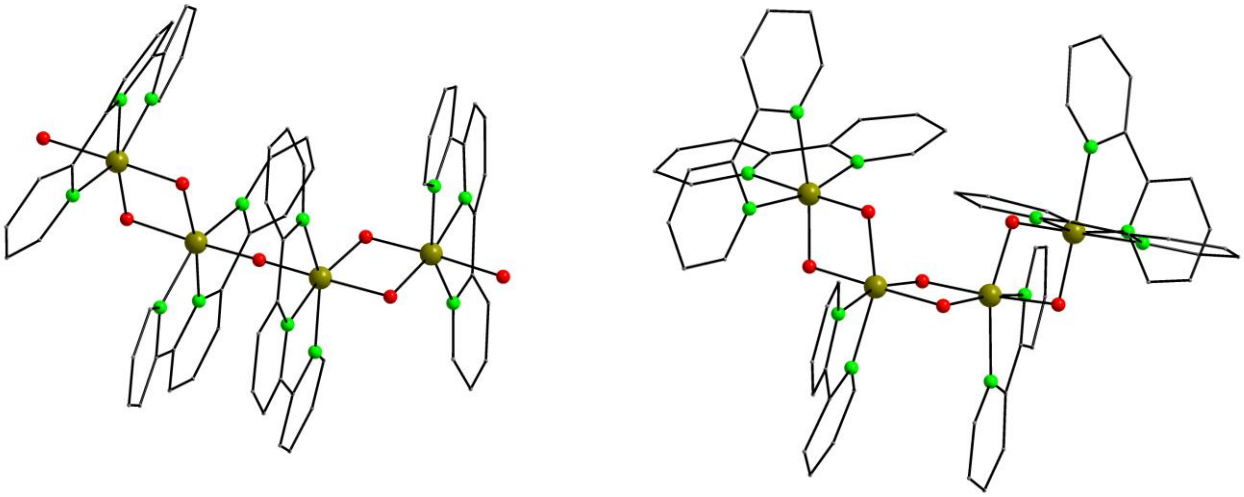

Figure 1.6. Molecular structure of the "dimer of dimers" complex synthesized by Brudvig, Crabtree and coworkers (left) and the bis-μ-oxo chain by Girerd and coworkers (right). H atoms are omitted for clarity. Colour scheme: Mn^{IV}, olive green; O, red; N, green; C, gray. Reproduced from Refs. 59 and 60.

The aforementioned Mn_4 complexes, in the absence of sufficient crystallographic data from the native OEC, have provided great insight into understanding the properties of the OEC. However more recently, X-ray diffraction (XRD) models have confirmed that none of these models have the exact structural and/or all of the spectroscopic features as the native enzyme.

In 2001, through protein crystallography, the first XRD model of PSII was established.[3a] Although this low-resolution model (3.8 Å) did not confirm the exact composition of the inorganic core, the structure was within reach. An imperative milestone was reached in 2004 by Ferreira and coworkers,[3b] establishing the "London model" of the OEC at a resolution of 3.5 Å. This model offered the first, yet incomplete suggestion of the topology of the inorganic core, indicating the presence of a $\{Mn_3CaO_4\}$ cubane with a fourth Mn ion attached through one of the

four O-bridges of the cubane (Scheme 1.3, left). The "London model" provided a defined target towards synthetic models of the OEC. This model was redefined by the "Berlin model" at a lower resolution of 3.0 Å,[62] that offered an improved view of the immediate environment of the cluster. This model was able to show the location of and the interactions between the protein subunits and cofactors, uncovering near-atomic details of the cluster. As mentioned in the previous section of this thesis, the first atomic-resolution (1.9 Å) model of the OEC was reported by Umena and coworkers in 2011.[2] This model of the inorganic core exhibits a similar view to that of the "London model" but with an altered connectivity (Scheme 1.3, right). This high-resolution model is the basis for all structural models to be compared to in order to confirm its structural efficiency as the precise location of the atoms and geometric arrangement of the $\{Mn_4CaO_5\}$ cluster has been determined through this structure.

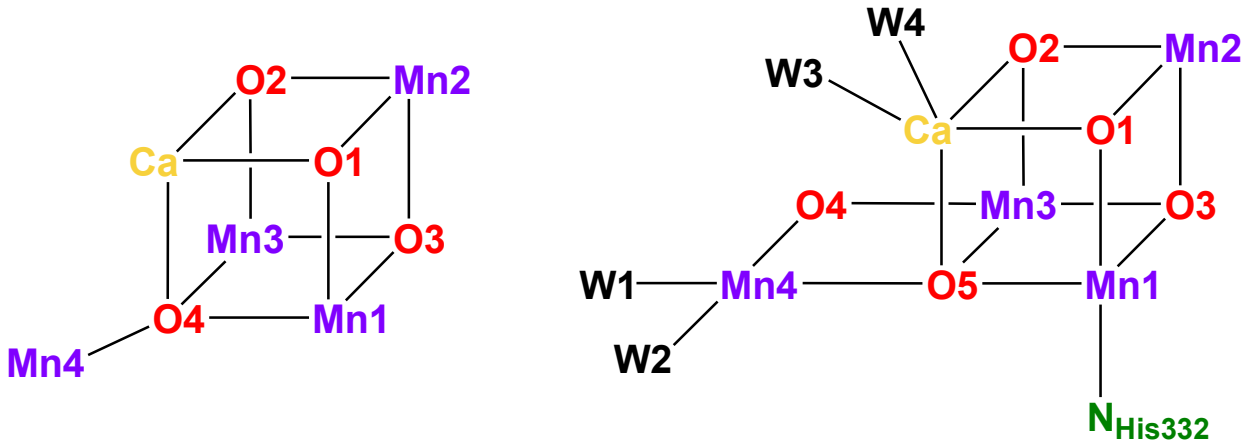

Scheme 1.3. Schematic diagram of the "London model" for the OEC core (left) and the current model for the $\{Mn_4CaO_5\}$ cluster (right). Reproduced from Ref. 39.

The structural understanding of the OEC has been determined through detailed XRD studies; however, changes in the structure due to reductive X-ray damage is a concern.[63,64,65]

Therefore, EPR and XAS[36,66,67] along with X-ray free-electron laser (XFEL)[68] techniques have been implemented in conjunction with XRD to afford more complete structural data of the OEC with the hopes of reducing radiation damage. It was not until 2015 that a 1.95 Å resolution model by Suga and coworkers[63] was established that was free from radiation damage. This structure was elucidated as relevant to the S_1 state of the OEC catalytic cycle.

Although there is still some debate about the exact structural data of OEC, even with the achievement of the 1.9 Å resolution model, the current literature is consistent with describing the complex as a heterometallic Mn–Ca cluster bridged exclusively by oxido groups and possessing a $\{Mn_3CaO_4\}$ distorted cubane conformation with an external Mn atom linked to the cubane through two bridging O^{2-} ions.

1.4 ***Mechanisms of O–O Bond Formation***

Due to the structural uncertainties of the S_n states of the OEC, the mechanism of O–O bond formation during the water oxidation process remains debatable. Based on data from XAS, EPR, XRD and kinetic substrate water exchange studies several mechanisms for O–O bond formation have been proposed.[1f,13a,13b, 69 , 70 , 71] These mechanistic proposals differ from one another in nature and location of the substrate oxido (O^{2-}) moieties that undergo O–O bond formation to yield O_2.

Since the 1.9 Å crystal structure of the OEC was reported, early proposals of water oxidation such as the manganese-only admantane[42] and the double-pivot[50] mechanisms (Scheme 1.4) proved to be incorrect on a structural basis. The crystal structure exhibits four terminal water-derived ligands suitable for O–O bond formation (Scheme 1.3), but does not clearly

identify the two substrate water molecules involved in the mechanism. The situation is further complicated by the fact that oxido bridges may also be associated in O–O bond formation. However, with this crystal structure it has become possible to interpret the extensive experimental data and narrow down the potential mechanistic proposals and the probable site of O–O bond formation on the $\{Mn_4CaO_5\}$ cluster.[72] The current mechanisms[67] for O–O bond formation are shown in Scheme 1.5 and these include: (a) nucleophilic attack (high-valent Mn^{V}-oxido or Mn^{IV}-oxido);[1f,73,74,75,76,77] (b) interaction between two oxido-bridges within a diamond-like subcore;[1e] (c) interaction between a terminal oxo-radical and a bridging oxygen;[71,78,79] and (d) the interaction of two terminal oxygen-based ligands in close proximity.[80]

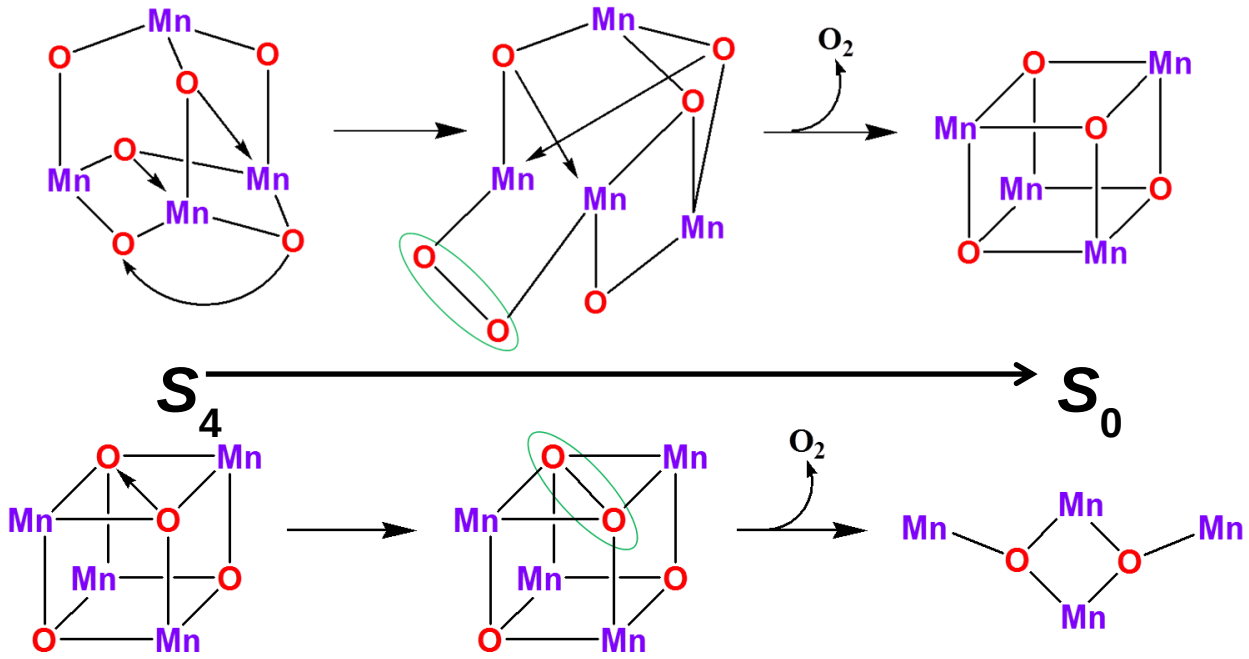

Scheme 1.4. Proposed water oxidation mechanism between a $\{Mn_4O_6\}$ adamantane-type structure and a $\{Mn_4O_4\}$ cubane (top) and from a $\{Mn_4O_4\}$ cubane to a $\{Mn_4O_2\}$ butterfly-like structure (bottom). Each mechanism shows the transition from the S_4 to S_0 state, O–O bond formation and release of O_2. Reproduced from Refs. 42 and 50.

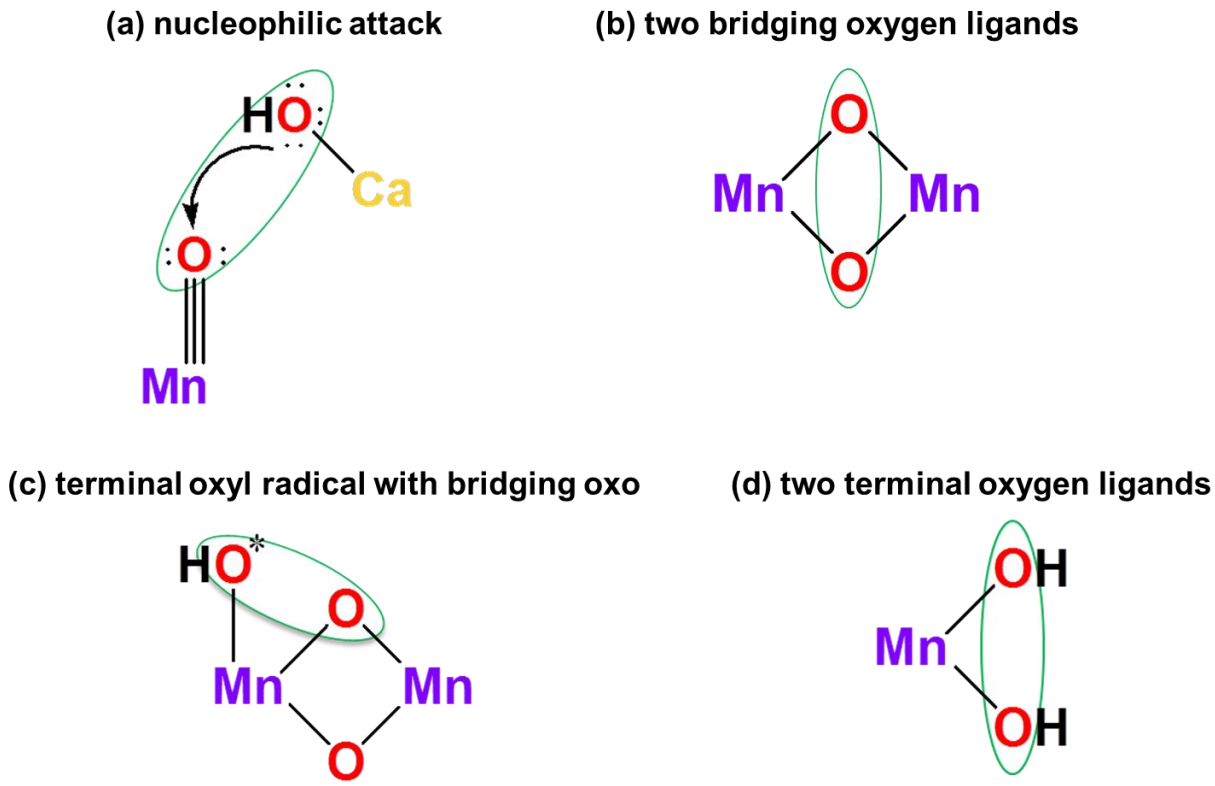

Scheme 1.5. Current mechanistic schemes for O–O bond formation by the $\{Mn_4CaO_5\}$ cluster, minimally depicted with metal-oxido species. Reproduced from Ref. 67.

Isotopic-labeling studies using mass spectrometry and magnetic resonance techniques have been used to study substrate water exchange.[32,34a, 81] These results have indicated that mechanism (c), the oxido/oxyl radical coupling mechanism, is most likely to occur. In regards to identifying the possible substrate binding sites for this mechanism, there is strong evidence in the literature for the direct ligation of the W_s to Ca^{II} and Mn.[32,34,82,83] Therefore, from the crystal structure of the OEC, three candidates exist for W_s: O1, O2 and O5 as they are all bridges between the Ca^{II} and Mn ions. From electron nuclear double resonance detected NMR (EDNMR) spectroscopy experiments[81] only one exchangeable bridge was identified as either O4

or O5. Thus, O1, O2 and O3 could be barred as substrates, in conjunction with O4 as it is not coordinated to Ca^{II}. This EDNMR analysis thereby identifies O5 as W_s. Assuming no major structural rearrangements of the OEC as it passes through the S_n cycle, then of the two Ca-bound water molecules, only W3 is in a suitable position for O–O bond formation with O5 (Scheme 1.3). This assignment is unlikely though based on the substrate water exchange rates,[32,34,82] which does not favour Ca^{II} as a binding site of W_f. Therefore, W_f must be either W1 or W2, and based on its geometric position W2 appears to be more likely for O–O bond formation (Scheme 1.3).[84] This deduction is relatively consistent with what Siegbahn and coworkers[71] have suggested based on theoretical calculations.

A new, significant milestone was reached by Suga and coworkers[85] in 2017, where they reported the structure of an intermediate state of the OEC using time-resolved serial femtosecond X-ray crystallography with an XFEL at a resolution of 2.35 Å. For a first time, this structure was able to identify the formation of an O–O bond between the well-known μ_4-O5 and a newly inserted oxygen atom (O6; Figure 1.7). The O6 atom is very close to O5 (distance of 1.5 Å), strongly suggesting this is the site for O–O bond formation, consistent with Siegbahn's oxido/oxyl radical mechanism,[71] EPR measurements[86,87] and quantum mechanics/molecular mechanics (QM/MM) calculations.[88] This achievement can really contribute to enhancing the knowledge on oxygen evolution and promoting the development of the new generation of synthetic models of the OEC.

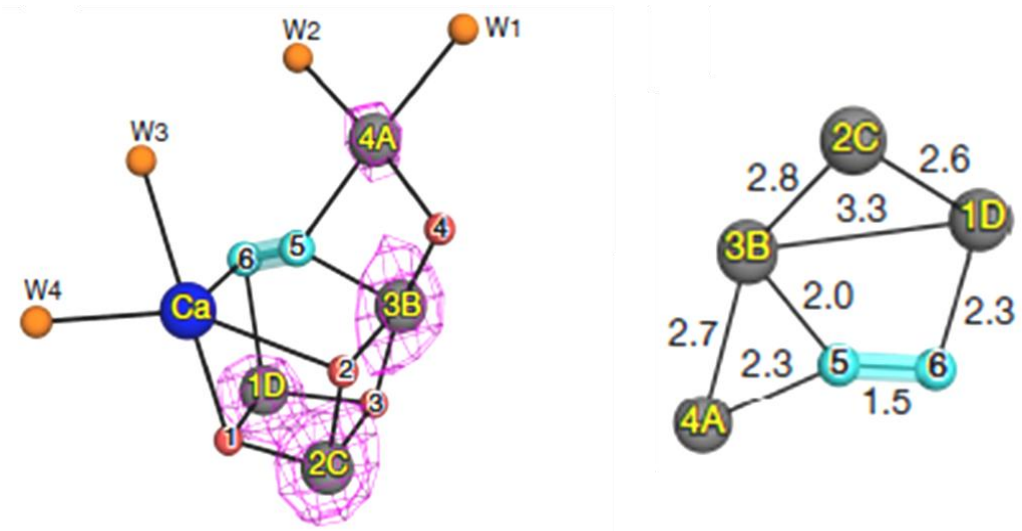

Figure 1.7. Molecular structure of the OEC at an intermediate state (left) with the position of the newly inserted O6 relative to its nearby atoms (right). Distances are in Å. The gray atoms labeled as 1D–4A represent the four Mn ions and the red and cyan atoms labeled 1–6 represent the oxygen atoms. Reproduced from Ref. 85 with permission from Nature Publishing Group.

1.5 ***Synthetic Approaches and Structural Models for Mimicking the OEC***

Synthetic biomimetic complexes have been targeted to enhance our knowledge on the structural, spectroscopic and mechanistic studies of biological systems together with investigating the possibilities of catalysis. A structural analogue is a compound that allows inference of structural characteristics common to the native site by possessing very close similarities to the targeted features. Structural analogues can differ in terms of atoms, functional groups or substructures. A functional analogue is a compound that possesses similar physical, chemical, spectroscopic or catalytic properties to the native site (Scheme 1.6). A successful analogue achieves the combination of both structural and functional modeling.[89]

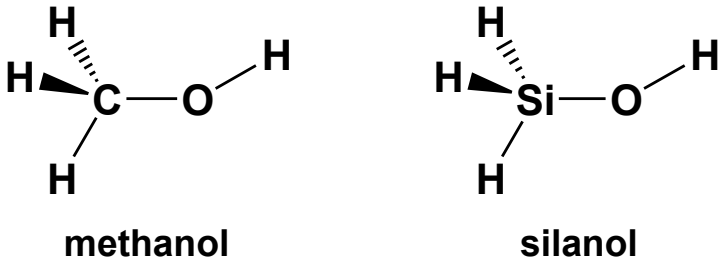

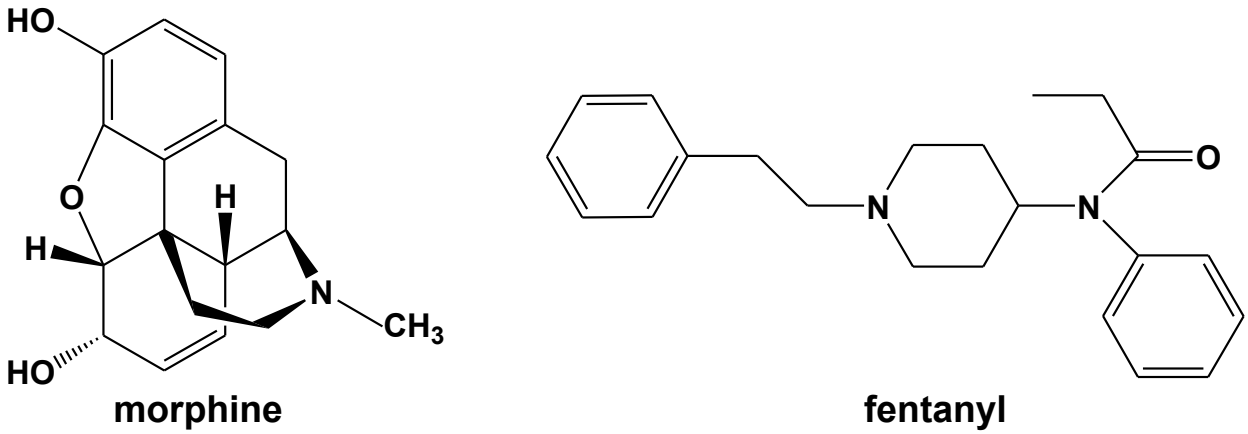

Scheme 1.6. Methanol and silanol are structural analogues as they display similar structures to one another (top). Morphine and fentanyl are functional analogues as they have the same mechanism of action, but are structurally quite different from one another (bottom).

Currently, there are two main approaches when it comes to the synthesis of biomimetic complexes. The first and most common approach towards models of the OEC is called "serendipitous assembly" or "self-assembly".[90] The distinctive feature of this approach is its complete flexibility. Simple metal salts or low-in-nuclearity metal clusters in the presence of multitopic ligands are combined in a variety of reaction solvents and conditions. Many mononuclear, dinuclear, trinuclear and tetranuclear Mn complexes have been prepared as models this way.[1f,36,37,38,40,74, 91] The second approach follows routes similar to those employed by synthetic organic chemists, where atoms and molecules are treated as building blocks to target a

specific product. This approach is known as the "design approach" or "ligand-directed approach".[92] This method uses ligands with specific binding modes as well as metals with well-defined coordination sites and geometries. By using this method, a high level of design is introduced into the synthetic model with some predictability to what the final product may be.

Synthetic Mn coordination clusters have played an important role in understanding the OEC, inspiring both structural and mechanistic proposals. Early model complexes, detailed in Section 1.3 and reviewed in the literature,[39,41,45,49,51-60,91] have been instrumental for XAS, EPR, water exchange and computational studies, providing pivotal information for understanding the OEC. However, with the elucidation of the composition and arrangement of the atoms in the OEC, synthetic models have moved from strictly homometallic Mn complexes to heterometallic Mn–Ca models in order to mimic the native enzyme more accurately. Based on Ca K-edge XAS data,[7] the Ca^{II} ion was proposed to be closely associated with the tetramanganese motif of the OEC, with a Mn–Ca separation of 3.4 Å, which was later confirmed and in agreement with the "London model" crystal structure revealing a $\{Mn_3CaO_4\}$ cubane motif.[3b] Synthetic Mn–Ca complexes were targeted not only as analogues of the OEC but also to understand and explain the effect of the redox inactive metal on the chemistry of Mn cluster compounds.

The first high oxidation state Mn–Ca cluster was synthesized by Christou and coworkers in 2005. [93] This high nuclearity cluster compound with a formula of $[Mn_{13}Ca_2O_{10}(OH)_2(OMe)_2(O_2CPh)_{18}(H_2O)_4]$ contained two $\{Mn_4CaO_4\}$ subunits within it, with one being very similar in structure to the "London model" (Figure 1.8). A Ca K-edge XAS study on this cluster revealed a Mn–Ca separation of ~3.5 Å akin to the one in the OEC. From a bioinorganic perspective, the pentadecanuclearity of this complex is too large to model the OEC. This complex, however, has provided a foundation on how to approach the synthesis of the

native {Mn_4Ca} unit responsible for oxygen evolution, specifically by modifying the reaction system to foster the formation of lower nuclearity products.

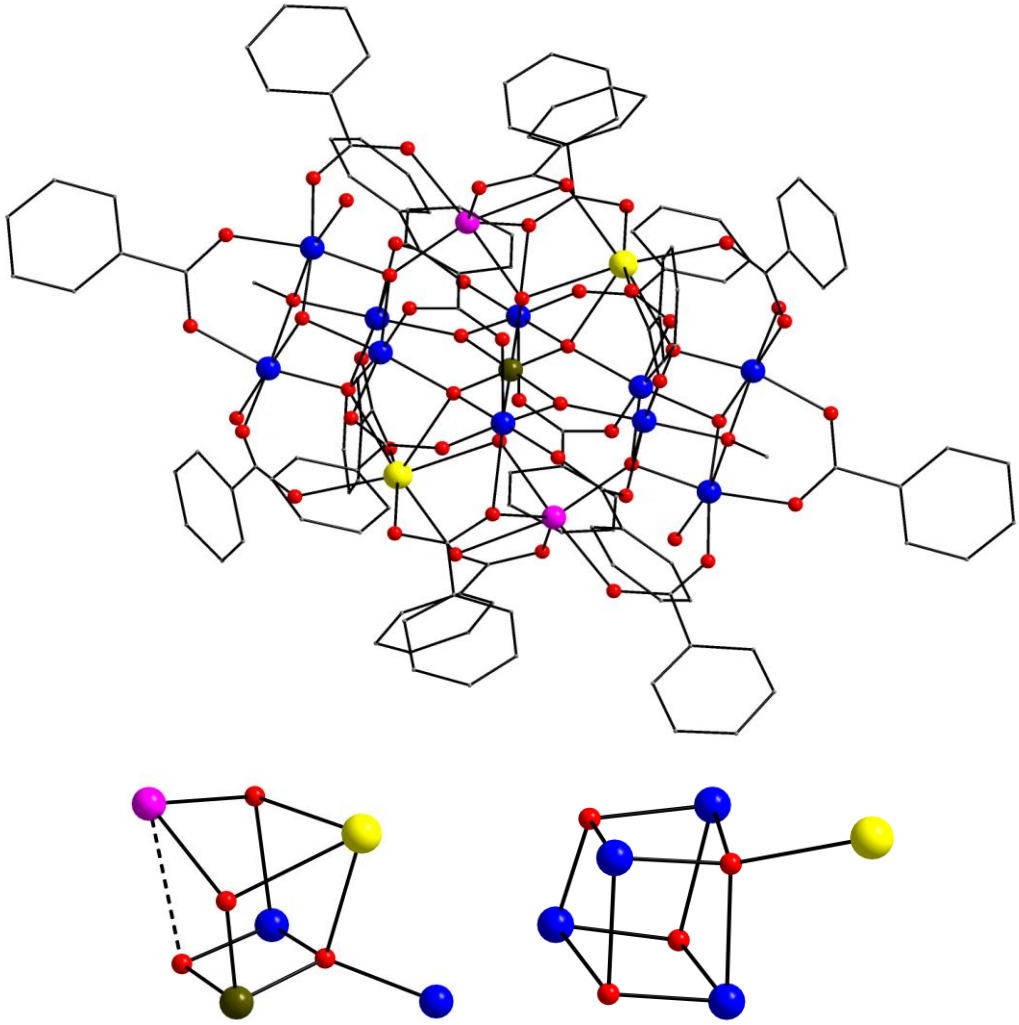

Figure 1.8. Molecular structure of the {$Mn_{13}Ca_2$} complex reported by Christou and coworkers (top) and the two cubane subunits within the complex (bottom). On the left is the {Mn_4CaO_4} unit resembling the "London model" of the OEC; the dashed line indicates the weak Mn–O bond. On the right is the {Mn_4O_4} cubane with an external Ca^{II} attached to it. H atoms are omitted for clarity. Colour scheme: Mn^{II}, magenta; Mn^{III}, blue; Mn^{IV}, olive green; Ca^{II}, yellow; O, red; C, gray. Reproduced from Ref. 93.

Two heterometallic Mn–Ca complexes have been reported in the literature with the correct 4Mn:Ca metal stoichiometry, although both complexes have low oxidation states and oxido content, making them more relevant to the low-valent scheme of the OEC. The first complex reported by Powell and coworkers[94] contains a trigonal bipyramidal arrangement of metals with three Mn^{III} atoms forming the triangular plane with Mn^{II} and Ca^{II} atoms in the apical positions (Figure 1.9, top). The three Mn^{III} metal centers are chelated by a tridentate Schiff base ligand (condensed from *o*-vanillin and 2-hydroxypropylamine) through the deprotonated phenol and propanol O atoms and the imino N atom. The Mn^{III} atoms are linked through an oxido ligand, two μ-Cl atoms and a bidentate acetate group. Two deprotonated phenol and one deprotonated propanol O atoms bridge the triangular arrangement to the Mn^{II} with a terminal Cl^- completing its coordination sphere. Conversely, two deprotonated propanol and one deprotonated phenol O atoms serve to bridge the Ca^{II} to the triangular arrangement. Peripheral ligation of the Ca^{II} is provided by the central oxido ligand and terminally bound water and methanol molecules. Similar $\{Mn^{III}_3M^{II}Na\}$ (M = Mn, Ca) complexes were isolated by the same group that showed O_2 evolution in the presence of O-atom transfer agents and water.[95] The second complex produced by Stamatatos and coworkers[96] displayed a square pyramidal topology with the four Mn^{III} atoms forming the near-planar square base with the Ca^{II} atom in the apical position (Figure 1.9, bottom). The edges of the $\{Mn_4\}$ square unit are composed of diatomic oximate groups and the ideal planarity of the $\{Mn_4\}$ square unit is due to the large Mn–N–O–Mn torsion angles, close to linearity. The Mn^{III} atoms are linked to the Ca^{II} through the oximate O atoms and four bidentate bridging benzoate groups. This cluster contains no bridging oxido ligands and is relevant to the lower oxidation S_1 state of the OEC.

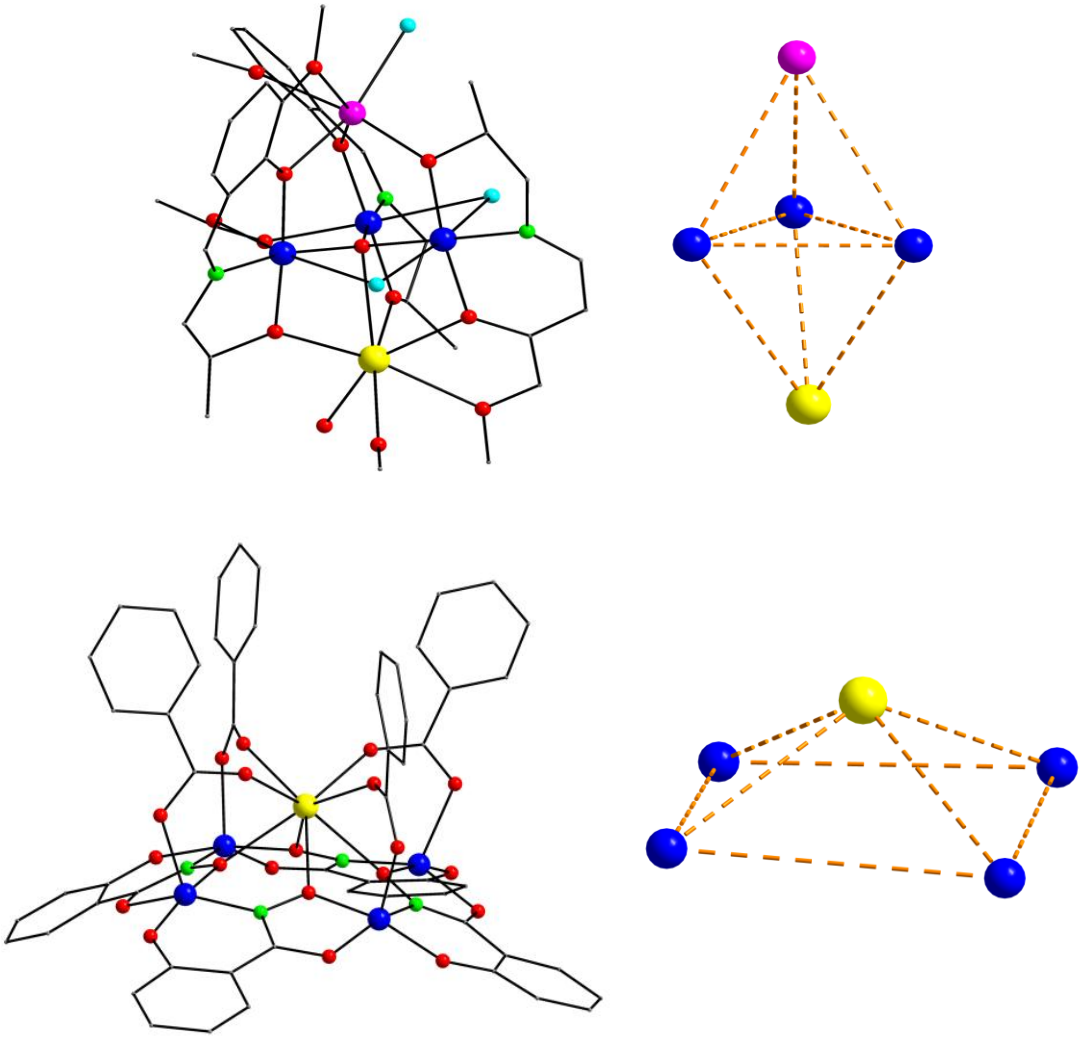

Figure 1.9. Molecular structures of the {Mn_4Ca} compounds relevant to the lower oxidation species of the OEC. The overall molecular structures are shown on the left with the metal topologies of these complexes on the right. The complex synthesized by Powell and coworkers exhibits a trigonal bipyramidal metal topology (top), while the complex by Stamatatos and coworkers displays a square pyramidal metal topology (bottom). The orange dashed lines represent the virtual Mn···Mn and Mn···Ca bonds. H atoms are omitted for clarity. Colour scheme: Mn^{II}, magenta; Mn^{III}, blue; Ca^{II}, yellow; O, red; N, green; Cl, cyan; C, gray. Reproduced from Refs. 94 and 96.

Considering the fast development of the field of heterometallic Mn–Ca chemistry, all the structurally characterized Mn–Ca cluster compounds, apart from the ones that will be discussed in this thesis, reported to date are listed in Table 1.1, together with some of the most significant features from a bioinorganic perspective (i.e., metal stoichiometry and Mn oxidation states). From Table 1.1, it is apparent that there is a variety of Mn–Ca complexes in the literature, unique in their metal stoichiometry, topology, Mn oxidation states and nature of their ancillary ligands. The most successful synthetic models will be highlighted and discussed here.

Table 1.1. Chemical Formulae and Structural Details for the Mn–Ca Cluster Compounds Reported to Date.

Formula[a,b]	Metal Stoichiometry	Mn Oxidation States	Ref.
$[Mn_3CaO_3(OH)(L1)(ON_4O)(O_2CMe)]^+$	3Mn:1Ca	3 Mn^{IV}	109
$[Mn_3CaO_4(L1)(ON_4O)(O_2CMe)]$	3Mn:1Ca	3 Mn^{IV}	109
$[Mn_3CaAgO_4(L1)(ON_4O)(O_2CMe)(OTf)]$	3Mn:1Ca	3 Mn^{IV}	109
$[Mn_3CaO_4(L1)(O_2CMe)_3(THF)]$	3Mn:1Ca	3 Mn^{IV}	107
$[Mn_6CaO_2(L1)_2(O_2CMe)_6]^{2+}$	6Mn:1Ca	2 Mn^{II}, 4 Mn^{III}	107
$[Mn_3CaO_2(L1)(O_2CMe)_2(DME)(OTf)]^{2+}$	3Mn:1Ca	2 Mn^{III}, 1 Mn^{IV}	97
$[Mn_3CaO_2(L1)(O_2CMe)_2(DME)(OTf)]^+$	3Mn:1Ca	3 Mn^{III}	97
$[Mn_3CaO_2(L1)(O_2CMe)_2(H_2O)_3]^{3+}$	3Mn:1Ca	2 Mn^{III}, 1 Mn^{IV}	97
$[Mn_3CaNaO(L2)_3(N_3)_3(MeOH)]^+$	3Mn:1Ca	3 Mn^{III}	95
$[Mn_{13}Ca_2O_{10}(OH)_2(OMe)_2(O_2CPh)_{18}(H_2O)_4]$	13Mn:2Ca	2 Mn^{II}, 10 Mn^{III}, 1 Mn^{IV}	93
$[Mn_4CaO_4(O_2CBu^t)_8(Bu^tCO_2H)_2(py)]$	4Mn:1Ca	2 Mn^{III}, 2 Mn^{IV}	111
$[Mn_4CaO_4(O_2CBu^t)_8(Bu^tCO_2H)(py)_2]$	4Mn:1Ca	2 Mn^{III}, 2 Mn^{IV}	111

$[Mn_4CaO_4(O_2CBu^t)_8(Bu^tCO_2H)_2(qn)]$	4Mn:1Ca	2 Mn^{III}, 2 Mn^{IV}	111
$[Mn_6Ca_2O_2(Me\text{-}sao)_6(O_2CEt)_6(H_2O)_2]_n$	6Mn:2Ca	6 Mn^{III}	98
$[Mn_4CaOCl_3(L3)_3(O_2CMe)(H_2O)_{1.5}(MeOH)_{0.3}]^+$	4Mn:1Ca	1 Mn^{II}, 3 Mn^{III}	94
$[Mn_2Ca_2(L4)_2(DMF)_4]$	2Mn:2Ca	2 Mn^{II}	99
$[MnCa_2(L4H)_2(DMF)_4]$	1Mn:2Ca	1 Mn^{II}	99
$[Mn_3CaNa(sal)_6(H_2O)_6]_n$	3Mn:1Ca	3 Mn^{III}	100
$[Mn_2Ca_2(tpaa)_2(H_2O)_{12}][Mn(tpaa)]_2$	2Mn:2Ca	2 Mn^{II}	101
$[MnCa_2(Hcit)_2(H_2O)_4]_n$	1Mn:2Ca	1 Mn^{II}	102
$[Mn_6Ca_2O_9(O_2CBu^t)_{10}(H_2O)_4]$	6Mn:2Ca	6 Mn^{IV}	103
$[Mn_6Ca_2O_9(O_2CBu^t)_{10}(H_2O)_3(CH_3CO_2C_2H_5)]$	6Mn:2Ca	6 Mn^{IV}	103
$[Mn_6Ca_2O_9(O_2CBu^t)_{11}][Mn_3O(O_2CBu^t)_6(py)_3]$	6Mn:2Ca	6 Mn^{IV}	103
$[Mn_4Ca_2Cl_4(OEtOMe)_8]$	4Mn:2Ca	4 Mn^{II}	104
$[MnCa_2(O_2CCCl_2)_6(bipy)_2(H_2O)(MeOH)]$	1Mn:2Ca	1 Mn^{II}	105
$[Mn_3Ca_2O_4(O_2CBu^t)_8(Bu^tCO_2H)_4]$	3Mn:2Ca	3 Mn^{IV}	110
$[Mn_6Ca_2O_9(O_2CPhBu^t)_{10}(Bu^tPhCO_2H)_5]$	6Mn:2Ca	6 Mn^{IV}	106
$[Mn_4Ca(O_2CPh)_4(shi)_4]^{2-}$	4Mn:1Ca	4 Mn^{III}	96

[a] Excluding all lattice solvate molecules and counterions.

[b] Abbreviations: n.r. = not reported; $L1H_3$ = 1,3,5-tris(2-di(2'-pyridyl)hydroxymethylphenyl)benzene; THF = tetrahydrofuran; HON_4OH = N,N'-dimethyl-N,N'-diacetylethylenediamine dioxime; OTf^- = trifluoromethanesulfonate; $L2H_3$ = 2-(2,3-dihydroxypropyliminomethyl)-6-methoxyphenol; $L3H_2$ = 2-[[(2-hydroxypropyl)imino]methyl]-6-methoxyphenol; $L4H_4$ = *p*-*t*-butylthiacalix[4]arene; DME = 1,2-dimethoxyethane; qn = isoquinoline; Me-$saoH_2$ = 2-hydroxyphenylethanone oxime; L5H = 2-naphthoic acid; L6H = 9-anthracenecarboxylic acid; L7H = 1-pyrenecarboxylic acid; DMF = dimethylformamide; H_2sal = salicylic acid; H_3tpaa = 6,6',6"-nitrilotris(methylene)tripicolinic acid; H_4cit = citric acid;

MeOEtOH = 2-methoxyethanol; bipy = 2,2'-bipyridine; Bu^tPhCO_2H = *p*-tert-butylbenzoic acid; $shiH_3$ = salicyclhydroxime.

[c]From magnetic susceptibility data.

Taking a designed approach, Agapie and coworkers [107] synthesized the desired $\{Mn_3CaO_4\}$ inorganic core that structurally models the trimanganese-calcium cubane found within the native OEC (Figure 1.10). To access this structure, a trinucleating ligand framework was employed, designed to bind three metals within close proximity to one another, accommodate multiple coordination modes and be oxidatively robust. The three Mn atoms are all in the 4+ oxidation state supporting this complex as a feasible structure found in the latter stages of the S_n cycle.

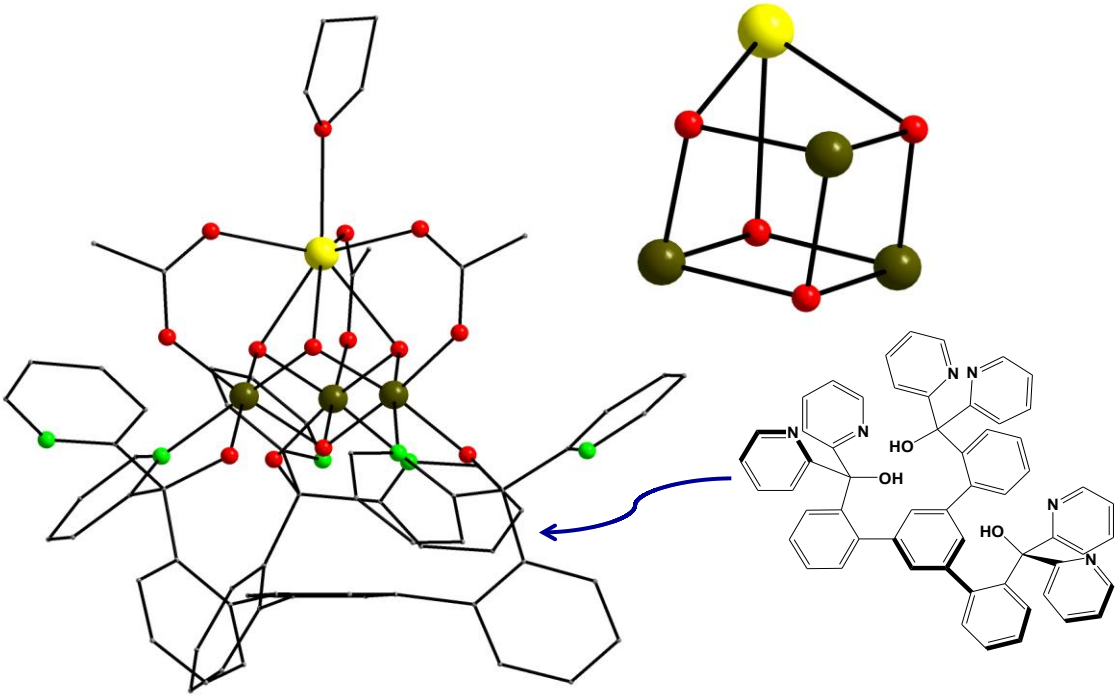

Figure 1.10. Molecular structure, inorganic core and trinucleating ligand reported by Agapie and coworkers. This complex structurally models the desired $\{Mn_3CaO_4\}$ cubane of the native OEC. H atoms are omitted for clarity. Colour scheme: Mn^{IV}, olive green; Ca^{II}, yellow; O, red; N, green; C, gray. Reproduced from Ref. 107.

Another highlight of this ligand is that it promotes site-differentiated functionalization,[108] binding three metals of the $\{M_4X_4\}$ biomimetic core and leaving the fourth metal center open to ligand substitution or replacement by a heterometal. This methodology would allow the dangler Mn atom to be inserted. The same group was able to coordinate a fifth metal ion, Ag^+, resulting in a $\{Mn_3CaAgO_4\}$ cluster that models the topology of the OEC displaying both the cubane motif with the dangler transition metal (Figure 1.11).[109] This complex provided a more rational way of accessing more accurate models of the OEC.

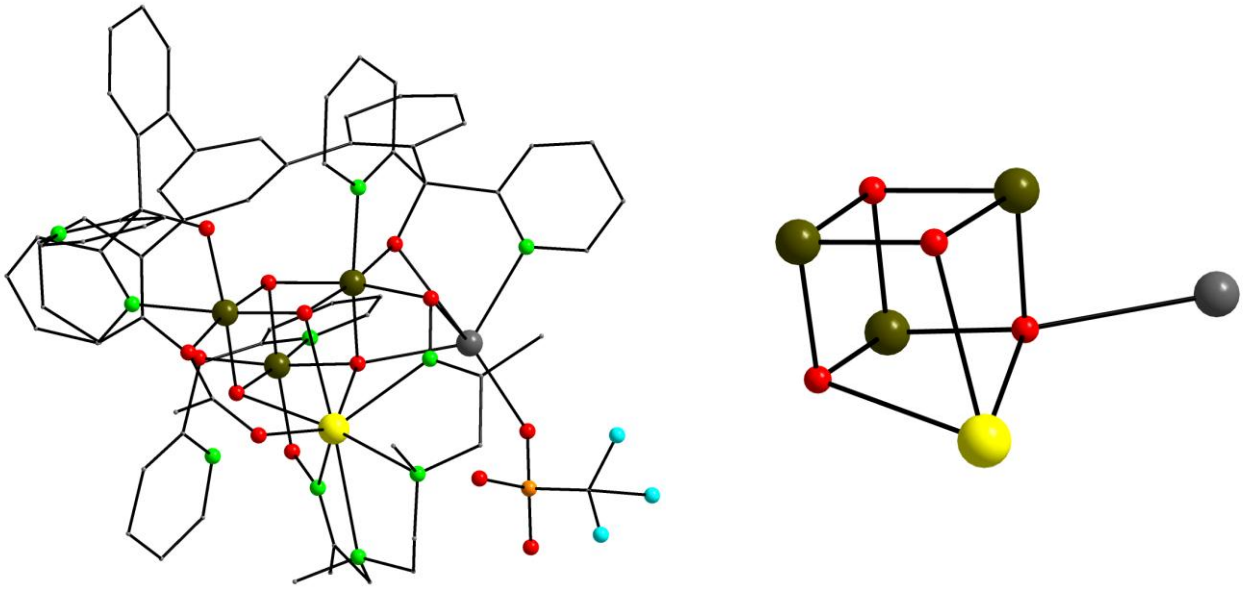

Figure 1.11. Molecular structure of the $\{Mn_3CaAgO_4\}$ cluster displaying the cubane motif with a dangler transition metal. H atoms are omitted for clarity. Colour scheme: Mn^{IV}, olive green; Ag^{I}, silver; Ca^{II}, yellow; O, red; N, green; F, cyan; S, orange; C, gray. Reproduced from Ref.109.

Foregoing the rational design approach, Christou and coworkers[110] reported the synthesis of an asymmetric $\{Mn_3CaO_4\}$ cubane with an external Ca atom attached to it (Figure 1.12). This model has the Mn atoms all in the 4+ oxidation state, the overall topology very close to that of the native enzyme and the nature of the metals relevant to the biological catalyst. Magnetic susceptibility studies have established this complex to have an $S = 9/2$ ground state, which was also confirmed by EPR spectroscopy. The Davies ENDOR data revealed similar hyperfine couplings to the OEC S_2 state.[47,61] The isolation of this complex is an important feat for the foundation of future work with the hope of replacing the external Ca with Mn.

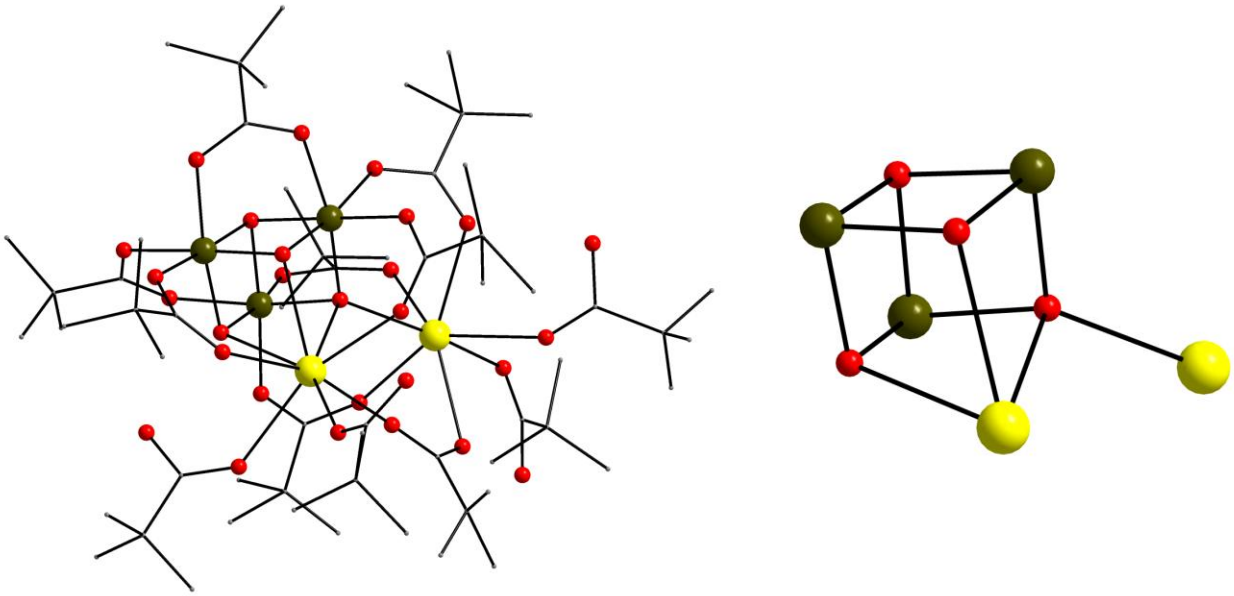

Figure 1.12. Molecular structure of the $\{Mn_3Ca_2\}$ cluster consisting of an asymmetric $\{Mn_3CaO_4\}$ cubane with an external Ca^{II} atom. H atoms are omitted for clarity. Colour scheme: Mn^{IV}, olive green; Ca^{II}, yellow; O, red; C, gray. Reproduced from Ref.110.

More recently, Zhang and coworkers[111] were able to isolate a $\{Mn_3CaO_4\}$ inorganic cubane with an external Mn atom, mimicking for the first time the correct metal stoichiometry and topology of the native enzyme (Figure 1.13). This complex is mixed-valent with two of the Mn atoms in the 3+ oxidation state and two in the 4+ oxidation state, in complete analogy to the OEC in its S_1 state. Like the native OEC, this complex can undergo four redox transitions[67,69,112] and exhibits two magnetic resonance signals at g = 2 and g = 4.9, similar to the well-known signals observed for the S_2 state of the native OEC.[47,61] Although this model is the most relevant to the native enzyme to date, it still deviates in several functionally crucial aspects. It is worthy to note that this complex was made under the exact same conditions as the $\{Mn_3Ca_2\}$ cluster of Christou and coworkers (Figure 1.12), with the only difference being the nature of the reaction solvent (MeCN versus MeCN/pyridine/ethyl acetate); this further emphasizes the structural

sensitivity of cluster compounds upon exposure to different synthetic conditions (i.e., solvents, temperature, pH, etc.).

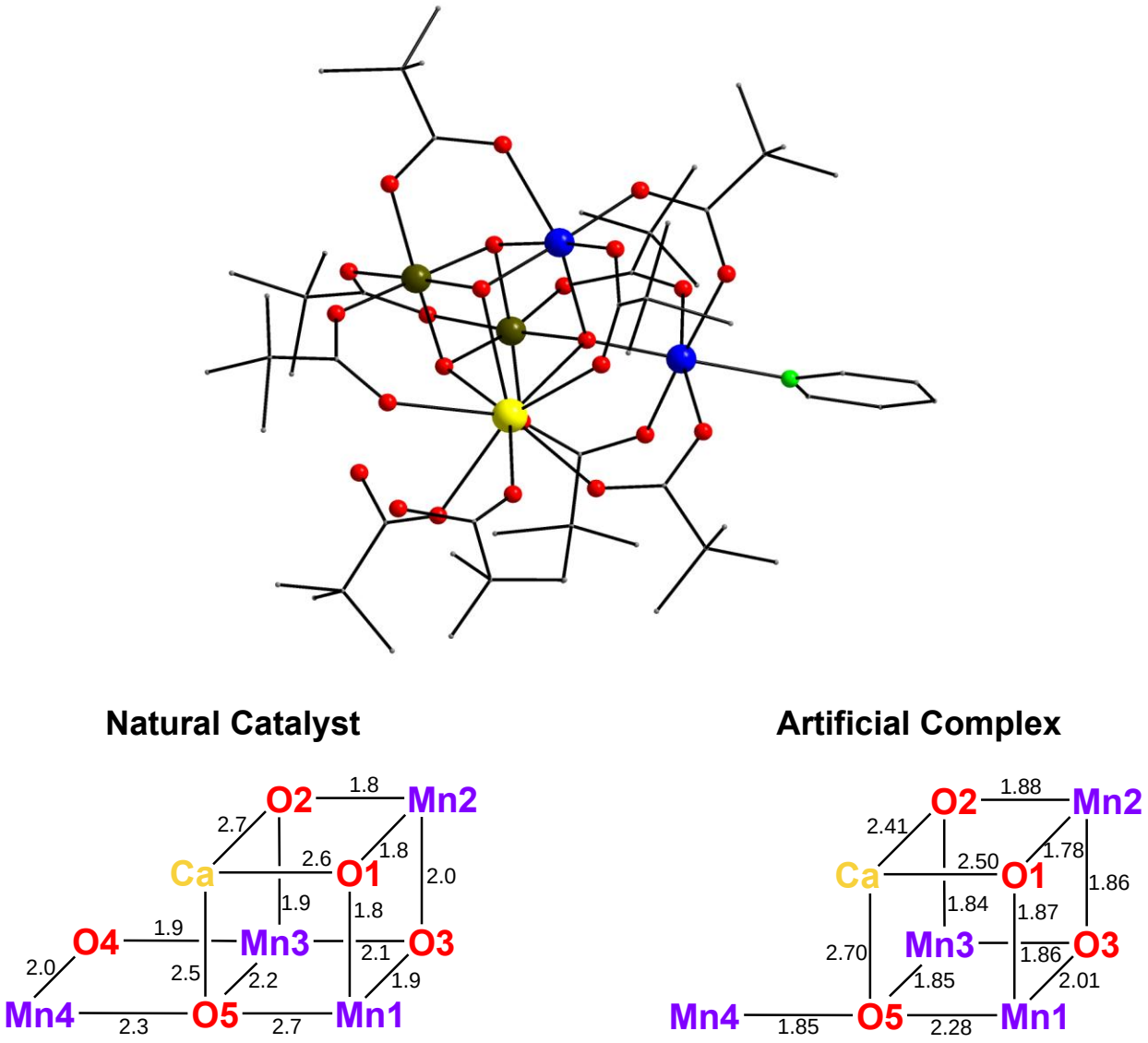

Figure 1.13. Molecular structure of the most successful synthetic model of the OEC to date (top). Schematic diagram of the $\{Mn_4CaO_5\}$ core of the native OEC (bottom, left) and the $\{Mn_4CaO_4\}$ inorganic core of Zhang and coworkers (bottom, right). Distances are in Å. H atoms are omitted for clarity. Colour scheme: Mn^{III}, blue; Mn^{IV}, olive green; Ca^{II}, yellow; O, red; N, green; C, gray. Reproduced from Ref.111.

These complexes have provided valuable insight into the structural, spectroscopic and physicochemical properties of the OEC. The future of this research field is oriented towards the development of more accurate functional models of the OEC, thus providing new directions to the understanding and designing improved catalysts for artificial photosynthesis.

1.6 ***The Choice of the Organic Chelating/Bridging Ligands***

An important factor in the synthesis of biomimetic metal complexes is the choice of the primary organic chelating/bridging ligands or "ligand blends" to stabilize crystalline products. The ligands coordinated to the native $\{Mn_4CaO_5\}$ cluster have been identified as exclusively oxido bridges, amino acid residues and water molecules (Table 1.2).[2] This gives rise to a saturated ligand environment of the OEC, in which each Mn atom is six-coordinate and the Ca^{II} atom is seven-coordinate. The ligands employed for synthetic models have important implications for the symmetry, topology and nuclearity of the cluster, as well as its spectroscopic, physicochemical and catalytic properties.

Table 1.2. Ligands of the $\{Mn_4CaO_5\}$ Cluster Compound within the Native OEC.

Atom	Ligands[a]
Mn1	O1; O3; O5; E189; H332; D342
Mn2	O1; O2; O3; D342; A344; E354
Mn3	O2; O3; O4; O5; E333; E354
Mn4	O4; O5; D170; E333; W1; W2

Ca	O1; O2; O5; D170; A344; W3; W4

[a]Abbreviations: E189 = D1-Glu 189; D170 = D1-Asp 170; E333 = D1-Glu 333; D342 = D1-Asp 342; A344 = D1-Ala 344; E354 = CP43-Glu 354; H332 = D1-His 332; O = oxygen from oxido groups; W = water.

The family of organic ligands that I decided to explore towards the synthesis of new structural models of the OEC was based on the oxime functionality. There is currently a renewed interest of oximes and research efforts are driven by a number of considerations, including the desire to make useful bioinorganic models. Oximes are considered reasonable models for the biologically important imidazole group of the histidine amino acid. The oximate group (>C=N–O^-) has also proven to be extremely versatile for binding to Mn atoms in high oxidation states (Mn^{III} and Mn^{IV}),[113] which is a targeted structural feature of the OEC.[39] The oximate group can coordinate to a metal ion(s) in a variety of different modes (Scheme 1.7),[113a, 114] accommodating one to three metal centers.

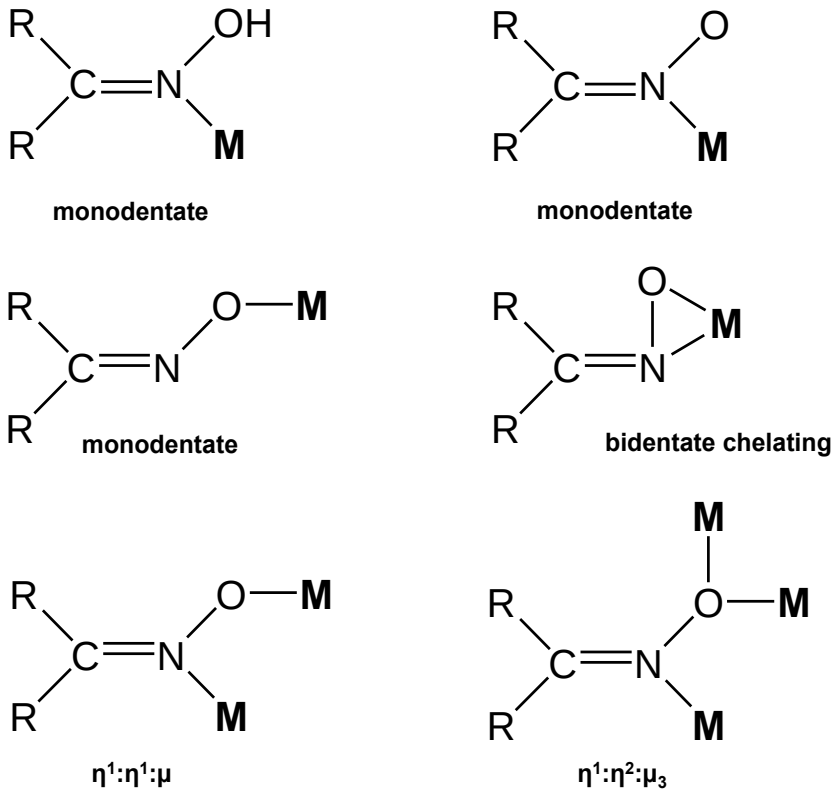

Scheme 1.7. The crystallographically established coordination modes of the oxime and oximate groups (R = various; M = metal). Symbols "η" and "μ" denote the "hapticity" of the donor atoms and the "bridging" fashion of the entire group, respectively.

The type of isomerism about a C=C double bond is also possible with the C=N double bond, although in this case only three groups are connected to the double-bonded atoms. The method that can be applied is based on the Cahn-Ingold-Prelog (CIP) system.[115] The two functional groups at the carbon atom are ranked by the CIP sequence rules (atomic number). The isomer with the higher ranking group and the –OH group on the same side of the double bond is the *Z* (for the German word *zusammen* meaning together) or *syn* isomer; the other is the *E* (for *entgegen* meaning opposite) or *anti* isomer (Scheme 1.8). If there is more than one oxime group in a molecule, the number of isomers increase (i.e., *Z*, *Z*; *Z*, *E*; and *E*, *E*). The employment of

oximes in the synthesis of models of the OEC can lead to the isolation of new molecular species with interesting properties that can further enrich our knowledge of the OEC.

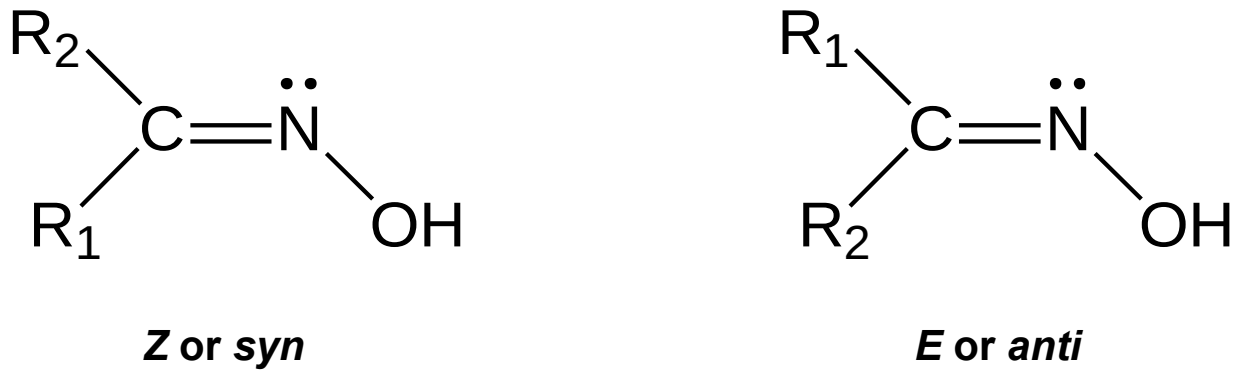

Scheme 1.8. The *Z*–*E* isomerism of the oxime group, assuming that R_1 takes precedence over R_2 according to the CIP sequence rules.

The first organic ligand that I decided to explore was salicylhydroxamic acid ($shaH_2$, Scheme 1.9). Literature has shown that hydroxamic acids are excellent ligands in the area of coordination chemistry [116, 117] and are photosynthetically effective groups. [118] Pecoraro and coworkers[119] have elegantly shown that $shaH_2$ could potentially undergo a metal-assisted amide-iminol tautomerism, and thus transform to salicylhydroxime ($shiH_3$, Scheme 1.9). The latter is an oximate-based ligand with four coordination sites available for binding to both Mn and Ca metal centers.

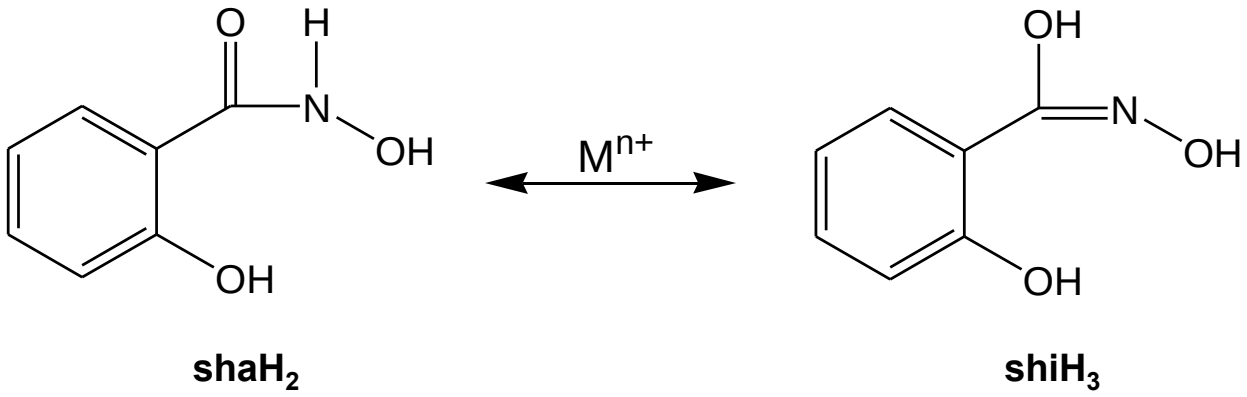

Scheme 1.9. Metal-assisted amide-iminol tautomerism of salicylhydroxamic acid ($shaH_2$) to salicylhydroxime ($shiH_3$).

Previous use of this ligand in homometallic Mn chemistry[120] has revealed that the oximate group of the shi^{3-} ligand afforded, in every instance, a metallacrown motif of either a [12–$MC_{Mn(III)N(shi)}$–4] or [15–$MC_{Mn(III)N(shi)}$–5] arrangement, surrounding a central or slightly displaced Mn^{II} atom (Figure 1.14). Although these complexes in the literature have not been synthesized as models of the OEC, but for magnetism applications and other biological functions, one highlight to take away is that there is a potential of replacing the central Mn^{II} with a Ca^{II} metal center to make the complexes more biologically relevant. The Mn–Ca complexes that I have synthesized with shi^{3-} will be discussed in Chapters 2 and 3 of this thesis.

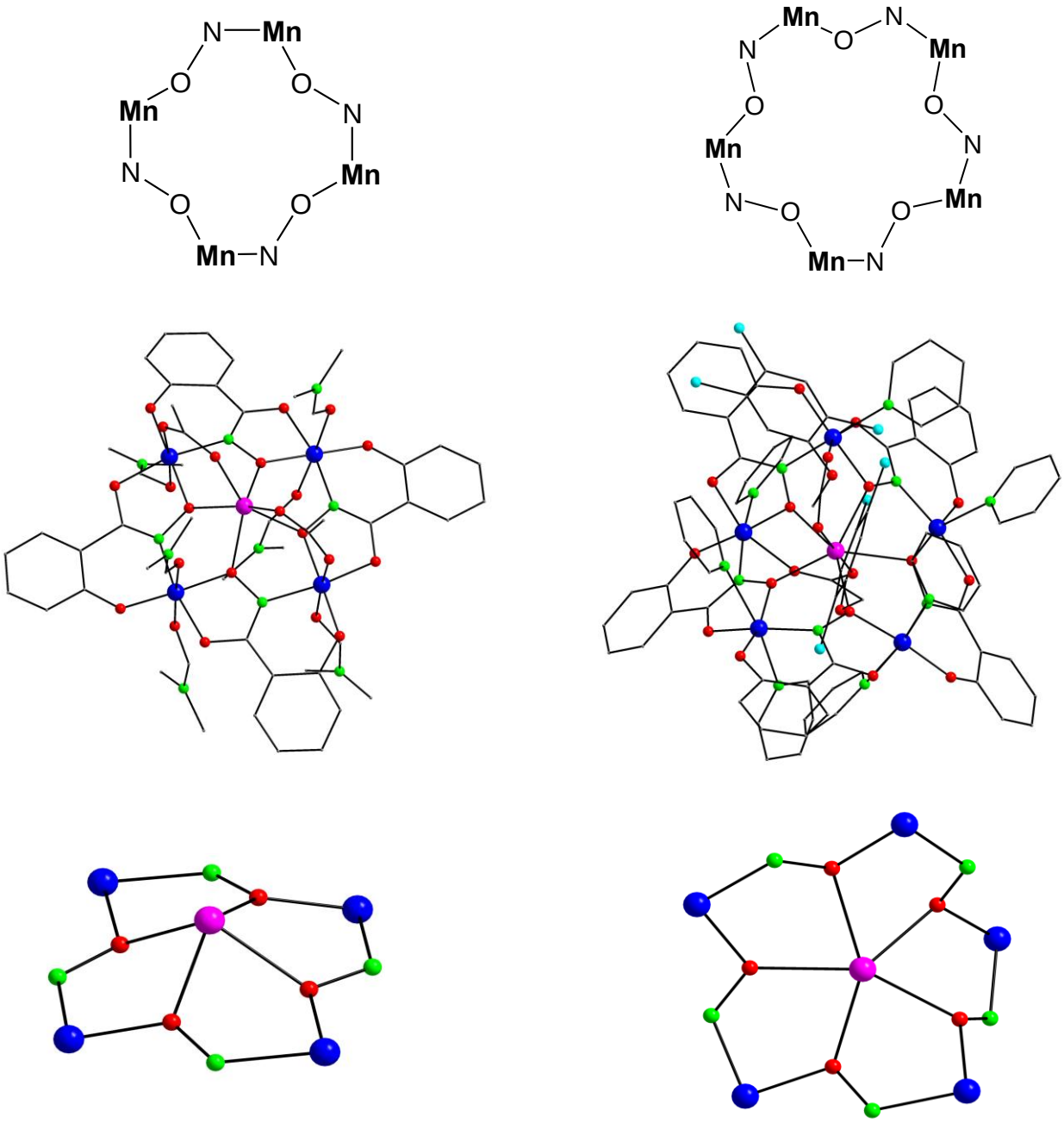

Figure 1.14. Two representative examples of the [12-$MC_{Mn(III)N(shi)}$-4] and [15-$MC_{Mn(III)N(shi)}$-5] metallacrown motifs with central Mn^{II} atoms. Schematic representations of the metallacrown arrangements (above), the molecular diagrams of the entire molecules (middle) and inorganic cores (bottom) are illustrated. H atoms are omitted for clarity. Colour scheme: Mn^{II}, magenta; Mn^{III}, blue; O, red; N, green; Cl, cyan; C, gray. Reproduced from Refs. 120b and 120d.

Simple pyridyl oximes have the general structures depicted in Scheme 1.10 and consist of a pyridyl group, at positions 2-, 3- or 4-, attached to the oxime carbon atom. The R group can be a donor or a non-donor group. Pyridyl oximes can also contain multiple pyridyl and/or oxime functionalities within the same molecule.

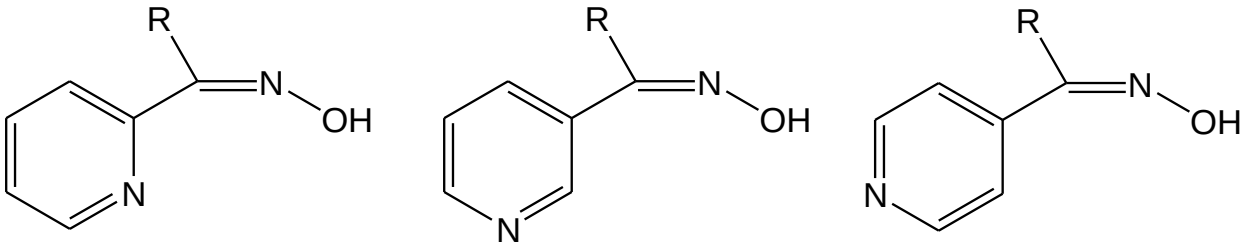

Scheme 1.10. General structures of pyridyl oximes (R = various).

Pyridyl oximes consisting of one oxime group, one pyridyl group and no other donor atoms are the most common in the literature and most of these ligands contain a 2-pyridyl group. Examples of simple 2-pyridyl mono- and di-oximes found in homometallic Mn chemistry are illustrated in Scheme 1.11. The applications of these complexes is strictly towards producing single-molecule magnets (SMMs), as oximes are known to promote strong magnetic exchange interactions between the Mn metal centers. A recent search on the structural database (Cambridge Structural Database; CSD) revealed the absence of any crystallographically characterized Mn–Ca heterometallic compound bearing a pyridyl oxime or pyridyl dioxime ligand.

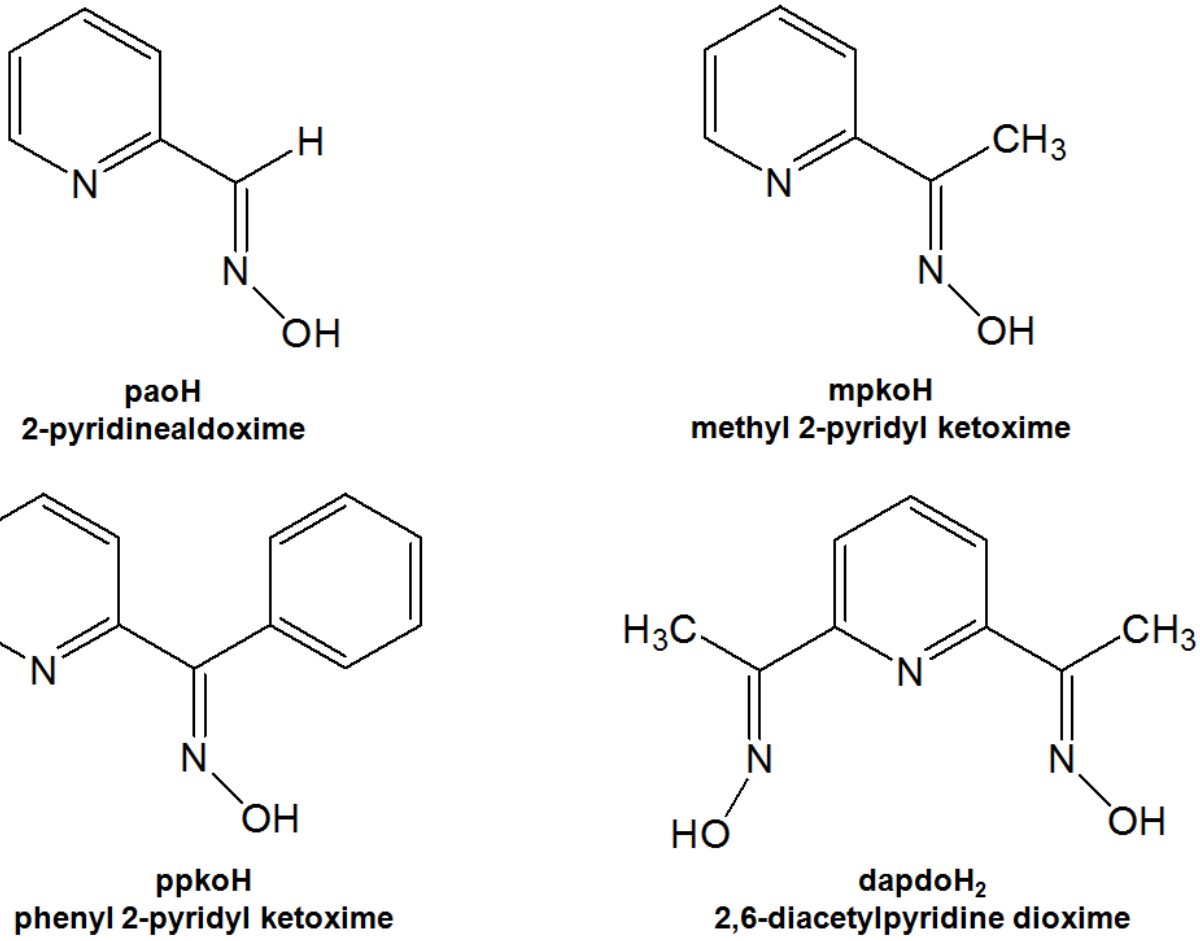

Scheme 1.11. Examples of 2-pyridyl mono- and di-oximes employed in homometallic Mn chemistry.

The pyridyl-containing mono- and di-oxime ligands employed in my research projects were quinoline-2-aldoxime (qaoH; Scheme 1.12), a relative to paoH, and dapdoH_2 (Scheme 1.11) respectively. Both qaoH and dapdoH_2 ligands are not commercially available but their synthesis is straightforward, involving the general reaction between the corresponding carbonyl-based precursor and hydroxylamine. Surprisingly, given its structural similarity with the ligand paoH, qaoH ligand has never been previously utilized in Mn chemistry; in fact, this ligand has only been previously reported once in the literature. In 2013, Dawood and coworkers [121]

synthesized a [Pd^{II}(qaoH)Cl_2] complex that was found to be an extremely active precatalyst for Suzuki cross-coupling reactions, important for industrial applications. In contrast, the dapdoH_2 ligand has been previously employed in homometallic Mn chemistry for the synthesis of high-spin molecules and single-molecule magnets.[122] For a first time these ligands will be reported in Mn–Ca chemistry, with bioinorganic implications, as a part of Chapter 4 of this thesis.

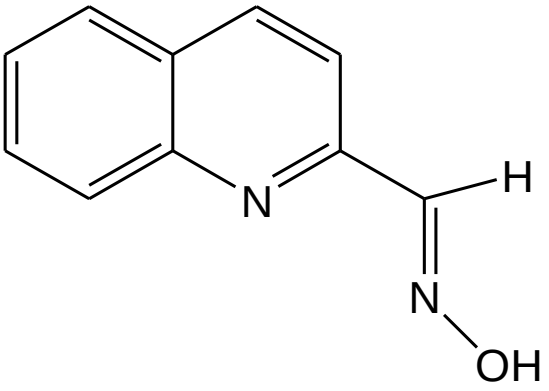

qaoH

Scheme 1.12. Structural formulae and abbreviation of quinoline-2-aldoxime (qaoH).

It is evident from the literature that carboxylates (RCO_2^-; R = various) have been widely used in coordination chemistry as ancillary ligands, as they are bidentate bridging ligands and can foster the formation of polynuclear metal compounds (metal clusters). They often occupy peripheral sites, offering additional thermodynamic and kinetic stability to the resulting products. They are flexible and versatile, adopting a variety of different ligation modes (Scheme 1.13).[123] Carboxylates can also act as bases in solution, facilitating the further deprotonation of OH-containing groups resulting in oxido species, which can potentially aid in forming the desired

cubane core of the OEC. In relation to the native enzyme, carboxylates can mimic the coordination ability of the amino acid residues.

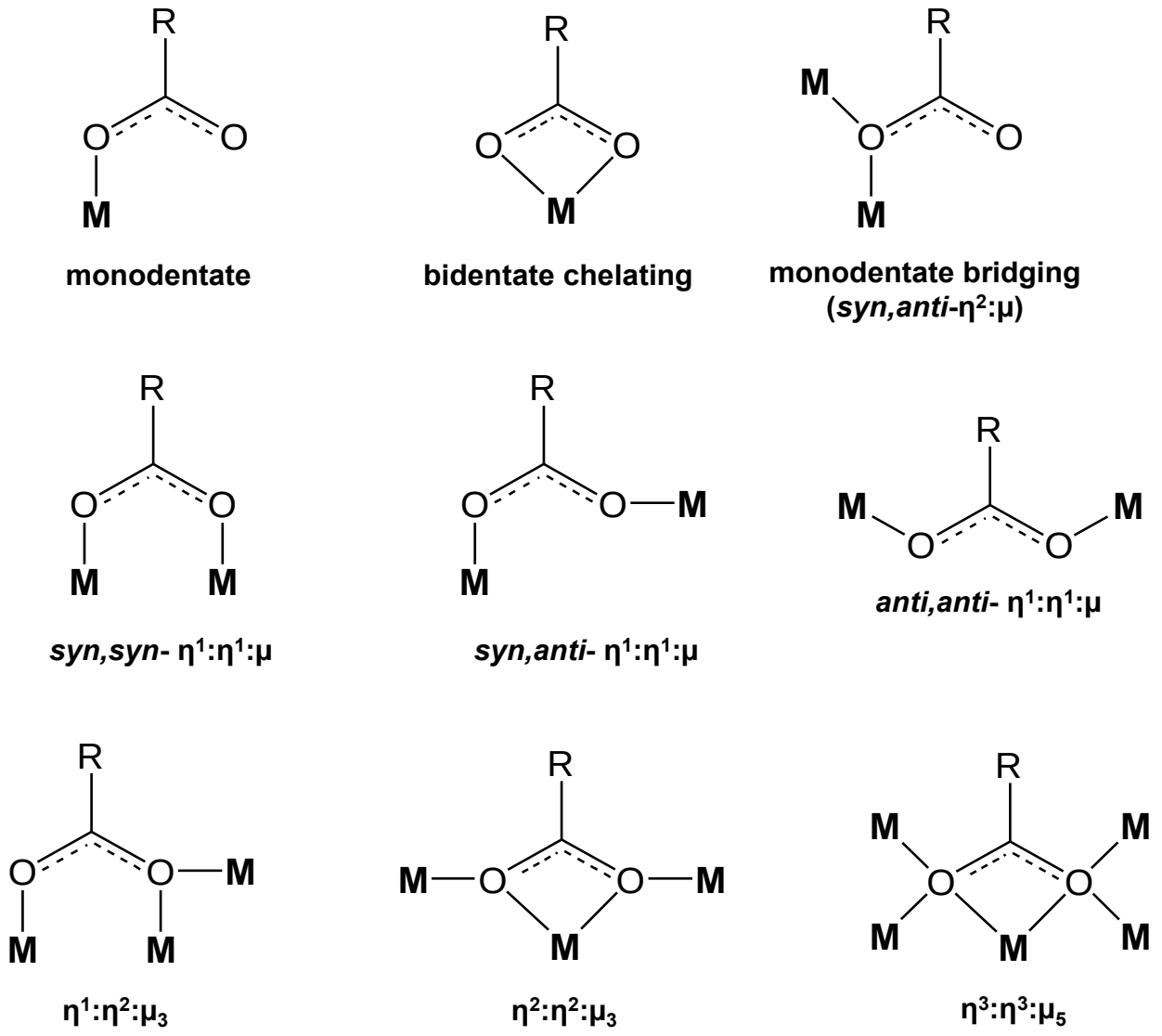

Scheme 1.13. The crystallographically established coordination modes of carboxylate ligands (R = various; M = metal). Symbols "η" and "μ" denote the "hapticity" of the donor atoms and the "bridging" fashion of the entire group, respectively.

1.7 ***Long- and Short-Term Research Objectives***

The long-term research objective of the present thesis is the synthesis of new structural models of the OEC in PSII with the correct metal stoichiometry and topology, the physiologically relevant oxidation states of the Mn ions (exclusively III and IV) and a ligand framework that would support access to multiple oxidation states. In an attempt to reach this research goal, my research endeavours were divided into the following short-term research objectives: (i) the synthesis of Mn–Ca clusters bearing different oximate-based ligands; (ii) the growth of single-crystals suitable for X-ray diffraction studies in order to elucidate the crystal structures of the targeted compounds; (iii) the complete spectroscopic and physicochemical characterization of all compounds in solution and/or solid-state, utilizing but not limited to IR, UV-vis, ESI-MS and elemental analyses techniques; and (iv) the performance of magnetic susceptibility studies in order to assess the bulk magnetic properties of the paramagnetic complexes.

For the synthesis of new Mn–Ca clusters, three different oximate-based groups were used in the present thesis as primary organic chelating/bridging ligands. Specifically, the ligands salicylhydroxamic acid ($shaH_2$), quinoline-2-aldoxime (qaoH) and 2,6-diacetylpyridine dioxime ($dapdoH_2$) have been explored for their ability to form heterometallic Mn–Ca clusters as potential models of the OEC.

Chapter 2

Emissive $\{Mn^{III}_4Ca\}$ Clusters with Square Pyramidal Topologies: Syntheses and Structural, Spectroscopic and Physicochemical Characterization

2.1 *Preface*

Kinetically distinct species in the photoactivation process have been established,[18,20] and reduction of the S_n intermediates in the Kok cycle has led to species in oxidation states lower than S_0. These lower oxidation state species are generated upon loss of molecular O_2 during the catalytic turnover. The ligand set environment is then responsible for the reorganization, reoxidation and reoxygenation of the $\{Mn_4CaO_x\}$ cluster.[124] Thus, the synthesis and detailed study of synthetic analogues (molecular models) of such lower oxidation species would greatly enhance our understanding of the spectroscopic, physical and catalytic properties of the water-oxidizing complex (WOC), as well as its reactivity and functional characteristics. In addition, the incorporation of optically active organic groups in an inorganic $\{Mn_4Ca\}$ core could provide access to additional physical properties such as luminescence and photocatalysis.

Towards the search for new molecular materials with implications in both bioinorganic chemistry and materials science, and specifically in the synthesis of structural models of the OEC with optical properties, some of the most crucial synthetic challenges to confront are: (i) the Mn_4Ca metal stoichiometry, (ii) the extended, distorted cubane conformation, (iii) the stability of the preferred Mn oxidation states, (iv) the choice of the ancillary bridging ligands and (v) the optical response to an external stimulus. With this in mind, a program aiming at the synthesis of new heterometallic Mn–Ca clusters that would possess as many of the above-mentioned

structural and physiochemical features as possible was initiated.[96] The synthetic route employed was based on self-assembly, which included one-pot reactions between various Mn and Ca sources in the presence of carefully selected chelating/bridging ligands. With regard to the choice of organic ligands, $shaH_2$ can transform to $shiH_3$ (Scheme 1.9), an oximate-based ligand.[119] Oximate-based ligands (>C=N–O^-) are known to stabilize Mn atoms with moderate-to-high oxidation states and can also foster the formation of polynuclear metal complexes.[113,125] In addition, carboxylate groups with fluorescence substituents, such as naphthalene, anthracene and pyrene (Scheme 2.1),[164] can potentially provide ancillary ligation to an inorganic metal core and simultaneously introduce optical efficiency and stability in solution into the corresponding cluster compounds. Our group has recently shown that the employment of 2-naphthoic acid (L1-H), 9-anthracenecarboxylic acid (L2-H) and 1-pyrenecarboxylic acid (L3-H) in Mn^{III} cluster chemistry can lead to a new family of $[Mn^{III}_3O(LX)_3(mpko)_3](ClO_4)$ triangular clusters (X = 1, 2 or 3; $mpko^-$ is the anion of methyl 2-pyridyl ketone oxime) with dual single-molecule magnetic and emissive properties.[126]

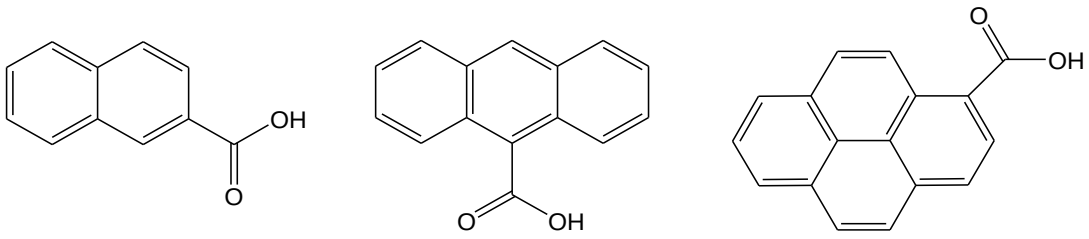

L1-H **L2-H** **L3-H**

Scheme 2.1. Structural formulae and abbreviations of the fluorescence carboxylate ligands used in this thesis.

In this Chapter, it is shown that the use of $shaH_2$ and fluorescence carboxylate ligands (LX; X = 1, 2 or 3) in Mn–Ca chemistry can lead to a new family of oxido-free $\{Mn^{III}_4Ca\}$ clusters with some relevance to low oxidation states of the OEC, featuring a distorted square pyramidal topology, an inherent structural stability in solution, and redox and optical activities arising from the metal ions and fluorescence ligands.

2.2 ***Experimental Section***

2.2.1 Physical Measurements

Elemental analysis: Elemental analyses (C, H and N) were performed on a PerkinElmer 2400 Series II Analyzer.

FT-IR spectroscopy: Infrared (IR) spectra were recorded in the solid state on a Bruker FT-IR spectrometer (ALPHA Platinum ATR single reflection) in the 4000-450 cm^{-1} range.

UV-visible spectroscopy: UV-visible (UV-vis) spectra were recorded in MeCN solution at concentrations ~10^{-5} M on a Beckman Coulter DU Series 700 dual beam spectrophotometer.

Mass spectroscopy: Electrospray ionization (ESI) mass spectra (MS) were taken on a Bruker HCT Ultra mass spectrometer in MeCN solutions.

Photoluminescence studies: Excitation and emission spectra were recorded in MeCN solutions (~10^{-5} M) using a PTI FeliX32 spectrofluorometer.

Electrochemical studies: Electrochemical studies were performed under argon using a BASi EC-epsilon Autoanalyzer and a standard three-electrode assembly (glassy carbon working, Pt wire auxiliary and $Ag/AgNO_3$ reference) with 0.1 M $NBu^n_4PF_6$ as supporting electrolyte.

Quoted potentials are versus the ferrocene/ferrocenium couple, used as an internal standard. The scan rates for the cyclic voltammetry were 100 mV/s. Distilled solvents were employed and the concentrations of the complexes were approximately 1 mM.

Magnetic susceptibility measurements: Variable-temperature direct current (*dc*) magnetic susceptibility studies were performed at the Chemistry Department of the University of Florida on a Quantum Design MPMS-XL SQUID susceptometer equipped with a 7 T magnet and operating in the 1.8–400 K range. The Superconducting Quantum Interference Device (SQUID) allow for the complete study of the magnetic properties of bulk and molecule-based materials at various temperatures and magnetic fields. The *dc* scan mode provides continual plotting and capture of raw magnetic data points at static or sweeping fields and temperatures. Samples were embedded in solid eicosane to prevent torquing. Pascal's constants were used to estimate the diamagnetic correction, which was subtracted from the experimental susceptibility to give the molar paramagnetic susceptibility (χ_M).[127]

2.2.2 Synthesis

General considerations: All manipulation were performed under aerobic conditions using chemicals and solvents as received without any further purification. All chemicals were purchased from Sigma-Aldrich, TCI and Alfa Aesar. *Perchlorate salts are potentially explosive; such compounds should be synthesized and used in small quantities, and treated with utmost care at all times.*

$(NHEt_3)_2[Mn_4Ca(L1)_4(shi)_4]$ (1): To a stirred, colourless solution of $shaH_2$ (0.15 g, 1.0 mmol) and NEt_3 (0.42 mL, 3.0 mmol) in CH_2Cl_2 (30 mL), solid 2-naphthoic acid (L1-H; 0.17 g,

1.0 mmol) was added. The resulting pale yellow suspension was kept under magnetic stirring at room temperature for about 10 min, followed by the consecutive addition of solids $Mn(ClO_4)_2{\cdot}6H_2O$ (0.16 g, 0.5 mmol) and $Ca(ClO_4)_2{\cdot}4H_2O$ (0.16 g, 0.5 mmol). The resulting ecru suspension was stirred for 2 h, during which time all the solids dissolved and the colour of the solution changed to dark brown. The solution was filtered, and a mixture of Et_2O/C_6H_{14} (60 mL, 1:1 v/v) diffused into the filtrate. After five days, brown plate-like crystals of **1** had appeared and were collected by filtration, washed with CH_2Cl_2 (2 x 5 mL) and Et_2O (2 x 5 mL), and dried under vacuum; the yield was 30%. The crystalline solid was analyzed as **1**: C, 57.67; H, 4.38; N, 4.80 %. Found: C, 57.43; H, 4.25; N, 4.99 %. Selected ATR data (cm^{-1}): 3050 (wb), 2985 (m), 1595 (vs), 1565 (s), 1509 (m), 1467 (m), 1432 (s), 1388 (m), 1315 (m), 1244 (m), 1153 (m), 1097 (m), 1033 (s), 937 (m), 863 (m), 792 (m), 753 (mb), 681 (s), 648 (mb), 480 (m). UV-vis: λ/nm in MeCN: 243, 270, 331.

$(NHEt_3)_2[Mn_4Ca(L2)_4(shi)_4]$ (2): To a stirred, colourless solution of $shaH_2$ (0.15 g, 1.0 mmol) and NEt_3 (0.56 mL, 4.0 mmol) in CH_2Cl_2 (30 mL), solid 9-anthracenecarboxylic acid (L2-H; 0.18 g, 0.8 mmol) was added. The resulting pale yellow suspension was kept under magnetic stirring at room temperature for about 15 min, followed by the consecutive addition of solids $Mn(ClO_4)_2{\cdot}6H_2O$ (0.29 g, 0.8 mmol) and $Ca(ClO_4)_2{\cdot}4H_2O$ (0.06 g, 0.2 mmol). The resulting ecru suspension was stirred for 2 h, during which time all the solids dissolved and the colour of the solution changed to dark brown. The solution was filtered, and Et_2O (60 mL) diffused into the filtrate. After three days, X-ray quality dark-brown plate-like crystals of **2**$\cdot 4CH_2Cl_2$ had appeared and were collected by filtration, washed with CH_2Cl_2 (2 x 5 mL) and Et_2O (2 x 5 mL), and dried under vacuum; the yield was 60%. The crystalline solid was analyzed as **2**: C, 61.61; H, 4.34; N, 4.31 %. Found: C, 61.39; H, 4.25; N, 4.34 %. Selected ATR data

(cm^{-1}): 3041 (m), 2983 (m), 1589 (vs), 1565 (s), 1513 (m), 1486 (m), 1468 (m), 1429 (s), 1384 (m), 1313 (vs), 1274 (m), 1254 (m), 1154 (m), 1096 (m), 1031 (m), 937 (s), 884 (m), 861 (s), 797 (m), 733 (vs), 681 (s), 646 (s), 615 (vs), 524 (m), 481 (m), 457 (m). UV-vis: λ/nm in MeCN: 250, 288, 347, 356, 382.

$(NHEt_3)_5[Mn_4Ca(L2)_4(shi)_4(shiH_2)_2](ClO_4)$ (3): To a stirred, colourless solution of $shaH_2$ (0.05 g, 0.3 mmol) and NEt_3 (0.13 mL, 0.9 mmol) in CH_2Cl_2 (30 mL), solid 9-anthracenecarboxylic acid (L2-H; 0.07 g, 0.3 mmol) was added. The resulting pale yellow suspension was kept under magnetic stirring at room temperature for about 15 min, followed by the consecutive addition of solids $Mn(ClO_4)_2{\cdot}6H_2O$ (0.11 g, 0.3 mmol) and $Ca(ClO_4)_2{\cdot}4H_2O$ (0.06 g, 0.2 mmol). The resulting ecru suspension was stirred for 2 h, during which time all the solids dissolved and the colour of the solution changed to dark brown. The solution was filtered, and a mixture of Et_2O/C_6H_{14} (60 mL, 1:1 v/v) diffused into the filtrate. After four weeks, dark-red plate-like crystals of **3**·$2CH_2Cl_2$ had appeared and were collected by filtration, washed with CH_2Cl_2 (2 x 5 mL) and Et_2O (2 x 5 mL), and dried under vacuum; the yield was 20%. The crystalline solid was analyzed as solvent-free **3**: C, 60.28; H, 5.75; N, 6.92 %. Found: C, 60.10; H, 5.52; N, 7.12 %. Selected ATR data (cm^{-1}): 3040 (s), 2981 (mb), 1593 (vs), 1567 (s), 1515 (m), 1431(s), 1383 (m), 1311 (vs), 1256 (m), 1155 (m), 1093 (m), 1032 (m), 1024 (s), 936 (m), 898 (m), 861 (s), 756 (s), 734 (s), 679 (s), 647 (s), 619 (vs), 524 (m), 478 (m), 456 (m). UV-vis: λ/nm in MeCN: 252, 284, 350, 358, 381.

$(NHEt_3)_2[Mn_4Ca(L3)_4(shi)_4]$ (4): To a stirred, colourless solution of $shaH_2$ (0.15 g, 1.0 mmol) and NEt_3 (0.56 mL, 4.0 mmol) in CH_2Cl_2 (30 mL) solid 1-pyrenecarboxylic acid (L3-H; 0.20 g, 0.8 mmol) was added. The resulting pale yellow suspension was kept under magnetic stirring at room temperature for about 15 min, followed by the consecutive addition of solids

$Mn(ClO_4)_2 \cdot 6H_2O$ (0.29 g, 0.8 mmol) and $Ca(ClO_4)_2 \cdot 4H_2O$ (0.06 g, 0.2 mmol). The resulting ecru suspension was stirred for 2 h, during which time all the solids dissolved and the colour of the solution changed to dark brown. The solution was filtered and left to evaporate slowly at room temperature. After five days, X-ray quality dark-brown plate-like crystals of **4**$\cdot 5CH_2Cl_2$ had appeared and were collected by filtration, washed with CH_2Cl_2 (2 x 5 mL) and Et_2O (2 x 5 mL), and dried under vacuum; the yield was 50%. The crystalline solid was analyzed as solvent-free **4**: C, 63.41; H, 4.14; N, 4.11 %. Found: C, 63.76; H, 4.42; N, 3.98 %. Selected ATR data (cm^{-1}): 3035 (m), 2984 (m), 1591 (vs), 1567 (s), 1510 (m), 1469 (m), 1432 (s), 1386 (m), 1353 (s), 1311 (m), 1255 (m), 1178 (m), 1152 (m), 1095 (m), 1033 (s), 936 (s), 839 (s), 787 (m), 753 (m), 712 (vs), 678 (vs), 645 (m), 612 (vs), 533 (m), 479 (s). UV-vis: λ/nm in MeCN: 250, 288, 342, 360, 382.

2.2.3 Single-crystal X-ray Crystallography

Selected crystals of **1**, **2**$\cdot 4CH_2Cl_2$, and **3**$\cdot 2CH_2Cl_2$ were manually harvested and mounted on cryoloops using adequate oil.[128] Diffraction data were collected at 150.0(2) K on a Bruker X8 Kappa APEX II Charge-Coupled Device (CCD) area-detector diffractometer controlled by the APEX2 software package[129] (Mo Kα graphite-monochromated radiation, λ = 0.71073 Å), and equipped with an Oxford Cryosystems Series 700 cryostream monitored remotely with the software interface Cryopad.[130] Images were processed with the software SAINT+.[131] The majority of single-crystals chosen for data collection showed very weak X-ray diffractions patterns under Mo Kα radiation; it was not feasible to obtain any better data for complexes **1**–**3** than the ones reported herein. Attempts to work with larger in size crystals failed to give

acceptable data due to crystal twinning problems. To confirm that the intensity of conventional X-rays hinders the acquisition of high quality crystal data, access to synchrotron radiation was necessary. Selectively for complex **4**·5CH_2Cl_2, good quality X-ray diffraction data from a small, but single, crystal were collected under the synchrotron radiation beam at the Swiss-Norwegian BM01a beamline (European Synchrotron Radiation Facilities - ESRF, Grenoble, France), at 100(2) K, on the multipurpose PILATUS@SNBL diffractometer equipped with a PILATUS2m detector, using a highly monochromatic synchrotron radiation with wavelength (λ) fixed at 0.68239 Å. Images were processed using the software CrysAlis^{Pro}.[132] All the data were corrected for absorption by the multi-scan semi-empirical method implemented in SADABS.[133] The structures were solved by direct methods implemented in SHELXS-97,[134,135] and refined from successive full-matrix least-squares cycles on F^2 using SHELXL-97.[135,136]

The non-hydrogen atoms were successfully refined using anisotropic displacement parameters, except from one Et_3NH^+ cation in the structures of **1** and **2**·4CH_2Cl_2 which were refined with isotropic parameters. Hydrogen atoms bonded to carbon, nitrogen or oxygen atoms were located at their idealized positions using appropriate HFIX instructions in SHELXL; 43 for the aromatic carbons, 23 for the –CH_2 group, 137 for the terminal –CH_3 methyl groups, 13 for the –NH group and 147 for the –OH group. All these atoms were included in subsequent refinement cycles in riding-motion approximation with isotropic thermal displacements parameters (U_{iso}) fixed at 1.2 or 1.5 × U_{eq} of the relative atom.

Substantial electron density was found on the data of **1**, **2**·4CH_2Cl_2 and **3**·2CH_2Cl_2, most likely as a consequence of additional disordered solvent molecules. Several attempts to locate and model remaining solvent molecules revealed to be ineffective, and the investigation for the total potential solvent area using the software package PLATON[137] confirmed unequivocally the

occurrence of cavities with potential solvent accessible void volume. Therefore, the original data sets were treated with the SQUEEZE[137b] subroutines to eliminate the contribution of these highly disordered molecules in the solvent-accessible volume. The programs used for molecular graphics were MERCURY and DIAMOND.[138] Unit cell parameters and structure solution and refinement data for all complexes are listed in Table 2.1.

Table 2.1. Crystallographic Data for Complexes **1–4**.

Parameter	**1**	**2**·4CH_2Cl_2	**3**·2CH_2Cl_2	**4**·5CH_2Cl_2
Formula[a]	$C_{84}H_{76}Mn_4CaN_6O_{20}$	$C_{104}H_{92}Mn_4CaN_6O_{20}Cl_8$	$C_{134}H_{148}Mn_4CaN_{11}O_{30}Cl_5$	$C_{113}H_{94}Mn_4CaN_6O_{20}Cl_{10}$
FW[a]/g mol^{-1}	1749.35	2289.28	2829.72	2470.28
Crystal type	brown plate	brown plate	brown plate	red plate
Crystal size/mm	0.35×0.18×0.05	0.38×0.21×0.11	0.25×0.14×0.03	0.08×0.05×0.03
Crystal system	Orthorhombic	Monoclinic	Monoclinic	Triclinic
Space group	*P*bcn	$P2_1/n$	$P2_1/n$	$P\bar{1}$
a / Å	17.774(2)	21.872(2)	14.7076(12)	16.5865(2)
b / Å	26.125(4)	19.242(2)	29.524(2)	17.4560(2)
c / Å	17.139(2)	26.024(2)	31.846(2)	19.3789(3)
α / º	90	90	90	110.620(1)
β / º	90	91.153(4)	101.206(3)	94.871(1)
γ / º	90	90	90	94.214(1)
V / $Å^3$	7958.4(2)	10950.2(16)	13564.8(2)	5200.2(1)

Z	4	4	4	1
T / K	150.0(2)	150.0(2)	150.0(2)	100(2)
ρ_{calc} / g cm^{-3}	1.460	1.389	1.386	1.578
μ / mm^{-1}	0.762	0.760	0.577	0.771
θ range / °	3.65 - 25.03	3.65 - 25.03	3.66 - 25.03	3.52 - 23.97
Index ranges	$0 \le h \le 21$	$-25 \le h \le 26$	$-17 \le h \le 17$	$-19 \le h \le 19$
	$0 \le k \le 31$	$-22 \le k \le 22$	$-35 \le k \le 35$	$-20 \le k \le 20$
	$0 \le l \le 20$	$-30 \le l \le 30$	$-37 \le l \le 37$	$-22 \le l \le 20$
Collected reflections	6968	139672	168834	54493
Independent reflections	4534 (R_{int} = 0.1645)	19125 (R_{int} = 0.0476)	23889 (R_{int} = 0.0765)	15587 (R_{int} = 0.0307)
Final $R^{b,c}$ indices [$I>2\sigma(I)$]	$R1$ = 0.1554	$R1$ = 0.0925	$R1$ = 0.0969	$R1$ = 0.0784
	$wR2$ = 0.4217	$wR2$ = 0.2370	$wR2$ = 0.1991	$wR2$ = 0.2322
$(\Delta\rho)_{max,min}$ / e Å^{-3}	4.111, –0.713	3.599, –1.200	1.799, –1.188	1.897, −1.613

[a]Including solvate molecules. [b]R1 = $\Sigma(||F_o| - |F_c||)/\Sigma|F_o|$. [c]$w$R2 = $[\Sigma[w(F_o^2 - F_c^2)^2]/\Sigma[w(F_o^2)^2]]^{1/2}$, $w = 1/[\sigma^2(F_o^2) + (ap)^2 + bp]$, where $p = [\max(F_o^2, 0) + 2F_c^2]/3$.

2.3 ***Results and Discussion***

2.3.1 Synthetic Comments and IR Spectra

The majority of synthetic procedures for heterometallic Mn–Ca complexes rely on the reactions of readily available MnX_2 and CaX_2 starting materials (X^- = various) with a potentially chelating/bridging organic ligand. This route has led to numerous, mixed Mn–Ca complexes with different metal stoichiometries, Mn oxidation level descriptions and structural topologies.[93,94,95,103,104,107,110, 139 , 140] An alternative route refers to the comproportionation reactions between Mn(II) and Mn(VII) reagents, in the presence of CaX_2 salts, under acidic conditions. This flexible and unpredictable strategy does not require the co-presence of an organic chelate and has provided access to the complex $[Mn^{IV}_3Ca_2O_4(O_2CBu^t)_8(Bu^tCO_2H)_4]$,[110] one of the closest structural models of the asymmetric-cubane OEC unit. In the present study, the first route was followed and thus reactions involving salicylhydroxamic acid ($shaH_2$) chelate and Mn/Ca inorganic salts were explored, in the presence of various fluorescence carboxylate groups. The simultaneous presence of 'competing' carboxylate groups (i.e., $MeCO_2^-$, $Bu^tCO_2^-$, etc) on the metal starting materials would likely complicate the reaction mixtures, and their use has thus been avoided.

A variety of reactions differing in the Mn/Ca/$shaH_2$ ratio, the fluorescence carboxylic acids, the inorganic ions present, the organic base and/or the reaction solvent(s) were explored in identifying the following successful systems. The one-pot reaction of $Mn(ClO_4)_2{\cdot}6H_2O$ and $Ca(ClO_4)_2{\cdot}4H_2O$ with $shaH_2$ in a 1:1:2 molar ratio in CH_2Cl_2 in the presence of 2 and 6 equivalents of each 2-naphthoic acid (L1-H) and NEt_3 gave a dark brown solution that, upon filtration and slow diffusion with Et_2O/hexanes, afforded brown crystals of the mixed-metal complex $(NHEt_3)_2[Mn^{III}_4Ca(L1)_4(shi)_4]$ (**1**) in 30% yield (based on the total available Ca). The formation of representative **1** is summarized by the balanced Eqn. 2.1.

$$4\ Mn(ClO_4)_2{\cdot}6H_2O + Ca(ClO_4)_2{\cdot}4H_2O + 4\ shiH_3 + 4\ L1\text{-}H + O_2 + 12\ NEt_3 \rightarrow$$

$$(NHEt_3)_2[Mn^{III}{}_4Ca(L1)_4(shi)_4] + 10\ (NHEt_3)(ClO_4) + 30\ H_2O \qquad \textbf{Eqn. 2.1}$$

The coordinated anion of shi^{3-} was resulted from the metal ion-assisted transformation of $shaH_2$ under basic conditions. The reaction is an oxidation, undoubtedly by O_2 under the prevailing basic conditions. The NEt_3 has the role of proton acceptor to facilitate the deprotonation of the $shaH_2$ and L1-H molecules. Employment of different organic bases, such as NMe_3, $Bu^n{}_3N$ and Me_4NOH, did not afford crystalline materials but only oily products that I was not able to further characterize. The reaction solvent was found to be of critical importance for the crystallization of all reported compounds **1**–**4**; various reactions in polar solvents gave amorphous precipitates that were probably mixtures of different products. Once the identity of **1** was established by single-crystal X-ray diffraction studies (*vide infra*), I managed to optimize the synthesis and increase the yield (~70%) of the crystalline compound by adjusting the Mn/Ca/$shaH_2$/L1-H/NEt_3 ratio to 4:1:5:4:20. The latter ratio was also adopted for the synthesis of isostructural compounds $(NHEt_3)_2[Mn_4Ca(L2)_4(shi)_4]$ (**2**) and $(NHEt_3)_2[Mn_4Ca(L3)_4(shi)_4]$ (**4**) in yields of 60 and 50%, respectively, under different crystallization methods (slow diffusion with Et_2O for **2** and slow evaporation at room temperature for **4**). Interestingly, and only in case of 9-anthracenecarboxylic acid (L2-H), the metals-to-ligands ratio proved to slightly affect the chemical identity of $(NHEt_3)_2[Mn_4Ca(L\text{-}X)_4(shi)_4]$ (X = 1 (**1**), 2 (**2**), 3 (**4**)). Hence, the reaction of $Mn(ClO_4)_2{\cdot}6H_2O$ and $Ca(ClO_4)_2{\cdot}4H_2O$ with $shaH_2$ in a 3:2:3 molar ratio in CH_2Cl_2 in the presence of 3 and 9 equivalents of each L2-H and NEt_3 gave a dark brown solution that, upon filtration and slow diffusion with Et_2O/hexanes, afforded brown crystals of

$(NHEt_3)_5[Mn_4Ca(L2)_4(shi)_4(shiH_2)_2](ClO_4)$ (**3**) in 20% yield. The formation of **3** is summarized by the balanced Eqn. 2.2.

$$4\ Mn(ClO_4)_2{\cdot}6H_2O + Ca(ClO_4)_2{\cdot}4H_2O + 6\ shiH_3 + 4\ L2\text{-}H + O_2 + 14\ NEt_3 \rightarrow$$

$$(NHEt_3)_5[Mn_4Ca(L2)_4(shi)_4(shiH_2)_2](ClO_4) + 9\ (NHEt_3)(ClO_4) + 30\ H_2O \qquad \textbf{Eqn. 2.2}$$

Complex **3** is again a $\{Mn_4Ca\}$ species albeit with two additional $shiH_2^-$ ions acting as terminal ligands (*vide infra*). It is clear that these reaction systems are very complicated, undoubtedly with many species in equilibrium, and thus are sensitive to small changes in reaction conditions. Finally, the substitution of ClO_4^- ions in the MnX_2 and CaX_2 precursors by other inorganic ions, such as Cl^- or NO_3^-, did not lead to any crystalline material under various crystallization techniques and workup conditions. Compounds **1**–**4** are all stable and crystalline solids at room temperature, and nonsensitive toward air and moisture. They are all soluble in MeCN, MeOH, DMF and DMSO, and partially soluble in almost all other organic solvents such as benzene, THF and toluene. Given the pronounced ability of polar and protic solvents to reduce high-oxidation state Mn species,[141] it was avoided to dissolve the reported compounds in MeOH and I have instead focused on the spectroscopic and physicochemical characterization of **1**–**4** in MeCN solutions.

All complexes **1**–**4** have very similar IR spectra (see Appendix). Several bands appear in the ~1595–1380 cm^{-1} range, assigned to contributions from the stretching vibrations of the aromatic rings of shi^{3-} and fluorescence ligands, which overlap with stretches of the carboxylate bands;[142] they, thus, do not represent pure vibrations and render exact assignments difficult. Contributions from the $\nu(C{=}N)_{oximate}$ modes of shi^{3-} would be also expected in this region. It is

very likely that the strong bands at 1595 and 1432 cm^{-1} (**1**), 1589 and 1429 cm^{-1} (**2**), 1593 and 1431 cm^{-1} (**3**) and 1591 and 1432 cm^{-1} (**4**) in the spectra of **1**–**4** are attributed to the $\nu_{as}(CO_2)$ and $\nu_s(CO_2)$ modes, respectively; the former should also involve a ring stretching character. The difference Δ [$\Delta = \nu_{as}(CO_2) - \nu_s(CO_2)$] is small (<163 cm^{-1}) in all cases, as expected for the predominant bidentate bridging mode of carboxylate ligation (*vide infra*).[143] The bands at ~3050 and ~2980 cm^{-1} can be assigned to the stretching vibrations of ν(N-H) modes from the presence of Et_3NH^+ countercations.[144]

2.3.2 Description of Structures

Complexes **1**, **2**, and **4** are isostructural and differ only in the nature of the fluorescence carboxylate ligand and lattice solvate molecules; the latter will not be further discussed. Given the superior quality of X-ray diffraction data for compound **4** obtained through synchrotron radiation, and consequently its more precise metric parameters (bond distances and angles), only the structure of representative complex **4** will be described in detail. The crystal structure of **4** consists of a $[Mn_4Ca(L3)_4(shi)_4]^{2-}$ dianion (Figure 2.1, top), two Et_3NH^+ cations, and five lattice CH_2Cl_2 molecules. Complex **4**·$5CH_2Cl_2$ crystallizes in the triclinic space group $P\bar{1}$ with the {Mn_4Ca} dianion in a general position. In contrast, complexes **1** (Figure 2.1, middle) and **2**·$4CH_2Cl_2$ (Figure 2.1, bottom) crystallize in the orthorhombic *Pbcn* and monoclinic $P2_1/n$ space groups, respectively. Selected interatomic distances and angles for complexes **1**, **2** and **4** are listed in Table 2.2.

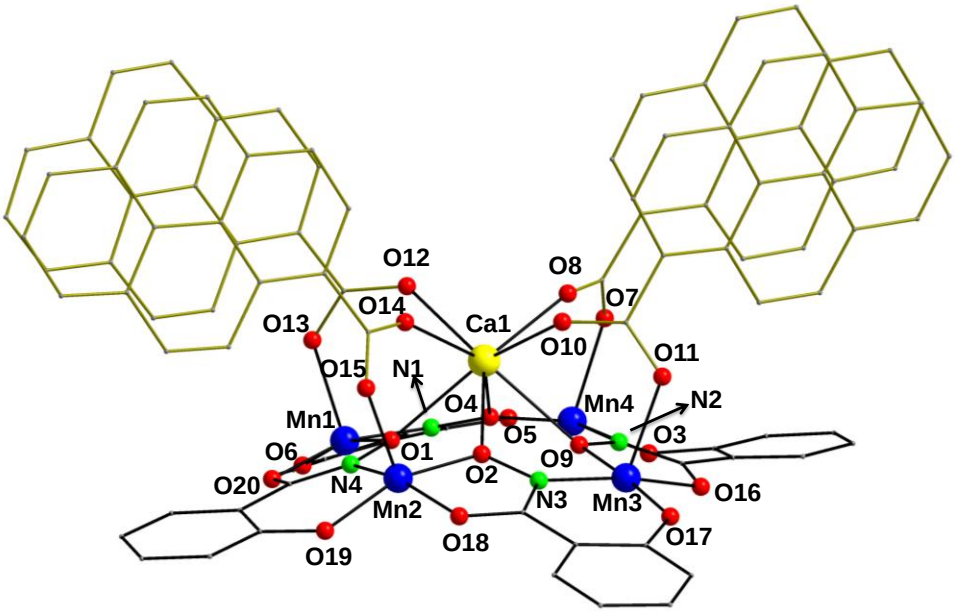
O12
O8
O14
O7
O13
Ca1
O10
O11
O15
N1
O4
Mn4
N2
Mn1
O5
O3
O6
O1
O9
O2
O20
N4
N3
Mn3
O16
Mn2
O18
O17
O19

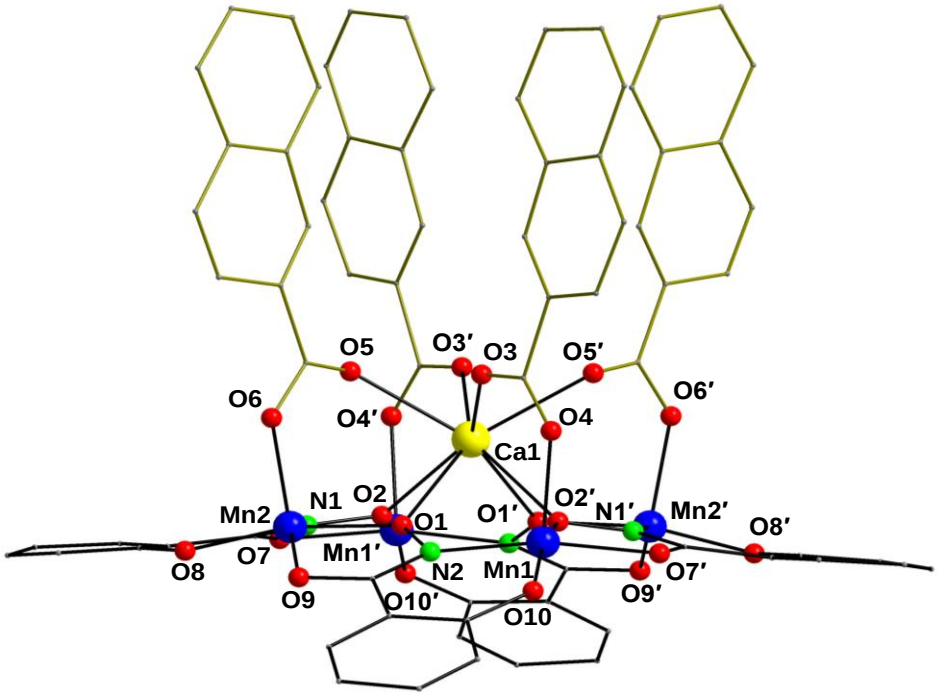
O5
O3′
O3
O5′
O6
O6′
O4′
O4
Ca1
Mn2
N1
O2
O2′
O1
O1′
N1′
Mn2′
O8′
O8
O7
Mn1′
N2
Mn1
O7′
O9
O10′
O9′
O10

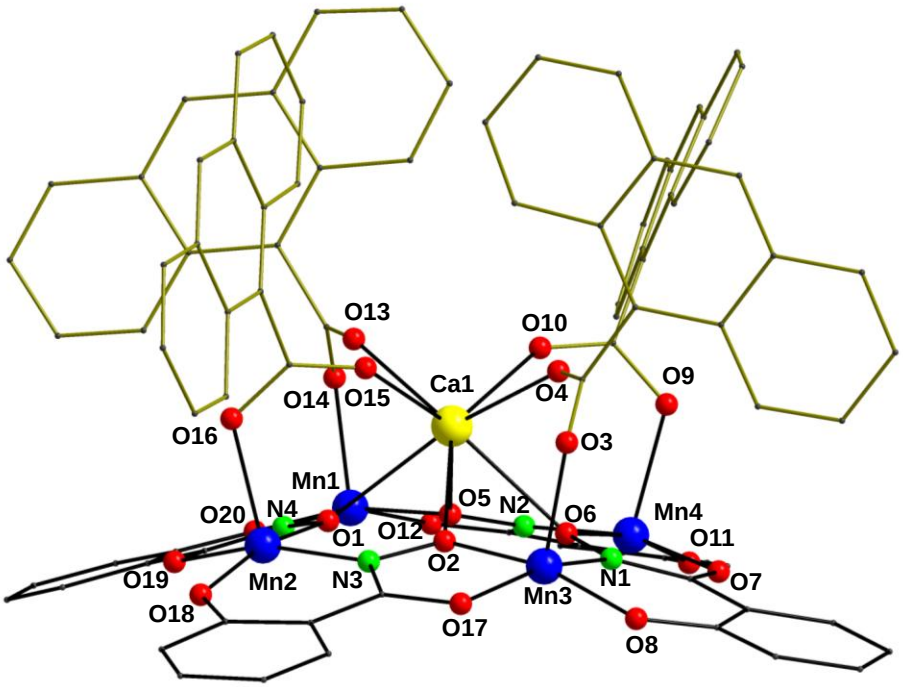

Figure 2.1. Partially labeled representation of the structures of the anions present in complexes **4** (top), **1** (middle) and **2** (bottom), with the gold thick bonds emphasizing the different carboxylate moieties. H atoms are omitted for clarity. Colour scheme: Mn^{III}, blue; Ca^{II}, yellow; O, red; N, green; C, gray. Symmetry operation for the primed atoms in **1**: *–x*, *y*, 1/2–*z*.

The core of **4** consists of four Mn^{III} and one Ca^{II} atoms arranged in a slightly distorted square pyramidal topology (Figure 2.2, top left), with the Ca^{II} atom occupying the apical position and the Mn^{III} atoms forming the square base. The Mn···Mn···Mn angles are spanning the range 88.1–91.8°, deviating only slightly from the ideal 90°, and the Mn···Ca···Mn angles of the four triangular faces lie within the 75.3–76.1° range. The Mn^{III} atoms form a near-planar square, with each of the edges bridged by a diatomic oximate group from a shi^{3-} ligand, thus giving Mn···Mn separations of 4.589(1)–4.645(1) Å. The almost perfectly planar Mn_4 unit is clearly due to the large Mn–O–N–Mn torsion angles of 171.5° (Mn1–O1–N4–Mn2), 165.3° (Mn2–O2–N3–Mn3),

171.3^{o} (Mn3–O9–N2–Mn4) and 169.2^{o} (Mn4–O4–N1–Mn1), very close to the ideal linearity of 180^{o}. The linkage between the basal Mn^{III} atoms and the apical Ca^{II} atom is provided by the oximate O atoms of shi^{3-} ligands and the four $\eta^1:\eta^1:\mu$ bidentate bridging pyrene carboxylate ($L3^{-}$) groups. The Mn···Ca separations [3.773(1), 3.804(1), 3.729(1) and 3.721(1) Å] in the square pyramid of **4** are in close proximity with conclusions from Ca EXAFS studies on the {Mn_4Ca} extended cubane of the OEC (approximately 3.4 Å).7 Differences between the Mn···Ca separations of **4** and those of OEC are to be expected given the different core topologies, greater distance uncertainties in the crystal structure of a large PSII multicomponent assembly, structural perturbations caused by the polypeptide environment, and the fact that some of the Mn atoms of OEC in the PSII crystal structure will be at a higher oxidation state (i.e., Mn^{IV}), leading to shorter bond distances on average.[110,145] Ligation around each Mn^{III} atom is completed by the alkoxido and phenoxido O atoms from shi^{3-} groups; the latter are thus $\eta^1:\eta^1:\eta^1:\eta^2:\mu_3$ (Figure 2.2, top right). The complex therefore contains an overall $[Mn_4Ca(\mu\text{-}NO)_4]^{10+}$ core (Figure 2.2, bottom left) which can also be described as a [12-$MC_{Mn(III)N(shi)}$-4] metallacrown[146] surrounding a Ca^{II} atom. The latter lies 1.873 Å out of the Mn_4 plane.

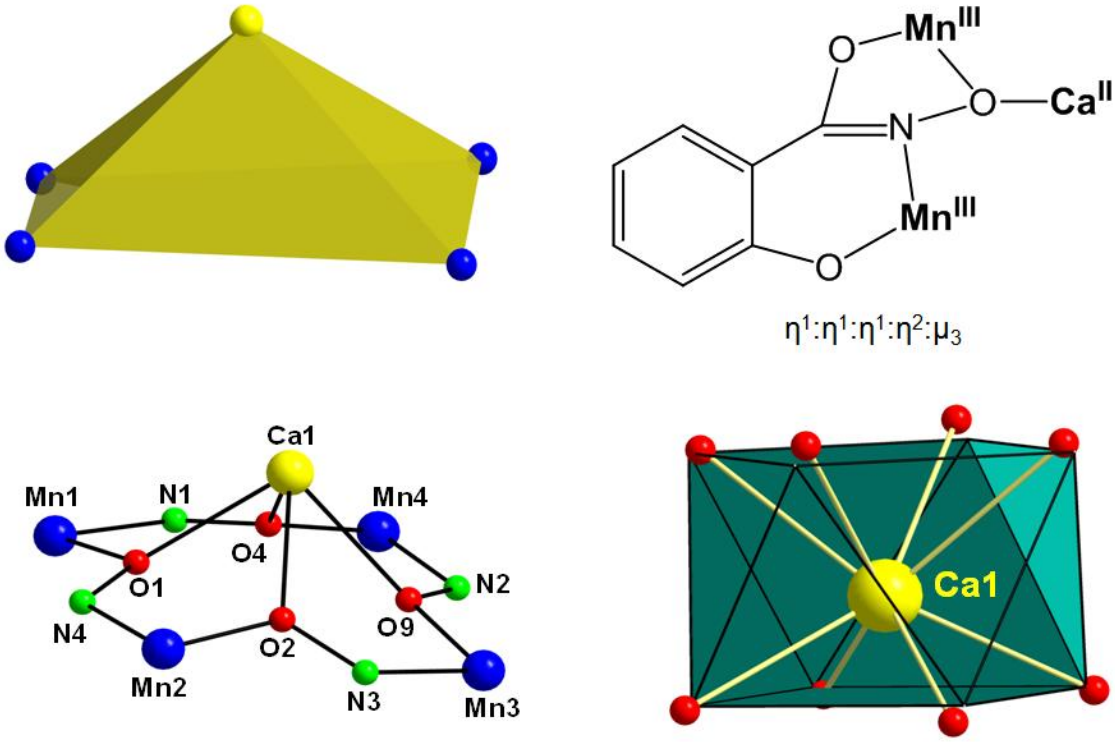

Figure 2.2. Representation of the {Mn_4Ca} square pyramidal topology (top left) and the coordination mode of the shi^{3-} groups (top right). Labeled representation of the complete $[Mn_4Ca(\mu_3\text{-}NO)_4]^{10+}$ core of the representative complex **4** (bottom left) and the square antiprismatic geometry of the Ca^{II} atom in **4**; the points connected by the black lines define the ideal polyhedron. Colour scheme: Mn^{III}, blue; Ca^{II}, yellow; O, red; N, green.

Table 2.2. Selected Interatomic Distances (Å) and Angles (°) for Complexes **1**,[a] **2**·4CH_2Cl_2, **3**·2CH_2Cl_2 and **4**·5CH_2Cl_2.

	1		
Mn(1)···Mn(2)	4.610(2)	Mn(2)···Mn(2′)	6.550(2)
Mn(1)···Mn(2′)	4.621(2)	Mn(1)···Ca(1)	3.678(2)
Mn(1)···Mn(1′)	6.495(2)	Mn(2)···Ca(1)	3.628(2)
Mn(1)-O(4)	2.122(7)	Mn(2)-O(1)	1.896(6)
Mn(1)-O(2′)	1.894(5)	Mn(2)-O(6)	2.050(7)
Mn(1)-O(7′)	1.974(7)	Mn(2)-O(8)	1.831(7)

Mn(1)-O(10)	1.839(6)	Mn(2)-O(9)	1.976(6)
Mn(1)-N(2)	1.933(6)	Mn(2)-N(1)	1.935(6)
Ca(1)-O(1)	2.376(6)	Ca(1)-O(3)	2.385(9)
Ca(1)-O(2)	2.353(5)	Ca(1)-O(5)	2.384(9)
Mn(1)-O(2′)-N(1′)-Mn(2′)	170.6	Mn(1′)-O(2)-Ca(1)	119.6(3)
Mn(2)-O(1)-N(2)-Mn(1)	174.1	Mn(2)-O(1)-Ca(1)	115.8(3)

2·4CH_2Cl_2			
Mn(1)···Mn(2)	4.612(1)	Mn(2)···Mn(4)	6.543(1)
Mn(2)···Mn(3)	4.630(1)	Mn(1)···Ca(1)	3.731(1)
Mn(3)···Mn(4)	4.636(1)	Mn(2)···Ca(1)	3.726(1)
Mn(4)···Mn(1)	4.615(1)	Mn(3)···Ca(1)	3.696(1)
Mn(1)···Mn(3)	6.533(1)	Mn(4)···Ca(1)	3.760(2)
Mn(1)-O(5)	1.880(4)	Mn(3)-O(2)	1.885(4)
Mn(1)-O(12)	1.944(4)	Mn(3)-O(3)	2.146(5)
Mn(1)-O(14)	2.069(5)	Mn(3)-O(8)	1.859(4)
Mn(1)-O(20)	1.860(4)	Mn(3)-O(17)	1.945(4)
Mn(1)-N(4)	1.963(5)	Mn(3)-N(1)	1.976(5)
Mn(2)-O(1)	1.868(4)	Mn(4)-O(6)	1.881(4)
Mn(2)-O(16)	2.115(4)	Mn(4)-O(7)	1.944(4)
Mn(2)-O(18)	1.862(4)	Mn(4)-O(9)	2.140(5)
Mn(2)-O(19)	1.947(4)	Mn(4)-O(11)	1.867(4)
Mn(2)-N(3)	1.974(5)	Mn(4)-N(2)	1.968(5)
Ca(1)-O(1)	2.466(4)	Ca(1)-O(6)	2.476(4)
Ca(1)-O(2)	2.428(4)	Ca(1)-O(10)	2.365(4)
Ca(1)-O(4)	2.405(4)	Ca(1)-O(13)	2.350(5)
Ca(1)-O(5)	2.503(4)	Ca(1)-O(15)	2.389(4)
Mn(1)-O(5)-N(2)-Mn(4)	179.2	Mn(1)-O(5)-Ca(1)	115.9(2)
Mn(2)-O(1)-N(4)-Mn(1)	177.0	Mn(2)-O(1)-Ca(1)	117.9(2)
Mn(3)-O(2)-N(3)-Mn(2)	175.0	Mn(3)-O(2)-Ca(1)	117.4(2)
Mn(4)-O(6)-N(1)-Mn(3)	175.6	Mn(4)-O(6)-Ca(1)	118.7(2)

3·2CH_2Cl_2			
Mn(1)···Mn(2)	4.617(3)	Mn(2)···Mn(4)	6.407(3)
Mn(2)···Mn(3)	4.569(2)	Mn(1)···Ca(1)	3.749(1)
Mn(3)···Mn(4)	4.641(3)	Mn(2)···Ca(1)	3.790(1)
Mn(4)···Mn(1)	4.535(2)	Mn(3)···Ca(1)	3.744(1)
Mn(1)···Mn(3)	6.566(5)	Mn(4)···Ca(1)	3.752(1)

Mn(1)-O(5)	1.875(4)	Mn(3)-O(2)	1.870(4)
Mn(1)-O(15)	1.951(4)	Mn(3)-O(3)	2.088(4)
Mn(1)-O(17)	2.158(4)	Mn(3)-O(8)	1.861(4)
Mn(1)-O(23)	1.851(4)	Mn(3)-O(20)	1.942(4)
Mn(1)-N(5)	1.970(5)	Mn(3)-N(1)	1.989(5)
Mn(2)-O(1)	1.893(4)	Mn(4)-O(6)	1.890(4)
Mn(2)-O(19)	2.283(4)	Mn(4)-O(7)	1.941(4)
Mn(2)-O(21)	1.873(4)	Mn(4)-O(9)	2.309(4)
Mn(2)-O(22)	1.961(4)	Mn(4)-O(11)	2.270(4)
Mn(2)-O(24)	2.244(4)	Mn(4)-O(14)	1.869(4)
Mn(2)-N(4)	1.976(5)	Mn(4)-N(3)	1.980(5)
Ca(1)-O(1)	2.468(4)	Ca(1)-O(6)	2.452(4)
Ca(1)-O(2)	2.440(4)	Ca(1)-O(10)	2.354(4)
Ca(1)-O(4)	2.397(4)	Ca(1)-O(16)	2.427(4)
Ca(1)-O(5)	2.399(4)	Ca(1)-O(18)	2.331(4)
Mn(1)-O(5)-N(3)-Mn(4)	154.4	Mn(1)-O(5)-Ca(1)	122.1(2)
Mn(2)-O(22)-N(5)-Mn(1)	164.9	Mn(2)-O(1)-Ca(1)	120.2(2)
Mn(3)-O(2)-N(4)-Mn(2)	163.5	Mn(3)-O(2)-Ca(1)	120.1(2)
Mn(4)-O(6)-N(1)-Mn(3)	173.5	Mn(4)-O(6)-Ca(1)	119.0(2)

4·5CH_2Cl_2			
Mn(1)···Mn(2)	4.589(2)	Mn(2)···Mn(4)	6.593(4)
Mn(2)···Mn(3)	4.599(2)	Mn(1)···Ca(1)	3.729(1)
Mn(3)···Mn(4)	4.645(3)	Mn(2)···Ca(1)	3.721(1)
Mn(4)···Mn(1)	4.595(2)	Mn(3)···Ca(1)	3.804(1)
Mn(1)···Mn(3)	6.426(3)	Mn(4)···Ca(1)	3.773(1)
Mn(1)-O(1)	1.872(3)	Mn(3)-O(9)	1.889(3)
Mn(1)-O(6)	1.846(3)	Mn(3)-O(11)	2.165(3)
Mn(1)-O(13)	2.070(3)	Mn(3)-O(16)	1.975(3)
Mn(1)-O(20)	1.931(3)	Mn(3)-O(17)	1.865(3)
Mn(1)-N(1)	1.956(3)	Mn(3)-N(3)	1.975(3)
Mn(2)-O(2)	1.881(3)	Mn(4)-O(3)	1.890(3)
Mn(2)-O(15)	2.073(3)	Mn(4)-O(4)	1.871(3)
Mn(2)-O(18)	1.931(3)	Mn(4)-O(5)	1.950(3)
Mn(2)-O(19)	1.863(3)	Mn(4)-O(7)	2.118(3)
Mn(2)-N(4)	1.959(4)	Mn(4)-N(2)	1.975(4)
Ca(1)-O(1)	2.422(3)	Ca(1)-O(9)	2.495(3)
Ca(1)-O(2)	2.423(3)	Ca(1)-O(10)	2.335(3)
Ca(1)-O(4)	2.448(3)	Ca(1)-O(12)	2.389(4)

Ca(1)-O(8)	2.421(3)	Ca(1)-O(14)	2.375(3)
Mn(1)-O(1)-N(4)-Mn(2)	171.5	Mn(1)-O(1)-Ca(1)	120.0(1)
Mn(2)-O(2)-N(3)-Mn(3)	165.3	Mn(2)-O(2)-Ca(1)	119.1(2)
Mn(3)-O(9)-N(2)-Mn(4)	171.4	Mn(3)-O(9)-Ca(1)	119.7(1)
Mn(4)-O(4)-N(1)-Mn(1)	169.2	Mn(4)-O(4)-Ca(1)	121.2(1)

[a]Symmetry code: $' = 1–x, –y, –z$.

All Ca–O bonds are in the range 2.335(3)–2.495(3) Å. All Mn^{III} atoms in **1**, **2** and **4** are five-coordinate with almost perfect square pyramidal geometries. This is confirmed by analysis of the shape-determining bond angles using the approach of Reedijk and Addison,[147] which yields an average value for the trigonality index, τ, of 0.04 for the four metal ions, where τ is 0 and 1 for perfect square pyramidal and trigonal bipyramidal geometries, respectively. The Mn oxidation states were established by charge balance considerations, metric parameters and bond valence sum calculations (BVS, Table 2.3).[148] In all the compounds, the Ca^{II} atom is eight-coordinate in a CaO_8 environment possessing square antiprismatic geometry. That was confirmed by the Continuous Shape Measure (CShM) approach which essentially allows one to numerically evaluate by how much a particular structure deviates from an ideal shape.[149] The best fit was obtained for the square antiprism (Figure 2.2, bottom right) with a CShM value of 0.77. Values of CShM between 0.1 and 3 usually correspond to a not negligible but still small distortion from ideal geometry.[150]

Table 2.3. BVS Calculations[a] for Mn atoms in **1–4**.

Complex	Atom	Mn^{II}	Mn^{III}	Mn^{IV}
1	Mn1	3.27	<u>3.04</u>	3.12
	Mn2	3.35	<u>3.11</u>	3.20
2	Mn1	3.30	<u>3.05</u>	3.14
	Mn2	3.24	<u>3.00</u>	3.09

	Mn3	3.18	2.95	3.03
	Mn4	3.20	2.96	3.05
3	Mn1	3.21	2.97	3.06
	Mn2	3.27	3.03	2.86
	Mn3	3.25	3.01	3.10
	Mn4	3.28	3.03	3.13
4	Mn1	3.38	3.13	3.22
	Mn2	3.31	3.07	3.16
	Mn3	3.10	2.87	2.95
	Mn4	3.17	2.94	3.02

[a]The underlined value is one closest to the charge for which it was calculated. The oxidation state is the nearest whole number to the underlined value.

Complex $(NHEt_3)_5[Mn_4Ca(L2)_4(shi)_4(shiH_2)_2](ClO_4)$ (**3**) has a very similar structure (Figure 2.3) with that of **2**, the only significant difference being the terminal (η^1) coordination of two singly-deprotonated $shiH_2^-$ ligands on two Mn^{III} atoms (Mn2 and Mn4). As a result, Mn2 and Mn4 exhibit a near-octahedral geometry which takes the form of an axially elongated Jahn-Teller (JT) distortion, as expected for a high-spin d^4 ion in this geometry. The JT axes in both Mn sites involve the anthracene carboxylate and $shiH_2^-$ phenoxido O atoms. The non-coordinated N, and oximato and alkoxido O atoms of $shiH_2^-$ are strongly H-bonded to two Et_3NH^+ countercations.

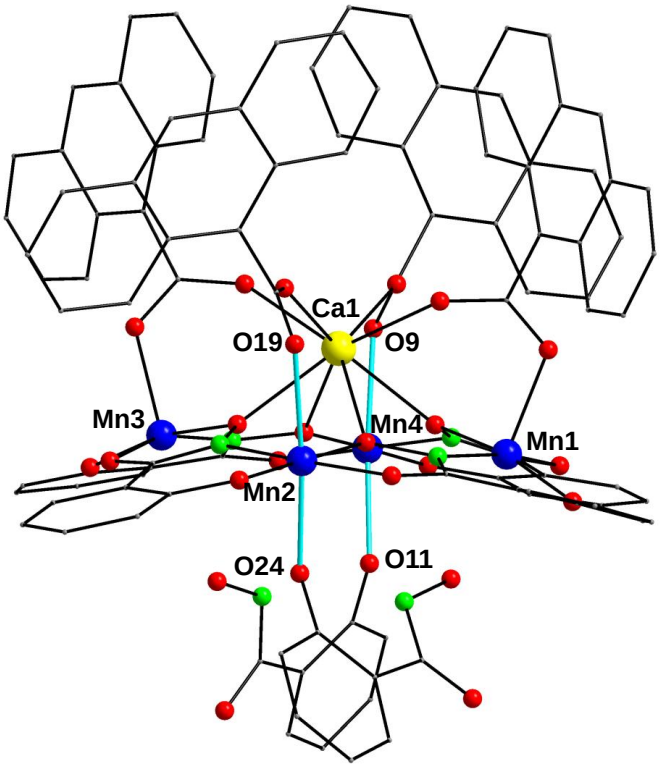

Figure 2.3. Partially labeled representation of the structure of the anion present in complex **3**, with the cyan thick bonds emphasizing the JT axes of the six-coordinate Mn^{III} atoms. H atoms are omitted for clarity. Colour scheme: Mn^{III}, blue; Ca^{II}, yellow; O, red; N, green; C, gray.

From a supramolecular viewpoint, all reported compounds **1**–**4** show similar intramolecular H-bonding interactions which include the Et_3NH^+ cations as donors and the O atoms of carboxylate ligands as acceptors. The pyrene-analogue **4** shows two sets of intramolecular π–π stacking interactions between adjacent centroids, as defined by C9–C24 (centroid A) / C30–C45 (centroid B) and C47–C62 (centroid C) / C64–C79 (centroid D); their distances are: centroid A··· centroid B = 3.807 Å and centroid C··· centroid D = 3.835 Å (Figure 2.4). Finally, the crystal structures of all complexes exhibit intermolecular interactions which involve the aromatic rings of the ligands and H-bonding interactions between the countercations,

lattice solvate molecules and coordinated ligands. The shortest, intermolecular Mn···Mn distances between neighboring cluster compounds are 6.461 (for **1**), 8.445 (for **2**), 8.789 (for **3**) and 6.881 Å (for **4**).

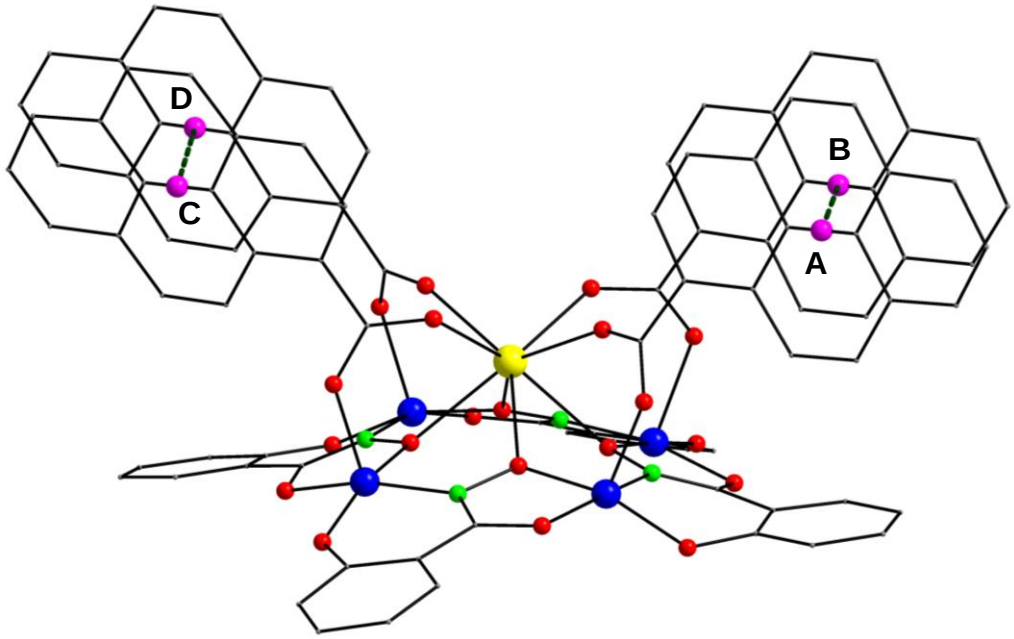

Figure 2.4. The intramolecular π–π stacking interactions between adjacent centroids of the pyrene groups observed in the structure of complex **4**.

It is quite intriguing that Mn–Ca heterometallic chemistry has not been so extensively developed as Mn-3d′ and Mn-4f mixed-metal chemistry although it has attracted the interest of many inorganic synthetic chemists the last three decades or so. Complexes **1**–**4** join only a handful of previous Mn–Ca compounds,[93,94,95,103,104,107,110,139] and together with $(NHEt_3)_2[Mn^{III}_4Ca(O_2CPh)_4(shi)_4]$[96] are the only structurally characterized species with a 4Mn:1Ca ratio and all Mn atoms in 3+ oxidation state.

2.3.3 Electronic Spectra and Electrospray Ionization Mass Spectrometry (ESI-MS)

UV-vis and ESI-MS studies have been performed in order to probe the structural integrity of **1**–**4** in solution and elucidate any possible photophysical properties. The electronic absorption spectra of isostructural complexes **1**, **2** and **4** were recorded in MeCN solutions of concentrations ~10^{-5} M (Figure 2.5). All three compounds show the characteristic bands (shoulders and/or sharp peaks) of naphthalene, anthracene, and pyrene functional groups slightly shifted to higher wavenumbers, consistent with coordination of the fluorescence carboxylate ligands to the metal centers.[151] The high intensity absorption bands in the 240–350 nm region are assigned to π–π* transitions within the aromatic organic ligands while the less intense bands at ~380 nm are possibly due to LMCT effects.[152] Note that the absorption bands of neutral salicylhydroxamic acid (218, 236 and 300 nm) appear to overlap with the bands of polyaromatic carboxylate ligands upon coordination with the metal centers. Hence, the conclusions from the UV-vis studies were very promising that compounds **1**, **2** and **4** retain their solid-state {Mn_4Ca} structures in solution, and confirmation was sought by electrospray ionization (ESI) mass spectrometry (MS).

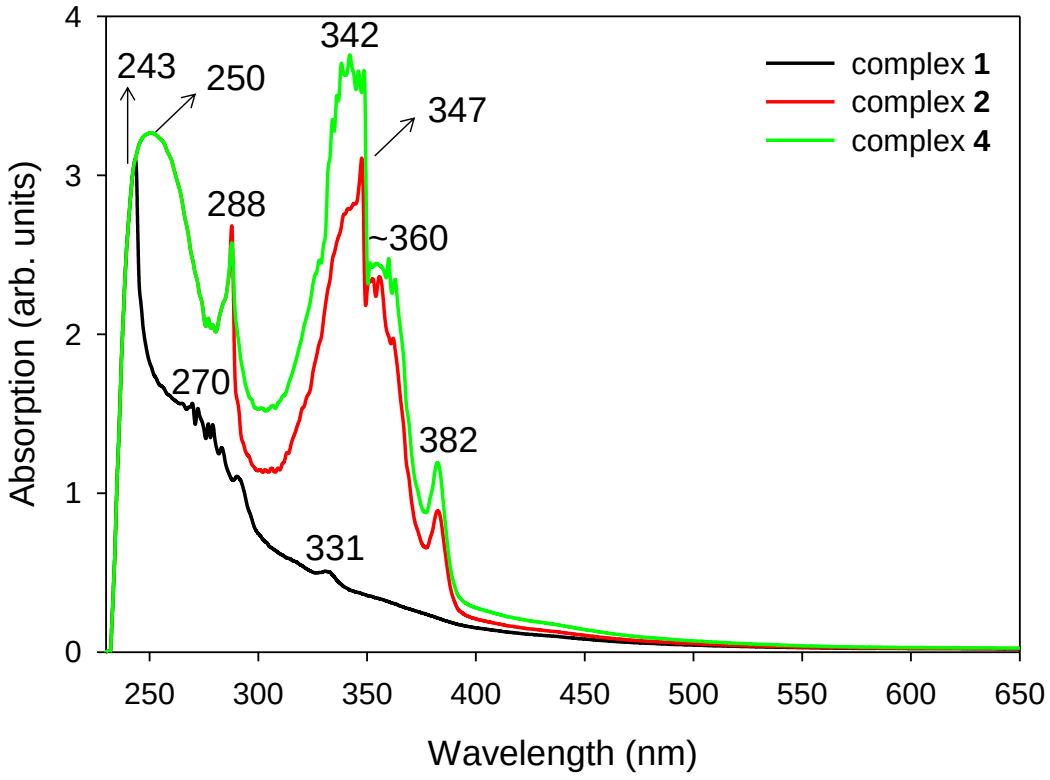

Figure 2.5. Absorption spectra of complexes **1**, **2** and **4** in MeCN (~10^{-5} M).

Negative (–) ion ES-MS studies were conducted to investigate the stability of complexes **1**, **2** and **4** in the aprotic MeCN solvent. Unfortunately, due to the paramagnetic nature of **1**–**4**, solution NMR spectroscopy could not provide any useful structural information. In contrast, ESI-MS is a soft technique that (i) allows the detection of multiply charged ions, (ii) does not alter the connectivity of the compounds (through disassembly and reassembly processes) and (iii) causes very little fragmentation.[153] Although very rare in volatile transition metal cluster chemistry, all three described compounds proved to preserve their core structures in solution with high intensity ion signals corresponding to the sole presence of {Mn_4Ca} cores without major fragment ions. For complexes **1**, **2** and **4**, the strong intensity peaks at 772, 872 and 920 *m/z* nicely reproduce the doubly charged $[Mn_4Ca(L1)_4(shi)_4]^{2-}$, $[Mn_4Ca(L2)_4(shi)_4]^{2-}$ and

$[Mn_4Ca(L3)_4(shi)_4]^{2-}$ species, respectively (Figure 2.6). In support of these assignments is the excellent match observed between the acquired isotopic patterns of $[Mn_4Ca(LX)_4(shi)_4]^{2-}$ ions (X = 1–3) and the theoretically calculated distributions (Figure 2.6, insets), allowing me to confirm the structural integrity of **1**, **2** and **4** in MeCN. The very low intensity peaks at 1373, 1523 and 1595 *m/z* can be assigned to the least abundant, singly anionic fragments $[Mn_4Ca(L1)_3(shi)_4]^-$, $[Mn_4Ca(L2)_3(shi)_4]^-$ and $[Mn_4Ca(L3)_3(shi)_4]^-$, respectively, which correspond to the reported $\{Mn_4Ca\}$ core structures with the dissociation of one carboxylate ligand.

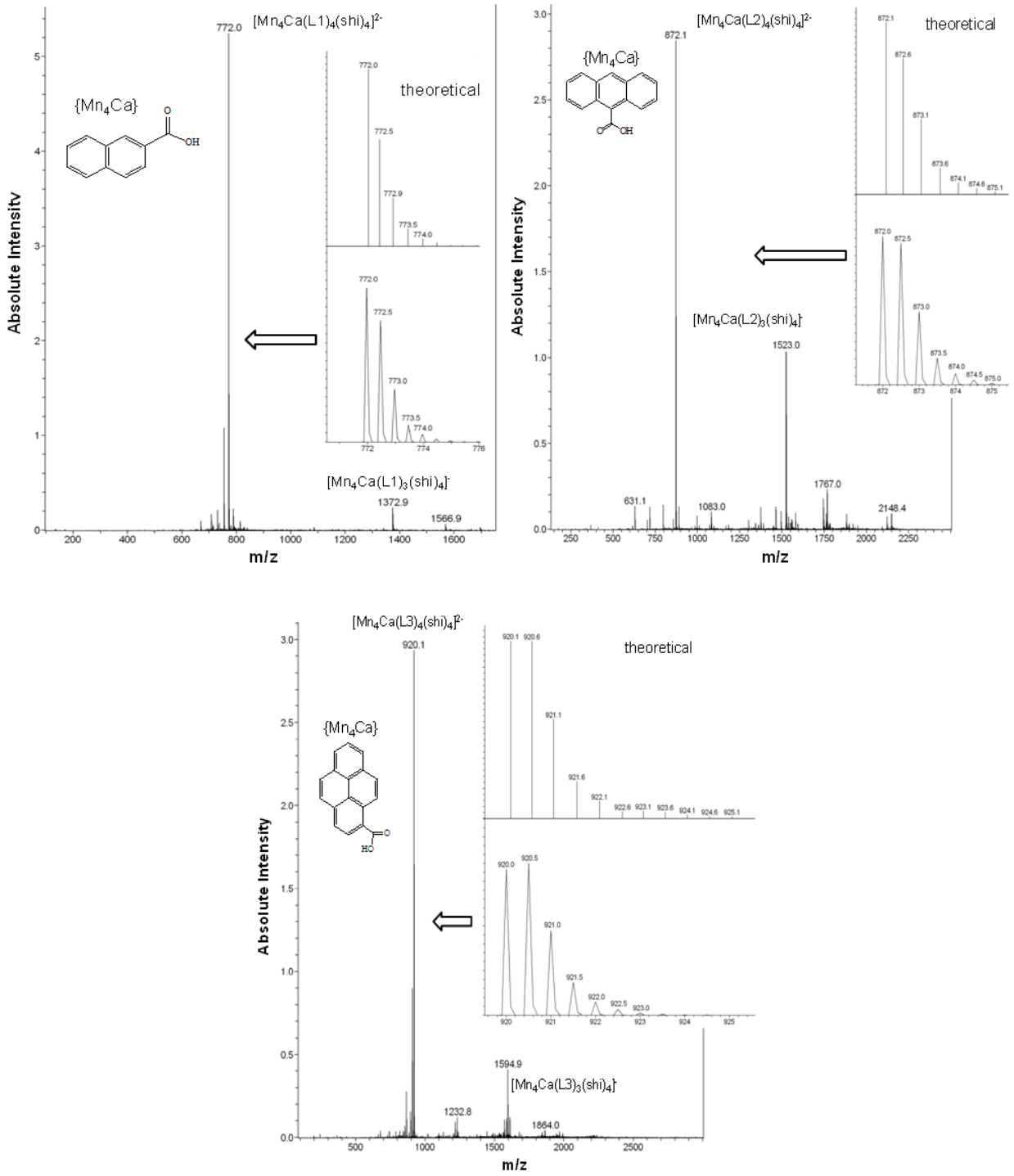

Figure 2.6. Negative ion ES mass spectra of **1** (top left), **2** (top right) and **4** (bottom) in MeCN. Insets illustrate the zoomed region around the predominant $[Mn_4Ca(LX)_4(shi)_4]^{2-}$ dianions (X = 1–3) and the corresponding, theoretically calculated, isotopic distributions.

2.3.4 Electrochemistry

The redox activity of electrochemically prominent metal complexes can be assessed by cyclic voltammetry. This technique is of significant importance in both molecular magnetism and bioinorganic chemistry. For example, in molecular magnetism arena, electrochemical studies on various $[Mn^{III}_8Mn^{IV}_4O_{12}(O_2CR)_{16}(H_2O)_4]$ compounds have revealed a rich redox chemistry involving several quasi-reversible oxidation and reduction processes.[154] Four different oxidation levels of this family of clusters have been isolated and the corresponding 1-, 2-, 3- and 4-electron reduced species were characterized in the solid-state and demonstrated their distinct single-molecule magnetism properties compared to the parent $\{Mn_{12}\}$ complex.[155] In the bioinorganic and biomimetic fields related to PSII, it is now well-documented that Mn ions within OEC show a high degree of redox and chemical versatility, while the protein residues and coordination environment are both critical for modulating the redox potentials and providing pathways for electron- and proton-transfer effects.[156] For example, in the S_0 state of OEC cycle, EPR, XANES and ENDOR studies have proposed two different formal oxidation states, II/III/IV/IV and III/III/III/IV, for the Mn atoms that correspond to the low- and high-valent schemes, respectively.[27,157]

Toward that end, the electrochemical properties of complexes **1**, **2** and **4** were studied in MeCN and all showed that they exhibit very similar redox processes. The cyclic voltammogram (CV) of complex **1** is shown in Figure 2.7, top. It displays a well-defined reversible oxidation at ~0.43 V and an irreversible reduction that corresponds to the broad peak at –0.47 V. The CV spectra of the anthracene-analogue **2** (Figure 2.7, middle) and pyrene-substituted **4** (Figure 2.7,

bottom) show very similar patterns comprising well-defined reversible oxidations at ~0.44 and ~0.42 V, and irreversible reductions associated with the appearance of weak and broad peaks at –0.78 and –0.79 V, respectively. For the reversible oxidation couple of all three studied compounds, the forward and reverse waves are well formed with a peak separation of 70 (**1**), 190 (**2**) and 100 (**4**) mV comparable to that of ferrocene under the same conditions; this is indicative of a one-electron process.[158]

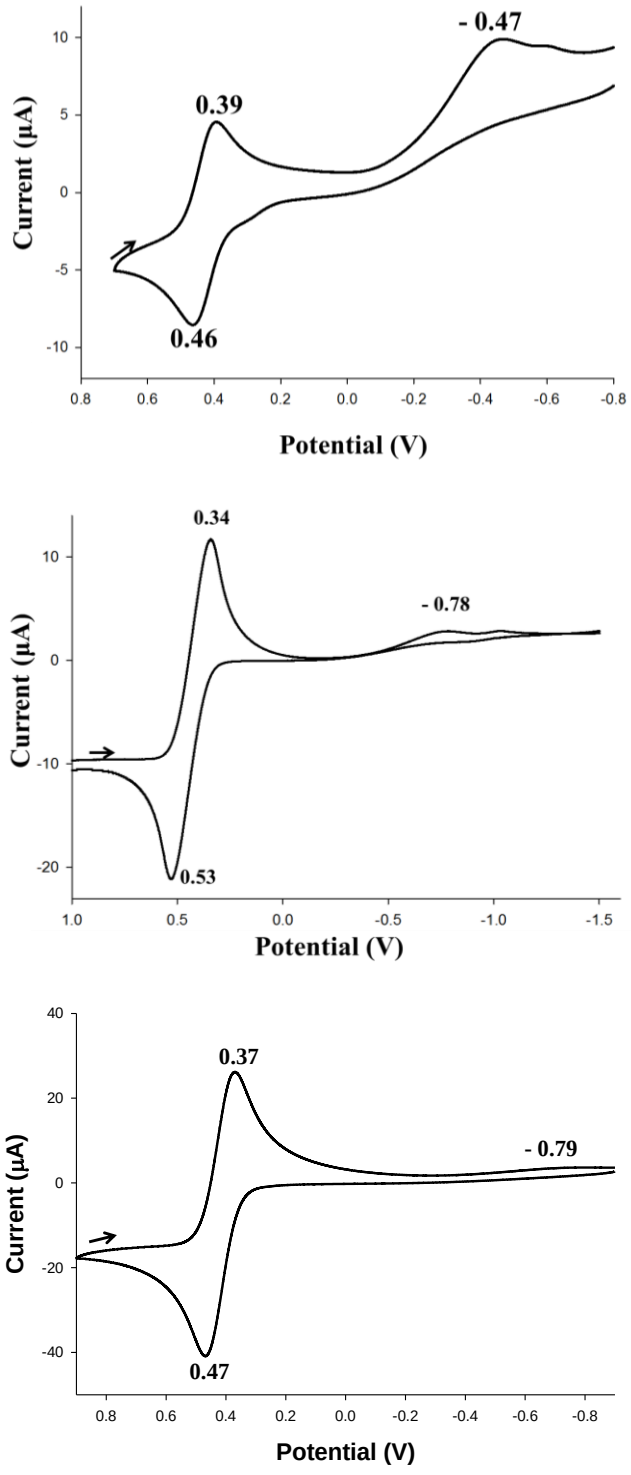

Figure 2.7. Cyclic voltammograms at 100 mV s^{-1} for complexes **1** (top), **2** (middle) and **4** (bottom) in MeCN containing 0.1 M $NBu^{n}_{4}PF_{6}$ as supporting electrolyte. The indicated potentials are versus Fc/Fc^{+}.

In summary, all complexes exhibited a similar oxidation but the reduction waves seemed to be slightly different. Such small discrepancies most likely result from the different nature of the carboxylate ligand. It is known that in isostructural, high oxidation state Mn complexes the identity, basicity and steric and electronic properties of the carboxylate ligands affect the sensitivity of metal ions' redox potentials.[159] The electrochemical results may be illustrated as: $[Mn_4Ca]^+ \leftrightarrow [Mn_4Ca] \rightarrow [Mn_4Ca]^-$. Synthetic efforts to isolate and structurally characterize the monocation are objectives for the future to address and accomplish.

2.3.5 Photophysical Studies

The pronounced ability of complexes **1**–**4** to retain their structures in solution prompted me to further investigate their optical activity at room temperature conditions. It was thus decided to perform excitation/emission studies in MeCN solutions of **1**, **2** and **4** at concentrations ~10^{-5} M. Very recently, Chia and Tay overviewed the difficulties in obtaining emissions from transition metal complexes, usually produced from triplet excited states, as a result of the fast intersystem crossing facilitated by the strong spin-orbit coupling.[160] It is also known that quenching of the emission intensity due to paramagnetic effects is a common feature in 3d-metal complexes.[161] In order to tackle this problem, the use of organic bridging groups with emission dyes seems to be a promising route.

The fluorescence behaviours of the free, uncoordinated $shaH_2$ and LX-H (X = 1–3) ligands are well-known in both solid-state and solution. For instance, and with relevance to our studies, $shaH_2$ in MeCN shows a maximum emission at 450 nm upon maximum excitation at 346

nm.[162] Complex **1** shows an intense emission at 396 nm upon excitation at the maximum observed at 300 nm (Figure 2.8, top); the location of the emission peak is at the same area where naphthalene emits but slightly shifted, indicative of charge transfer from the ligands to the cluster core.[151,163] A light-brown solution of complex **2** in MeCN also shows a very strong "blue"-shifted emission upon excitation at the UV-region, with the three emission peaks at 391, 410, and 433 nm attributed to the characteristic peaks of anthracene chromophore (Figure 2.8, middle).[164] Interestingly, complex **4** displays two sharp emission peaks at 392 and 408 nm, upon UV excitation at 380 nm, which are characteristic of the corresponding monomer and excimer emissions of the pyrene unit (Figure 2.8, bottom).[126,165] The formation of a pyrene excimer requires an excited molecule to come in contact with another molecule in its ground state within the excited state lifetime. In order for this to occur, the pyrene units must be well isolated from each other such that excitation is localized on one of the molecules and then diffusion of the molecule will allow for an encounter between an excited pyrene and a ground state one. In such ideal case, the fluorescence emission of pyrene excimers appears as a broad, structureless band located at 470–500 nm.[166] In complex **4** the excimer peak has been "blue"-shifted, and this is likely due to its coordination with the metal centers and the presence of significant intramolecular π–π^* interactions which bring the pyrene units into close contacts.

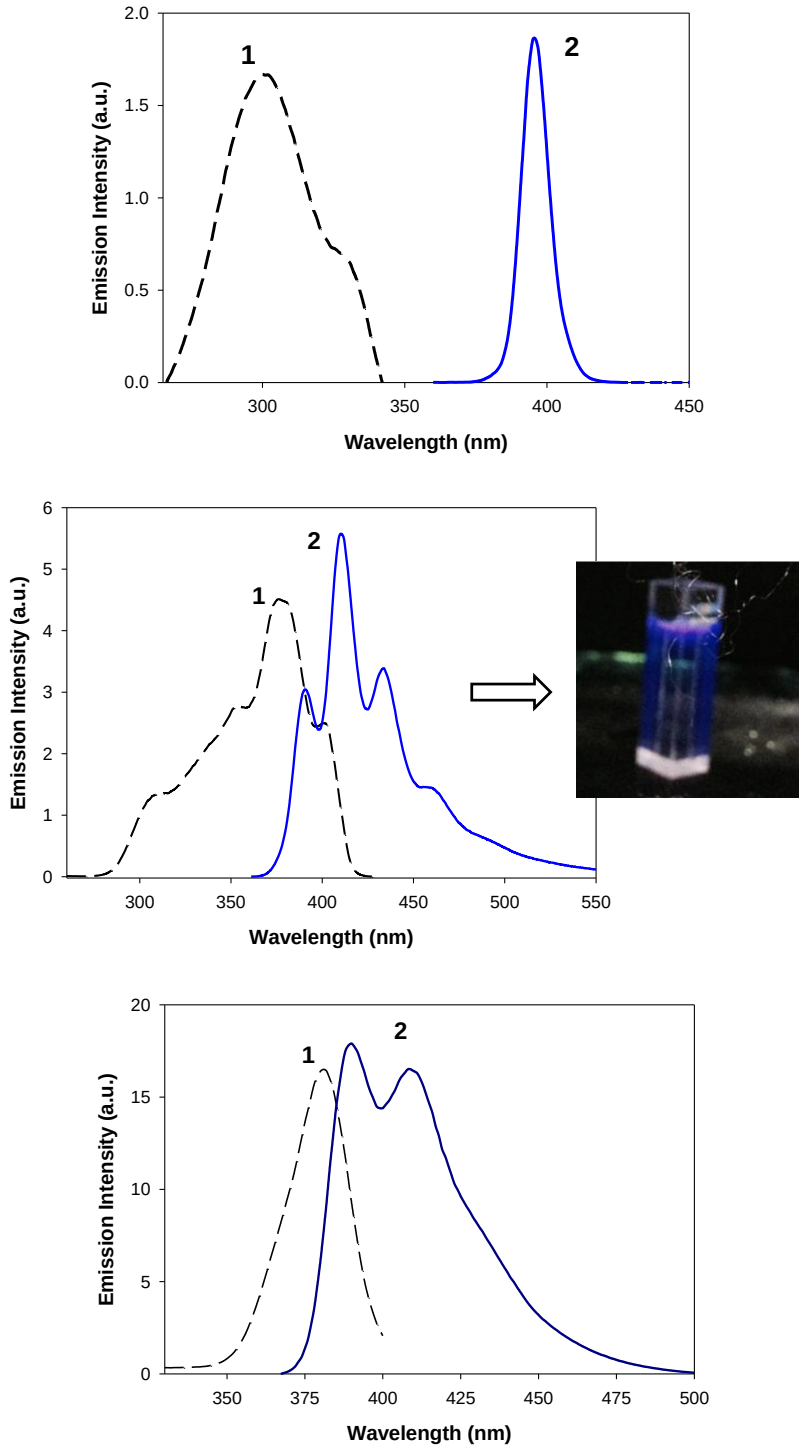

Figure 2.8. Excitation (1) and emission (2) spectra of complexes **1** (top), **2** (middle) and **4** (bottom) in MeCN. The inset highlights a photograph of complex **2** under a UV lamp.

2.3.6 Solid-State Magnetic Susceptibility Studies

Variable-temperature direct current (*dc*) magnetic susceptibility measurements were performed on powdered polycrystalline samples of complexes **1**, **3** and **4**, restrained in eicosane to prevent torquing, in a 1 kG (0.1 T) field and in the 5.0-300 K range. The data are shown as $\chi_M T$ versus T plots in Figure 2.9. The isostructural complexes **1** and **4** exhibited similar magnetic behaviour (*vide infra*), and it was thus decided to perform magnetic studies on the slightly different complex **3** instead of **2**; however, the magnetic response was again similar to that of **1** and **4**. The $\chi_M T$ product for all three compounds steadily decreases from 12.09 (**1**), 12.19 (**3**) and 9.53 (**4**) cm^3Kmol^{-1} at 300 K to 1.32 (**1**), 1.35 (**3**) and 0.62 (**4**) cm^3Kmol^{-1} at 5.0 K. The 300 K values are close to or less than (in case of the pyrene-analogue **4**) the spin-only (g = 2) value of 12 cm^3Kmol^{-1} for four non-interacting Mn^{III} ions, similar to the $\chi_M T$ value of the previously reported $[Mn_4Ca(O_2CPh)_4(shi)_4]^{2-}$.[96] The shape of the $\chi_M T$ versus T curves clearly indicate the presence of predominant antiferromagnetic exchange interactions between the four Mn^{III} atoms, and a resulting S = 0 ground state for each of the reported compounds.

To determine the individual pairwise exchange parameters J_{ij} between Mn_iMn_j pairs within the magnetic cores, the $\chi_M T$ versus T data for complexes **1**, **3** and **4** were fit to the theoretical expression for a $\{Mn^{III}_4\}$ square (inset of Figure 2.9, top) using the isotropic Heisenberg spin Hamiltonian given by Eqn. 2.3.

$$H = -2J(\hat{S}_1 \cdot \hat{S}_2 + \hat{S}_2 \cdot \hat{S}_3 + \hat{S}_3 \cdot \hat{S}_4 + \hat{S}_1 \cdot \hat{S}_4) \qquad \textbf{Eqn. 2.3}$$

In light of the very similar Mn–O–N–Mn torsion angles and Mn···Mn separations within the $\{Mn_4\}$ square, all interactions between neighbouring Mn^{III} atoms were considered as equivalent (1-*J* model). The fit parameters were thus *J* and *g*. A temperature-independent paramagnetism (TIP) term was also included in all cases. Data below 30 K were omitted in order to avoid effects from Zeeman interactions, magnetic anisotropy (zero-field splitting, *D*) and crystal structure disorders; these are all factors that are not included in the above model.[126] Good fits were obtained for all three complexes, and these are shown as solid lines in Figure 2.9. The best-fit parameters were: $J = -3.17(4)$ cm^{-1}, $g = 1.97(1)$ and TIP = 6×10^{-3} cm^3 mol^{-1} for **1**; $J = -2.73(2)$ cm^{-1}, $g = 2.10(4)$ and TIP = 10^{-3} cm^3 mol^{-1} for **3**; and $J = -2.98(2)$ cm^{-1}, $g = 1.86(2)$ and TIP = 8×10^{-4} cm^3 mol^{-1} for **4**. The fits of the data indicate $S = 0$ ground states and $S = 1$ first excited states lying 6.34, 5.46 and 5.96 cm^{-1} higher in energy, respectively. Attempts to include a *D* term into the fitting process, using the program PHI,[167] failed to give a better low-temperature fit. Fits of the data to a 2-*J* model, assuming that the next-nearest neighbour interactions across the diagonal Mn sites are not zero, gave results of comparable quality. These, however, could lead to overparameterization problems, and therefore the long $Mn^{III}\cdots Mn^{III}$ exchange interactions can be ignored. Finally, none of the magnetically studied complexes showed peak maxima in the χ_M versus *T* plots. The antiferromagnetic interactions in all compounds are as expected for systems coupled solely through oximate bridges with very large M–O–N–M (M = 3d-metal ion) torsion angles (>160°).[168]

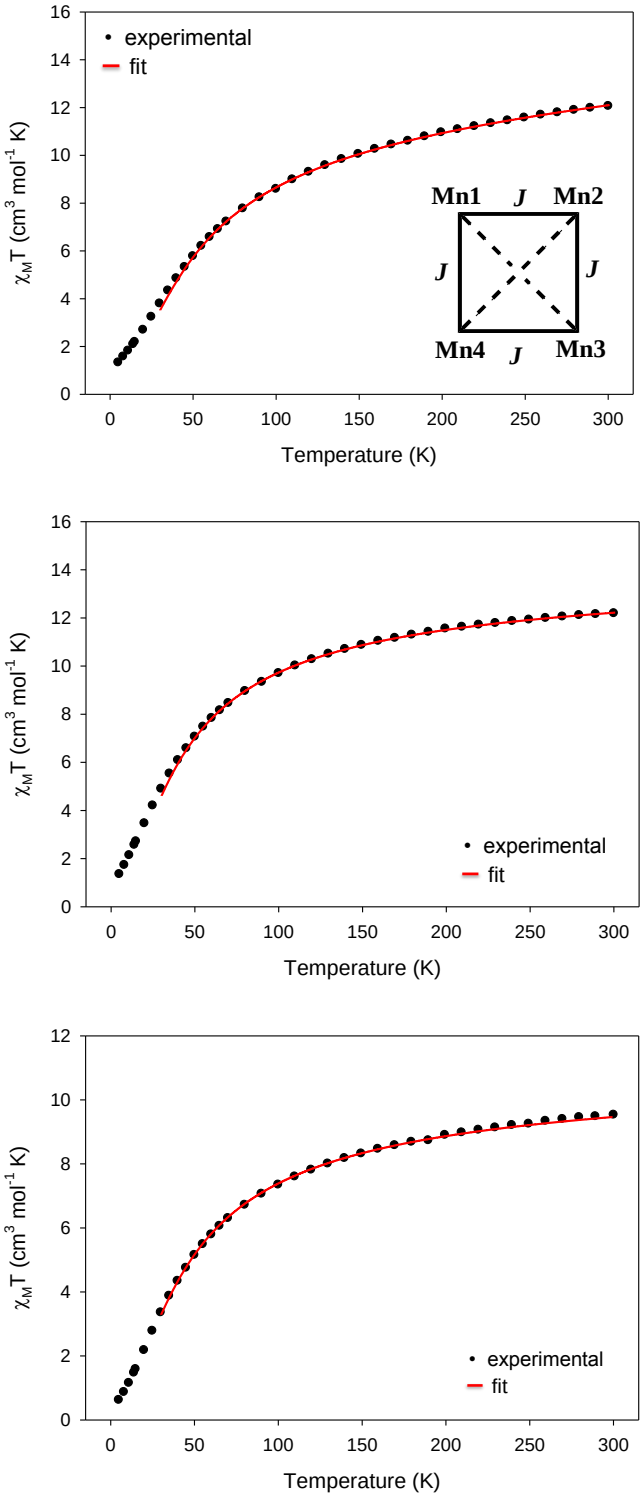

Figure 2.9. $\chi_M T$ versus T plots for **1** (top), **3** (middle) and **4** (bottom) at 0.1 T *dc* field. The red solid line is the fit of the corresponding data; see the text for the fit parameters. Inset: 1-*J* coupling scheme used for all complexes.

2.3.7 Relevance of Complexes 1–4 to Low-Oxidation States of the OEC: A Qualitative Approach

In the absence of advanced XAS, EXAFS and ENDOR studies, which would shine more light into the similarities of **1**–**4** with OEC, I provide instead a qualitative and brief discussion of the relevance of reported compounds to some species of the native enzyme. Complexes **1**–**4** have the same Mn_4Ca content and carboxylate ligation as the OEC. I recognize that within the structures of all complexes the average Mn···Mn (between closest neighbours) and Mn···Ca separations are ~4.6 and ~3.7 Å, respectively, significantly longer than the corresponding values of 2.7–3.3 and ~3.4 Å for the OEC in PSII. However, the structures of the reported compounds may be relevant to the OEC in other ways. On the basis of the S_1 Kok state of the OEC being at the $2Mn^{III},2Mn^{IV}$ oxidation level, then the $4Mn^{III}$ level of **1**–**4** would place them at the S_{-1} state. Hydrazine (N_2H_4), hydroxylamine (NH_2OH) and nitric oxide are known to be able to reduce the OEC to S_{-1}, S_{-2} and even S_{-3} states.[12,169] These are not involved in the water oxidation catalytic cycle, but may be related to intermediates during the *in vivo* assembly of the OEC. Assuming these involve Mn-based reductions, then they would be at the $4Mn^{III}$, $Mn^{II},3Mn^{III}$ and $2Mn^{II},2Mn^{III}$ levels, respectively; an EPR signal assignable to a $Mn^{II}Mn^{III}$ subunit has been detected for S_{-2}.[170] It is thus possible that the structures of complexes **1**–**4** may be of more relevance to these lower oxidation state forms of the OEC that will have a lower preference for oxido bridges than to the higher oxidation states that have a cubane structure and are involved in the catalytic cycle. Along these lines, the similarity between the oximato N–O bridging unit of shi^{3-} within **1**–**4** and the M–N–O–M unit seen in hydroxylamine-bridged metal complexes[171] is

intriguing and suggests that **1**–**4** may be providing insights into the kind of subunits that might be generated on reduction of the OEC with NH_2OH.

2.4 ***Conclusions and Perspectives***

To summarize, I have shown that salicylhydroxime scaffold can provide the means of obtaining new heterometallic Mn–Ca clusters with the same Mn_4Ca stoichiometry as the OEC and the four Mn ions in a moderate 3+ oxidation level. In addition, the incorporation of fluorescent carboxylate groups as supporting ligands about the paramagnetic $\{Mn_4Ca\}$ core has also enabled me to gain access into some interesting photophysical properties such as "blue"-shifted emissions at room temperature. The reported compounds are also very rare examples of metal clusters that retain their solid-state structures in solution, as accurately confirmed by electrospray ionization mass spectrometry. This is most likely due to the pronounced stability of the $\{Mn_4Ca\}$ metallacrown core induced by the four donor atoms of the salicylhydroximate ligand.

It must be admitted that the core of **1**–**4** is different from the distorted-cubane core found in the native OEC, but may be relevant to lower oxidation level species that are intermediates during assembly of the OEC *in vivo*, or those generated by treatment of the OEC with strong reducing agents. By taking into account the well-defined reversible oxidation observed in all studied $\{Mn^{III}_4Ca\}$ compounds, methods to isolate the one-electron oxidized species are currently in progress. This could in principle facilitate the stabilization of O^{2-} groups and consequently the formation of an oxido-bridged metal core, structurally closer to that seen in the OEC and more susceptible in resembling the S_0 state of the Kok cycle.

Chapter 3

Structural Diversities in Heterometallic Mn–Ca Cluster Chemistry from the Use of Salicylhydroxamic Acid: $\{Mn^{III}_4Ca_2\}$, $\{Mn^{II/III}_6Ca_2\}$, $\{Mn^{III/IV}_8Ca\}$ and $\{Mn^{III}_8Ca_2\}$ Complexes with Relevance to Both High- and Low-Valent States of the Oxygen-Evolving Complex

3.1 *Preface*

Several multinuclear, homometallic Mn clusters at various oxidation state levels and descriptions have been extensively reported over the last two decades or so,[172] but heterometallic Mn–Ca molecular cluster chemistry has been only sparingly developed.[173] The research groups of Agapie,[107] Zhang,[111] Christou and Stamatatos[110] have reported some of the closest structural models to the native OEC core, all containing the desired $\{Mn_3CaO_4\}$ cubane core and Mn atoms in high oxidation states (i.e., Mn^{IV}). In all cases, different chelating and bridging ligands have been utilized, including carboxylates and pyridyl polyalcohols, among others. These molecular compounds nicely resemble some of the latter *S* states (S_2 and S_3) of the catalytic Kok cycle within the native OEC.

My interest, similar as in Chapter 2, is in the exploration of lower oxidation species (S_n states; n = –1, –2, –3) of the catalytic cycle through the synthesis of heterometallic Mn–Ca complexes with unique structural motifs, diverse topologies and different Mn oxidation state descriptions that would not require for their stabilization and crystallization to occur in the presence of bridging oxido groups. The employment of salicylhydroxime (shiH_3, Scheme 1.9) in Mn–Ca chemistry has previously led me to the synthesis of the first family of oxido-free

{Mn^{III}_4Ca} complexes with a square pyramidal topology and the exact metal stoichiometry as that found in the native OEC, discussed in Chapter 2. In this chapter, I will discuss the new synthetic conditions I have discovered, unveiling four different heterometallic Mn–Ca/shi^{3-} complexes with diverse nuclearities, metal stoichiometries and oxidation state descriptions of relevance to both high- and low-oxidation states of the OEC. The synthesis, structures and magnetic properties of the heterometallic {$Mn^{III}_4Ca_2$}, {$Mn^{II/III}_6Ca_2$}, {$Mn^{III/IV}_8Ca$} and {$Mn^{III}_8Ca_2$} complexes are reported herein.

3.2 ***Experimental Section***

3.2.1 Physical Measurements

Elemental analysis: Elemental analyses (C, H and N) were performed on a PerkinElmer 2400 Series II Analyzer.

FT-IR spectroscopy: Infrared (IR) spectra were recorded in the solid state on a Bruker FT-IR spectrometer (ALPHA Platinum ATR single reflection) in the 4000–400 cm^{-1} range.

Magnetic susceptibility measurements: Variable-temperature direct current (*dc*) magnetic susceptibility studies were performed at the University of Florida Chemistry Department on a Quantum Design MPMS-XL SQUID susceptometer equipped with a 7 T magnet and operating in the 1.8–400 K range. The Superconducting Quantum Interference Device (SQUID) allows for the complete study of the magnetic properties of bulk and molecule-based materials at various temperatures and magnetic fields. The *dc* scan mode provides continual plotting and capture of raw magnetic data points at static or sweeping fields and

temperatures. Samples were embedded in solid eicosane to prevent torquing. Pascal's constants were used to estimate the diamagnetic correction, which was subtracted from the experimental susceptibility to give the molar paramagnetic susceptibility (χ_M).[127]

3.2.2 Synthesis

General considerations: All manipulations were performed under aerobic conditions using chemicals and solvents as received, unless otherwise stated. The starting materials $Mn(O_2CPh)_2{\cdot}2H_2O$, $[Mn_3O(O_2CPh)_6(py)_3](ClO_4)$ and $[Mn_3O(O_2CPh)_6(py)_2(H_2O)]$ (py = pyridine) were prepared as described elsewhere.[174] *Perchlorate salts are potentially explosive; such compounds should be synthesized and used in small quantities, and treated with utmost care at all times.*

$[Mn_4Ca_2(O_2CPh)_4(shi)_4(H_2O)_3(Me_2CO)]$ (5). To a stirred, colourless solution of $shaH_2$ (0.31 g, 2.0 mmol) in Me_2CO (30 mL) the solids $[Mn_3O(O_2CPh)_6(py)_3](ClO_4)$ (0.87 g, 0.7 mmol) and $CaBr_2{\cdot}xH_2O$ (0.20 g, 1.0 mmol) were added together. The resulting brown suspension was stirred for 1 h, during which time all the solids dissolved and the colour of the solution changed to dark brown. The solution was filtered and left to evaporate slowly at room temperature. After five days, brown plate-like crystals of **5**$\cdot 3Me_2CO \cdot 2.8H_2O$ appeared and were collected by filtration, washed with Me_2CO (2 × 5 mL) and Et_2O (2 × 5 mL), and dried in air; the yield was 60%. The crystalline solid was analyzed as **5**$\cdot 2H_2O$: C, 46.23; H, 3.42; N, 3.65 %. Found: C, 46.43; H, 3.58; N, 3.54 %. Selected ATR data (cm^{-1}): 3058 (wb), 1595 (s), 1567 (s), 1543 (m), 1509 (s), 1432 (m), 1389 (vs), 1316 (s), 1244 (m), 1157 (m), 1100 (m), 1068 (w), 1023 (m), 929 (s), 864 (w), 838 (w), 749 (w), 721 (vs), 678 (vs), 648 (s), 602 (vs), 531 (w), 477 (s), 408 (m).

(pyH)[$Mn_6Ca_2Cl_2(O_2CPh)_7(shi)_4(py)_4$] (6). To a stirred, colourless suspension of $shaH_2$ (0.08 g, 0.5 mmol) in CH_2Cl_2 (30 mL) the solids [$Mn_3O(O_2CPh)_6(py)_2(H_2O)$] (0.54 g, 0.5 mmol) and $CaCl_2·6H_2O$ (0.11 g, 0.5 mmol) were added together. The resulting red suspension was stirred for 2 h, during which time all the solids dissolved and the colour of the solution changed to brown. The solution was filtered, and Et_2O (60 mL) diffused into the filtrate. After ten days, red rod-like crystals of **6**·$2Et_2O·CH_2Cl_2$ appeared and were collected by filtration, washed with CH_2Cl_2 (2 × 5 mL) and Et_2O (2 × 5 mL), and dried in air; the yield was 45%. The crystalline solid was analyzed as solvent-free **6**: C, 52.68; H, 3.34; N, 5.42 %. Found: C, 52.59; H, 3.25; N, 5.64 %. Selected ATR data (cm^{-1}): 3041 (m), 1597 (s), 1569 (s), 1512 (m), 1487 (m), 1468 (m), 1445 (m), 1432 (m), 1393 (vs), 1359 (s), 1319 (s), 1250 (m), 1218 (m), 1176 (m), 1099 (m), 1067 (m), 1037 (s), 927 (s), 865 (s), 838 (m), 754 (m), 719 (vs), 672 (vs), 647 (s), 475 (vs), 434 (m).

($NHEt_3)_2$[$Mn_8Ca(OEt)_2(shi)_{10}(EtOH)_2$] (7). To a stirred, colourless solution of $shaH_2$ (0.08 g, 0.5 mmol) and NEt_3 (0.21 mL, 1.5 mmol) in EtOH (30 mL) the solids $Mn(NO_3)_2·4H_2O$ (0.13 g, 0.5 mmol) and $Ca(NO_3)_2·4H_2O$ (0.12 g, 0.5 mmol) were added together. The resulting dark red suspension was stirred for 1 h, during which time all the solids dissolved and the colour of the solution changed to very dark brown. The solution was filtered and left to evaporate slowly at room temperature. After two weeks, dark-brown plate-like crystals of **7**·$3EtOH·H_2O$ appeared and were collected by filtration, washed with cold EtOH (2 × 5 mL) and Et_2O (2 × 5 mL), and dried in air; the yield was 30%. The crystalline solid was analyzed as **7**·$2H_2O$: C, 43.86; H, 4.19; N, 7.14 %. Found: C, 43.71; H, 4.12; N, 7.22 %. Selected ATR data (cm^{-1}): 3375 (mb), 3062 (m), 2966 (mb), 1595 (s), 1564 (s), 1471 (vs), 1384 (vs), 1314 (vs), 1257 (s), 1153 (m), 1098 (m), 1034 (s), 950 (s), 860 (s), 752 (s), 672 (vs), 641 (s), 591 (sb), 461 (m).

$(NHEt_3)_4[Mn_8Ca_2(CO_3)_4(shi)_8]$ (8). To a stirred, colourless solution of $shaH_2$ (0.08 g, 0.5 mmol) and NEt_3 (0.21 mL, 1.5 mmol) in $CHCl_3$ (30 mL) the solids $Mn(O_2CPh)_2 \cdot 2H_2O$ (0.17 g, 0.5 mmol) and $Ca(ClO_4)_2 \cdot 4H_2O$ (0.16 g, 0.5 mmol) were added together. The resulting dark red suspension was stirred for 3 h, during which time all the solids dissolved and the colour of the solution changed to dark brown. The solution was filtered and left to evaporate slowly at room temperature. After one month, brown plate-like crystals of **8**·$9CHCl_3$ appeared and were collected by filtration, washed with $CHCl_3$ (2 × 5 mL) and Et_2O (2 × 5 mL), and dried under vacuum; the yield was 20%. The crystalline solid was analyzed as **8**·$2CHCl_3$: C, 40.22; H, 3.85; N, 6.54 %. Found: C, 40.36; H, 3.99; N, 6.48 %. Selected ATR data (cm^{-1}): 2993 (mb), 1595 (s), 1566 (s), 1508 (s), 1468 (m), 1448 (m), 1432 (s), 1375 (vs), 1316 (s), 1255 (s), 1155 (m), 1098 (m), 1066 (m), 1027 (s), 935 (s), 863 (s), 749 (vs), 720 (vs), 673 (vs), 645 (vs), 609 (vs), 532 (m), 443 (s), 415 (m).

3.2.3 Single-crystal X-ray Crystallography

A brown single-crystal of complex **5**·$3Me_2CO \cdot 2.8H_2O$ was mounted in capillary with drops of mother liquid because they were destroyed immediately when immersed into the crystallographic oil; this was confirmed by the presence of many partially occupied solvate molecules. Diffraction measurements were made at room temperature on a Rigaku R-AXIS SPIDER Image Plate diffractometer using graphite-monochromated Cu Kα radiation. Data collection (ω-scans) and processing (cell refinement, data reduction and empirical absorption correction) were performed using the CrystalClear program package.[175] The structure was solved by direct methods using SHELXS-97,[134,135] and refined by full-matrix least-squares techniques

on F^2 with SHELXL, version 2014/6.[176] All non-H atoms were refined anisotropically, except from those belonging to partially occupied solvate molecules which were refined isotropically. All H atoms were introduced at calculated positions as riding on their respective atoms. No H atoms for the partially occupied solvate molecules were included in the refinement. The O2W and O41 atoms that belong to the coordinated H_2O and acetone molecules are disordered with site occupancies of 0.5.

Data for complexes **6**·2Et_2O·CH_2Cl_2 and **7**·3EtOH·H_2O were collected on beamline 11.3.1 at the Advanced Light Source, Lawrence Berkeley National Lab. Samples were mounted on MiTeGen kapton loops and placed in a 100(2) K nitrogen cold stream provided by an Oxford Cryostream 700 Plus low temperature apparatus on the goniometer head of a Bruker D8 diffractometer equipped with a PHOTON100 CMOS detector operating in shutterless mode. Diffraction data were collected using monochromated synchrotron radiation [silicon(111) to a wavelength of 0.8856(1) Å and 0.7749(1) Å for **6** and **7**, respectively)]. An approximate full sphere of data was collected using a combination of φ and ω scans with scan speeds of 1 s/4° for the φ scans, and 1 and 3 s/° for the ω scans at $2\theta = 0$ and –45°, respectively. The structures were solved by intrinsic phasing (SHELXT) and refined by full-matrix least squares on F^2 (SHELXL-2014). All non-H atoms were refined anisotropically. H atoms were geometrically calculated and refined as riding atoms. For complex **6**, the coordinated pyridine molecules were found to be disordered and the carbon atoms have been modeled over two sites with complementary occupancies. Some minor rotational disorder was also found for the aromatic rings of the shi^{3-} and $PhCO_2^-$ groups. The free pyridinium cation is rotationally disordered over two sites, such that the –NH group can occupy one of the two symmetry-related sites. The C and N atoms that occupy this site have been refined with occupancies of 0.5, with the same *xyz* coordinates and

isotropic displacement parameters as each other. The partial occupancy of the CH_2Cl_2 molecule was found to be disordered over two symmetry-related sites, and the atoms were refined isotropically with site occupancies of 0.5. The C3E–C4E ethyl chain of the Et_2O molecule was found to be disordered; however, only the major orientation of this chain could be modelled satisfactorily (occupancy 0.81). For complex **7**, all non-H atoms belonging to the cluster were located. The aromatic ring of one shi^{3-} ligand was found to be disordered and has been modeled over two sites with complementary site occupancies. In addition to the cluster compound, there are two triethylammonium ($NHEt_3^+$) cations, three guest EtOH molecules and a H_2O molecule. The two $NHEt_3^+$ cations were found to be disordered and have been modeled over two locations. Similarly, the EtOH molecules were each found to be disordered and have been modeled over two or three different positions. Equivalent atoms have been constrained to have equal U_{ij} values. Different orientations of the same molecule have been restrained to have equal bond lengths and angles by use of the RESI and SAME commands. The ammonium H atom belonging to the minor orientation of the N1a cation has been held in place by use of SDAI commands keeping an equal distance between the H atom and the three C atoms bound to the central N atom. All ammonium and hydroxido H atoms were located at the difference map, fixed at distances of 0.88 and 0.84 Å from the N or O atoms, respectively, to which they are bound, and given a thermal displacement parameter of 1.2 or 1.5 times that of the corresponding N or O atom to which they are bound. Not all hydroxido or water H atoms could be located during the refinement. These "missing" hydrogen atoms have been included in the molecular formula but not in the final model.

A selected crystal of complex **8**·9$CHCl_3$ was manually harvested and mounted on a cryoloop using adequate oil.[128] All the single-crystals chosen for data collection showed very

weak X-ray diffraction patterns under the accessible Mo Kα radiation. It was not feasible to obtain any better diffraction for this complex, but the reported data are of enough quality to adequately confirm the metals' connectivity and most of the molecules in the crystal lattice. Diffraction data were collected at 150.0(2) K on a Bruker X8 Kappa APEX II Charge-Coupled Device (CCD) area-detector diffractometer controlled by the APEX2 software package[129] (Mo Kα graphite-monochromated radiation, λ = 0.71073 Å), and equipped with an Oxford Cryosystems Series 700 cryostream monitored remotely with the software interface Cryopad.[130] Images were processed with the software SAINT+,[131] and absorption effects corrected with the multiscan method implemented in SADABS.[177] The structure was solved using the algorithm implemented in SHELXT-2014,[135,178] and refined by successive full-matrix least-squares cycles on F^2 using the latest SHELXL-v.2014.[135,179] The non-H atoms were successfully refined using anisotropic displacement parameters. H atoms bonded to carbon were placed at their idealized positions using the appropriate HFIX instructions in SHELXL and included in subsequent refinement cycles in riding-motion approximation with isotropic thermal displacements parameters (U_{iso}) fixed at 1.2 or 1.5 × U_{eq} of the relative atom. Considerable electron density was found on the data of the crystal structure, probably due to additional disordered solvate molecules occupying the spaces created by the packing arrangement of the complexes. Efforts to accurately locate, model and refine these residues turned to be ineffective, and the investigation for the total potential solvent area using the software package PLATON[137a,180] confirmed the existence of cavities with potential solvent accessible void volume. Thus, the original data sets were treated with the program SQUEEZE,[137b] which calculates the contribution of the smeared electron density in the lattice voids and adds this to the calculated structure factors from the structural model when refining against the *hkl* file.

The programs used for molecular graphics were MERCURY[138a] and DIAMOND.[138b] Unit cell parameters and structure solution and refinement data for all complexes are listed in Table 3.1.

Table 3.1. Crystallographic Data for Complexes **5–8**.

Parameter	**5**·3Me_2CO·2.8H_2O	**6**·2Et_2O·CH_2Cl_2	**7**·3EtOH·H_2O	**8**·9$CHCl_3$
Formula[a]	$C_{68}H_{71.6}Mn_4Ca_2N_4O_{29.8}$	$C_{111}H_{100}Mn_6Ca_2N_9O_{28.5}Cl_4$	$C_{93.88}H_{107.62}Mn_8CaN_{12}O_{36.94}$	$C_{93}H_{105}Mn_8Ca_2N_{12}O_{36}Cl_{27}$
FW[a] / g mol^{-1}	1721.61	2567.59	2474.64	3443.71
Crystal type	brown plate	red rod	dark-brown plate	brown plate
Crystal size / mm	0.28×0.49×0.80	0.20×0.04×0.04	0.08×0.07×0.06	0.16×0.16×0.08
Crystal system	Monoclinic	Orthorhombic	Orthorhombic	Monoclinic
Space group	*C*2/*c*	*Pnna*	*Pbca*	$P2_1/c$
a / Å	26.9129(5)	20.4296(8)	19.897(2)	17.0486(7)
b / Å	14.1766(3)	24.9250(10)	21.418(2)	20.8611(8)
c / Å	24.1414(4)	21.6928(8)	47.738(5)	21.1323(8)
α / º	90	90	90	90
β / º	92.403(1)	90	90	111.309(2)
γ / º	90	90	90	90
V / $Å^3$	9202.7(3)	11046.1(7)	20344(4)	7001.9(5)

Z	4	4	8	2
T / K	293	100.0(2)	100.0(2)	150(2)
ρ_{calc} / g cm^{-3}	1.243	1.544	1.616	1.633
μ / mm^{-1}	5.951	1.705	1.388	1.359
θ range / °	6.60–64.99	2.34–39.33	2.63–29.42	3.65–25.03
Index ranges	$-31 \le h \le 31$	$-29 \le h \le 29$	$-25 \le h \le 25$	$-20 \le h \le 20$
	$-13 \le k \le 16$	$-35 \le k \le 35$	$-26 \le k \le 27$	$-24 \le k \le 24$
	$-28 \le l \le 28$	$-31 \le l \le 31$	$-60 \le l \le 60$	$-25 \le l \le 25$
Collected reflections	44128	245372	171165	88540
Independent reflections	7680 (R_{int} = 0.0732)	16916 (R_{int} = 0.0507)	21624 (R_{int} = 0.0928)	7805 (R_{int} = 0.0831)
Final $R^{b,c}$ indices [$I>2\sigma(I)$]	$R1$ = 0.0711[d]	$R1$ = 0.0735	$R1$ = 0.0547	$R1$ = 0.1351
	$wR2$ = 0.2008[d]	$wR2$ = 0.1932	$wR2$ = 0.1321	$wR2$ = 0.3940
$(\Delta\rho)_{max,min}$ / e Å^{-3}	0.668, –0.513	1.427, –1.363	0.977, –0.562	5.790, –1.591

[a]Including solvate molecules. [b]$R1 = \Sigma(||F_o| - |F_c||)/\Sigma|F_o|$. [c]$wR2 = [\Sigma[w(F_o^2 - F_c^2)^2]/\Sigma[w(F_o^2)^2]]^{1/2}$, $w = 1/[\sigma^2(F_o^2) + (ap)^2 + bp]$, where $p = [\max(F_o^2, 0) + 2F_c^2]/3$. [d] For 5879 reflections with $I>2\sigma(I)$.

3.3 ***Results and Discussion***

3.3.1 Synthetic Comments and IR Spectra

Two different synthetic strategies were employed for the synthesis and crystallization of the reported heterometallic Mn–Ca cluster compounds. The first utilizes either the charged $[Mn_3O(O_2CPh)_6(py)_3]^+$ triangle as starting material, which comprises 3 Mn^{III} atoms, or the mixed-valence, neutral $[Mn_3O(O_2CPh)_6(py)_2(H_2O)]$ triangle ($2Mn^{III}$ and $1Mn^{II}$), in the presence of CaX_2 sources [X^- = halides; Br (for **5**) and Cl (for **6**)] and $shaH_2$. In this first route, no external organic base was used because the role of proton acceptor could be undertaken by the carboxylate groups, pyridine molecules and/or oxido ions of the $\{Mn_3\}$ starting materials. The oxide-centered and carboxylate-bridged $\{Mn_3\}$ triangles have been proven to be invaluable sources for the synthesis of high-nuclearity, homometallic $\{Mn_x\}$ clusters of various large nuclearities and high oxidation states for the metal atoms.[181] The second route that was followed includes the reactions between simpler, monomeric Mn^{II}- and Ca^{II}-containing starting materials in the presence of the chelating/bridging organic ligand $shaH_2$ and base NEt_3. The latter was used to facilitate the deprotonation of the $shaH_2$/$shiH_3$ ligands and subsequently generate $NHEt_3^+$ cations in solution, which can potentially counterbalance the anionic charge of a cluster compound in solution and help with the crystallization of the resulting salt in the solid state. Finally, various solvents and metal/$shaH_2$ ratios were explored to target for the crystallization of the reported molecular compounds.

Therefore, the one-pot reaction of $[Mn_3O(O_2CPh)_6(py)_3](ClO_4)$ and $CaBr_2{\cdot}xH_2O$ with $shaH_2$ in a 1:1.5:3 molar ratio in Me_2CO gave a dark brown solution that, upon filtration and slow evaporation at room temperature, afforded brown crystals of the complex $[Mn^{III}_4Ca_2(O_2CPh)_4(shi)_4(H_2O)_3(Me_2CO)]$ (**5**) in 60% yield (based on the total available Ca). A similar reaction with that of **5**, albeit with $[Mn_3O(O_2CPh)_6(py)_2(H_2O)]$ and $CaCl_2{\cdot}6H_2O$ in the

presence of $shaH_2$, in a molar ratio of 1:1:1 and in the solvent CH_2Cl_2, led to a brown solution that, upon filtration and slow diffusion with Et_2O, afforded red crystals of a new, mixed-valence complex $(pyH)[Mn^{II}_2Mn^{III}_4Ca_2Cl_2(O_2CPh)_7(shi)_4(py)_4]$ (**6**) in 45% yield (based on the total available Ca). The formation of complexes **5** and **6** is summarized in the balanced Eqns. 3.1 and 3.2, respectively.

$$4\,[Mn_3O(O_2CPh)_6(py)_3](ClO_4) + 6\,CaBr_2 + 12\,shiH_3 + 5\,H_2O + 3\,Me_2CO \rightarrow$$
$$3\,[Mn_4Ca_2(O_2CPh)_4(shi)_4(H_2O)_3(Me_2CO)] + 12\,PhCO_2H + 12\,(pyH)Br + 4\,HClO_4 \qquad \textbf{Eqn. 3.1}$$

$$2\,[Mn_3O(O_2CPh)_6(py)_2(H_2O)] + 2\,CaCl_2{\cdot}6H_2O + 4\,shiH_3 + py \rightarrow$$
$$(pyH)[Mn_6Ca_2Cl_2(O_2CPh)_7(shi)_4(py)_4] + 5\,PhCO_2H + 2\,HCl + 16\,H_2O \qquad \textbf{Eqn. 3.2}$$

Analogous reactions with different carboxylate-based $\{Mn_3\}$ triangles as starting materials (i.e., acetates, propionates, pivalates, etc.), all failed to yield single-crystals suitable for X-ray diffraction studies. I had thus turned my synthetic endeavors towards one-pot reactions between $Mn(NO_3)_2{\cdot}4H_2O$, $Ca(NO_3)_2{\cdot}4H_2O$, $shaH_2$ and NEt_3 in various molar ratios and solvents. Only from the 1:1:1:3 reaction of the aforementioned precursors in solvent EtOH that I was able to grow dark-brown crystals of a nonanuclear, mixed-valence complex $(NHEt_3)_2[Mn^{III}_4Mn^{IV}_4Ca(OEt)_2(shi)_{10}(EtOH)_2]$ (**7**) in 30% yield (based on the total available Ca). It becomes apparent that the reaction solvent has an important role in the synthesis and crystallization of **7**; both bridging EtO^- groups and terminally-bound EtOH molecules were found in the structure of **7** (*vide infra*). Reactions in different alcohols did not yield any crystalline materials but only amorphous precipitates that I was unable to redissolve and

crystallize. Expanding this synthetic protocol further, I decided to perform the 1:1:1:3 reaction between $Mn(O_2CPh)_2{\cdot}2H_2O$, $Ca(ClO_4)_2{\cdot}4H_2O$, $shaH_2$ and NEt_3 in solvent $CHCl_3$. The resulting brown solution was left to evaporate slowly at room temperature and, over a period of approximately 1 month, brown crystals formed in yields as high as 20%, which turned out to be a new decanuclear complex $(NHEt_3)_4[Mn^{III}{}_8Ca_2(CO_3)_4(shi)_8]$ (**8**). The coordinated CO_3^{2-} ions (*vide infra*) were presumably derived from the hydrolysis of atmospheric CO_2 during aerobic reactions.[153c,182] This could also explain the prolonged crystallization period of **8** when compared to the other compounds **5**–**7**. The formation of complexes **7** and **8** is summarized in the balanced Eqns. 3.3 and 3.4, respectively.

$$8\ Mn(NO_3)_2{\cdot}4H_2O + Ca(NO_3)_2{\cdot}4H_2O + 10\ shiH_3 + 3\ O_2 + 20\ NEt_3 + 4\ EtOH \rightarrow$$
$$(NHEt_3)_2[Mn_8Ca(OEt)_2(shi)_{10}(EtOH)_2] + 18\ (NHEt_3)(NO_3) + 42\ H_2O \qquad \textbf{Eqn. 3.3}$$

$$8\ Mn(O_2CPh)_2{\cdot}2H_2O + 2\ Ca(ClO_4)_2{\cdot}4H_2O + 8\ shiH_3 + 2\ O_2 + 24\ NEt_3 + 4\ CO_2 \rightarrow$$
$$(NHEt_3)_4[Mn_8Ca_2(CO_3)_4(shi)_8] + 16\ (NHEt_3)(O_2CPh) + 4\ (NHEt_3)(ClO_4) + 24\ H_2O \qquad \textbf{Eqn. 3.4}$$

The reactions that gave **7** and **8** are both oxidations, undoubtedly by O_2 under the prevailing basic conditions. None of the anions accompanying the metal ions' starting materials appear to participate in the molecular structures of **7** and **8**. NEt_3 has the role of proton acceptor to facilitate the deprotonation of the $shiH_3$ groups and solvate molecules (i.e., EtOH to EtO^-). In addition, both anionic clusters **7** and **8** are stabilized by $NHEt_3^+$ countercations. Employment of different organic bases, such as NMe_3, $Bu^n{}_3N$ and Me_4NOH, did not afford crystalline materials but only oily products that I was not able to further characterize. In all complexes **5**–**8**, the

coordinated shi^{3-} groups resulted from the metal ion-assisted transformation of $shaH_2$ under the reported synthetic conditions (*vide infra*). Finally, by adjusting the experimental molar ratios of the precursors to the stoichiometric equivalents, in an attempt to optimize the isolated yields, I failed to reproduce the crystals of all reported complexes.

Unfortunately, complexes **5**–**8** do not appear to retain their solid-state structures in solutions of various solvent media (i.e., MeCN, CH_2Cl_2 and THF), as it was confirmed by electrospray ionization mass spectrometry (ESI-MS). It is very possible that this diversity of species in solution is one of the main reasons for crystallizing and structurally characterizing in the solid-state four different compounds from the Mn–Ca/$shaH_2$ reaction system. I have thus concentrated on the solid-state characterization of these species, which includes IR spectroscopy and magnetic susceptibility studies. All complexes **5**–**8** have similar IR spectra (see Appendix), which are dominated by the stretching vibrations of the aromatic rings of shi^{3-} in the ~1595–1380 cm^{-1} range; these bands in complexes **5** and **6** overlap with stretches from the carboxylate groups, thus rendering their exact assignments very difficult.[142] Contributions from the $\nu(C{=}N)_{oximate}$ modes of shi^{3-} would be also expected in this region. It is very likely that the strong bands at 1595/1432 cm^{-1} and 1597/1432 cm^{-1} in the spectra of **5** and **6** are attributed to the $\nu_{as}(CO_2)$ and $\nu_s(CO_2)$ modes, respectively; the former should also involve a ring stretching character. The difference Δ [$\Delta = \nu_{as}(CO_2) - \nu_s(CO_2)$] is small (<165 cm^{-1}) in both cases, as expected for the predominant bidentate bridging mode of carboxylate ligation (*vide infra*).[96,143a] The bands at ~3060, ~2990 and ~2970 cm^{-1} in complexes **5**, **7** and **8** can be assigned to the stretching vibrations of ν(N–H) modes from the presence of $NHEt_3^+$ countercations.[96,144] Finally, the carbonate-related IR bands in **8** could be tentatively assigned to the bands located at ~1448 and 863 cm^{-1}, as previously observed in other carbonate-bridged metal complexes.[183]

3.3.2 Description of Structures

The Mn oxidation states in all complexes **5**–**8** were established by charge balance considerations, metric parameters and BVS calculations (Table 3.2).[148] Selected interatomic distances and angles for complexes **5**–**8** are listed in Table 3.3.

The crystal structure of **5** consists of $[Mn_4Ca_2(O_2CPh)_4(shi)_4(H_2O)_3(Me_2CO)]$ molecules (Figure 3.1, top) and lattice Me_2CO and H_2O solvate molecules; the latter two will not be further discussed. The centrosymmetric core of **5** comprises four Mn^{III} and two Ca^{II} atoms arranged in a slightly distorted octahedral topology (Figure 3.1, bottom right), with the Ca^{II} atoms occupying the apical positions and the Mn^{III} atoms forming the square base. The Mn···Mn···Mn angles are 89.7 and 90.3°, deviating only slightly from the ideal 90°, and the Mn···Ca···Mn angles of the eight triangular faces lie within the 75.6–77.5° range. The Mn^{III} atoms form a near-planar square, with each of the edges bridged by a diatomic oximate group from a shi^{3-} ligand, thus giving Mn···Mn separations of 4.623(1) and 4.652(1) Å. The almost perfectly planar Mn_4 unit is clearly due to the large Mn–O–N–Mn torsion angles of 176.7 and 177.6° for the Mn1–O2–N1–Mn2 and Mn2–O12′–N11′–Mn1′ units (and their symmetry-related counterparts), respectively, very close to the ideal linearity of 180°. The Ca^{II} atoms are displaced by 1.784 Å out of the Mn_4 best mean plane. The linkage between the basal Mn^{III} atoms and the apical Ca^{II} atoms is provided by the oximate O atoms (O2, O2′, O12 and O12′) of shi^{3-} ligands and the four $\eta^1{:}\eta^1{:}\mu$ bidentate bridging benzoate groups; the latter are in pairs of two above and below the Mn_4 basal plane.

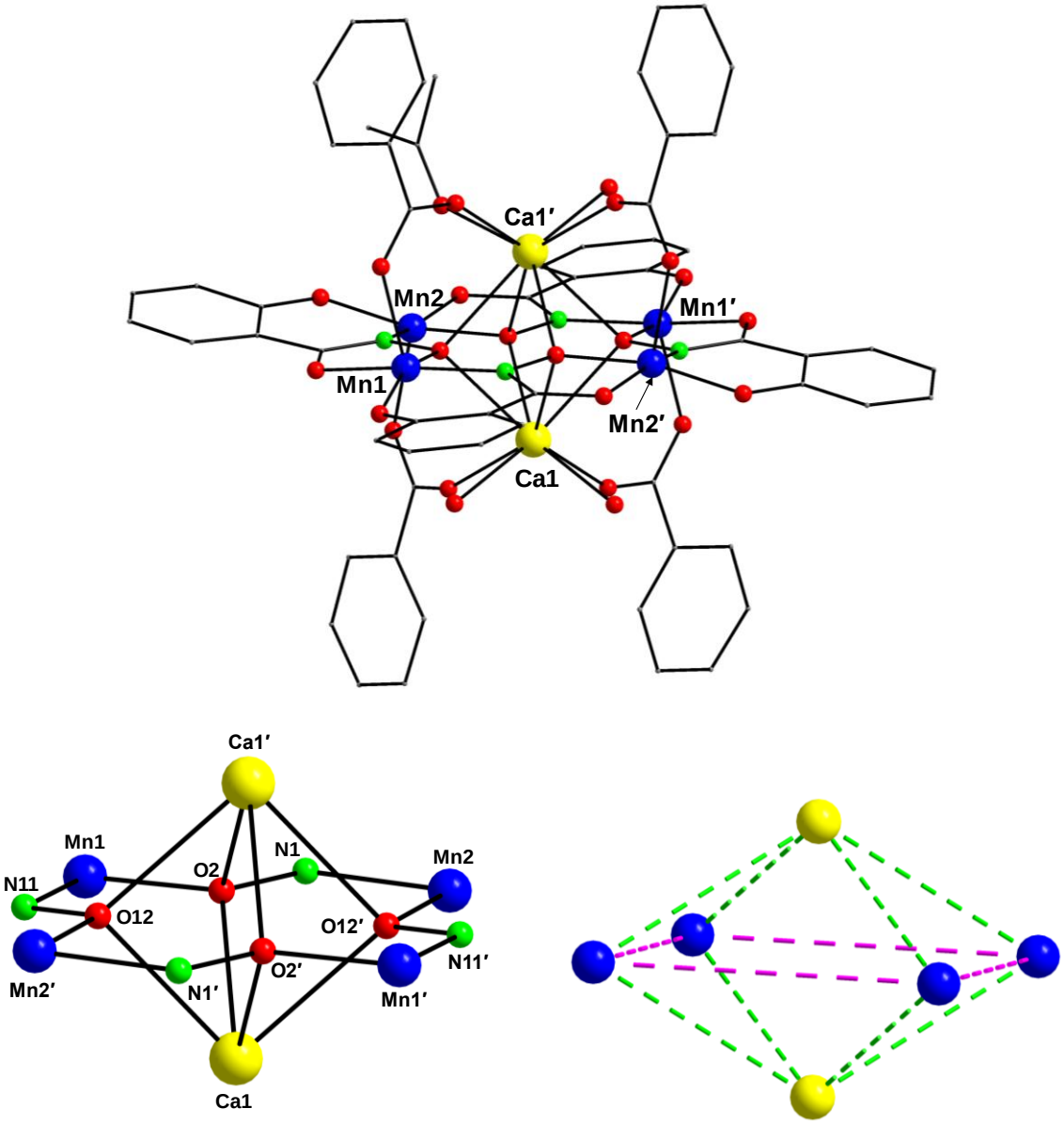

Figure 3.1. Partially labeled representations of the structure of **5** (top), its complete $[Mn_4Ca_2(\mu_3\text{-}NO)_4]^{12+}$ core (bottom left) and the $\{Mn_4Ca_2\}$ octahedral topology (bottom right). The green and purple dashed lines represent virtual Mn···Ca and Mn···Mn bonds. H atoms are omitted for clarity. Colour scheme: Mn^{III}, blue; Ca^{II}, yellow; O, red; N, green; C, gray. Symmetry operation for the primed atoms in **5**: 0.5–*x*, 0.5–*y*, –*z*.

Ligation around each Mn^{III} atom is completed by the alkoxido and phenoxido O atoms from the shi^{3-} groups; the latter are thus $\eta^1:\eta^1:\eta^1:\eta^3:\mu_4$ (Scheme 3.1). The complex therefore contains an overall $[Mn_4Ca_2(\mu_3\text{-}NO)_4]^{12+}$ core (Figure 3.1, bottom left) which can also be described as a $[12\text{-}MC_{Mn(III)N(shi)}\text{-}4]$ metallacrown[146] with two Ca^{II} atoms displaced out of the arrangement. All Ca–O bonds are in the range 2.264(3)–2.595(3) Å. All Mn^{III} atoms in **5** are five-coordinate with almost perfect square pyramidal geometries. This was confirmed by analysis of the shape-determining bond angles using the approach of Reedijk and Addison,[147] which yields an average value for the trigonality index, τ, of 0.05 for the four metal ions. The Ca^{II} atoms are eight-coordinate in a CaO_8 environment possessing square antiprismatic geometries that was confirmed by the CShM approach. The best fit was obtained for the square antiprism (Figure 3.2) with a CShM value of 2.21.

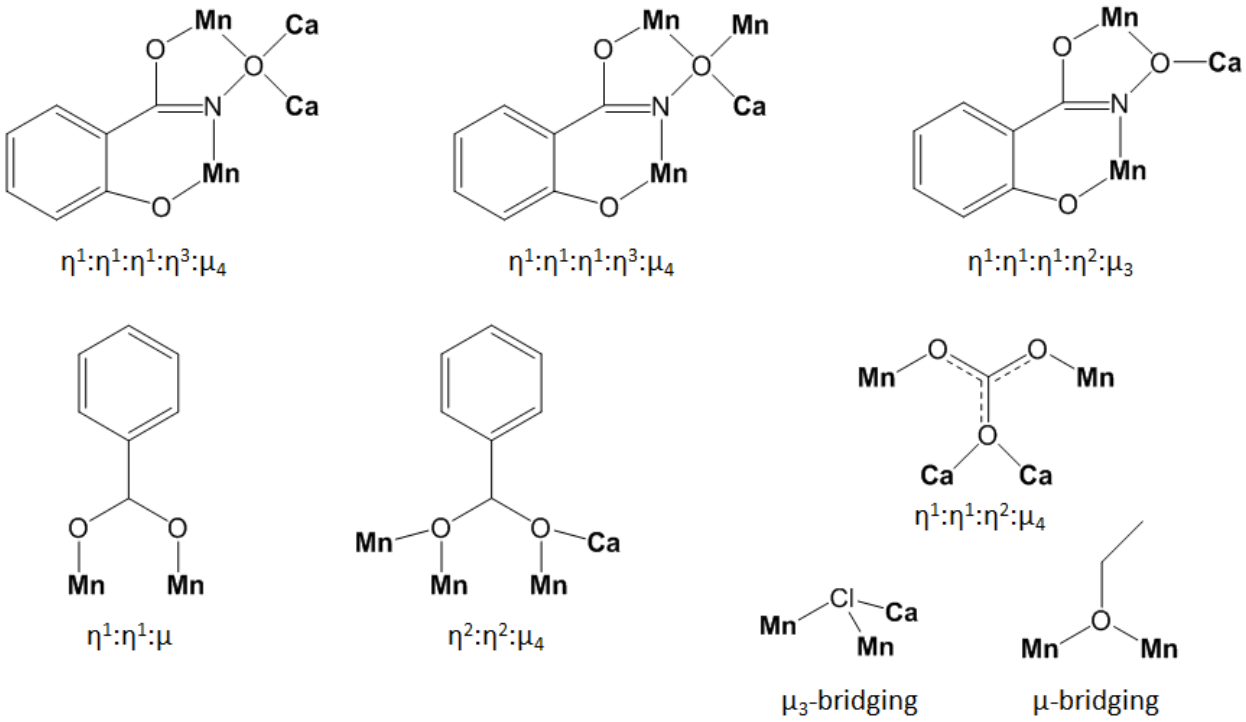

Scheme 3.1. Coordination modes of all bridging ligands in complexes **5**–**8**.

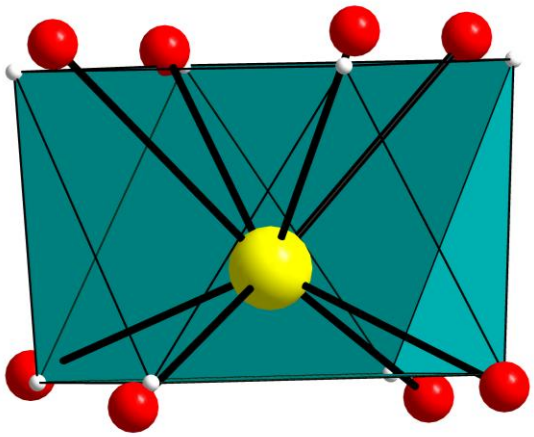

Figure 3.2. Square antiprismatic coordination geometry of the Ca^{II} atoms in **5**; the points connected by the black lines define the vertices of the ideal polyhedron. Colour scheme: Ca^{II}, yellow; O, red.

The coordination spheres of the Ca^{II} atoms in **5** are completed by three and one terminally bound H_2O and Me_2CO molecules, respectively. Recall that four coordinated H_2O molecules were found in the active site of the native OEC, two of which are bound to the Ca^{II} atom. These H_2O molecules could serve as substrates for the overall catalytic reaction to proceed, including subsequent deprotonations with metal-centered oxidations preceding O–O bond formation.[84] To that end, complex **5** may be of some interest to the catalytic cycle of the OEC.

Table 3.2. BVS Calculations[a] for Mn Atoms in **5–8**.

Complex	Atom	Mn^{II}	Mn^{III}	Mn^{IV}
5	Mn1	3.230	<u>3.05</u>	3.14
	Mn2	3.21	<u>2.97</u>	3.06
6	Mn1	<u>2.01</u>	1.65	1.68

	Mn2	3.21	2.98	3.06
	Mn3	3.20	2.97	3.05
7	Mn1	3.36	3.11	3.21
	Mn2	3.37	3.12	3.22
	Mn3	4.44	4.14	4.22
	Mn4	4.30	3.98	4.10
	Mn5	4.41	4.11	4.19
	Mn6	3.13	2.90	2.98
	Mn7	3.33	3.09	3.18
	Mn8	4.39	4.06	4.19
8	Mn1	3.37	3.12	3.21
	Mn2	3.36	3.11	3.20
	Mn3	3.34	3.09	3.18
	Mn4	3.36	3.11	3.20

[a]The underlined value is one closest to the charge for which it was calculated. The oxidation state is the nearest whole number to the underlined value.

Table 3.3. Selected Interatomic Distances (Å) and Angles (°) for Complexes **5**·3Me_2CO·2.8H_2O,[a] **6**·2Et_2O·H_2O,[b] **7**·3EtOH·H_2O and **8**·9$CHCl_3$ [c].

5·3Me_2CO·2.8H_2O			
Mn(1)-O(11)	1.828(3)	Mn(2)-O(1)	1.848(3)
Mn(1)-O(2)	1.922(3)	Mn(2)-O(12′)	1.904(3)
Mn(1)-O(3)	1.942(3)	Mn(2)-O(13′)	1.957(3)
Mn(1)-O(31)	2.095(3)	Mn(2)-O(21)	2.109(3)
Mn(1)-N(11)	1.950(3)	Mn(2)-N(1)	1.964(3)
Ca(1)-O(22)	2.264(3)	Ca(1)-O(2)	2.514(3)
Ca(1)-O(32′)	2.272(4)	Ca(1)-O(2′)	2.531(3)
Ca(1)-O(1W)	2.447(4)	Ca(1)-O(12′)	2.538(3)
Ca(1)-O(2W/41)	2.46(2)/ 2.48(3)	Ca(1)-O(12)	2.595(3)
Mn(1)-O(2)-N(1)-Mn(2′)	176.7(1)	Mn(2)-O(12′)-N(11′)-Mn(1′)	177.6(1)

6·2Et_2O·H_2O			
Mn(1)-O(12)	2.241(3)	Ca(1)-O(1)	2.522(2)
Mn(1)-O(13)	2.125(3)	Ca(1)-O(4)	2.564(2)
Mn(1)-O(12′)	2.213(3)	Ca(1)-O(8)	2.331(3)

Mn(1)-Cl(1)	2.486(1)	Ca(1)-O(9)	2.315(2)
Mn(1)-N(1P)	2.255(3)	Ca(1)-O(9′)	2.315(2)
Mn(1)-N(2P)	2.250(4)	Ca(1)-O(8′)	2.331(3)
Mn(2)-O(3)	1.847(3)	Ca(1)-O(1′)	2.522(2)
Mn(2)-O(4)	1.904(2)	Ca(1)-O(4′)	2.564(2)
Mn(2)-O(5)	1.945(3)	Ca(2)-O(1)	2.608(2)
Mn(2)-O(7)	2.137(3)	Ca(2)-O(4)	2.552(2)
Mn(2)-N(1)	1.959(3)	Ca(2)-O(11)	2.444(3)
Mn(2)-O(11)	2.662(3)	Ca(2)-Cl(1)	2.750(9)
Mn(3)-O(1)	1.914(2)	Ca(2)-O(11′)	2.444(3)
Mn(3)-O(2)	1.939(3)	Ca(2)-O(4′)	2.552(2)
Mn(3)-O(6)	1.853(2)	Ca(2)-O(1′)	2.608(2)
Mn(3)-O(10)	2.113(3)	Ca(2)-Cl(1′)	2.750(9)
Mn(3)-N(2)	1.962(3)		
Mn(3)-Cl(1)	2.870(3)		
Mn(2)-O(4)-N(2′)-Mn(3′)	176.2(1)	Mn(1)-O(12)-Mn(1′)	99.5(1)
Mn(3)-O(1)-N(1)-Mn(2)	174.1(1)	Mn(1)-Cl(1)-Mn(3′)	169.8(1)

7·3EtOH·H_2O			
Mn(1)-O(2)	1.921(3)	Mn(5)-O(16)	1.855(3)
Mn(1)-O(3)	1.922(3)	Mn(5)-O(19)	1.866(3)
Mn(1)-O(13)	1.852(3)	Mn(5)-O(29)	1.925(3)
Mn(1)-O(1E)	2.186(3)	Mn(5)-O(30)	1.886(2)
Mn(1)-O(2S)	2.399(3)	Mn(5)-N(6)	1.991(3)
Mn(1)-N(5)	1.950(3)	Mn(5)-N(7)	1.924(3)
Mn(2)-O(1)	1.880(3)	Mn(6)-O(20)	2.112(3)
Mn(2)-O(5)	2.124(3)	Mn(6)-O(21)	1.924(3)
Mn(2)-O(6)	1.918(3)	Mn(6)-O(22)	1.870(3)
Mn(2)-O(24)	2.407(3)	Mn(6)-O(1E)	1.924(3)
Mn(2)-O(2E)	1.897(3)	Mn(6)-N(8)	1.992(3)
Mn(2)-N(1)	1.971(3)	Mn(6)-O(3)	2.533(3)
Mn(3)-O(4)	1.866(3)	Mn(7)-O(23)	1.921(3)
Mn(3)-O(7)	1.854(3)	Mn(7)-O(24)	1.931(3)
Mn(3)-O(11)	1.909(3)	Mn(7)-O(25)	1.854(3)
Mn(3)-O(12)	1.889(2)	Mn(7)-O(1S)	2.415(3)
Mn(3)-N(2)	1.914(3)	Mn(7)-O(2E)	2.169(3)
Mn(3)-N(3)	1.998(3)	Mn(7)-N(9)	1.958(3)
Mn(4)-O(10)	1.853(3)	Mn(8)-O(8)	1.902(2)
Mn(4)-O(14)	1.934(3)	Mn(8)-O(9)	1.889(3)

Mn(4)-O(15)	1.866(3)	Mn(8)-O(26)	1.919(3)
Mn(4)-O(17)	1.910(3)	Mn(8)-O(27)	1.865(3)
Mn(4)-O(18)	1.917(3)	Mn(8)-O(28)	1.855(3)
Mn(4)-N(4)	1.941(3)	Mn(8)-N(10)	1.942(3)
Ca(1)-O(3)	2.495(3)	Ca(1)-O(18)	2.744(3)
Ca(1)-O(6)	2.415(3)	Ca(1)-O(21)	2.418(2)
Ca(1)-O(9)	2.731(3)	Ca(1)-O(24)	2.557(3)
Ca(1)-O(12)	2.510(2)	Ca(1)-O(27)	2.543(3)
Ca(1)-O(15)	2.562(3)	Ca(1)-O(30)	2.493(3)
Mn(1)-O(3)-N(1)-Mn(2)	164.9(1)	Mn(7)-O(24)-N(8)-Mn(6)	162.3(1)
Mn(2)-O(6)-N(2)-Mn(3)	171.8(1)	Mn(8)-O(9)-N(3)-Mn(3)	161.5(1)
Mn(2)-O(24)-N(8)-Mn(6)	99.4(2)	Mn(8)-O(27)-N(9)-Mn(7)	168.3(1)
Mn(3)-O(12)-N(4)-Mn(4)	173.9(1)	Mn(1)-O(3)-Mn(6)	93.9(1)
Mn(4)-O(15)-N(5)-Mn(1)	165.0(1)	Mn(1)-O(1E)-Mn(6)	105.9(1)
Mn(4)-O(18)-N(6)-Mn(5)	162.7(1)	Mn(2)-O(24)-Mn(7)	93.6(1)
Mn(5)-O(30)-N(10)-Mn(8)	174.2(1)	Mn(2)-O(2E)-Mn(7)	102.7(1)
Mn(6)-O(21)-N(7)-Mn(5)	174.7(1)		

8·9$CHCl_3$			
Mn(1)-O(16)	1.806(8)	Mn(3)-O(3)	1.814(9)
Mn(1)-O(1)	1.884(7)	Mn(3)-O(7)	1.884(7)
Mn(1)-O(2)	2.000(9)	Mn(3)-O(11)	1.987(8)
Mn(1)-O(4)	2.048(8)	Mn(3)-O(8′)	2.045(8)
Mn(1)-N(4)	1.953(9)	Mn(3)-N(1)	1.969(8)
Mn(2)-O(12)	1.838(9)	Mn(4)-O(14)	1.847(8)
Mn(2)-O(6)	1.889(7)	Mn(4)-O(18)	1.869(7)
Mn(2)-O(15)	1.992(7)	Mn(4)-O(17)	1.949(8)
Mn(2)-O(5′)	2.021(8)	Mn(4)-O(9)	2.058(9)
Mn(2)-N(2)	1.940(8)	Mn(4)-N(3)	1.960(8)
Ca(1)-O(6)	2.347(7)	Ca(1)-O(10′)	2.435(7)
Ca(1)-O(1)	2.352(8)	Ca(1)-O(13)	2.440(8)
Ca(1)-O(7)	2.354(7)	Ca(1)-O(10)	2.441(7)
Ca(1)-O(18)	2.359(7)	Ca(1)-O(13′)	2.461(7)
Mn(1)-O(1)-N(1)-Mn(3)	178.2(4)	Mn(3)-O(7)-N(2)-Mn(2)	179.1(4)
Mn(2)-O(6)-N(3)-Mn(4)	179.5(4)	Mn(4)-O(18)-N(4)-Mn(1)	178.4(4)

[a]Symmetry code: ′ = $-x+\frac{1}{2}$, $-y+\frac{1}{2}$, $-z$; [b]Symmetry code: ′ = x, $-y+\frac{1}{2}$, $-z+\frac{3}{2}$; [c]Symmetry code: ′ = $-x$, $-y$, $-z$.

The crystal structure of **6** consists of $[Mn_6Ca_2Cl_2(O_2CPh)_7(shi)_4(py)_4]^-$ anions (Figure 3.3, top) counterbalanced by pyH^+ cations. In addition, there are CH_2Cl_2 and Et_2O solvate molecules in the crystal lattice, which will not be further discussed. The structure of the anion of **6** comprises a $\{Mn^{III}_4Ca_2\}$ octahedron, reminiscent to the discrete structure of complex **5**, linked to an additional $\{Mn^{II}_2\}$ dimer through two bridging Cl^- ions and two $\eta^2{:}\eta^2{:}\mu_4$ $PhCO_2^-$ groups (Scheme 3.1). The Mn···Mn···Mn angles within the $\{Mn^{III}_4Ca_2\}$ octahedron are 89.6 and 90.4°, again deviating only slightly from the ideal 90°, and the Mn···Ca···Mn angles of the eight triangular faces lie within the 74.5–79.0° range. The two Ca^{II} atoms lie 1.990 Å (Ca1) and 1.582 Å (Ca2) out of the Mn_4 square plane. Similar to complex **5**, the linkage between the basal Mn^{III} atoms and the apical Ca^{II} atoms is provided by the oximate O atoms (O1, O1′, O4 and O4′) of shi^{3-} ligands and four $\eta^1{:}\eta^1{:}\mu$ bidentate bridging benzoate groups, which are all pointed towards Ca1. The two Mn^{II} atoms, which are located below Ca2, are further bridged to each other through an $\eta^1{:}\eta^1{:}\mu$ $PhCO_2^-$ group, while their coordination spheres are completed by four terminally bound pyridine molecules. The $Mn^{II}\cdots Mn^{II}$ distance is 3.400(1) Å. The overall metal topology of **6** (Figure 3.3, bottom right) and its $[Mn^{II}_2Mn^{III}_4Ca_2(\mu_3\text{-}Cl)_2(\mu_4\text{-}O_2CPh)_2(\mu_4\text{-}NO)_4]^{12+}$ core (Figure 3.3, bottom left) are finally stabilized by the coordinated alkoxido and phenoxido O atoms from the $\eta^1{:}\eta^1{:}\eta^1{:}\eta^3{:}\mu_4$ shi_3^- groups.

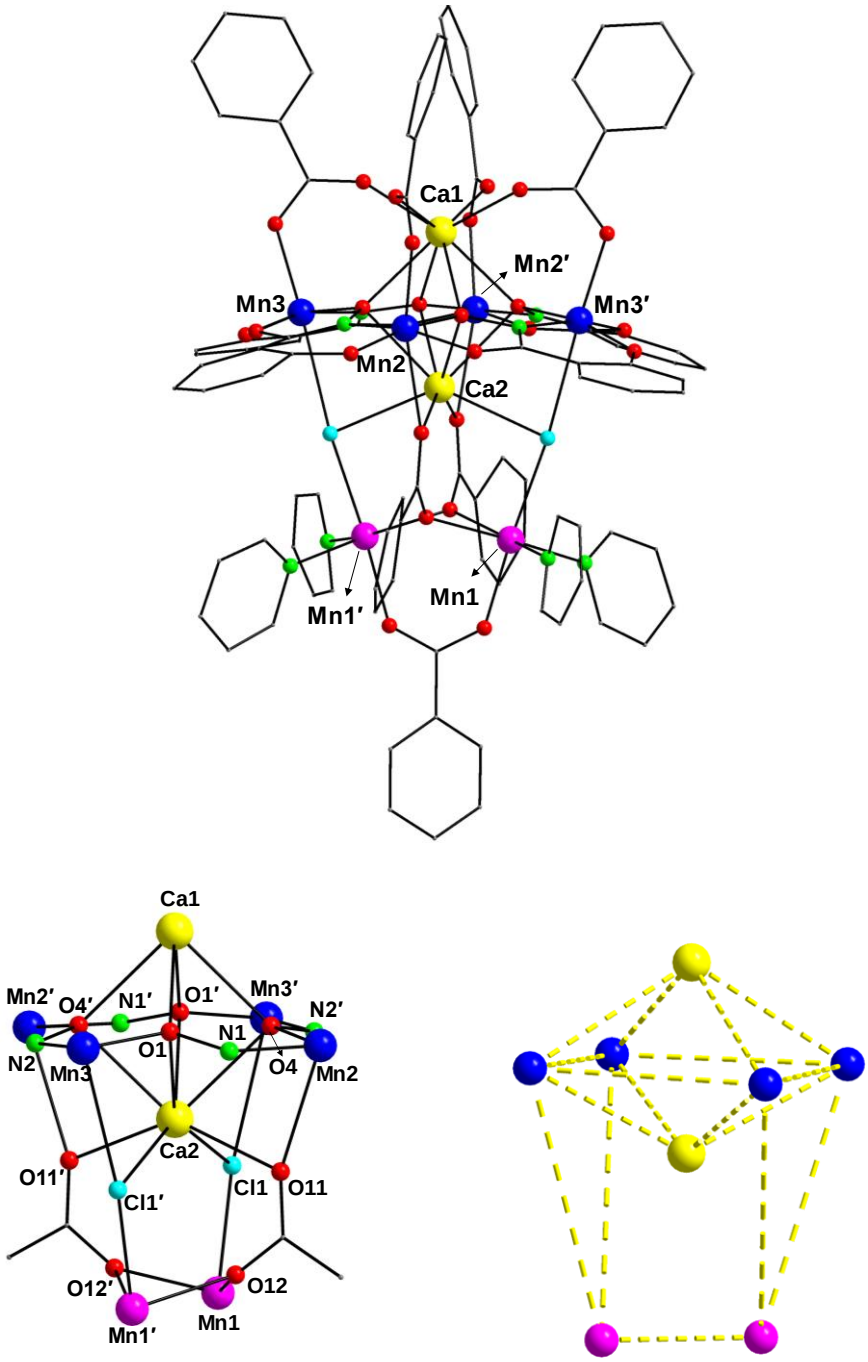

Figure 3.3. Partially labeled representations of the anion of complex **6** (top), its complete $[Mn^{II}_2Mn^{III}_4Ca_2(\mu_3\text{-}Cl)_2(\mu_4\text{-}O_2CPh)_2(\mu_3\text{-}NO)_4]^{12+}$ core (bottom left) and the $\{Mn_6Ca_2\}$ topology (bottom right). The yellow dashed lines represent the virtual Mn···Ca and Mn···Mn bonds. H atoms are omitted for clarity. Colour scheme: Mn^{II}, magenta; Mn^{III}, blue; Ca^{II}, yellow; O, red; N, green; Cl, cyan; C, gray. Symmetry operation for the primed atoms in **6**: *x*, 0.5–*y*, 1.5–*z*.

All Mn atoms in **6** are six-coordinate with distorted octahedral geometries. In the case of the Mn^{III} atoms (Mn2, Mn2′, Mn3 and Mn3′), the octahedra take the form of axially elongated Jahn-Teller (JT) distortions, as expected for high-spin d^4 ions in this geometry. The JT axes in all Mn^{III} sites involve the carboxylate O atoms and the Cl^- groups. In addition, both Ca^{II} atoms in **6** are eight-coordinate albeit with different coordination geometries, as established by CShM. The best fit was obtained for the square antiprism (Ca1) and biaugmented trigonal prism (Ca2) with CShM values of 1.19 and 3.98, respectively (Figure 3.4). Given the presence of Cl^- groups in the vicinity of the active site of the native OEC and their structural role in both maintaining the coordination environment of the $\{Mn_4Ca\}$ cluster and functioning as either proton exit channels or water inlet channels,[2] complex **6** could be structurally interesting as it is only, to the best of our knowledge, the second Cl-bridged Mn–Ca cluster reported to date (Table 1.1).

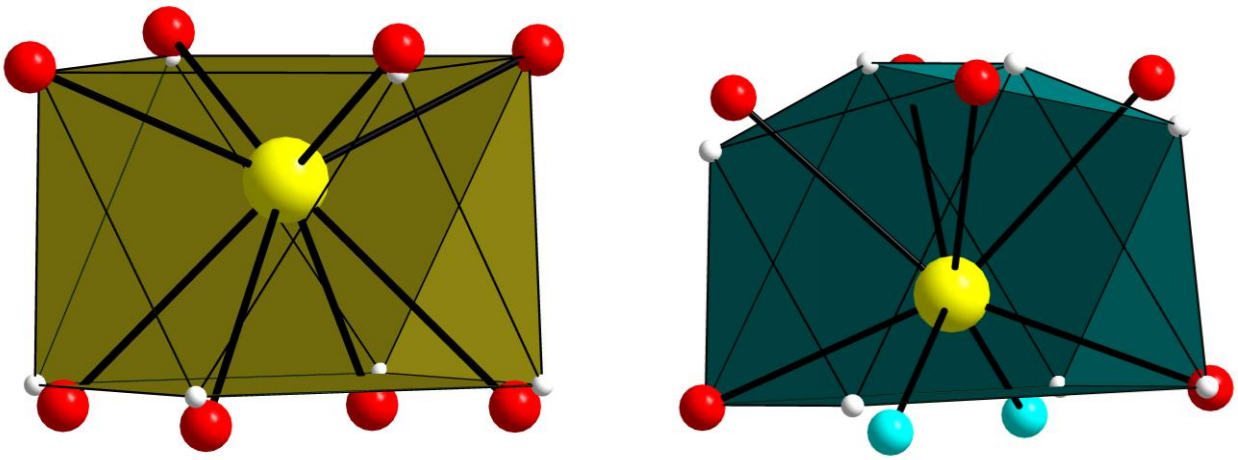

Figure 3.4. Square antiprismatic (left) and biaugmented trigonal prismatic (right) coordination geometries of Ca1 and Ca2 atoms in **6**, respectively; the points connected by the black lines define the vertices of the ideal polyhedra. Color scheme: Ca^{II}, yellow; O, red; Cl, cyan.

The crystal structure of **7** consists of $[Mn_8Ca(OEt)_2(shi)_{10}(EtOH)_2]^{2-}$ dianions (Figure 3.5, top), each of which is counterbalanced by two $NHEt_3^+$ cations. In addition, there are EtOH and H_2O solvate molecules in the crystal lattice, which will not be further discussed. The asymmetric dianion of **7** comprises four Mn^{III} (Mn1, Mn2, Mn6 and Mn7) and four Mn^{IV} (Mn3, Mn4, Mn5 and Mn8) atoms (Table 3.2), bridged together through the oximate groups of eight $\eta^1:\eta^1:\eta^1:\eta^2:\mu_3$ and two $\eta^1:\eta^1:\eta^1:\eta^3:\mu_4$ shi^{3-} groups (Scheme 3.1). Furthermore, there are also two EtO^- groups bridging two different pairs of Mn^{III} atoms (Mn1/Mn6 and Mn2/Mn7). The eight Mn atoms are arranged in a very distorted ring-like topology with the four Mn^{III} and Mn^{IV} atoms being on opposite sides and the oximate O atoms serving to link the Mn_8 "ring" with the central Ca^{II} atom. As a result, the Ca^{II} atom is surrounded by ten O atoms and possesses a coordination geometry that can be described as sphenocorona (CShM = 2.84; Figure 3.6). All Mn atoms are six-coordinate with near-octahedral geometries, while the axially elongated Mn^{III} octahedra are JT-distorted with oximate and alkoxido O atoms occupying the four JT axes.

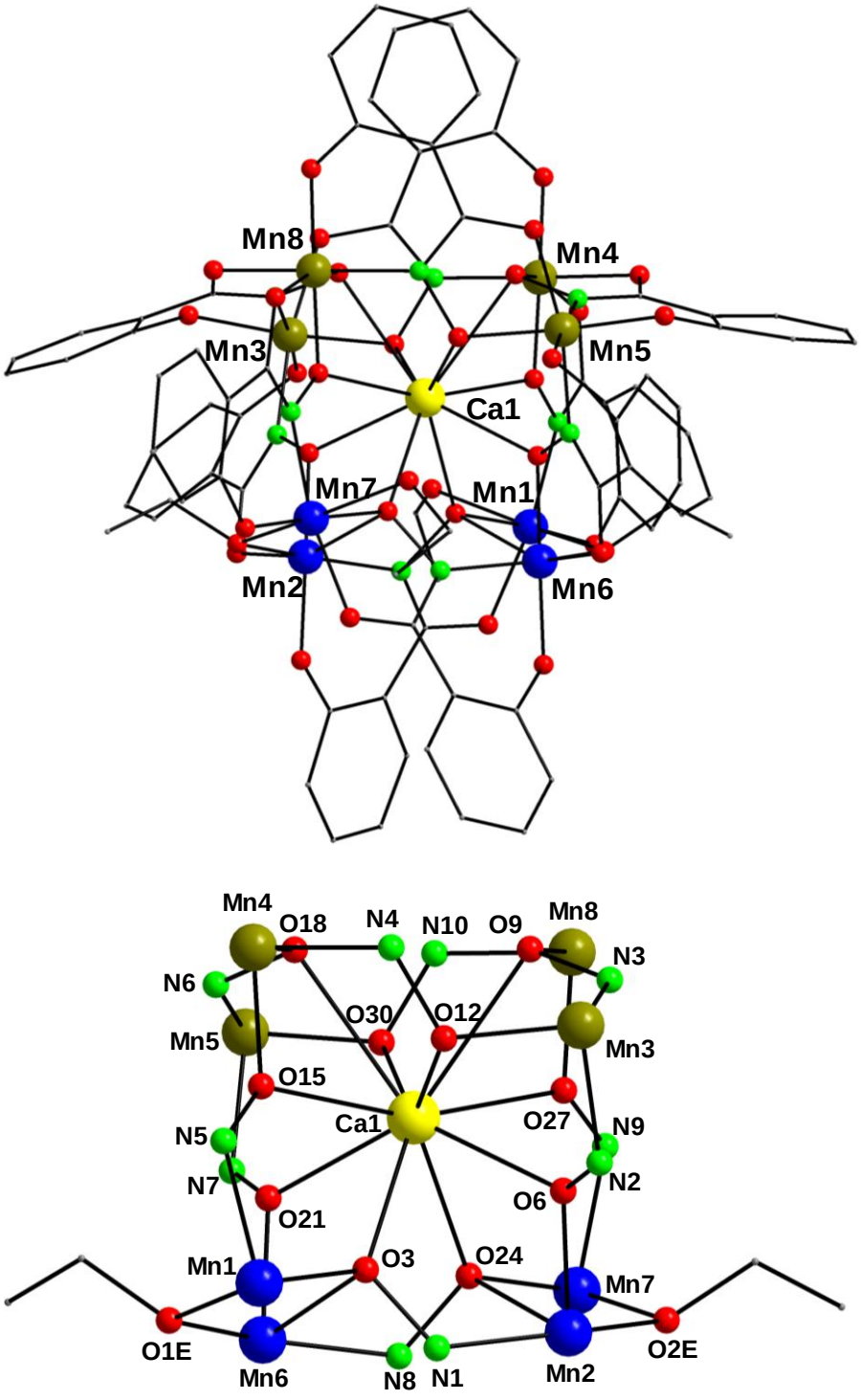

Figure 3.5. Partially labeled representations of dianion of complex **7** (top) and its complete $[Mn^{III}_4Mn^{IV}_4Ca(\mu\text{-}OEt)_2(\mu_4\text{-}NO)_2(\mu_3\text{-}NO)_8]^{18+}$ core (bottom). H atoms are omitted for clarity. Colour scheme: Mn^{III}, blue; Mn^{IV}, olive green; Ca^{II}, yellow; O, red; N, green; C, gray.

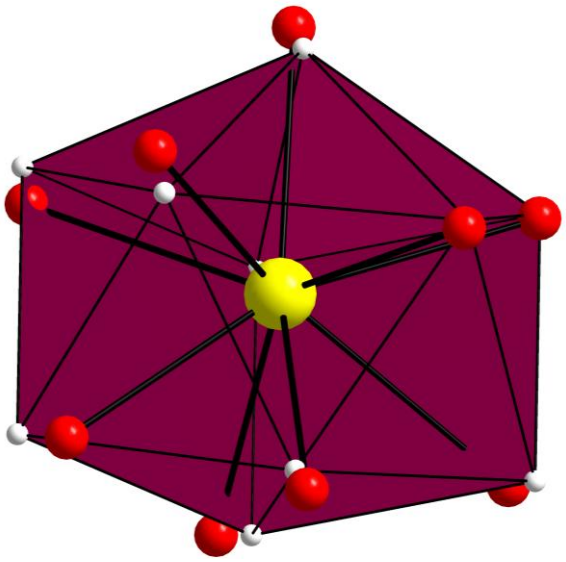

Figure 3.6. Sphenocorona coordination geometry of the Ca^{II} atom in **7**; the points connected by the black lines define the vertices of the ideal polyhedron. Colour scheme: Ca^{II}, yellow; O, red.

Complex **7** has an overall $[Mn^{III}_4Mn^{IV}_4Ca(\mu\text{-}OEt)_2(\mu_4\text{-}NO)_2(\mu_3\text{-}NO)_8]^{18+}$ core (Figure 3.5, bottom). The Mn···Mn and Mn···Ca distances span the range 3.283(1)–7.599(1) Å and 3.545(1)–4.048(1) Å, respectively, whereas the Mn–O–N–Mn torsion angles lie within the 96.9–174.7° range. The smallest torsion angles (~97–99°) are between the Mn^{III}···Mn^{III} pairs and they deviate significantly from linearity. This is most likely the main reason for the stabilization of the asymmetric structure of **7**, and consequently for a first time in Mn–Ca/shi^{3-} chemistry I observed a structural motif that does not contain any discrete or repeating $\{Mn_4Ca\}$ square pyramidal units. Finally, complex **7** is a rare example of a heterometallic Mn–Ca cluster containing both Mn^{III} and Mn^{IV} atoms, and the first non-oxido bridged complex with an unprecedented 8:1 Mn-to-Ca metal ratio (Table 1.1).

The crystal structure of **8** consists of $[Mn_8Ca_2(CO_3)_4(shi)_8]^{4-}$ tetraanions (Figure 3.7, top), each of which is counterbalanced by four $NHEt_3^+$ cations. The latter cations are H-bonded with the coordinated carbonato O atoms. In addition, there are $CHCl_3$ solvate molecules in the crystal lattice, which will not be further discussed. The centrosymmetric complex $[Mn_8Ca_2(CO_3)_4(shi)_8]^{4-}$ is arranged as two parallel {Mn_4Ca} square pyramids that are linked to each other through four $\eta^1{:}\eta^1{:}\eta^2{:}\mu_4$ CO_3^{2-} groups (Scheme 3.1). The two Ca^{II} atoms are both pointed towards the center of a cavity that is formed by the rectangular cuboidal (or rectangular parallelepiped) arrangement of the eight external Mn^{III} atoms (Figure 3.7, bottom right). As a result, the {Mn_8Ca_2} compound possesses a virtual D_{2h} point group. The opposite faces of the rectangular cuboid comprise the atoms Mn(1,2,3,4)/Mn(1′,2′,3′,4′) and Mn(1,3,2′,4′)/Mn(1′,3′,2,4) with Mn···Mn distances spanning the range 4.612(3)–4.638(1) Å and 4.623(2)–6.122(3) Å, respectively. The Mn···Mn···Mn angles lie within the 89.7–90.1° range, very close to the ideal 90° for a perfect rectangular cuboid. The linkage between the basal Mn^{III} atoms and the apical Ca^{II} atoms within each {Mn_4Ca} square pyramid is provided by the oximate O atoms (O1, O7, O6, O18 and their symmetry-related partners) of eight shi^{3-} ligands; the latter are thus $\eta^1{:}\eta^1{:}\eta^1{:}\eta^2{:}\mu_3$ (Scheme 3.1). The four basal Mn^{III} atoms form a near-planar square, with each of the edges bridged by a diatomic oximate group from a shi^{3-} ligand. The almost perfectly planar Mn_4 units are clearly due to the large Mn–O–N–Mn torsion angles of ~179°, very close to the ideal linearity of 180°. The linkage between the Mn atoms of the two {Mn_4Ca} square pyramids is provided by the *anti-anti* O atoms of the four bridging CO_3^{2-} groups (Scheme 3.1). Ca1 and Ca1′ lie 1.556 Å below and above the corresponding Mn_4 best mean planes, respectively.

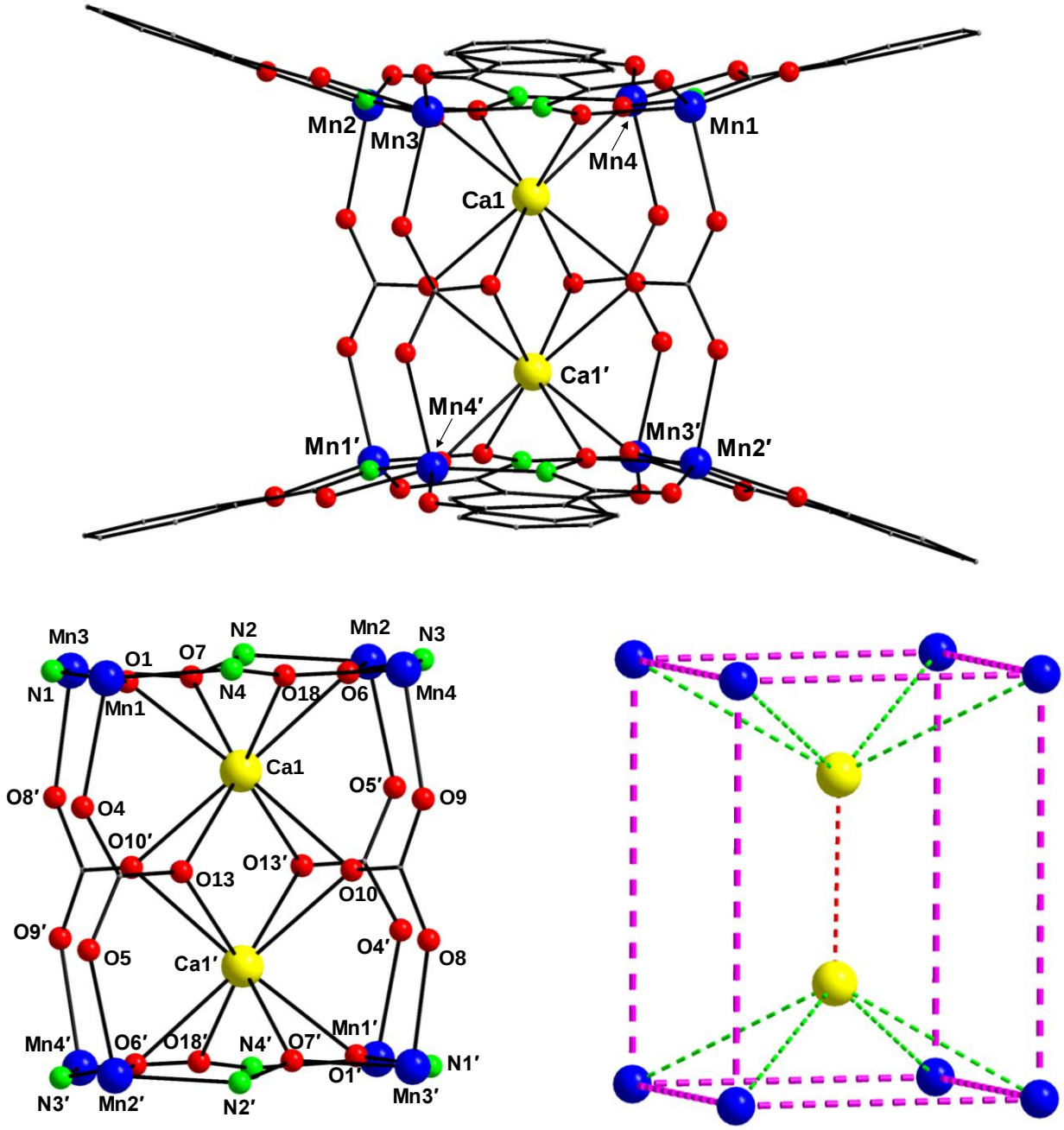

Figure 3.7. Partially labeled representations of the tetranion of complex **8** (top), its complete $[Mn^{III}_8Ca_2(\mu_4\text{-}CO_3)_4(\mu_3\text{-}NO)_8]^{12+}$ core (bottom left) and the $\{Mn_8Ca_2\}$ rectangular cuboidal topology (bottom right). The green, purple and red dashed lines represent the virtual Mn···Ca, Mn···Mn and Ca···Ca bonds. H atoms are omitted for clarity. Colour scheme: Mn^{III}, blue; Ca^{II}, yellow; O, red; N, green; C, gray. Symmetry operation for the primed atoms in **8**: *–x*, *–y*, *–z*.

The complex therefore contains an overall $[Mn_8Ca_2(\mu_4\text{-}CO_3)_4(\mu_3\text{-}NO)_8]^{12+}$ core (Figure 3.7, bottom left) which can also be described as two carbonato-bridged [12-$MC_{Mn(III)N(shi)}$-4] metallacrown units surrounding two Ca^{II} atoms. Alternatively, complex **8** can be also seen as a $\{Mn_8\}$ molecular "capsule" that accommodates two Ca^{II} atoms in its cavity (Figure 3.8). To the current degree of knowledge, a more possible scenario is that two solution-stable $\{Mn_4Ca\}$ units were assembled and linked together through the CO_3^{2-} groups rather than the two Ca^{II} atoms templating the formation of the outer $\{Mn_8\}$ unit. All Mn^{III} atoms in **8** are five-coordinate with almost perfect square pyramidal geometries (τ = 0.07–0.09). Both Ca^{II} atoms are eight-coordinate in CaO_8 environments possessing square antiprismatic geometries with a CShM value of 1.86 (Figure 3.9). Finally, complex **8** is the first heterometallic Mn–Ca complex bearing coordinated carbonato groups and the first Mn–Ca complex with an 8:2 metal stoichiometry (Table 1.1).

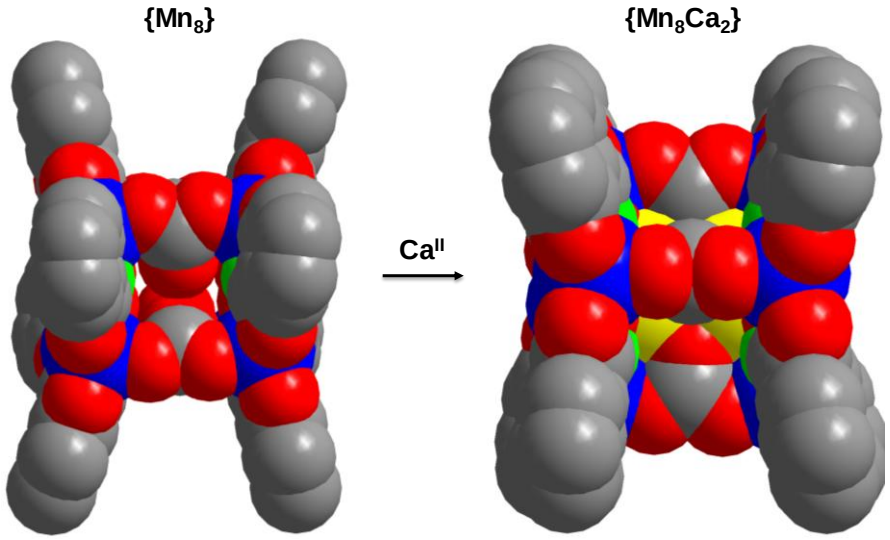

Figure 3.8. Space-filling representations of the "vacant" $\{Mn_8\}$ molecular capsule of **8** (left) and its complete $\{Mn_8Ca_2\}$ structure (right) resulting from the filling of the cavity by two Ca^{II} atoms. Colour scheme: Mn^{III}, blue; Ca^{II}, yellow; O, red; N, green; C, gray.

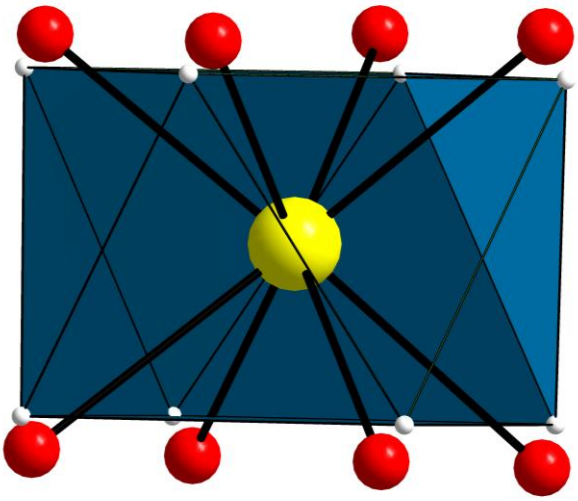

Figure 3.9. Square antiprismatic coordination geometry of the Ca^{II} atoms in **8**; the points connected by the black lines define the vertices of the ideal polyhedron. Colour scheme: Ca^{II}, yellow; O, red.

Considering the fast-development of the field of heterometallic Mn–Ca chemistry, it becomes apparent, from Table 1.1, that complexes **5**–**8** are quite unique in their metal ions stoichiometries, topological arrangements, oxidation state descriptions and the nature of the ligands bound to the metal ions.

3.3.3 Solid-State Magnetic Susceptibility Studies

Variable-temperature direct current (*dc*) magnetic susceptibility measurements were performed on powdered polycrystalline samples of analytically pure complexes **5**·$2H_2O$, **6**, **7**·$2H_2O$, and **8**·$2CHCl_3$, restrained in eicosane to prevent torquing, in a 1 kG (0.1 T) field and in the 5.0–300 K range. The data are shown as $\chi_M T$ versus T plots in Figure 3.10. All complexes

show very similar magnetic responses in terms of exhibiting a continuous decrease of their $\chi_M T$ products from 300 to 5 K. This is clearly due to the antiferromagnetic exchange interactions between the paramagnetic metal centers, undoubtedly propagated by the oximate bridges with very large (close to linearity) Mn–O–N–Mn torsion angles. This behaviour is consistent with all previously characterized Mn-oximate complexes with large torsion angles.[96,168] More specifically, the $\chi_M T$ product for all four complexes steadily decreases from 9.28 (**5**), 17.53 (**6**), 15.03 (**7**), and 20.16 (**8**) cm^3Kmol^{-1} at 300 K to 0.74 (**5**), 0.87 (**6**), 0.88 (**7**), and 0.91 (**8**) cm^3Kmol^{-1} at 5.0 K. The 300 K values are less than the spin-only (g = 2) values of 12.00 (**5**), 20.75 (**6**), 19.50 (**7**), and 24.00 (**8**) cm^3Kmol^{-1} for the corresponding number of non-interacting Mn^{III} (**5** and **8**), $Mn^{II/III}$ (**6**), and $Mn^{III/IV}$ (**7**) ions. Given the very small $\chi_M T$ values for all complexes at low temperatures and the topological arrangement of the Mn atoms, it is very likely that compounds **5**–**8** all possess S = 0 spin ground state values. This was confirmed quantitively by determining the individual pairwise exchange parameters J_{ij} between Mn_iMn_j pairs within the magnetic cores, when the overall topology and symmetry of the compound allowed me to do so.

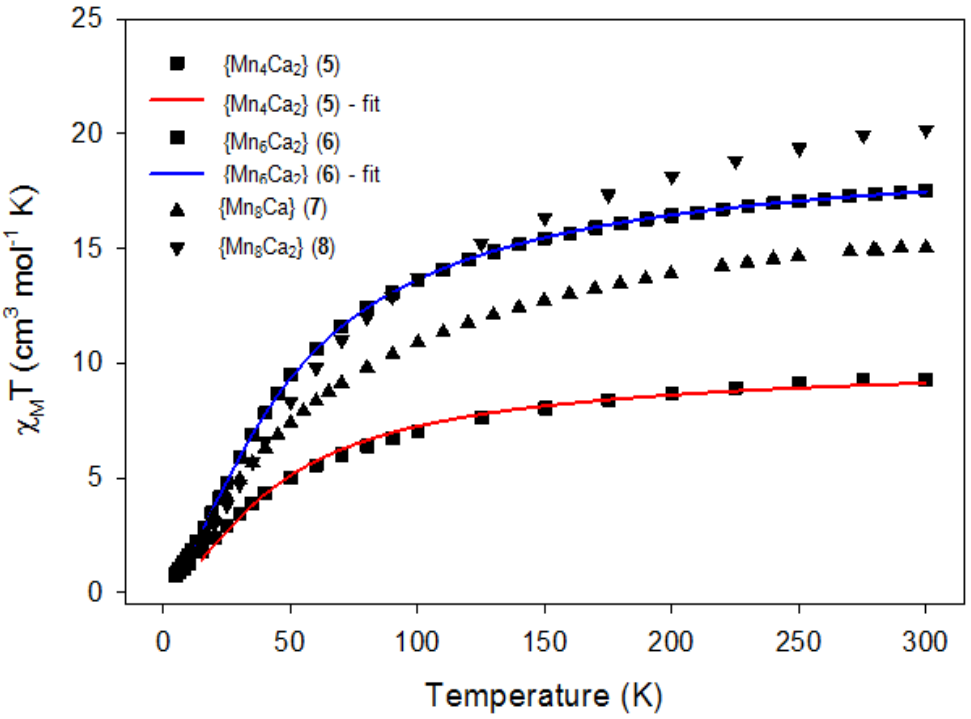

Figure 3.10. $\chi_M T$ versus T plots for complexes **5–8** at 0.1 T *dc* field. The red and blue solid lines are the fits of the corresponding data; see the text for the fit parameters.

To this end, the $\chi_M T$ versus T data for complex **5** were fit to the theoretical expression for a $\{Mn^{III}_4\}$ square using the isotropic Heisenberg spin Hamiltonian given by Eqn 3.5.

$$H = -2J(\hat{S}_1 \cdot \hat{S}_2 + \hat{S}_2 \cdot \hat{S}_3 + \hat{S}_3 \cdot \hat{S}_4 + \hat{S}_1 \cdot \hat{S}_4) \qquad \textbf{Eqn. 3.5}$$

Considering the very similar Mn–O–N–Mn torsion angles and Mn···Mn separations within the Mn_4 square, all interactions between neighboring Mn^{III} atoms were considered as equivalent (1-*J* model). The fit parameters were thus *J* and *g*. A good fit of the experimental data (red solid line in Figure 3.10) in the temperature range 300–15 K was obtained using the program PHI ($H = -2J_{ij}\hat{S}_i \cdot \hat{S}_j$ convention).[167] The best-fit parameters were: $J = -2.94(1)$ cm^{-1} and

g = 1.96(1), in very good agreement with the previously reported $\{Mn^{III}_4Ca\}$ complexes possessing square pyramidal topologies. Data below 15 K were omitted to avoid effects from Zeeman interactions, magnetic anisotropy and crystal structure disorders; these are all factors that are not included in the above model.[96] The fit of the data indicates an S = 0 ground state with an S = 1 first excited state lying 5.88 cm^{-1} higher in energy. Attempts to include a D term in the fitting process and/or a second J-coupling constant, to account for any non-zero next-nearest neighbour interactions across the diagonal Mn sites, failed to give me any better low-temperature fits.

For the $\{Mn^{II}_2Mn^{III}_4Ca_2\}$ complex **6**, I employed a similar Heisenberg spin Hamiltonian (Eqn. 3.6), but this time two coupling constants were included to account for the interactions between the Mn^{III} atoms within the $\{Mn_4\}$ square (J_1), as promoted by the oximate bridges, and the interaction between the two carboxylate-bridged Mn^{II} atoms (J_2). The best-fit parameters were: J_1 = –2.88(1) cm^{-1}, J_2 = –4.13(1) cm^{-1}, and g = 1.95(1), and these were derived from the program PHI for the entire temperature range (blue solid line in Figure 3.10), thus confirming the overall antiferromagnetic response of the compound and the stabilization of an S = 0 spin ground state.

$$H = -2J_1(\hat{S}_2\cdot\hat{S}_3 + \hat{S}_3\cdot\hat{S}_{2'} + \hat{S}_{2''}\cdot\hat{S}_{3'} + \hat{S}_{3''}\cdot\hat{S}_2) - 2J_2(\hat{S}_1\cdot\hat{S}_{1'}) \qquad \textbf{Eqn. 3.6}$$

The employment of a third J-coupling constant to consider any possible interaction between the Mn^{II} and Mn^{III} atoms gave a negligible value (~0 cm^{-1}). This is reasonable since the Mn^{II} and Mn^{III} atoms in **6** are solely bridged by the Cl^- groups, which are expected to provide a very weak to negligible superexchange magnetic pathway when forming an almost linear angle

between the metal centers [Mn(1)–Cl(1)–Mn(3′) = 169.8(1)°], and the bonding is weak as well [Mn(1)–Cl(1) = 2.486(1) Å and Mn(3)–Cl(1) = 2.870(3) Å].

The larger nuclearities and low symmetries of complexes **7** and **8** rendered the fitting of the magnetic data impossible. A powerful complement to *dc* studies for determining the ground state of a system is alternating current (*ac*) magnetic susceptibility measurements, which preclude any complications arising from the presence of a *dc* field. These were performed for both **7** and **8** in a 3.5 G *ac* field oscillating at different frequencies. The in-phase susceptibility (χ_M') is shown as $\chi_M'T$ versus T plots in Figure 3.11 and reveals some pertinent and common features for both complexes **7** and **8**: (i) $\chi_M'T$ decreases linearly with decreasing temperature in the 1.8–14 K range, indicating the depopulation of a high density of excited states with spin S greater than that of the ground state; and (ii) linear extrapolation of the $\chi_M'T$ data down to 0 K gives a value of ~0 cm^3Kmol^{-1} for both **7** and **8**, indicative of $S = 0$ ground states.

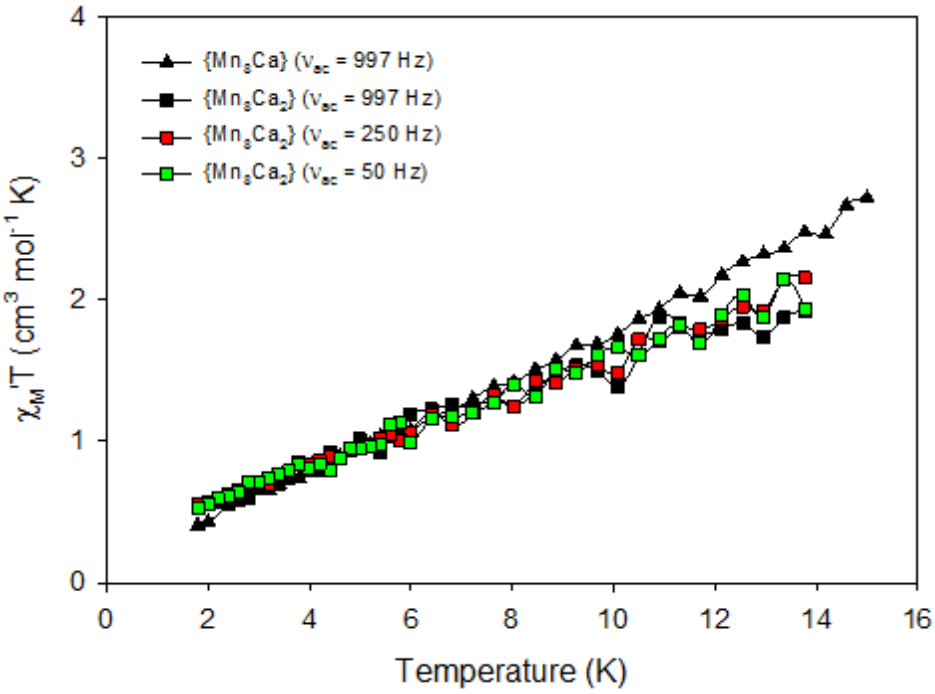

Figure 3.11. The in-phase (as $\chi_M'T$) versus *T ac* susceptibility signals for **7** and **8**, under a 3.5 G oscillating field operating at the indicated frequencies.

3.3.4 Relevance of Complexes 5–8 to Different Oxidation States of the OEC: A Qualitative Approach

In addition to the bridging/chelating shi^{3-} ligand, most of the reported compounds contain carboxylate, chloride, water, and/or carbonate groups akin to the coordination environment of the metal ions in the native enzyme. I recognize that within the structures of **5**–**8**, the Mn···Mn (between closest neighbours) and Mn···Ca separations span the range 4.623–4.652 and 3.680–3.773 (**5**), 4.624–6.283 and 3.620–3.856 Å (**6**), 3.180–6.639 and 3.545–4.048 Å (**7**), and 4.612–6.122 and 3.601–3.635 Å (**8**), respectively; these values are significantly larger than the corresponding values of 2.7–3.3 and ~3.4 Å for the OEC in PSII. This is clearly due to the

absence of bridging oxido groups and the presence of Mn^{II}/Mn^{III} atoms within **5**–**8**. However, the structures of the reported compounds may be of some relevance to the OEC in other ways. Since the S_1 Kok state of the OEC occurs at the $2Mn^{III},2Mn^{IV}$ oxidation level with a ground state spin of $S = 0$, then the $Mn^{III}_4Mn^{IV}_4$ level of **7** could be related to this S_1 state. In contrast, the lower Mn^{III}_4, $Mn^{II}_2Mn^{III}_4$ and Mn^{III}_8 levels of **5**, **6** and **8**, respectively, would place them at the S_{-1} or other reduced states of the catalytic cycle. Furthermore, the similarity between the oximate N–O bridging unit of shi^{3-} within **5**–**8** and the M–O–N–M unit found in hydroxylamine-bridged metal complexes[171] is interesting and suggests that **5**–**8**, similar to **1**–**4**, may provide insights into the type of subunits that might be generated upon reduction of the OEC with NH_2OH.

3.4 ***Conclusions and Perspectives***

In conclusion, it was shown in this chapter that salicylhydroxime ($shiH_3$) is a versatile chelating/bridging ligand that can support the formation of heterometallic Mn–Ca clusters with unprecedented topologies, metal stoichiometries and oxidation state descriptions. The reaction schemes employed in this work were quite diverse, ranging from the use of $\{Mn^{III}_3\}$ and $\{Mn^{II/III}_3\}$ oxido/carboxylate-based triangles to simple Mn^{II} and Ca^{II} starting materials, and the resulting crystalline products were proved to exhibit different structural motifs and ancillary bridging ligands, such as $PhCO_2^-$, EtO^-, Cl^- and CO_3^{2-}. The combined results also demonstrate the ability of shi^{3-} to stabilize Mn ions in high oxidation states (i.e., Mn^{IV}) without requiring the support of oxido groups. It must be admitted that the inorganic cores and metal stoichiometries of **5**–**8** are different from the extended $\{Mn_4Ca\}$ cubane core of the native OEC. This, however, does not preclude some relevance of the reported compounds to both the high-valent scheme

($Mn^{III}_4Mn^{IV}_4$; **7**) and lower oxidation level species (**5**, **6**, and **8**) that are intermediates during assembly of the OEC *in vivo*, or those generated by treatment of the OEC with strong reducing agents.

I am still seeking ways and new synthetic conditions to stabilize Mn–Ca/shi^{3-} complexes with coordinated and bridging O^{2-} groups, as a means of obtaining heterometallic cluster compounds with more relevance to the S_0–S_3 states within the high-valent scheme of the catalytic Kok cycle. In addition, future perspectives of this work include the synthesis and systematic investigation of various new hydroxamic acids and oxime-based ligands in Mn–Ca coordination chemistry. Finally, the {Mn_4Ca_2} octahedral arrangement of **5** is very similar to the one seen before in Mn–Ce chemistry albeit with different bridging and ancillary ligands.[184] This is important when targeting for the deliberate replacement of Ca^{II} atoms by paramagnetic and anisotropic 4*f*-metal ions in an attempt to synthesize molecule-based magnets.

Chapter 4

New Insights in Mn–Ca Chemistry from the Use of Oximate-Based Ligands: $\{Mn^{II/III}_{22}Ca_2\}$ and $\{Mn^{IV}_{2}Ca_2\}$ Complexes with Relevance to Both Low- and High-Valent States of the Oxygen-Evolving Complex

4.1 *Preface*

The burgeoning development of polynuclear metal cluster chemistry in recent years was spearheaded by the intense investigation of novel organic and/or inorganic bridging and chelating ligands.[90,172b,172c,185] Ligands with N- and/or O-donor atoms have also contributed to the emergence of many diverse physicochemical properties of cluster compounds. In the molecular magnetism arena, for instance, ligands were proved to affect the nature of the magnetic exchange interactions between the metal ions,[186] the orientation of magnetic anisotropy axes [187] and subsequently the magnetization dynamics of the molecular compounds. [188] Furthermore, different classes of organic chelating/bridging ligands have been employed as: (i) "antennas" for energy transfer purposes in the field of optics,[189] (ii) spectators and actors in catalysis[190] and (iii) contrast agents for magnetic reasonance imaging.[191]

Bioinorganic chemistry is a thriving field of research and the impact of the ligands on the biocatalytic and biomimetic properties of polynuclear metal complexes has been manifested by the specific arrangement of the metal ions within the active site of PSII.1[f] Thus, the quest for new organic chelating/bridging ligands for heterometallic Mn–Ca chemistry is ongoing, with efforts focused on the incorporation of ligand moieties satisfying the requirements of the OEC. Simple carboxylates, hydroxamic acids and polyalcohol-based ligands have been used in the

synthesis of Mn–Ca complexes, leading to species with diverse topologies, oxidation state descriptions and spectroscopic/physicochemical properties.[96,107,110,111,173] Oximes and dioximes have been extensively used in homometallic Mn cluster chemistry geared toward magnetism applications;[192] however, this class of ligands has no precedent in the Mn–Ca literature of biomimetic species. These ligands exhibit some interesting structural and electronic properties, among of which are their ability to (i) stabilize Mn ions in high oxidation states,[113] (ii) support the formation and crystallization of Mn–O^{2-} inorganic cores[122f,193] and (iii) potentially coordinate to oxophilic metal ions, such as Ca^{II}, due to the strong α-nucleophile character of the oximate functionality. In addition, oximes are photosynthetically effective ligands and, in conjunction with hydrazine and nitric oxide, can reduce the OEC to S_{-1}, S_{-2} and S_{-3} states.[12b,169]

In this chapter, the initial employment of quinoline-2-aldoxime (qaoH; Scheme 1.12) and 2,6-diacetylpyridine dioxime (dapdoH_2; Scheme 1.11) in heterometallic Mn–Ca chemistry, which has afforded a mixed-valence {$Mn^{II/III}_{22}Ca_2$} cluster and a butterfly-like {$Mn^{IV}_2Ca_2$} complex, respectively, is reported. The synthesis, structures and magnetic properties of the heterometallic {$Mn^{II/III}_{22}Ca_2$} and {$Mn^{IV}_2Ca_2$} complexes are reported herein.

4.2 ***Experimental Section***

4.2.1 Physical Measurements

Elemental analysis: Elemental analyses (C, H and N) were performed on a PerkinElmer 2400 Series II Analyzer.

FT-IR spectroscopy: Infrared (IR) spectra were recorded in the solid state on a Bruker FT-IR spectrometer (ALPHA Platinum ATR single reflection) in the 4000–400 cm^{-1} range.

Magnetic susceptibility measurements: Variable-temperature direct current (*dc*) magnetic susceptibility studies were performed on a Quantum Design MPMS-XL SQUID susceptometer equipped with a 7 T magnet and operating in the 1.8–400 K range. Samples were embedded in solid eicosane to prevent torquing. Pascal's constants were used to estimate the diamagnetic correction, which was subtracted from the experimental susceptibility to give the molar paramagnetic susceptibility (χ_M).[127]

4.2.2 Synthesis

General considerations: All manipulations were performed under aerobic conditions using chemicals and solvents as received, unless otherwise stated. The organic ligands qaoH and $dapdoH_2$ were prepared as described elsewhere.[122a,194] The starting materials $Mn(O_2CPh)_2{\cdot}2H_2O$ and $Ca(O_2CPh)_2{\cdot}H_2O$ were synthesized in quantitative yields (>95%) from the 1:2 reaction of $MnCl_2{\cdot}4H_2O$ or $CaCl_2{\cdot}2H_2O$ and NaO_2CPh in H_2O.

$[Mn_{22}Ca_2O_{14}(OH)_4(OMe)_6(O_2CPh)_{22}(qao)_2(MeCN)_2(H_2O)_4](OH)_2$ (9): To a stirred, yellow solution of qaoH (0.03 g, 0.2 mmol) and NEt_3 (28 μL, 0.2 mmol) in MeCN/MeOH (15:3 mL) the solids $Mn(O_2CPh)_2{\cdot}2H_2O$ (0.07 g, 0.2 mmol) and $Ca(O_2CPh)_2{\cdot}H_2O$ (0.06 g, 0.2 mmol) were added together. The resulting dark orange suspension was stirred for 30 mins, during which time all the solids dissolved, and the colour of the solution changed to brown. The solution was filtered, and a mixture of Et_2O/C_6H_{14} (5/5 mL) diffused into the filtrate. After a month, brown needle-like crystals of **9** appeared and were collected by filtration, washed with cold MeCN (2 ×

3 mL) and Et_2O (2 × 3 mL), and dried in air; the yield was 20% (based on the total available Ca). The crystalline solid was analyzed as **9**·$4H_2O$: C, 43.90; H, 3.40; N, 1.67 %. Found: C, 43.75; H, 3.27; N, 1.81%. Selected ATR data (cm^{-1}): 1594 (m), 1567 (m), 1534 (m), 1491 (w), 1447 (w), 1386 (vs), 1303 (w), 1173 (w), 1143 (w), 1067 (w), 1020 (m), 984 (w), 936 (w), 829 (w), 710 (vs), 686 (m), 675 (m), 634 (w), 600 (m), 568 (m), 476 (w), 450 (w).

$[Mn_2Ca_2(OMe)_2(NO_3)_2(dapdo)_4]$ (10): To a stirred, colourless solution of dapdoH_2 (0.08 g, 0.4 mmol) and NEt_3 (56 μL, 0.4 mmol) in MeCN/MeOH (15:5 mL) the solids $Mn(O_2CPh)_2·2H_2O$ (0.07 g, 0.2 mmol) and $Ca(NO_3)_2·4H_2O$ (0.05 g, 0.2 mmol) were added together. The resulting ecru suspension was stirred for 2 h, during which time all the solids dissolved, and the colour of the solution changed to dark brown. The solution was filtered and left to evaporate slowly at room temperature. After one week, dark brown rod-like crystals of **10**·2MeCN appeared and were collected by filtration, washed with cold MeCN (2 × 3 mL) and Et_2O (2 × 3 mL), and dried in air; the yield was 40% (based on the total available Ca). The crystalline solid was analyzed as lattice solvent-free **10**: C, 40.01; H, 3.71; N, 17.19 %. Found: C, 40.22; H, 3.78; N, 17.12 %. Selected ATR data (cm^{-1}): 2808 (w), 1591 (m), 1533 (m), 1409 (m), 1365 (w), 1316 (m), 1278 (w), 1190 (w), 1167 (m), 1149 (m), 1118 (w), 1087 (m), 1065 (m), 1015 (s), 947 (m), 822 (w), 805 (s), 792 (m), 760 (m), 684 (m), 663 (s), 553 (vs), 478 (m), 440 (m).

4.2.3 Single-crystal X-ray Crystallography

Crystals of the complexes **9** and **10** were selected and mounted on MiteGen dual thickness micromounts TM using inert oil. Diffraction data were collected at 100(2) K on a

Bruker D8 VENTURE diffractometer equipped with a multilayer mirror monochromator and a Mo Kα microfocus sealed tube (λ = 0.71073 Å). Images were processed with the software SAINT+,[131] and absorption effects were corrected with the multi-scan method implemented in SADABS.[177] The structures were solved using the Bruker SHELXTL inside the APEX-III software package, and refined using the SHELXLE and PLATON programs.[137a, 195, 196] The programs used for molecular graphics were MERCURY[138a] and DIAMOND.[138b] Additional information on the crystallographic data collection and structure refinement details is summarized in Table 4.1.

Table 4.1. Crystallographic Data for Complexes **9** and **10**.

Parameter	**9**	**10**·2MeCN
Formula[a]	$C_{184}H_{162}Mn_{22}Ca_2N_6O_{76}$	$C_{38}H_{42}Mn_2Ca_2N_{14}O_{16}$
FW[a] / g mol^{-1}	4962.13	1140.88
Crystal type	brown needle	dark brown rod
Crystal size / mm	0.20×0.20×0.20	0.10×0.20×0.40
Crystal system	Triclinic	Monoclinic
Space group	*P*-1	$P2_1/n$
a / Å	17.226(5)	13.5003(12)
b / Å	18.581(4)	12.9259(12)
c / Å	19.604(3)	15.2726(13)
α / °	68.823(3)	90

β / °	68.416(8)	104.320(3)
γ / °	68.981(8)	90
V / Å^3	5253.1(2)	2582.3(4)
Z	1	2
T / K	100(2)	100(2)
ρ_{calc} / g cm^{-3}	1.587	1.520
μ / mm^{-1}	1.407	0.768
θ range / °	2.24–25.99	2.21–26.02
Index ranges	$-21 \le h \le 21$	$-16 \le h \le 16$
	$-22 \le k \le 22$	$-15 \le k \le 15$
	$-24 \le l \le 24$	$-18 \le l \le 18$
Collected reflections	221412	39911
Independent reflections	20527 (R_{int} = 0.0644)	5072 (R_{int} = 0.0773)
Final $R^{b,c}$ indices [$I>2\sigma(I)$]	$R1$ = 0.0533	$R1$ = 0.0479
	$wR2$ = 0.1473	$wR2$ = 0.1382
$(\Delta\rho)_{max,min}$ / e Å^{-3}	2.100, –2.507	1.108, –0.481

[a]Including solvate molecules. [b]$R1 = \Sigma(||F_o| - |F_c||)/\Sigma|F_o|$. [c]$wR2 = [\Sigma[w(F_o^2 - F_c^2)^2]/\Sigma[w(F_o^2)^2]]^{1/2}$, $w = 1/[\sigma^2(F_o^2) + (ap)^2 + bp]$, where $p = [\max(F_o^2, 0) + 2F_c^2]/3$.

4.3 ***Results and Discussion***

4.3.1 Synthetic Comments and IR Spectra

Various synthetic strategies have been employed for the synthesis and crystallization of heterometallic Mn–Ca cluster compounds, including self-assembly and comproportionation reactions, as discussed in Chapters 2 and 3 of this thesis. These synthetic routes have afforded numerous Mn–Ca complexes with different metal stoichiometries, Mn oxidation state descriptions and structural topologies.[93,94,95,97,100,101,103,104,110,137,138] In this present chapter the self-assembly synthetic route was followed and I have thus explored reactions involving the quinoline-2-aldoxime (qaoH) and 2,6-diacetylpyridine dioxime ($dapdoH_2$) chelates, respectively, various Mn^{II}- and Ca^{II}-containing starting materials and base NEt_3. The latter was used to facilitate the deprotonation of the qaoH/$dapdoH_2$ ligands and subsequently generate $NHEt_3^+$ cations in solution, which can potentially counterbalance the anionic charge of a cluster compound in solution and aid in the crystallization of the resulting product in the solid state. Finally, various solvents or solvent mixtures and metal-to-ligand ratios were explored to yield crystalline products of the reported molecular compounds.

Therefore, the one-pot reaction of $Mn(O_2CPh)_2{\cdot}2H_2O$ and $Ca(O_2CPh)_2{\cdot}H_2O$ with qaoH in a 1:1:1 molar ratio in MeCN/MeOH in the presence of 1 equivalent of NEt_3 gave a brown solution that, upon filtration and slow diffusion with Et_2O/C_6H_{14}, afforded dark red needle-like crystals of the complex $[Mn_{22}Ca_2O_{14}(OH)_4(OMe)_6(O_2CPh)_{22}(qao)_2(MeCN)_2(H_2O)_4](OH)_2$ (**9**) in 20% yield (based on the total available Ca). The formation of complex **9** is summarized in the balanced Eqn. 4.1.

$$22\ Mn(O_2CPh)_2{\cdot}2H_2O + 2\ Ca(O_2CPh)_2{\cdot}H_2O + 2\ qaoH + 4\ O_2 + 26\ NEt_3 + 2\ MeCN + 6\ MeOH \rightarrow$$

$$[Mn_{22}Ca_2O_{14}(OH)_4(OMe)_6(O_2CPh)_{22}(qao)_2(MeCN)_2(H_2O)_4](OH)_2 + 26\ (NHEt_3)(O_2CPh)$$

$$+ 30\ H_2O \qquad \textbf{Eqn. 4.1}$$

The reaction is an oxidation, undoubtedly by O_2 under the prevailing basic conditions. The NEt_3 has the role of proton acceptor to facilitate the deprotonation of qaoH and H_2O molecules. The employment of various other organic bases, such as NMe_3, NBu^n_3 and Me_4NOH did not afford crystalline materials but only oily products that I was not able to further characterize. Analogous reactions with different Mn^{II}- and Ca^{II}-carboxylate starting materials (i.e., acetates, propionates, pivalates, etc.), all failed to yield single-crystals suitable for X-ray diffraction studies. The reaction solvent mixture was found to be of critical importance for the crystallization of **9** as both solvents were found in the molecular structure of the compound; bridging MeO^- groups and terminally-bound MeCN molecules (*vide infra*). Reactions in other solvent mixtures either failed to give single-crystals suitable for X-ray diffraction studies or yielded amorphous precipitates that I was unable to redissolve and crystallize. Finally, by adjusting the experimental molar ratios of the precursors to the stoichiometric equivalents, in an attempt to optimize the isolated yields, I failed to reproduce the crystals of **9**.

Regarding the dapdoH_2 ligand system, the one-pot reaction of $Mn(O_2CPh)_2{\cdot}2H_2O$ and $Ca(NO_3)_2{\cdot}4H_2O$ with the corresponding ligand in a 1:1:2 molar ratio in MeCN/MeOH in the presence of 2 equivalents of NEt_3 gave a dark brown solution that, upon filtration and slow evaporation at room temperature, afforded dark brown rod-like crystals of the complex $[Mn_2Ca_2(OMe)_2(NO_3)_2(dapdo)_4]$ (**10**) in 40% yield (based on the total available Ca). The formation of complex **10** is summarized in the balanced Eqn. 4.2.

$$2\ Mn(O_2CPh)_2{\cdot}2H_2O + 2\ Ca(NO_3)_2{\cdot}4H_2O + 4\ dapdoH_2 + O_2 + 6\ NEt_3 + 2\ MeOH \rightarrow$$

$$[Mn_2Ca_2(OMe)_2(NO_3)_2(dapdo)_4] + 4\ (NHEt_3)(O_2CPh) + 2\ (NHEt_3)(NO_3) + 14\ H_2O \qquad \textbf{Eqn. 4.2}$$

Similar to complex **9** this reaction is an oxidation, undoubtedly by O_2 under the prevailing basic conditions. The NEt_3 has the role of proton acceptor to facilitate the complete, double deprotonation of the $dapdoH_2$ molecules. The employment of various other organic bases, Mn^{II}-carboxylate starting materials and Ca^{II} inorganic salts yielded oily products or failed to give single-crystals suitable for X-ray diffraction studies. Reactions in different solvents or solvent mixtures resulted in amorphous precipitates that I was unable to redissolve and crystallize, making it apparent that both MeOH and MeCN molecules are important in crystallizing complex **10**.

Unfortunately, complexes **9** and **10** do not appear to retain their solid-state structures in solutions of various solvent media (i.e., MeCN, CH_2Cl_2 and THF), as it was confirmed by electrospray ionization mass spectrometry (ESI-MS). I have thus concentrated on the solid-state characterization of these species, which includes IR spectroscopy and magnetic susceptibility studies. The IR spectra for complexes **9** and **10** can be found in the Appendix of this thesis. For both complexes several bands appear in the ~1595–1380 cm^{-1} range, assigned to contributions from the stretching vibrations of the aromatic rings of qao^- and $dapdo^{2-}$, which overlap with stretches of the carboxylate bands in **9**,[142] as well as contributions from the $\nu(C{=}N)_{oximate}$ modes of qao^- and $dapdo^{2-}$; they, thus, do not represent pure vibrations and render exact assignments difficult. It is very likely that the strong bands at 1594 and 1447 cm^{-1} in the spectrum of **9** are attributed to the $\nu_{as}(CO_2)$ and $\nu_s(CO_2)$ modes, respectively; the former should also involve a ring

stretching character. The difference $\Delta[\Delta = \nu_{as}(CO_2) - \nu_s(CO_2)]$ is small (147 cm^{-1}), as expected for the predominant bidentate bridging mode of carboxylate ligation (*vide infra*).[96,143a] Low frequency bands (600–400 cm^{-1}) found in the IR spectrum of **9** are attributed to the $\nu(Mn–O^{2-})$ vibration modes.[197] Lastly, the $\nu(NO_3^-)$ band in **10** could be tentatively assigned to the strong band located at 1382 cm^{-1}, as found in other metal complexes.[198]

4.3.2 Description of Structures

The Mn oxidation states in complexes **9** and **10** as well as the protonation states of the oxygen atoms in complex **9** were established by charge balance considerations, metric parameters and BVS calculations (Table 4.2 and Table 4.3).[148] Selected interatomic distances and angles for complexes **9** and **10** are listed in Table 4.4.

The crystal structure of **9** consists of a $[Mn_{22}Ca_2O_{14}(OH)_4(OMe)_6(O_2CPh)_{22}(qao)_2(MeCN)_2(H_2O)_4]^{2+}$ dication (Figure 4.1, top) and two OH^- counterions; the latter will not be further discussed. The presence of OH^- counterions in **9** is not unusual in high-nuclearity metal cluster chemistry.[122] The molecular structure of the centrosymmetric dication of **9** consists of 6 Mn^{II}, 16 Mn^{III}, and 2 Ca^{II} ions held together by 12 μ_4-O^{2-}, 2 μ_3-O^{2-}, 4 μ_3-OH^-, 4 μ_3-OMe^-, 2 μ-OMe^- and 2 μ_4-oximate groups from two $\eta^1{:}\eta^1{:}\eta^3{:}\mu_4$ qao^- ligands (Scheme 4.1). Peripheral ligation about the $[Mn^{II}_6Mn^{III}_{16}Ca^{II}_2(\mu_4\text{-}O)_{12}(\mu_3\text{-}O)_4(\mu_3\text{-}OH)_2(\mu_3\text{-}OMe)_4(\mu\text{-}OMe)_2(\mu_4\text{-}NO)_2]^{22+}$ inorganic core (Figure 4.1, bottom) is provided by 22 $PhCO_2^-$ groups that are either μ- or μ_3-bridging and terminally bound (Scheme 4.1), as well as two terminally bound MeCN and four terminally bound H_2O molecules located on the Ca1/Ca1′, Mn7/Mn7′ and Mn10/Mn10′ pairs, respectively. Four coordinated H_2O molecules are also

present in the active site of the native OEC, two which are bound to a Mn atom. These H_2O molecules could serve as substrates for the overall catalytic reaction to proceed, including subsequent deprotonations with metal-centered oxidations preceding O–O bond formation.

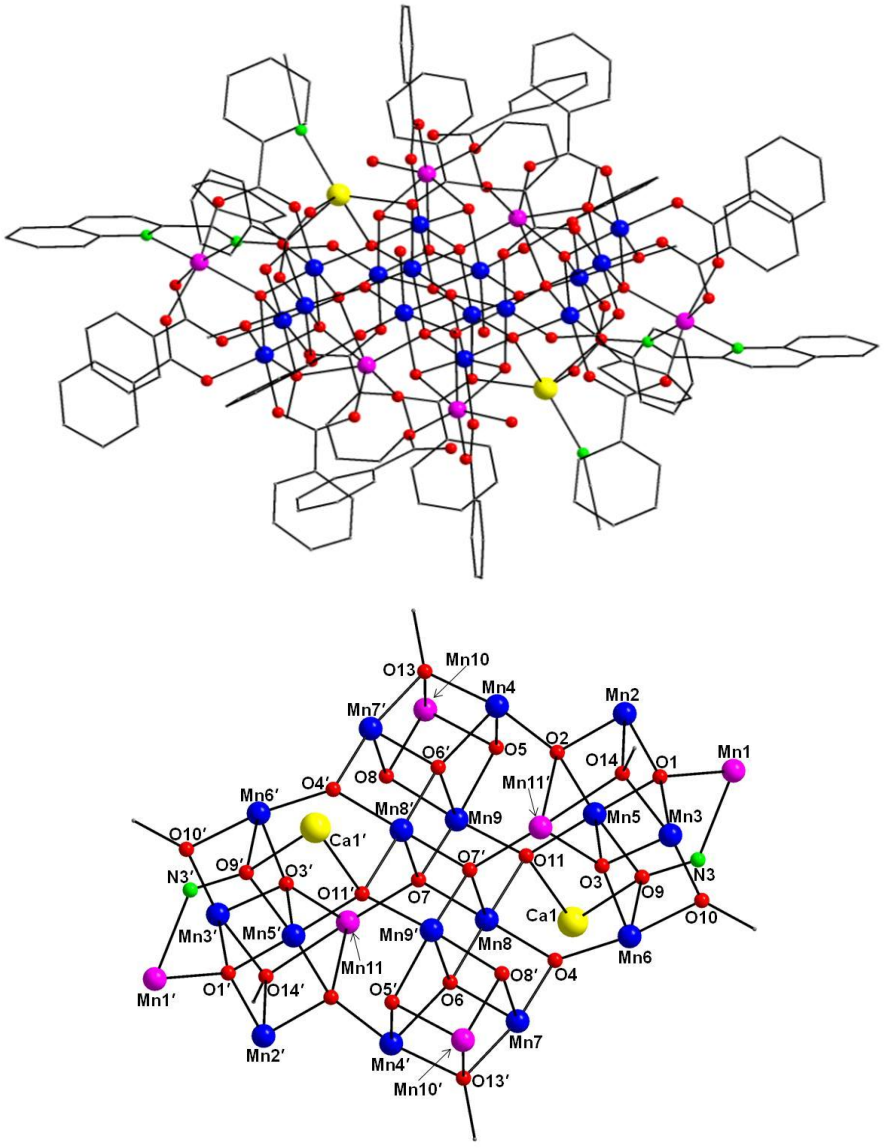

Figure 4.1. The structure of the dication in complex **9** (top) and a labeled representation of its complete core (bottom). H atoms are omitted for clarity. Colour scheme: Mn^{II}, magenta; Mn^{III}, blue; Ca^{II}, yellow; O, red; N, green, C, gray. Symmetry operation for the primed atoms in **9**: 1–*x*, 1–*y*, 1–*z*.

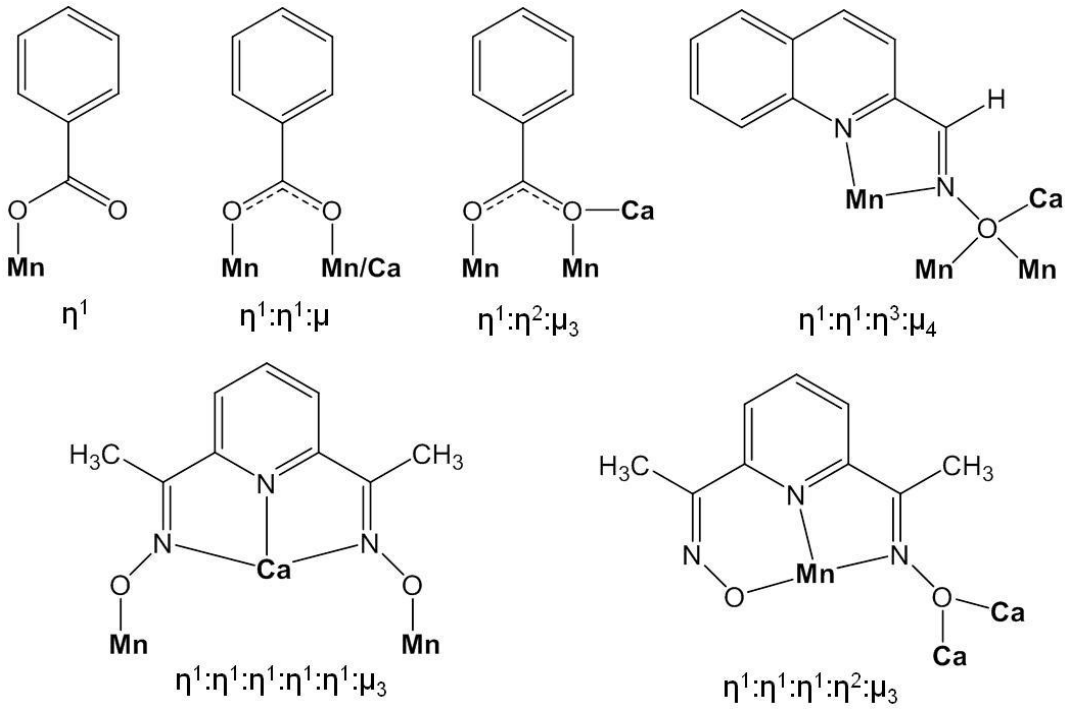

Scheme 4.1. Coordination modes of all organic ligands present in complexes **9** and **10**.

The unique topology of **9** can be described as four $\{Mn^{II}Mn^{III}{}_3O_4\}$ cubanes that are connected to each other through a central $\{Mn_2O_4\}$ unit comprising the atoms Mn8, Mn8′, O7 and O7′. Each of the external cubane subunits is further linked to a $\{Mn^{II}Mn^{III}Ca(\mu_3\text{-NO})\}$ unit through the bridging oxido, methoxido and oximate groups. As a result, within **9**, there are four symmetry-related $\{Mn_4O_4\}$ distorted cubanes attached to two "dangling" Ca^{II} atoms. The structures of these $\{Mn_4CaO_5\}$ and $\{Mn_4CaO_6\}$ subunits (Figure 4.2) are intriguing, especially when compared to the OEC. In particular, they possess a similar extended cubane topology to that of the native site, with Mn···Mn and Mn···Ca closest separations of 2.876–3.686 Å and 3.376–3.756 Å, respectively, comparable to the corresponding values of 2.7–3.3 Å and ~3.4 Å for the OEC in PSII. All Mn atoms in **9** are six-coordinate with distorted octahedral geometries.

In the case of the Mn^{III} atoms [Mn(2-9) and their symmetry-related partners], the octahedra are axially elongated due to the Jahn-Teller (JT) distortions, as expected for high-spin d^4 ions in this geometry. In addition, both Ca^{II} atoms in **9** are five-coordinate with an almost perfect square pyramidal geometry ($\tau = 0.05$).[147] Finally, the space-filling representation (Figure 4.3) shows that **9** adopts a nano-sized ellipsoidal conformation with dimensions of ~26 and ~20 Å, defined by the longest C···C distance, excluding the H-atoms.

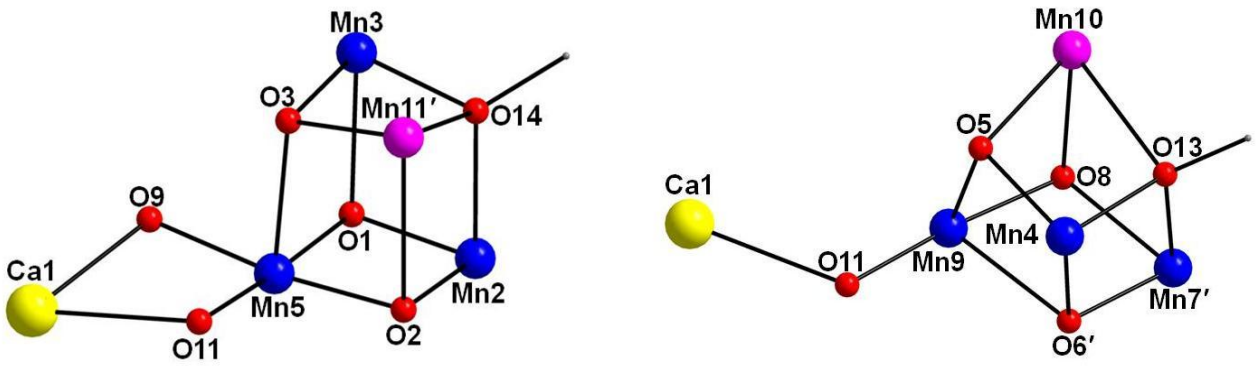

Figure 4.2. Two types of $\{Mn_4Ca\}$ extended cubane subunits found within complex **9**. Colour scheme as in Figure 4.1.

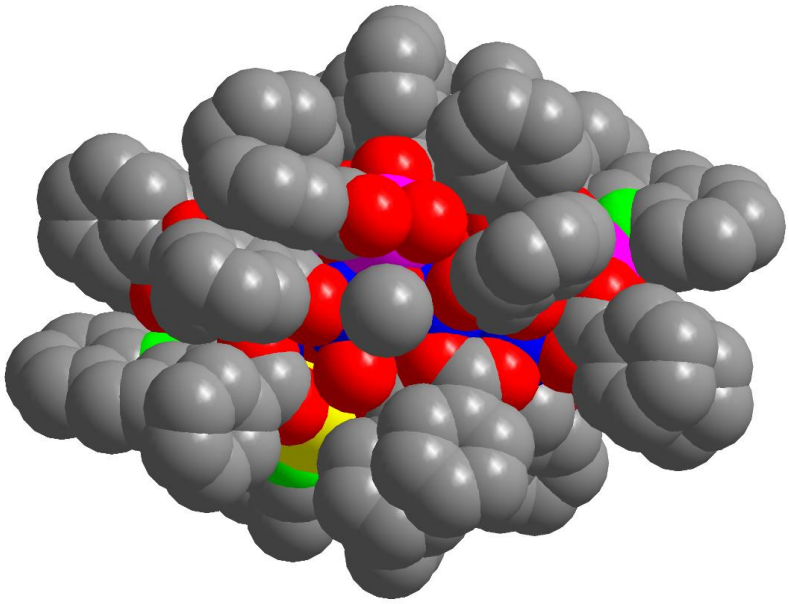

Figure 4.3. Space-filling representation of **9** showing its nearly ellipsoidal conformation with dimensions of ~26 and ~20 Å, defined by the longest C···C distances. Colour scheme: Mn^{II}, magenta; Mn^{III}, blue; Ca^{II}, yellow; O, red; N, green; C, gray.

Table 4.2. BVS Calculations[a] for Mn Atoms in **9** and **10**.

Complex	Atom	Mn^{II}	Mn^{III}	Mn^{IV}
9	Mn1	<u>2.07</u>	1.93	1.97
	Mn2	3.19	<u>2.92</u>	3.07
	Mn3	3.17	<u>2.90</u>	3.04
	Mn4	2.96	<u>2.71</u>	2.84
	Mn5	3.02	<u>2.76</u>	2.90
	Mn6	3.18	<u>2.90</u>	3.05
	Mn7	3.16	<u>2.85</u>	2.99
	Mn8	3.01	<u>2.75</u>	2.89
	Mn9	3.05	<u>2.79</u>	2.93
	Mn10	<u>1.92</u>	1.76	1.85
	Mn11	<u>1.85</u>	1.69	1.78
10	Mn1	4.28	3.99	<u>4.07</u>

[a]The underlined value is one closest to the charge for which it was calculated. The oxidation state is the nearest whole number to the underlined value.

Table 4.3. BVS Calculations[a] for Inorganic Oxygen Atoms in **9**.

Atom	BVS	Group
O1	1.87	O^{2-}
O2	1.86	O^{2-}
O3	1.83	O^{2-}
O4	1.83	O^{2-}
O5	1.14	OH^{-}
O6	1.75	O^{2-}
O7	1.76	O^{2-}
O8	1.04	OH^{-}
O11	1.82	O^{2-}
O12	0.32	H_2O
O38	0.22	H_2O

[a]An O BVS in the ~1.7–2.0, ~1.0–1.2, and ~0.2–0.4 ranges is indicative of non-, single- and double-protonation, respectively.

Table 4.4. Selected Interatomic Distances (Å) and Angles (°) for Complexes **9**[a] and **10**·2MeCN[b].

9			
Mn(1)-O(1)	2.085(3)	Mn(7)-O(4)	1.903(3)
Mn(1)-O(16)	2.204(3)	Mn(7)-O(6)	1.876(3)
Mn(1)-O(17)	2.162(4)	Mn(7)-O(8′)	2.261(3)
Mn(1)-O(41)	2.126(3)	Mn(7)-O(13′)	1.991(3)
Mn(1)-N(1)	2.264(4)	Mn(7)-O(29)	1.938(3)
Mn(1)-N(3)	2.296(4)	Mn(7)-O(38)	2.273(3)
Mn(2)-O(1)	1.856(3)	Mn(8)-O(4)	1.914(3)
Mn(2)-O(2)	1.898(3)	Mn(8)-O(6)	1.931(3)
Mn(2)-O(14)	2.277(3)	Mn(8)-O(7)	1.911(3)
Mn(2)-O(18)	1.983(3)	Mn(8)-O(7′)	2.387(3)
Mn(2)-O(19)	1.972(3)	Mn(8)-O(11)	1.940(3)
Mn(2)-O(20)	2.167(4)	Mn(8)-O(25)	2.322(3)
Mn(3)-O(1)	2.343(3)	Mn(9)-O(5)	1.962(3)
Mn(3)-O(3)	1.894(3)	Mn(9)-(O6′)	2.398(3)
Mn(3)-O(10)	1.922(3)	Mn(9)-O(7)	1.890(3)
Mn(3)-O(14)	1.953(3)	Mn(9)-O(8)	1.968(3)
Mn(3)-O(15)	1.942(3)	Mn(9)-O(11)	1.911(3)

Mn(3)-O(32)	2.126(3)	Mn(9)-O(24)	2.180(3)
Mn(4)-O(2)	1.881(3)	Mn(10)-O(5)	2.231(3)
Mn(4)-O(5)	2.083(3)	Mn(10)-O(8)	2.173(3)
Mn(4)-O(6′)	2.064(3)	Mn(10)-O(12)	2.160(4)
Mn(4)-O(13)	1.984(3)	Mn(10)-O(13)	2.543(15)
Mn(4)-O(21)	2.181(4)	Mn(10)-O(23)	2.105(4)
Mn(4)-O(22)	2.037(3)	Mn(10)-O(34)	2.067(3)
Mn(5)-O(1)	1.898(3)	Mn(11)-O(2′)	2.860(3)
Mn(5)-O(2)	1.930(3)	Mn(11)-O(3′)	2.122(3)
Mn(5)-O(3)	2.247(3)	Mn(11)-O(7)	2.093(3)
Mn(5)-O(9)	1.996(3)	Mn(11)-O(14)	2.289(3)
Mn(5)-O(11)	1.950(3)	Mn(11)-O(26)	2.070(3)
Mn(5)-O(40)	2.258(3)	Mn(11)-O(31′)	2.182(3)
Mn(6)-O(3)	1.885(3)	Ca(1)-O(9)	2.381(3)
Mn(6)-O(4)	1.873(3)	Ca(1)-O(11)	2.495(3)
Mn(6)-O(9)	2.452(3)	Ca(1)-O(25)	2.328(4)
Mn(6)-O(10)	1.938(3)	Ca(1)-O(27)	2.358(4)
Mn(6)-O(28)	1.945(3)	Ca(1)-N(2)	2.374(6)
Mn(6)-O(30)	2.198(3)		

Mn(5)-O(9)-N(3)-Mn(1)	1.0(3)	Mn(6)-O(9)-N(3)-Mn(1)	100.5(2)

Mn(1)-O(1)-Mn(2)	123.3(2)	Mn(5)-O(2)-Mn(11′)	89.3(1)
Mn(1)-O(1)-Mn(3)	114.6(1)	Mn(5)-O(3)-Mn(6)	101.5(1)
Mn(1)-O(1)-Mn(5)	117.5(2)	Mn(5)-O(3)-Mn(11′)	103.4(1)
Mn(2)-O(1)-Mn(3)	99.5(1)	Mn(5)-O(9)-Mn(6)	91.8(1)
Mn(2)-O(1)-Mn(5)	100.0(1)	Mn(5)-O(11)-Mn(8)	130.1(2)
Mn(2)-O(2)-Mn(4)	116.6(2)	Mn(5)-O(11)-Mn(9)	123.7(2)
Mn(2)-O(2)-Mn(5)	97.4(1)	Mn(6)-O(3)-Mn(11′)	144.1(2)
Mn(2)-O(2)-Mn(11′)	99.6(1)	Mn(6)-O(4)-Mn(7)	122.1(2)
Mn(2)-O(14)-Mn(3)	98.9(1)	Mn(6)-O(4)-Mn(8)	132.8(2)
Mn(2)-O(14)-Mn(11′)	107.7(1)	Mn(7)-O(4)-Mn(8)	96.6(1)
Mn(3)-O(1)-Mn(5)	97.6(1)	Mn(7)-O(6)-Mn(8)	97.0(1)
Mn(3)-O(3)-Mn(5)	101.0(1)	Mn(7)-O(8′)-Mn(10′)	101.6(1)
Mn(3)-O(3)-Mn(6)	100.5(1)	Mn(7)-O(13′)-Mn(10′)	97.8(1)
Mn(3)-O(3)-Mn(11′)	99.7(1)	Mn(8)-O(6)-Mn(9′)	95.7(1)
Mn(3)-O(10)-Mn(6)	97.7(1)	Mn(8)-O(7)-Mn(8′)	98.0(1)
Mn(3)-O(14)-Mn(11′)	92.5(1)	Mn(8)-O(7)-Mn(9)	97.2(1)
Mn(4)-O(2)-Mn(5)	126.5(2)	Mn(8)-O(7)-Mn(11)	122.2(1)
Mn(4)-O(2)-Mn(11′)	121.2(1)	Mn(8)-O(7′)-Mn(11′)	116.3(1)

Mn(4)-O(5)-Mn(9)	102.3(2)	Mn(8)-O(11)-Mn(9)	94.1(1)
Mn(4)-O(5)-Mn(10)	108.0(1)	Mn(9)-O(5)-Mn(10)	96.2(1)
Mn(4)-O(6′)-Mn(7′)	98.5(1)	Mn(9)-O(6′)-Mn(7′)	100.1(1)
Mn(4)-O(6′)-Mn(8′)	162.6(2)	Mn(9)-O(7)-Mn(8′)	95.8(1)
Mn(4)-O(6′)-Mn(9)	89.6(1)	Mn(9)-O(7)-Mn(11)	122.0(1)
Mn(4)-O(13)-Mn(7′)	97.4(1)	Mn(9)-O(8)-Mn(7′)	102.1(1)
Mn(4)-O(13)-Mn(10)	100.2(1)	Mn(9)-O(8)-Mn(10)	97.9(1)
Mn(5)-O(9)-Ca(1)	100.6(12)	Mn(8)-O(11)-Ca(1)	91.0(1)
Mn(5)-O(11)-Ca(1)	98.1(12)	Mn(8)-O(25)-Ca(1)	86.5(11)
Mn(6)-O(9)-Ca(1)	99.1(1)	Mn(9)-O(11)-Ca(1)	116.3(14)

10·2MeCN			
Mn(1)-O(1)	1.837(2)	Ca(1)-O(2)	2.417(2)
Mn(1)-O(3)	1.895(3)	Ca(1)-O(2′)	2.397(2)
Mn(1)-O(4)	1.862(3)	Ca(1)-O(5)	2.525(3)
Mn(1)-O(7′)	1.906(2)	Ca(1)-O(6)	2.480(3)
Mn(1)-N(1)	2.011(3)	Ca(1)-N(4′)	2.607(3)
Mn(1)-N(2)	2.003(3)	Ca(1)-N(5′)	2.474(3)
Ca(1)-O(1)	2.382(3)	Ca(1)-N(6′)	2.509(3)
Mn(1)-O(7′)-N(6′)-Ca(1)	21.5(3)	Mn(1)-O(1)-Ca(1)	114.5(1)
Mn(1)-O(3)-N(4)-Ca(1)	30.6(3)	Ca(1)-O(2)-Ca(1′)	98.6(9)
Ca(1)-O(2)-N(1)-Mn(1)	35.4(3)		

[a]Symmetry code: ′ = 1–*x*, 1–*y*, 1–*z*; [b]Symmetry code: ′ = 1–*x*, 1–*y*, 1–*z*.

The structure of **10** (Figure 4.4) contains an unusual ‘butterfly’-like core where the high-valence Mn^{IV} ions are located at the wing-tip positions and the two Ca^{II} ions occupying the ‘body’ sites. The metal ions are bridged by two μ-OMe^- (O1, O1′) and the oxime arms of two $\eta^1{:}\eta^1{:}\eta^1{:}\eta^1{:}\eta^1{:}\mu_3$ and two $\eta^1{:}\eta^1{:}\eta^1{:}\eta^2{:}\mu_3$ $dapdo^{2-}$ ligands (Scheme 4.1). The dioximate ligands appear to both chelate and bridge the Mn^{IV} and Ca^{II} ions by employing all four of their donor atoms albeit under different configurations. This emphasizes the versatility, flexibility and ability of $dapdo^{2-}$ to stabilize metal ions in various oxidation states, diverse sizes and different intrinsic characteristics (hardness, acidity and oxophilicity). The six-coordinate Mn^{IV} ions possess

distorted octadedral geometries, whereas two bidentate chelating NO_3^- groups complete eight-coordination around each Ca^{II} ion. The coordination geometry of both Ca^{II} ions is very distorted; the program SHAPE[150] was used to determine the CShM values of 3.71 and 3.88 for square antiprismatic and triangular dodecahedral geometries, respectively (Figure 4.5). The Mn···Mn and Mn···Ca distances are 6.717 Å and 3.561/4.067 Å, respectively. Complex **10** is the first non-oxido bridged Mn-Ca complex that contains exclusively Mn^{IV} ions; this is clearly supported by the oximate arms of $dapdo^{2-}$ ligands.

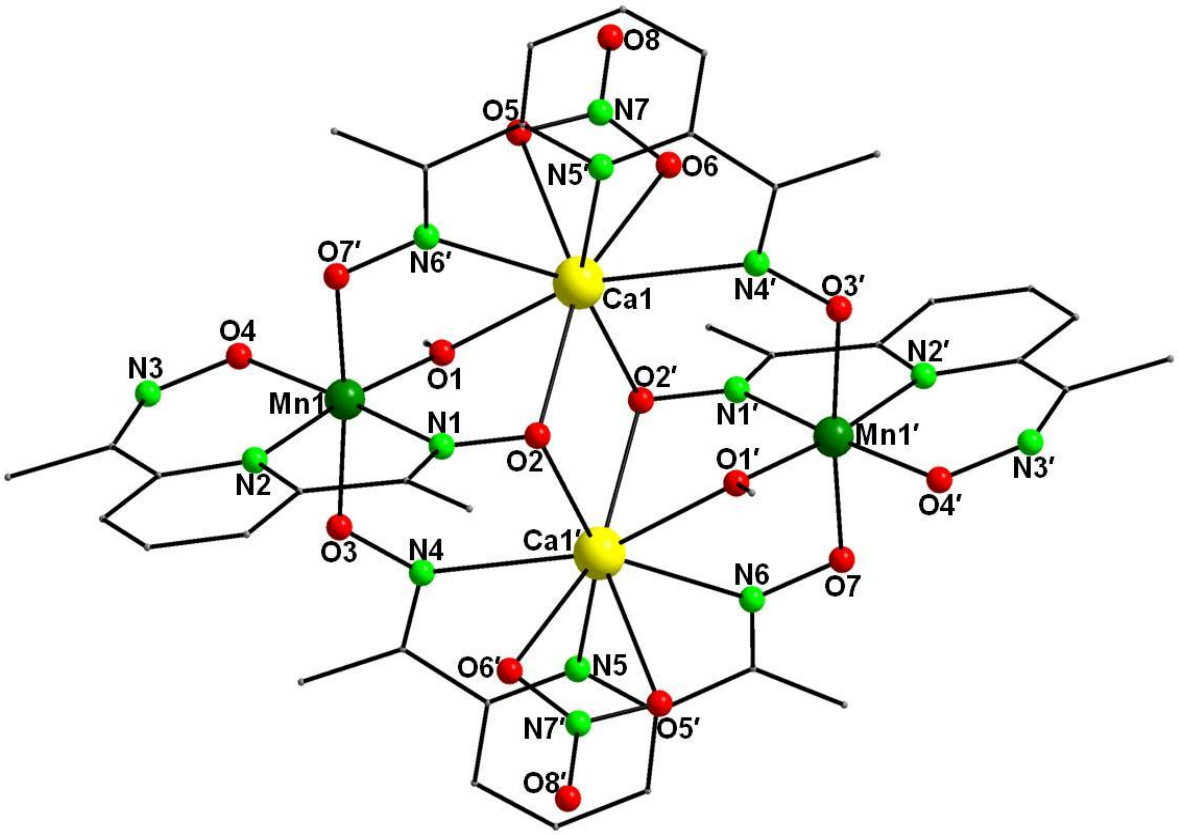

Figure 4.4. Labeled structure of **10**. H atoms are omitted for clarity. Colour scheme: Mn^{IV}, olive green; Ca^{II}, yellow; O, red; N, green; C, gray. Symmetry operation for the primed atoms in **10**: 1–*x*, 1–*y*, 1–*z*.

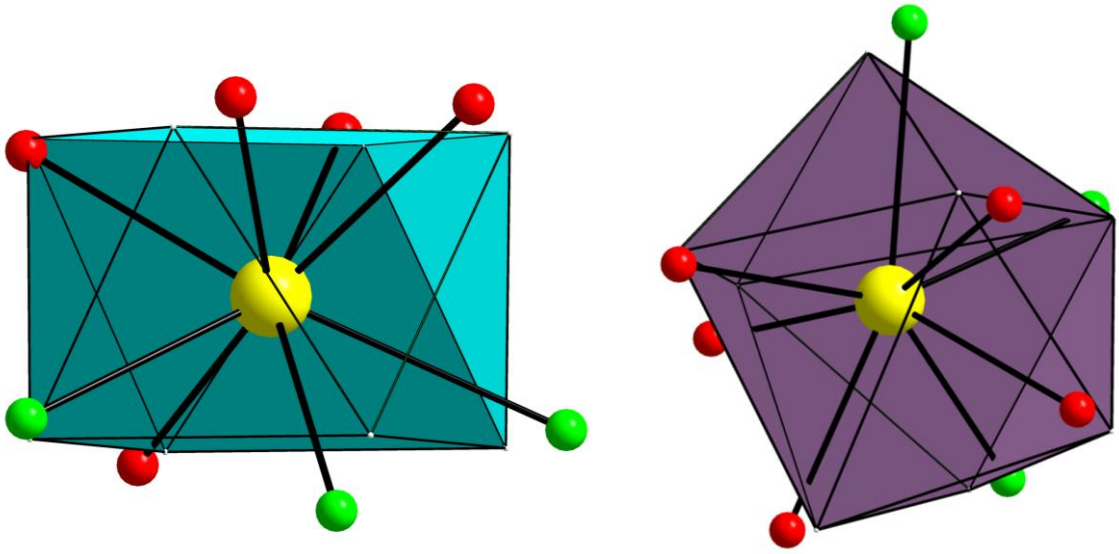

Figure 4.5. Distorted square antiprismatic (left) and triangular dodecahedral (right) coordination geometries of the eight-coordinate Ca^{II} ions in **10**. The points connected by the black thin lines define the vertices of the ideal polyhedron. Values of CShM between 0.1 and 3 usually correspond to a not negligible but still small distortion from ideal geometry, while values larger than 3 refer to very distorted coordination environments. Colour scheme: Ca^{II}, yellow; O, red; N, green.

4.3.3 Solid-State Magnetic Susceptibility Studies

Variable-temperature direct-current (*dc*) magnetic susceptibility measurements were performed on freshly-prepared and analytically-pure microcrystalline samples of **9** and **10** in the temperature range 2-300 K in an applied field of 0.1 T. The data are shown as $\chi_M T$ versus T plots in Figure 4.6. The value of the $\chi_M T$ product for **9** at 300 K is 41.74 $cm^3 \cdot mol^{-1} \cdot K$, significantly lower than the value of 74.25 $cm^3 \cdot mol^{-1} \cdot K$ (calculated with g = 2) expected for 6 Mn^{II} and 16 Mn^{III} non-interacting ions. The $\chi_M T$ of **9** steadily decreases with decreasing T, reaching a value of 1.56 $cm^3 \cdot mol^{-1} \cdot K$ at 2 K. The overall magnetic response of **9** is indicative of predominant

antiferromagnetic exchange interactions between the metal centers, and the low $\chi_M T$ value at 2 K suggests a very small spin ground state value. The latter was confirmed to be S = 0 by extrapolation of the $\chi'_M T$ *ac* data down to 0 K (Figure 4.7). The $\chi'_M T$ is heading to a value of ~0 $cm^3 \cdot mol^{-1} \cdot K$, in agreement with an S = 0 ground state. The structure of **9** is too complicated to allow for any accurate and precise rationalization of the S = 0. Although discrete $\{Mn_4O_4\}$ cubanes at various oxidation state descriptions are generally known to be ferromagnetically coupled for a wide range of Mn–O–Mn angles,[199] such cubane subunits in **9** are linked to each other via oxido groups, one of the strongest antiferromagnetic couplers in molecular magnetism. The Mn^{IV} ions in complex **10** are well separated from each other and there is a very weak to negligible magnetic interaction between them, as indicated by the temperature independence of the $\chi_M T$ product from 300–5 K. The $\chi_M T$ of **10** remains essentially constant to a value of ~3.7 $cm^3 \cdot mol^{-1} \cdot K$, very close to the theoretical value of 3.75 $cm^3 \cdot mol^{-1} \cdot K$ (calculated with g = 2) for two non-interacting Mn^{IV} (d^3; S = 3/2) ions. The low-T decrease (< 5 K) of the $\chi_M T$ could be tentatively ascribed to the onset of some weak magnetic coupling between the metal centres, of either intra- or intermolecular origin, zero-field splitting and/or Zeeman effects from the applied *dc* field.

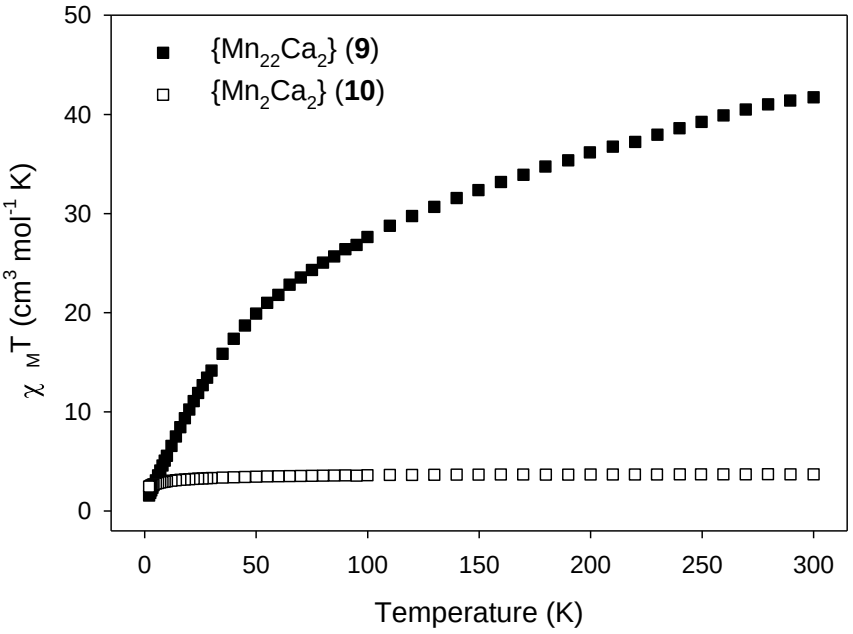

Figure 4.6. $\chi_M T$ versus T plots for complexes **9** and **10** in a 0.1 T *dc* field.

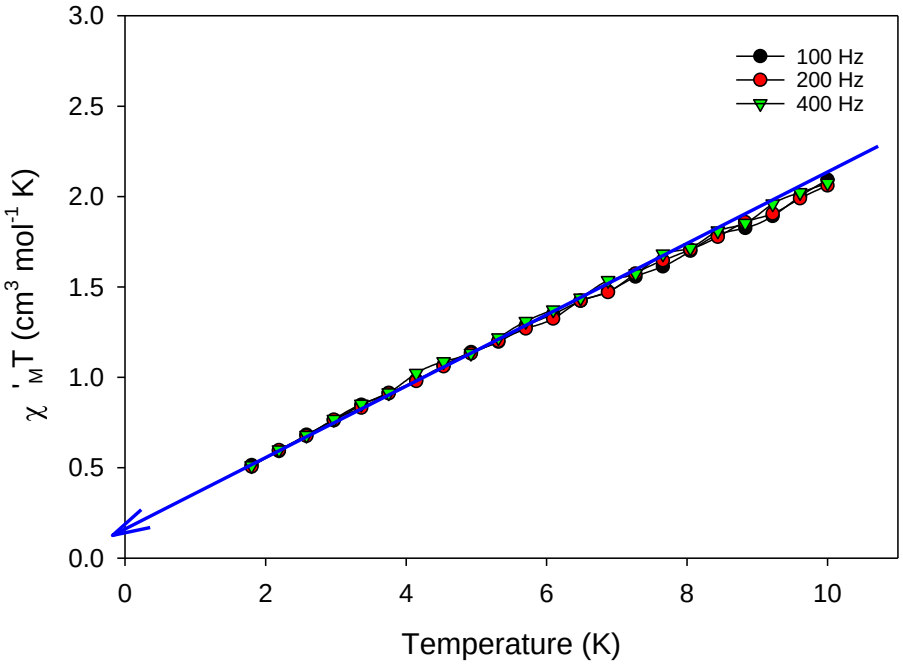

Figure 4.7. Temperature dependence of the in-phase (as $\chi'_M T$) *ac* magnetic susceptibility in zero *dc* field for **9**, measured in a 3.5 G *ac* field oscillating at the indicated frequencies. The blue arrow indicates the extrapolation of the $\chi'_M T$ data down to 0 K.

4.3.4 Relevance of Complexes 9 and 10 to the Structure and Different Oxidation States of the OEC: A Qualitative Approach

Complex **9** is the highest in nuclearity Mn–Ca cluster reported to date[93,200] and, although too high in nuclearity to model the exact structure of the native OEC, the presence of cubane-containing subunits within its structure render it a promising foundation for the low-valent species of OEC. These $\{Mn_4CaO_6\}$ and $\{Mn_4CaO_5\}$ subunits are intriguing with respect to the OEC, in that they possess a similar extended cubane topology to that of the native OEC and have Mn···Mn and Mn···Ca closest separations of 2.876–3.686 Å and 3.376–3.756 Å, respectively, which are in close proximity to the corresponding values of 2.7–3.3 Å and ~3.4 Å for the OEC in PSII. Both extended cubane subunits are mixed-valent with Mn^{II} (Mn11′; Mn10) and Mn^{III} (Mn2, Mn3, Mn5; Mn4, Mn7′, Mn9) ions, making these subunits structurally relevant to the low-valent S_0 state of the OEC. The suggested $S = 0$ spin ground state of this complex, however, proposes that this complex is magnetically equivalent to what is found at the high-valent S_1 state of the catalytic cycle.[24] The occurrence of these $\{Mn_4Ca\}$ subunits is encouraging and provides a foundation for isolating the $\{Mn_4Ca\}$ unit responsible for oxygen evolution.

Complex **10** is the first heterometallic Mn–Ca cluster of its stoichiometry (Mn:Ca = 2:2) to have the Mn atoms stabilized in such a high oxidation state (Mn^{IV}). Although the metal stoichiometry of this complex is not the same as the OEC, due to the oxidation state descriptions of the Mn ions, it can be related to one of the high-valent S_3 or S_4 states of the Kok cycle.[23c,39,67,201]

4.4 ***Conclusions and Perspectives***

In conclusion, I have shown that oximate and dioximate chelating/bridging ligands can support the formation and crystallization of structurally new Mn–Ca complexes with diverse nuclearities, topologies, metal stoichiometries and oxidation state descriptions. The first use of the ligands qaoH and $dapdoH_2$ in heterometallic Mn–Ca chemistry has afforded new $\{Mn^{II/III}{}_{22}Ca_2\}$ (**9**) and $\{Mn^{IV}{}_2Ca_2\}$ (**10**) clusters, respectively. Although the overall structures of the reported compounds are strictly not similar to that of the native OEC, I nevertheless believe that this work provides a foundation from which to tackle the synthesis of the discrete $\{Mn_4Ca\}$ unit responsible for the O_2 gas evolution. This could be accomplished by modifying the reaction conditions that yielded **9** to foster lower nuclearity products, hopefully with the correct topology and metal stroichiometry as those of the OEC. The incorporation of bridging oxido groups in **10** could also facilitate the formation of Mn^{IV}–Ca/O^{2-} complexes with dioximate ligands. Both the described strategies, and others, are currently under investigation.

References

[1] *(a)* Govindjee; Govindjee, R. Introduction to Photosynthesis. In *Bioenergetics of Photosynthesis*; Govindjee, Ed.; Academic Press: New York, NY, **1975**, pp. 2-50. *(b)* Govindjee. Introduction to Photosystem II. In *Photosystem II, The Light-Driven Water: Plastoquinone Oxidoreductase*. Satoh, K.; Wydrzynski, T.J., Eds.; Springer: Dordrecht, **2005**, pp. 11-22. *(c)* Satoh, K. Introduction to the Photosystem II Reaction Center – Isolation and Biochemical and Biophysical Characterization. In *Oxygenic Photosynthesis: The Light Reactions*. Ort, D.R.; Yocum, C.F., Eds.; Kluwer Academic Publishers: Dordrecht, **1996**, pp. 193-211. *(d)* Barber, J. *Q. Rev. Biophys.* **2003**, *36*, 71. *(e)* Yachandra, V.K.; Sauer, K.; Klein, M.P. *Chem. Rev.* **1996**, *96*, 2927. *(f)* McEvoy, J.P.; Brudvig, G.W. *Chem. Rev.* **2006**, *106*, 4455.

[2] Umena, Y.; Kawakami, K.; Shen, J.-R.; Kamiya, N. *Nature* **2011**, *473*, 55.

[3] *(a)* Zouni, A.; Witt, H.-T.; Kern, J.; Fromme, P.; KrauB, N.; Saenger, W.; Orth, P. *Nature* **2001**, *409*, 739. *(b)* Ferreira, K.N.; Iverson, T.M.; Maghlaoui, K.; Barber, J.; Iwata, S. *Science* **2004**, *303*, 1831. *(c)* Guskov, A.; Kern, J.; Gabdulkhakov, A.; Broser, M.; Zouni, A.; Saenger, W. *Nature Struct. Mol. Biol.* **2009**, *16*, 334.

[4] Kamiya, N.; Shen, J.-R. *Proc. Natl. Acad. Sci. USA* **2003**, *100*, 98.

[5] Govindjee; Kern, J.; Messinger, J.; Whitemarsh, J. Photosystem II. In *Encyclopedia of Life Sciences*. John Wiley & Sons, Ltd, Chichester, **2010**.

[6] *(a)* Kelley, P.M.; Izawa, S. *Biochim. Biophys. Acta* **1978**, *502*, 198. *(b)* Critchley, C. *Biochim. Biophys. Acta* **1985**, *811*, 33. *(c)* Ghanotakis , D.M.; Yocum, C.F. *Annu. Rev. Plant Physiol. Plant Mol. Biol.* **1990**, *41*, 255. *(d)* Yocum, C.F. *Biochim. Biophys. Acta* **1991**, *1059*, 1. *(e)* Debus, R.J. *Biochim. Biophys. Acta* **1992**, *1102*, 269.

[7] Cinco, R. M.; McFarlane Holman, K. L.; Robblee, J. H.; Yano, J.; Pizarro, S. A.; Bellacchio, E.; Sauer, K.; Yachandra, V. K. *Biochemistry* **2002**, *41*, 12928.

[8] *(a)* Yocum, C. F.; Yerkes, C. T.; Blankenship, R. E.; Sharp, R. R.; Babcock, G. T. *Proc. Natl. Acad. Sci. USA* **1981**, *78*, 7507. *(b)* Kim, S. H.; Gregor, W.; Peloquin, J. M.; Brynda, M.; Britt, R. D. *J. Am. Chem. Soc.* **2004**, *126*, 7228.

[9] *(a)* Murata, N.; Miyao, M.; Omata, T.; Matsunami, H.; Kuwabara, T. *Biochim. Biophys. Acta* **1984**, *765*, 363. *(b)* Ohno, T.; Satoh, K.; Katoh, S. *Biochim. Biophys. Acta* **1986**, *852*, 1.

[10] Kessler, E. *Arch. Biochem. Biophys.* **1955**, *59*, 527.

[11] Cheniae, G M.; Martin, I. F. *Biochem. Biophys. Res. Commun.* **1967**, *28*, 89.

[12] *(a)* Gaffron, H. *J. Gen. Physiol.* **1942**, *26*, 195. *(b)* Beck, W. F.; Brudvig, G. W. *Biochemistry* **1987**, *26*, 8285. *(c)* Lin, C.; Brudvig, G. W. *Photosynth. Res.* **1993**, *38*, 441.

[13] *(a)* Ghanotakis, D. F.; Topper, J. N.; Babcock, G. T.; Yocum, C. F. *FEBS Lett.* **1984**, *170*, 169. *(b)* Yocum, C. F. *Coord. Chem. Rev.* **2008**, *252*, 296. *(c)* Boussac, A.; Zimmermann, J. –L.; Rutherford, A. W. *Biochemistry* **1989**, *28*, 8984. *(d)* Sivaraja, M.; Tso, J.; Dismukes, G. C. *Biochemistry* **1989**, *28*, 9459. *(e)* Boussac, A.; Sétif, P.; Rutherford, A. W. *Biochemistry* **1992**, *31*, 1224.

[14] *(a)* Piccioni, R. G.; Mauzerall, D. C. *Biochim. Biophys. Acta* **1976**, *423*, 605. *(b)* Piccioni, R. G.; Mauzerall, D. C. *Biochim. Biophys. Acta* **1978**, *504*, 384. *(c)* Ghanotakis, D. F.; Babcock, G. T.; Yocum, C. F. *FEBS Lett.* **1984**, *167*, 127.

[15] Shen, J. -R. Structure-Function Relationships in the Mn_4CaO_5 Water-Splitting Cluster. In *The Biophysics of Photosynthesis*. Golbeck, J.; van der Est, A., Eds.; Springer: New York, NY, **2014**, pp. 321-349.

[16] Chow, W. S.; Aro, E. -M. Photoinactivation and Mechanisms of Recovery. In *Photosystem II, The Light-Driven Water: Plastoquinone Oxidoreductase*. Satoh, K.; Wydrzynski, T.J., Eds.; Springer: Dordrecht, **2005**, pp. 627-648.

[17] *(a)* Cheniae, G. M.; Martin, I. F. *Biochim. Biophys. Acta* **1971**, *253*, 167. *(b)* Miller, A. -F.; Brudvig, G. W. *Biochemistry* **1990**, *29*, 1385.

[18] Campbell, K. A.; Force, D. A.; Nixon, P. J.; Dole, F.; Diner, B. A.; Britt, R. D. *J. Am. Chem. Soc.* **2000**, *122*, 3754.

[19] Tyryshkin, A. M.; Watt, R. K.; Baranov, S. V.; Dasgupta, J.; Hendrich, M. P.; Dismukes, G. C. *Biochemistry* **2006**, *45*, 12876.

[20] Dasgupta, J.; Ananyev, G. M.; Dismukes, G. C. *Coord. Chem. Rev.* **2008**, *252*, 347.

[21] Zaltsman, L.; Ananyev, G. M.; Bruntrager, E.; Dismukes, G. C. *Biochemistry* **1997**, *36*, 8914.

[22] Dasgupta, J.; Tyryshkin, A. M.; Baranov, S. V.; Dismukes, G. C. *Appl. Magn. Reson.* **2010**, *37*, 137.

[23] *(a)* Joliot, P. *Biochim. Biophys. Acta* **1965**, *102*, 116. *(b)* Joliot, P.; Joliot, A. *Biochim. Biophys. Acta* **1968**, *153*, 625. *(c)* Kok, B.; Forbush, B.; McGloin, M. *Photochem. Photobiol.* **1970**, *11*, 457.

[24] Krewald, V.; Retegan, M.; Cox, N.; Messinger, J.; Lubitz, W.; DeBeer, S.; Neese, F.; Pantazis, D. A. *Chem. Sci.* **2015**, *6*, 1676.

[25] Schansker, G.; Goussias, C.; Petrouleas, V.; Rutherford, A. W. *Biochemistry* **2002**, *41*, 3057.

[26] Carrell, T. G.; Tyryshkin, A. M.; Dismukes, G. C. *J. Biol. Inorg. Chem.* **2002**, *7*, 2.

[27] Kulik, L. V.; Epel, B.; Lubitz, W.; Messinger, J. *J. Am. Chem. Soc.* **2007**, *129*, 13421.

[28] Roelofs, T. A.; Liang, W.; Latimer, M. J.; Cinco, R. M.; Rompel, A.; Andrews, J. C.; Sauer, K.; Yachandra, V. K.; Klein, M. P. *Proc. Natl. Acad. Sci. USA* **1996**, *93*, 3335.

[29] *(a)* Bergmann, U.; Grush, M. M.; Horne, C. R.; DeMarois, P.; Penner-Hahn, J. E.; Yocum, C. F.; Wright, D. W.; Dubé, C. E.; Armstrong, W. H.; Christou, G.; Eppley, H. J.; Cramer, S. P. *J. Phys. Chem. B* **1998**, *102*, 8350. *(b)* Visser, H.; Anxolabéhère-Mallart, E.; Bergmann, U.; Glatzel, P.; Robblee, J. H.; Cramer, S. P.; Girerd, J. -J.; Sauer, K.; Klein, M. P.; Yachandra, V. K. *J. Am. Chem. Soc.* **2001**, *123*, 7031. *(c)* Pizarro, S. A.; Glatzel, P.; Visser, H.; Robblee, J. H.; Christou, G.; Bergmann, U.; Yanchandra, V. K. *Phys. Chem. Chem. Phys.* **2004**, *6*, 4864.

[30] *(a)* Pace, R. J.; Jin, L.; Stranger, R. *Dalton Trans.* **2012**, *41*, 11145. *(b)* Gatt, P.; Petrie, S.; Stranger, R.; Pace, R. J. *Angew. Chem. Int. Ed.* **2012**, *51*, 12025.

[31] Radmer, R.; Ollinger, O. *FEBS Lett.* **1986**, *195*, 285.

[32] Messinger, J.; Badger, M.; Wydrzynski, T. *Proc. Natl. Acad. Sci. USA* **1995**, *92*, 3209.

[33] Pecoraro, V. L.; Hsieh, W. -Y. The Use of Model Complexes to Elucidate the Structure and Function of Manganese Redox Enzymes. In *Metal Ions in Biological Systems: Manganese and Its Role in Biological Processes*. Siegel, A.; Siegel, H., Eds.; Marcel Dekker, Inc.: New York, NY, **2000**, pp. 429-504.

[34] *(a)* Hillier, W.; Messinger, J.; Wydrzynski, T. *Biochemistry* **1998**, *37*, 16908. *(b)* Hillier, W.; Wydrzynski. T. *Biochemistry* **2000**, *39*, 4399.

[35] Hendry, G.; Wydrzynski, T. *Biochemistry* **2003**, *42*, 6209.

[36] Mukhopadhyay, S.; Mandal, S. K.; Bhaduri, S.; Armstrong, W. H. *Chem. Rev.* **2004**, *104*, 3981.

[37] Mullins, C. S.; Pecoraro, V. L. *Coord. Chem. Rev.* **2008**, *252*, 416.

[38] Christou, G. *Acc. Chem. Res.* **1989**, *22*, 328.

[39] Paul, S.; Neese, F.; Pantazis, D. A. *Green Chem.* **2017**, *19*, 2309.

[40] Manchanda, R.; Brudvig, G. W.; Crabtree, R. H. *Coord. Chem. Rev.* **1995**, *144*, 1.

[41] Wieghardt, K.; Bossek, U.; Gebert, W. *Angew. Chem. Int. Ed.* **1983**, *22*, 328.

[42] Brudvig, G. W.; Crabtree, R. H. *Proc. Natl. Acad. Sci. USA* **1986**, *83*, 4586.

[43] Hagen, K. S.; Westmoreland, T. D.; Scott, M. J.; Armstrong, W. H. *J. Am. Chem. Soc.* **1989**, *111*, 1907.

[44] Vincent, J. B.; Christou, G. *Adv. Inorg. Chem.* **1989**, *33*, 197.

[45] Li, Q.; Vincent, J. B.; Libby, E.; Chang, H. -R.; Huffman, J. C.; Boyd, P. D. W.; Christou, G.; Hendrickson, D. N. *Angew. Chem. Int. Ed.* **1988**, *27*, 1731.

[46] Bashkin, J. S.; Chang, H. -R.; Streib, W. E.; Huffman, J. C.; Hendrickson, D. N.; Christou, G. *J. Am. Chem. Soc.* **1987**, *109*, 6502.

[47] Völker, M.; Renger, G.; Rutherford, A. W. *Biochim. Biophys. Acta* **1986**, *851*, 424.

[48] *(a)* Govindjee; Kambara, T.; Coleman, W. *Photochem. Photobiol.* **1985**, *42*, 187. *(b)* Renger, G. *Angew. Chem. Int. Ed.* **1987**, *26*, 643. *(c)* Brudvig, G. W. *Bioenerg. Biomembr.* **1987**, *19*, 91.

[49] Ruettinger, W. F.; Campana, C.; Dismukes, G. C. *J. Am. Chem. Soc.* **1997**, *119*, 6670.

[50] Vincent, J. B.; Christou, G. *Inorg. Chim. Acta* **1987**, *136*, L41.

[51] Vincent, J. B.; Christmas, C.; Chang, H. -R.; Li, Q.; Boyd, P. D. W.; Huffman, J. C.; Hendrickson, D. N.; Christou, G. *J. Am. Chem. Soc.* **1989**, *111*, 2086.

[52] Bouwman, E.; Bolcar, M. A.; Libby, E.; Huffman, J. C.; Folting, K.; Christou, G. *Inorg. Chem.* **1992**, *31*, 5185.

[53] Cañada-Vilalta, C.; Huffman, J. C.; Christou, G. *Polyhedron* **2001**, *20*, 1785.

[54] (*a*) Libby, E.; McCusker, J. K.; Schmitt, E. A.; Folting, K.; Hendrickson, D. N.; Christou, G. *Inorg. Chem.* **1991**, *30*, 3486. (*b*) Kulawiec, R. J.; Crabtree, R. H.; Brudvig, G. W.; Schulte, G. K. *Inorg. Chem.* **1988**, *27*, 1309.

[55] Chan, M. K.; Armstrong, W. H.; *J. Am. Chem. Soc.* **1990**, *112*, 4985.

[56] Chan, M. K.; Armstrong, W. H. *J. Am. Chem. Soc.* **1989**, *111*, 9121.

[57] Blondin, G.; Davydov, R.; Philouze, C.; Charlot, M. -F.; Styring, S.; Åkermark, B.; Girerd, J. -J.; Boussac, A. *J. Chem. Soc., Dalton Trans.* **1997**, 4069.

[58] Chan, M. K.; Armstrong, W. H. *J. Am. Chem. Soc.* **1991**, *113*, 5055.

[59] Chen, H.; Faller, J. W.; Crabtree, R. H.; Brudvig, G. W. *J. Am. Chem. Soc.* **2004**, *126*, 7345.

[60] Philouze, C.; Blondin, G.; Girerd, J. -J.; Guilhem, J.; Pascard, C.; Lexa, D. *J. Am. Chem. Soc.* **1994**, *116*, 8557.

[61] Brynda, M.; Britt, R. D. The Manganese-Calcium Cluster of the Oxygen-Evolving System: Synthetic Models, EPR Studies, and Electron Structure Calculations. In *Metals in Biology: Applications of High-Resolution EPR to Metalloenzymes*; Hanson, G. R.; Berliner, L. J., Eds.; Springer: New York, NY, **2010**, pp. 203-271.

[62] Loll, B.; Kern, J.; Saenger, W.; Zouni, A.; Biesiadka, J. *Nature* **2005**, *438*, 1040.

[63] Suga, M.; Akita, F.; Hirata, K.; Ueno, G.; Murakami, H.; Nakajima, Y.; Shimizu, T.; Yamashita, K.; Yamamoto, M.; Ago, H.; Shen, J. -R. *Nature* **2015**, *517*, 99.

[64] Yano, J.; Kern, J.; Irrgang, K. –D.; Latimer, M. J.; Bergmann, U.; Glatzel, P.; Puskar, Y.; Biesiadka, J.; Loll, B.; Sauer, K.; Messinger, J.; Zouni, A.; Yachandra, V. K. *Proc. Natl. Acad. Sci. USA* **2005**, *102*, 12047.

[65] Southworth-Davies, R. J.; Medina, M. A.; Carmichael, I.; Garman, E. F. *Structure* **2007**, *15*, 1531.

[66] George, G. N.; Prince, R. C.; Cramer, S. P. *Science* **1989**, *243*, 789.

[67] Yano, J.; Yachandra, V. K. *Chem. Rev.* **2014**, *114*, 4175.

[68] Neutze, R.; Wouts, R.; van der Spoel, D.; Weckert, E.; Hajdu, J. *Nature* **2000**, *406*, 752.

[69] Dau, H.; Haumann, M. *Coord. Chem. Rev.* **2008**, *252*, 273.

[70] Britt, R. D.; Campbell, K. A.; Peloquin, J. M.; Gilchrist, M. L.; Aznar, C. P.; Dicus, M. M.; Robblee, J.; Messinger, J. *Biochim. Biophys. Acta* **2004**, *1655*, 158.

[71] Siegbahn, P. E. M. *Acc. Chem. Res.* **2009**, *42*, 1871.

[72] Cox, N.; Messinger, J. *Biochim. Biophys. Acta* **2013**, *1827*, 1020.

[73] Isobe, H.; Shoji, M.; Yamanaka, S.; Umena, Y.; Kawakami, K.; Kamiya, N.; Shen, J. -R.; Yamaguchi, K. *Dalton Trans.* **2012**, *41*, 13727.

[74] Sproviero, E. M.; Gascón, J. A.; McEvoy, J. P.; Brudvig, G. W.; Batista, V. S. *Coord. Chem. Rev.* **2008**, *252*, 395.

[75] Pecoraro, V. L.; Baldwin, M. J.; Caudle, M. T.; Hsieh, W. -Y.; Law, N. A. *Pure Appl. Chem.* **1998**, *70*, 925.

[76] Vrettos, J. S.; Limburg, J.; Brudvig, G. W. *Biochim. Biophys. Acta* **2001**, *1503*, 229.

[77] Yamanaka, S.; Isobe, H.; Kanda, K.; Saito, T.; Umena, Y.; Kawakami, K.; Shen, J. -R.; Kamiya, N.; Okumura, M.; Nakamura, H.; Yamaguchi, K. *Chem. Phys. Lett.* **2011**, *511*, 138.

[78] Messinger, J. *Phys. Chem. Chem. Phys.* **2004**, *6*, 4764.

[79] Cox, N.; Pantazis, D. A.; Neese, F.; Lubitz, W. *Acc. Chem. Res.* **2013**, *46*, 1588.

[80] Kusunoki, M. *Biochim. Biophys. Acta* **2007**, *1767*, 484.

[81] Rapatskiy, L.; Cox, N.; Savitsky, A.; Ames, W. M.; Sander, J.; Nowaczyk, M. M.; Rögner, M.; Boussac, A.; Neese, F.; Messinger, J.; Lubitz, W. *J. Am. Chem. Soc.* **2012**, *134*, 16619.

[82] *(a)* Hillier, W.; Wydrzynski, T. *Phys. Chem. Chem. Phys.* **2004**, *6*, 4882. *(b)* Hendry, G.; Wydrzynski, T. *Biochemistry* **2002**, *41*, 13328.

[83] Hillier, W.; Hendry, G.; Burnap, R. L.; Wydrzynski, T. *J. Biol. Chem.* **2001**, *276*, 46917.

[84] Siegbahn, P. E. M. *Biochim. Biophys. Acta* **2013**, *1827*, 1003.

[85] Suga, M.; Akita, F.; Sugahara, M.; Kubo, M.; Nakajima, Y.; Nakane, T.; Yamashita, K.; Umena, Y.; Nakabayashi, M.; Yamane, T.; Nakano, T.; Suzuki, M.; Masuda, T.; Inoue, S.; Kimura, T.; Nomura, T.; Yonekura, S.; Yu, L. -J.; Sakamoto, T.; Motomura, T.; Chen, J. -H.; Kato, Y.; Noguchi, T.; Tono, K.; Joti, Y.; Kameshima, T.; Hatsui, T.; Nango, E.; Tanaka, R.; Naitow, H.; Matsuura, Y.; Yamashita, A.; Yamamoto, M.; Nureki, O.; Yabashi, M.; Ishikawa, T.; Iwata, S.; Shen, J. -R. *Nature* **2017**, *543*, 131.

[86] Cox, N.; Retegan, M.; Neese, F.; Pantazis, D. A.; Boussac, A.; Lubitz, W. *Science* **2014**, *345*, 804.

[87] Pérez-Navarro, M.; Neese, F.; Lubitz, W.; Pantazis, D. A.; Cox, N. *Curr. Opin. Chem. Biol.* **2016**, *31*, 113.

[88] Shoji, M.; Isobe, H.; Yamaguchi, K. *Chem. Phys. Lett.* **2015**, *636*, 172.

[89] *(a)* Willett, P.; Barnard, J. M.; Downs, G. M. *Chem. Inf. Comput. Sci.* **1998**, *38*, 983. *(b)* Martin, Y. C.; Kofron, J. L.; Traphagen, L. M. *J. Med. Chem.* **2002**, *45*, 4350. *(c)* Holm. R. H.; Solomon, E. I. *Chem. Rev.* **2004**, *104*, 347.

[90] Winpenny, R. E. P. *J. Chem. Soc., Dalton Trans.* **2002**, 1.

[91] *(a)* Wieghardt, K. *Angew. Chem. Int. Ed.* **1989**, *28*, 1153. *(b)* Cady, C. W.; Crabtree, R. H.; Brudvig, G. W. *Coord. Chem. Rev.* **2008**, *252*, 444. *(c)* Pecoraro, V. L.; Baldwin, M. J.; Gelasco, A. *Chem. Rev.* **1994**, *94*, 807. *(d)* Yagi, M.; Kaneko, M. *Chem. Rev.* **2001**, *101*, 21. *(e)* Wu, A. J.; Penner-Hahn, J. E.; Pecoraro, V. L. *Chem. Rev.* **2004**, *104*, 903.

[92] Fielden. J.; Cronin, L. Coordination Clusters. In *Encyclopedia of Supramolecular Chemistry*. Atwood, J. L.; Steed, J. W., Eds.; CRC Press: New York, NY, **2004**, pp. 1.

[93] Mishra, A.; Wernsdorfer, W.; Abboud, K. A.; Christou, G. *Chem. Commun.* **2005**, 54.

[94] Hewitt, I. J.; Tang, J. -K.; Madhu, N. T.; Clérac, R.; Buth, G.; Anson, C. E.; Powell, A. K. *Chem. Commun.* **2006**, 2650.

[95] Nayak, S.; Nayek, H. P.; Dehnen, S.; Powell, A. K.; Reedijk, J. *Dalton Trans.* **2011**, *40*, 2699.

[96] Koumousi, E. S.; Mukherjee, S.; Beavers, C. M.; Teat, S. J.; Christou, G.; Stamatatos, T. C. *Chem. Commun.* **2011**, *47*, 11128.

[97] Tsui, E. Y.; Tran, R.; Yano, J.; Agapie, T. *Nat. Chem.* **2013**, *5*, 293.

[98] Kotzabasaki, V.; Siczek, M.; Lis, T.; Milios, C. J. *Inorg. Chem. Commun.* **2011**, *14*, 213.

[99] Fuller, R. O.; Koutsantonis, G. A.; Lozić, I.; Ogden, M. I.; Skelton, B. W. *Dalton Trans.* **2015**, *44*, 2132.

[100] Li, N.; Wang, M.; Ma, C. -B.; Hu, M. -Q.; Zhou, R. -W.; Chen, H.; Chen, C. -N. *Inorg. Chem. Commun.* **2010**, *13*, 730.

[101] Martin-Diaconescu, V.; Gennari, M.; Gerey, B.; Tsui, E. Y.; Kanady, J. S.; Tran, R.; Pécaut, J.; Maganas, D.; Krewald, V.; Gouré, E.; Duboc, C.; Yano, J.; Agapie, T.; Collomb, M. -N.; DeBeer, S. *Inorg. Chem.* **2015**, *54*, 1283.

[102] Wang, W.; Zhang, X.; Chen, F.; Ma, C.; Chen, C.; Liu, Q.; Liao, D.; Li, L. *Polyhedron* **2005**, *24*, 1656.

[103] Chen, C.; Zhang, C.; Dong, H.; Zhao, J. *Dalton Trans.* **2015**, *44*, 4431.

[104] Jerzykiewicz, L. B.; Utko, J.; Duczmal, M.; Sobota, P. *Dalton Trans.* **2007**, 825.

[105] Benniston, A. C.; Melnic, S.; Turta, C.; Arauzo, A. B.; Bartolomé, J.; Bartolomé, E.; Harrington, R. W.; Probert, M. R. *Dalton Trans.* **2014**, *43*, 13349.

[106] Escriche-Tur, L.; Jover, J.; Font-Bardia, M.; Aullón, G.; Corbella, M. *Inorg. Chem.* **2015**, *54*, 11596.

[107] Kanady, J. S.; Tsui, E. Y.; Day, M. W.; Agapie, T. *Science* **2011**, *333*, 733.

[108] *(a)* Stack, T. D. P.; Holm, R. H. *J. Am. Chem. Soc.* **1987**, *109*, 2546. *(b)* Stack, T. D. P.; Holm, R. H. *J. Am. Chem. Soc.* **1988**, *110*, 2484. *(c)* Ciurli, S.; Carrié, M.; Weigel, J. A.; Carney, M. J.; Stack, T. D. P.; Papaefthymiou, G. C.; Holm, R. H. *J. Am. Chem. Soc.* **1990**, *112*, 2654. *(d)* Ciurli, S.; Holm, R. H. *Inorg. Chem.* **1991**, *30*, 743. *(e)* Zhou, J.; Holm, R. H. *J. Am. Chem. Soc.* **1995**, *117*, 11353. *(f)* Zhou, J.; Raebger, J. W.; Crawford, C. A.; Holm, R. H. *J. Am. Chem. Soc.* **1997**, *119*, 6242.

[109] Kanady, J. S.; Lin, P. -H.; Carsch, K. M.; Nielsen, R. J.; Takase, M. K.; Goddard, III, W. A.; Agapie, T. *J. Am. Chem. Soc.* **2014**, *136*, 14373.

[110] Mukherjee, S.; Stull, J. A.; Yano, J.; Stamatatos, T. C.; Pringouri, K.; Stich, T. A.; Abboud, K. A.; Britt, R. D.; Yachandra, V. K.; Christou, G. *Proc. Natl. Acad. Sci.* **2012**, *109*, 2257.

[111] Zhang, C.; Chen, C.; Dong, H.; Shen, J. -R.; Dau, H.; Zhao, J. *Science* **2015**, *348*, 690.

[112] Peloquin, J. M.; Britt, R. D. *Biochim. Biophys. Acta* **2001**, *1503*, 96.

[113] *(a)* Milios, C. J.; Stamatatos, T.C.; Perlepes, S. P. *Polyhedron* **2006**, *25*, 134. *(b)* Milios, C. J.; Piligkos, S.; Brechin, E. K. *Dalton Trans.* **2008**, 1809.

[114] Pombeiro, A. J. L.; Kukushkin, V. Y. Fundamrntals: Ligands, Complexes, Synthesis, Purification and Structure. In *Comprehensive Coordination Chemistry II*, *Vol 1*; McCleverty, J. A.; Meyer, T. C., Eds.; Elsevier, Amsterdam, **2004**, pp. 631.

[115] McCarty, C. G. *syn-anti* Isomerizations and rearrangements. In *The chemistry of the carbon-nitrogen double bond*; Patai, S., Ed.; John Wiley & Sons, Chichester, **1970**, pp. 363-464.

[116] Agrawal, Y. K. *Russian Chem. Rev.* **1979**, *48*, 948.

[117] Marmion, C. J.; Griffith, D.; Nolan, K. B. *Eur. J. Inorg. Chem.* **2004**, 3003.

[118] Diethelm, R.; Miller, M. G.; Shibles, R.; Stewart, C. R. *Plant Cell Physiol.* **1990**, *31*, 179.

[119] *(a)* Zaleski, C. M.; Kampf, J. W.; Mallah, T.; Kirk, M. L.; Pecoraro, V. L. *Inorg. Chem.* **2007**, *46*, 1954. *(b)* Boron, III, T. T.; Kampf, J. W.; Pecoraro, V. L. *Inorg. Chem.* **2010**, *49*, 9104. *(c)* Zaleski, C. M.; Depperman, E. C.; Kampf, J. W.; Kirk, M. L.; Pecoraro, V. L. *Angew. Chem. Int. Ed.* **2004**, *43*, 3912. *(d)* Deb, A.; Boron, III, T. T.; Itou, M.; Sakurai, Y.; Mallah, T.; Pecoraro, V. L.; Penner-Hahn, J. E. *J. Am. Chem. Soc.* **2014**, *136*, 4889. *(e)* Chow, C. Y.; Trivedi, E. R.; Pecoraro, V. L.; Zaleski, C. M. *Comments Inorg. Chem.* **2015**, *35*, 214.

[120] For representative examples, see: *(a)* Dendrinou-Samara, C.; Psomas, G.; Iordanidis, L.; Tangoulis, V.; Kessissoglou, D. P. *Chem. Eur. J.* **2001**, *7*, 5041. *(b)* Lah, M. S.; Pecoraro, V. L.; *J. Am. Chem. Soc.* **1989**, *111*, 7258. *(c)* Kessissoglou, D. P.; Kampf, J. W.; Pecoraro, V. L. *Polyhedron* **1994**, *13*, 1379. *(d)* Dendrinou-Samara, C.; Alevizopoulou, L.; Iordanidis, L.; Samaras, E.; Kessissoglou, D. P. *J. Inorg. Biochem.* **2002**, *89*, 89. *(e)* Dendrinou-Samara, C.; Papadopoulos, A. N.; Malamatari, D. A.; Tarushi, A.; Raptopoulou, C. P.; Terzis, A.; Samaras, E.; Kessissoglou, D. P. *J. Inorg. Biochem.* **2005**, *99*, 864. *(f)* Emerich, B.; Smith, M.; Zeller, M.; Zaleski, C. M. *J. Chem. Crystallogr.* **2010**, *40*, 769. *(g)* Zaleski, C. M.; Lutter, J. C.; Zeller, M. *J. Chem. Crystallogr.* **2015**, *45*, 142.

[121] Dawood, K. M.; Farag, A. M.; El-Deftar, M. M.; Gardiner, M.; Abdelaziz, H. A. *Arkivoc* **2013**, *3*, 210.

[122] For representative examples, see: *(a)* Glynn, C. W.; Turnbull, M. M. *Transition Met. Chem.* **2002**, *27*, 822. *(b)* Khanra, S.; Weyhermüller, T.; Chadhuri, P. *Dalton Trans.* **2008**, 4885. *(c)* Escuer, A.; Cordero, B.; Solans, X.; Font-Bardia, M.; Calvet, T. *Eur. J. Inorg. Chem.* **2008**, 5082. *(d)* Stamatatos, T. C.; Luisi, B. S.; Moulton, B.; Christou, G. *Inorg. Chem.* **2008**, *47*, 1134. *(e)* Escuer, A.; Cordero, B.; Font-Bardia, M.; Calvet, T.; Roubeau, O.; Teat, S. J.; Fedi, S.; de Biani, F. F. *Dalton Trans.* **2010**, *39*, 4817. *(f)* Alexandropoulos, D. I.; Papatriantafyllopoulou,

C.; Li, C.; Cunha-Silva, L.; Manos, M. J.; Tasiopoulos, A. J.; Wernsdorfer, W.; Christou, G.; Stamatatos, T. C. *Eur. J. Inorg. Chem.* **2013**, 2286.

[123] Papefstathiuou, G. S.; Perlepes, S. P. *Comments Inorg. Chem.* **2002**, *23*, 249.

[124] Kanady, J. S.; Tran, R.; Stull, J.A.; Lu, L.; Stich, T.A.; Day, M. W.; Yano, J.; Britt, R. D.; Agapie, T. *Chem. Sci.* **2013**, *4*, 3986.

[125] Manoli, M.; Inglis, R.; Manos, M. J.; Nastopoulos, V.; Wernsdorfer, W.; Brechin, E. K.; Tasiopoulos, A. J. *Angew. Chem. Int. Ed.* **2011**, *50*, 4441.

[126] Alexandropoulos, D. I.; Mowson, A. M.; Pilkington, M.; Bekiari, V.; Christou, G.; Stamatatos, T. C. *Dalton Trans.* **2014**, *43*, 1965.

[127] Bain, G. A.; Berry, J. F. *J. Chem. Educ.* **2008**, *85*, 532.

[128] Kottke, T.; Stalke, D. J. *J. Appl. Cryst.* **1993**, *26*, 615.

[129] *APEX2*, Data Collection Software Version 2.1-RC13; Bruker AXS: Delft, The Netherlands, **2006**.

[130] *Cryopad*, Remote Monitoring and Control, Version 1.451; Oxford Cryosystems: Oxford, U.K., **2006**.

[131] *SAINT+*, Data Integration Engine v. 7.23a; Bruker AXS: Madison, WI, **1997-2005**.

[132] *CrysAlis*^{Pro} Software Package, Version 1.171; *Xcalibur Single Crystal CCD Diffractometer*, Oxford Diffraction (Agilent): Santa Clara, CA.

[133] Sheldrick, G. M. *SADABS v.2.01*, Bruker/Siemens Area Detector Absorption Correction Program; Bruker AXS: Madison, WI, **1998**.

[134] Sheldrick, G. M. *SHELXS-97*, Program for Crystal Structure Solution; University of Göttingen: Göttingen, Germany, **1997**.

[135] Sheldrick, G. M. *Acta Crystallogr., Sect. A* **2008**, *64*, 112.

[136] Sheldrick, G. M. *SHELXL-97*, Program for Crystal Structure Refinement; University of Göttingen: Göttingen, Germany, **1997**.

[137] *(a)* Spek, A. L. *J. Appl. Crystallogr.* **2003**, *36*, 7. *(b)* van der Sluis, P.; Spek, A. L. *Acta Crystallogr., Sect. A* **1990**, *46*, 194.

[138] *(a) Mercury*; Bruno, I. J.; Cole, J. C.; Edgington, P. R.; Kessler, M. K.; Macrae, C. F.; McCabe, P.; Pearson, J.; Taylor, R. *Acta Crystallogr., Sect. B* **2002**, *58*, 389. *(b)* Bradenburg, K. *DIAMOND*, Release 3.1f; Crystal Impact GbR: Bonn, Germany, **2008**.

[139] Gorun, S. M.; Stibrany, R. T.; Lillo, A. *Inorg. Chem.* **1998**, *37*, 836.

[140] *(a)* Tsui, E. Y.; Kanady, J. S.; Agapie, T. *Inorg. Chem.* **2013**, *52*, 13833. *(b)* Kanady, J. S.; Mendoza-Cortes, J. L.; Tsui, E. Y.; Nielsen, R. J.; Goddard III, W. A.; Agapie, T. *J. Am. Chem. Soc.* **2013**, *135*, 1073.

[141] *(a)* Tasiopoulos, A. J.; Wernsdorfer, W.; Abboud, K. A.; Christou, G. *Angew. Chem. Int. Ed.* **2004**, *43*, 6338. *(b)* King, P.; Wernsdorfer, W.; Abboud, K. A.; Christou, G. *Inorg. Chem.* **2005**, *44*, 8659.

[142] *(a)* Khairy, E. M.; Shoukry, M. M.; Khalil, M. M.; Mohamed, M. M. A. *Transition Met. Chem.* **1996**, *21*, 176. *(b)* Hall, M. D.; Failes, T. W.; Hibbs, D. E.; Hambley, T. W. *Inorg. Chem.* **2002**, *41*, 1223.

[143] *(a)* Deacon, G. B.; Phillips, R. J. *Coord. Chem. Rev.* **1980**, *33*, 227. *(b)* Stamatatos, T. C.; Raptopoulou, C. P.; Perlepes, S. P.; Boudalis, A. K. *Polyhedron* **2011**, *30*, 3026.

[144] Glazunov, V. P.; Mashkovsky, A. A.; Odinokov, S. E. *J. Chem. Soc., Faraday Trans. 2* **1979**, *75*, 629.

[145] *(a)* Messinger, J.; Robblee, J. H.; Bergmann, U.; Fernadez, C.; Glatzel, P.; Visser, H.; Cinco, R. M.; McFarlane, K. L.; Bellacchio, E.; Pizarro, S. A.; Cramer, S. P.; Sauer, K.; Klein, M. P.;

Yachandra, V. K. *J. Am. Chem. Soc.* **2001**, *123*, 7804. *(b)* Solomon, E. I.; Hedman, B.; Hodgson, K. O.; Dey, A.; Szilagyi, R. K. *Coord. Chem. Rev.* **2005**, *249*, 97.

[146] For an excellent review on metallacrowns and their nomenclature, see: Pecoraro, V. L.; Stemmler, A. J.; Gibney, B. P.; Bodwin, J.; Kampf, J. W.; Wang, H. Metallacrowns: A New Class of Molecular Recognition Agents. In *Progress in Inorganic Chemistry*; Karlin, K., Ed.; Wiley: Hoboken, NJ, **1996**; Vol *45*, p.p. 83.

[147] Addison, A. W.; Rao, T. N.; Reedijk, J.; Rijn, J.; Verschoor, G. C. *J. Chem. Soc., Dalton Trans.* **1984**, 1349.

[148] Liu, W.; Thorp, H. H. *Inorg. Chem.* **1993**, *32*, 4102.

[149] Zabrodksy, H.; Peleg, S.; Avnir, D. *J. Am. Chem. Soc.* **1993**, *115*, 8278.

[150] Alvarez, S.; Alemany, P.; Casanova, D.; Cirera, J.; Llunell, M.; Avnir, D. *Coord. Chem. Rev.* **2005**, *249*, 1693.

[151] Schwarz, F. P.; Wasik, S. P. *Anal. Chem.* **1976**, *48*, 524.

[152] Lever, A. B. P. *Inorganic Electronic Spectroscopy*; Elsevier: Amsterdam, **1997**.

[153] *(a)* Qi, Z.; Heinrich, T.; Moorthy, S.; Schalley, C. A. *Chem. Soc. Rev.* **2015**, *44*, 515. *(b)* Winter, R. S.; Yan, J.; Busche, C.; Mathieson, J. S.; Prescimone, A.; Brechin, E. K.; Long, D. -L.; Cronin, L. *Chem. Eur. J.* **2013**, *19*, 2976. *(c)* Mazarakioti, E. C.; Poole, K. M.; Cunha-Silva, L.; Christou, G.; Stamatatos, T. C. *Dalton Trans.* **2014**, *43*, 11456.

[154] *(a)* Bagai, R.; Christou, G. *Inorg. Chem.* **2007**, *46*, 10810. *(b)* Soler, M.; Wernsdorfer, W.; Abboud, K. A.; Huffman, J. C.; Davidson, E. R.; Hendrickson, D. N.; Christou, G. *J. Am. Chem. Soc.* **2003**, *125*, 3576.

[155] Bagai, R.; Christou, G. *Chem. Soc. Rev.* **2009**, *38*, 1011.

[156] *(a)* Rappaport, F.; Ishida, N.; Sugiura, M.; Boussac, A. *Energy Environ. Sci.* **2011**, *4*, 2520. *(b)* Tsui, E. Y.; Agapie, Th. *Proc. Natl. Acad. Sci. U. S. A.* **2013**, *110*, 10084.

[157] Randall, D. W.; Sturgeon, B. E.; Ball, J. A.; Lorigan, G. A.; Chan, M. K.; Klein, M. P.; Armstrong, W. H.; Britt, R. D. *J. Am. Chem. Soc.* **1995**, *117*, 11780.

[158] Sessoli, R.; Tsai, H. - L.; Schake, A. R.; Wang, S.; Vincent, J. B.; Folting, K.; Gatteschi, D.; Christou, G.; Hendrickson, D. N. *J. Am. Chem. Soc.* **1993**, *115*, 1804.

[159] Eppley, H. J.; Tsai, H. - L.; de Vries, N.; Folting, K.; Christou, G.; Hendrickson, D. N. *J. Am. Chem. Soc.* **1995**, *117*, 301.

[160] Chia, Y. Y.; Tay, M. G. *Dalton Trans.* **2014**, *43*, 13159.

[161] *(a)* Fleischauer, P. D.; Fleischauer, P. *Chem. Rev.* **1970**, *70*, 199, and references cited therein. *(b)* de Silva, A. P.; Gunaratne, H. Q. N.; Gunnlaugsson, T.; Huxley, A. J. M.; McCoy, C. P.; Rademacher, J. T.; Rice, T. E. *Chem. Rev.* **1997**, *97*, 1515.

[162] *(a)* Glorius, M.; Moll, H.; Bernhard, G. *Polyhedron* **2008**, *27*, 2113. *(b)* Weng, J. -H.; Shieh, Y. - J. *Photosynth. Res.* **2004**, *82*, 151.

[163] Uchida, K.; Takahashi, Y. *Int. J. Quantum Chem.* **1980**, *18*, 301.

[164] *(a)* Niko, Y.; Hiroshige, Y.; Kawauchi, S.; Konishi, G. *J. Org. Chem.* **2012**, *77*, 3986. *(b)* Wu, Y. -Y.; Lu, X. -W.; Qi, M.; Su, H. -C.; Zhao, X. -W.; Zhu, Q. -Y.; Dai, J. *Inorg. Chem.* **2014**, *53*, 7233. *(c)* Palacios, M. A.; Titos-Padilla, S.; Ruiz, J.; Manuel Herrera, J.; Pope, S. J. A.; Brechin, E. K. *Inorg. Chem.* **2014**, *53*, 1465. *(d)* Branchi, B.; Ceroni, P.; Balzani, V.; Klaerner, F. G.; Voegtle, F. *Chem. Eur. J.* **2010**, *16*, 6048. *(e)* Zhang, J.; Lee, J. -K.; Wu, Y.; Murray, R. W. *Nano Lett.* **2003**, *3*, 403. *(f)* Zhu, L.; Al-Kaysi, R. O.; Dillon, R. J.; Tham, F. S.; Bardeen, C. J. *Cryst. Growth Des.* **2011**, *11*, 4975. *(g)* Alberding, B. G.; Brown-Xu, S. E.; Chisholm, M. H.; Gustafson, T. L.; Reed, C. R.; Naseri, V. *Dalton Trans.* **2012**, *41*, 13097. *(h)* Al-Kaysi, R. O.;

Bardeen, C. J. *Adv. Mater.* **2007**, *19*, 1276. *(i)* Khanra, P.; Kuila, T.; Bae, S. H.; Kim, N. H.; Lee, J. H. *J. Mater. Chem.* **2012**, *22*, 24403. *(j)* Beedle, C. C.; Stephenson, C. J.; Heroux, K. J.; Wernsdorfer, W.; Hendrickson, D. N. *Inorg. Chem.* **2008**, *47*, 10798.

[165] *(a)* Winnik, F. M. *Chem. Rev.* **1993**, *93*, 587. (b) Hu, J. -Y.; Yamato, T. Synthesis and Photophysical Properties of Pyrene-Based Light-Emitting Monomers: Highly Blue Fluorescent Multiply-Conjugated-Shaped Architectures. In *Organic Light Emitting Diode - Material, Process and Devices*; Ko, S. H., Ed.; InTech: Rijeka, Croatia, **2011**.

[166] *(a)* Duhamel, J. *Langmuir* **2012**, *28*, 6527. *(b)* Seko, T.; Ogura, K.; Kawakami, Y.; Sugino, H.; Toyotama, H.; Tanaka, J. *Chem. Phys. Let.* **1998**, *291*, 438.

[167] Chilton, N. F.; Anderson, R. P.; Turner, L. D.; Soncini, A.; Murray, K. S. *J. Comput. Chem.* **2013**, *34*, 1164.

[168] For example, see: *(a)* Koumousi, E. S.; Raptopoulou, C. P.; Perlepes, S. P.; Escuer, A.; Stamatatos, T. C. *Polyhedron* **2010**, *29*, 204. *(b)* Pringouri, K. V.; Raptopoulou, C. P.; Escuer, A.; Stamatatos, T. C. *Inorg. Chim. Acta* **2007**, *360*, 69. *(c)* Verani, G. N.; Bothe, E.; Burdinski, D.; Weyhermüller, T.; Flörke, U.; Chaudhuri, P. *Eur. J. Inorg. Chem.* **2001**, 2161. *(d)* Gass, I. A.; Milios, C. J.; Collins, A.; White, F. J.; Budd, L.; Parsons, S.; Murrie, M.; Perlepes, S. P.; Brechin, E. K. *Dalton Trans.* **2008**, 2043.

[169] Riggs-Gelasco, P. J.; Mei, R.; Yocum, C. F.; Penner-Hahn, J. E. *J. Am. Chem. Soc.* **1996**, *118*, 2387.

[170] *(a)* Sarrou, J.; Ioannidis, N.; Deligiannakis, Y.; Petrouleas, V. *Biochemistry* **1998**, *37*, 3581. *(b)* Ioannidis, N.; Sarrou, J.; Schansker, G.; Petrouleas, V. *Biochemistry* **1998**, *37*, 16445.

[171] *(a)* Messinger, J.; Wacker, U.; Renger, G. *Biochemistry* **1991**, *30*, 7852. *(b)* Bösing, P.; Willner, A.; Pape, T.; Heppa, A.; Mitzel, N. W. *Dalton Trans*. **2008**, 2549. *(c)* Kuntzleman, T.; Yocum, C. F. *Biochemistry* **2005**, *44*, 2129.

[172] For recent reviews in polynuclear Mn clusters, see: *(a)* Kostakis, G. E.; Blatov, V. A.; Prosperio, D. M. *Dalton Trans.* **2012**, *41*, 4634. *(b)* Aromí, G.; Brechin, E. K. *Struct. Bonding (Berlin)* **2006**, *122*, 1. *(c)* Papatriantafyllopoulou, C.; Moushi, E. E.; Christou, G.; Tasiopoulos, A. J. *Chem. Soc. Rev.* **2016**, *45*, 1597.

[173] Gerey, B.; Gouré, E.; Fortage, J.; Pécaut, J.; Collomb, M. –N. *Coord. Chem. Rev.* **2016**, *319*, 1.

[174] *(a)* Vincent, J. B.; Chang, H. -R.; Folting, K.; Huffman, J. C.; Christou, G.; Hendrickson, D. N. *J. Am. Chem. Soc.* **1987**, *109*, 5703. *(b)* Wemple, M. W.; Tsai, H. -L.; Wang, S.; Claude, J. P.; Streib, W. E.; Huffman, J. C.; Hendrickson, D. N.; Christou, G. *Inorg. Chem.* **1996**, *35*, 6437.

[175] *CrystalClear*; Rigaku/MSC Inc.: The Woodlands, TX, **2005**.

[176] Sheldrick, G. M. *Acta Crystallogr., Sect. C: Struct. Chem.* **2015**, *71*, 3.

[177] Sheldrick, G. M. *SADABS, 2012/1*, Bruker AXS Area Detector Scaling and Absorption Correction Program; Bruker AXS: Madison, WI, **2012**.

[178] Sheldrick, G. M. *SHELXT*, Program for Crystal Structure Solution, version 2014/3; University of Göttingen: Göttingen, Germany, **2014**.

[179] Sheldrick, G. M. *SHELXL*, Program for Crystal Structure Refinement, version 2014; University of Göttingen, Göttingen, Germany, **2014**.

[180] Spek, A. L. *Acta Cryst. A* **1990**, *46*, C34.

[181] *(a)* Brechin, E. K.; Soler, M.; Davidson, J.; Hendrickson, D. N.; Parsons, S.; Christou, G. *Chem. Commun.* **2002**, 2252. *(b)* Brechin, E. K.; Soler, M.; Christou, G.; Helliwell, M.; Teat, S. J.; Wernsdorfer, W. *Chem. Commun.* **2003**, 1276.

[182] Hooper, T. N.; Inglis, R.; Palacios, M. A.; Nichol, G. S.; Pitak, M. B.; Coles, S. J.; Lorusso, G.; Evangelisti, M.; Brechin, E. K. *Chem. Commun.* **2014**, *50*, 3498.

[183] *(a)* Langley, S. K.; Moubaraki, B.; Murray, K. S. *Inorg. Chem.* **2012**, *51*, 3947. *(b)* Dermitzaki, D.; Lorusso, G.; Raptopoulou, C. P.; Psycharis, V.; Escuer, A.; Evangelisti, M.; Perlepes, S. P.; Stamtatos, T. C. *Inorg. Chem.* **2013**, *52*, 10235.

[184] Lampropoulos, C.; Thuijs, A. E.; Mitchell, K. J.; Abboud, K. A.; Christou, G. *Inorg. Chem.* **2014**, *53*, 6805.

[185] Tasiopoulos, A. J.; Perlepes, S. P. *Dalton Trans.* **2008**, 5537.

[186] *(a)* Kahn, O. *Molecular Magnetism*. VCH Publishers: New York, USA, **1993**. *(b)* Benelli, C.; Gatteschi, D. *Chem. Rev.* **2002**, *102*, 2369.

[187] Rinehart, J. D.; Long, J. R. *Chem. Sci.* **2011**, *2*, 2078.

[188] Layfield, R.; Murugesu, M. *Lanthanides and Actinides in Molecular Magnetism*. John Wiley & Sons, Ltd.: Weinheim, Germany, **2015**.

[189] Bünzli, J. –C. G.; Eliseeva, S. V. *Chem. Sci.* **2013**, 1939.

[190] Lundgren, R. J.; Stradiotto, M. Key Concepts in Ligand Design: An Introduction. In *Ligand Design in Metal Chemistry: Reactivity and Catalysis*. Stradiotto, M.; Lundgren, R. J.; Buchwald, S. L.; Milstein, D., Eds. Wiley: West Sussex, England, **2016**, pp. 1-13.

[191] Krause, W. *Contrast Agents I: Magnetic Reasonance Imaging-Topics in Current Chemistry*. Springer: Berlin, Germany, **2002**.

[192] *(a)* Stamatatos, T. C.; Fouget-Albiol, D.; Lee, S. –C.; Stoumpos, C. C.; Raptopoulou, C. P.; Terzis, A.; Wernsdorfer, Hill, S. O.; Perlepes, S. P.; Christou, G. *J. Am. Chem. Soc.* **2007**, *129*, 9484. *(b)* Milios, C. J.; Vinslava, A.; Wernsdorfer, W.; Moggach, S.; Parsons, S.; Perlepes, S. P.; Christou, G.; Brechin, E. *J. Am. Chem. Soc.* **2007**, *129*, 2754. *(c)* Nguyen, T. N.; Wernsdorfer, W.; Shiddiq, M.; Abboud, K. A.; Hill, S.; Christou, G. *Chem. Sci.* **2016**, *7*, 1156.

[193] Alexandropoulos, D. I.; Papatriantafyllopoulou, C.; Aromí, G.; Roubeau, O.; Teat, S. J.; Perlepes, S. P.; Christou, G.; Stamatatos, T. C. *Inorg. Chem.* **2010**, *49*, 3962.

[194] Abele, E.; Abele, R.; Rubina, K.; Lukevics, E. *Chem. Heterocycl. Compd.* **2005**, *41*, 137.

[195] *APEX-III*: Bruker AXS Inc., **2016**, Madison, Wisconsin, USA.

[196] Hübschle,C. B.; Sheldrick, G. M.; Dittrich, B. *J. Appl. Cryst.* **2011**, *44*, 1281.

[197] Wang, X.; Andrews, L. *J. Phys. Chem. A* **2006**, *110*, 10035.

[198] *(a)* Smith, B. C. Inorganic Compounds. In *Infrared Spectral Interpretation: A Systematic Approach*. CRC Press: Florida, USA, **1999**, pp. 71-73. *(b)* Stuart, B. H. Spectral Analysis. In *Infrared Spectroscopy: Fundamentals and Applications*. John Wiley & Sons, Ltd.: West Sussex, England, **2004**, pp. 45-70. *(c)* Coates, J. Interpretation of Infrared Spectra: A Practical Approach. In *Encyclopedia of Analytical Chemistry*. Meyers, R. A., Ed. John Wiley & Sons, Ltd.: West Sussex, England, **2000**, pp. 10815-10827.

[199] Kahn, O. *Magnetism: A Suprmolecular Function*. NATO ASI Series, Kluwer Academic Publishers: Dordrecht, Netherlands, **1996**.

[200] Chakov, A. E.; Thuijs, A. E.; Wernsdorfer, W.; Rheingold, A. L.; Abboud, K. A.; Christou, G. *Inorg. Chem.* **2016**, *55*, 8468.

[201] Kolling, D. R. J.; Cox, N.; Ananyev, G. M.; Pace, R. J.; Dismukes, G. C. *Biophys. J.* **2012**, *103*, 313.

Appendix

- IR spectra of the organic ligands and complexes **1–10**.

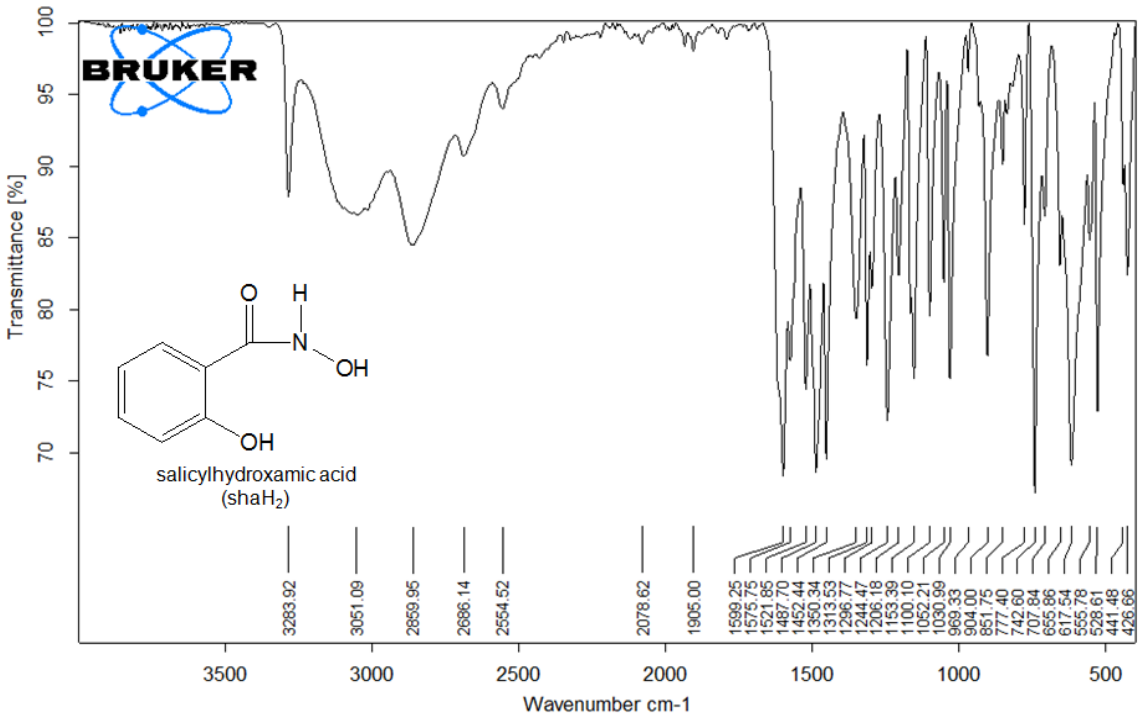

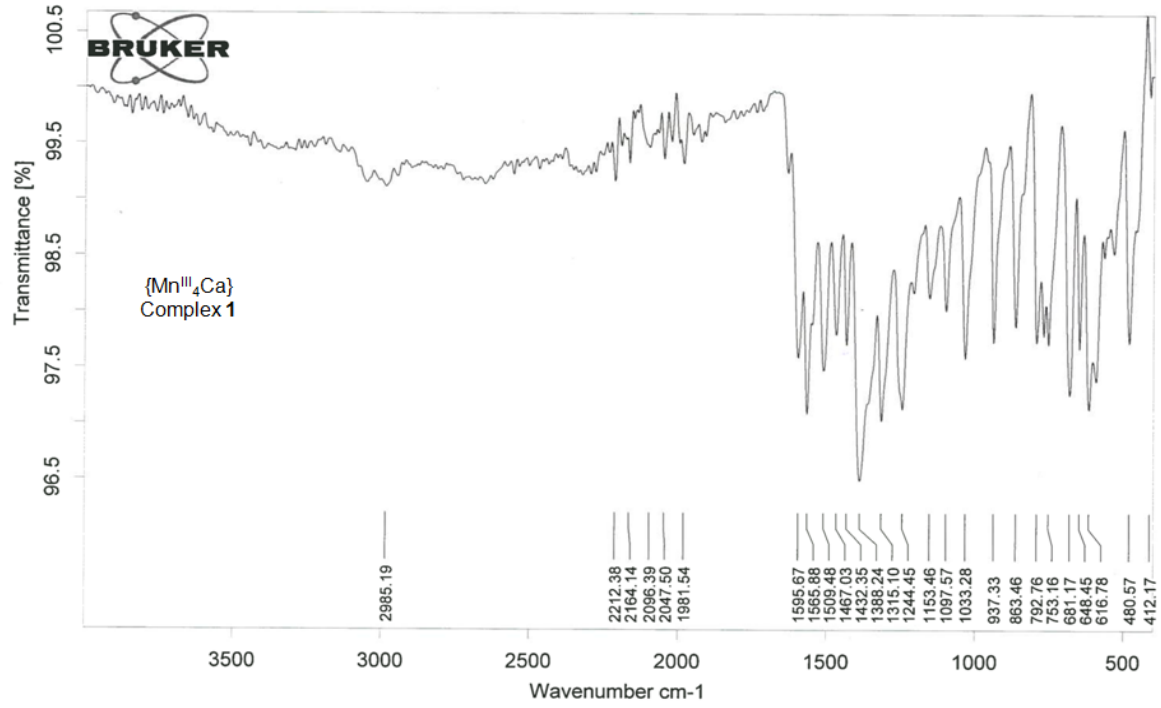

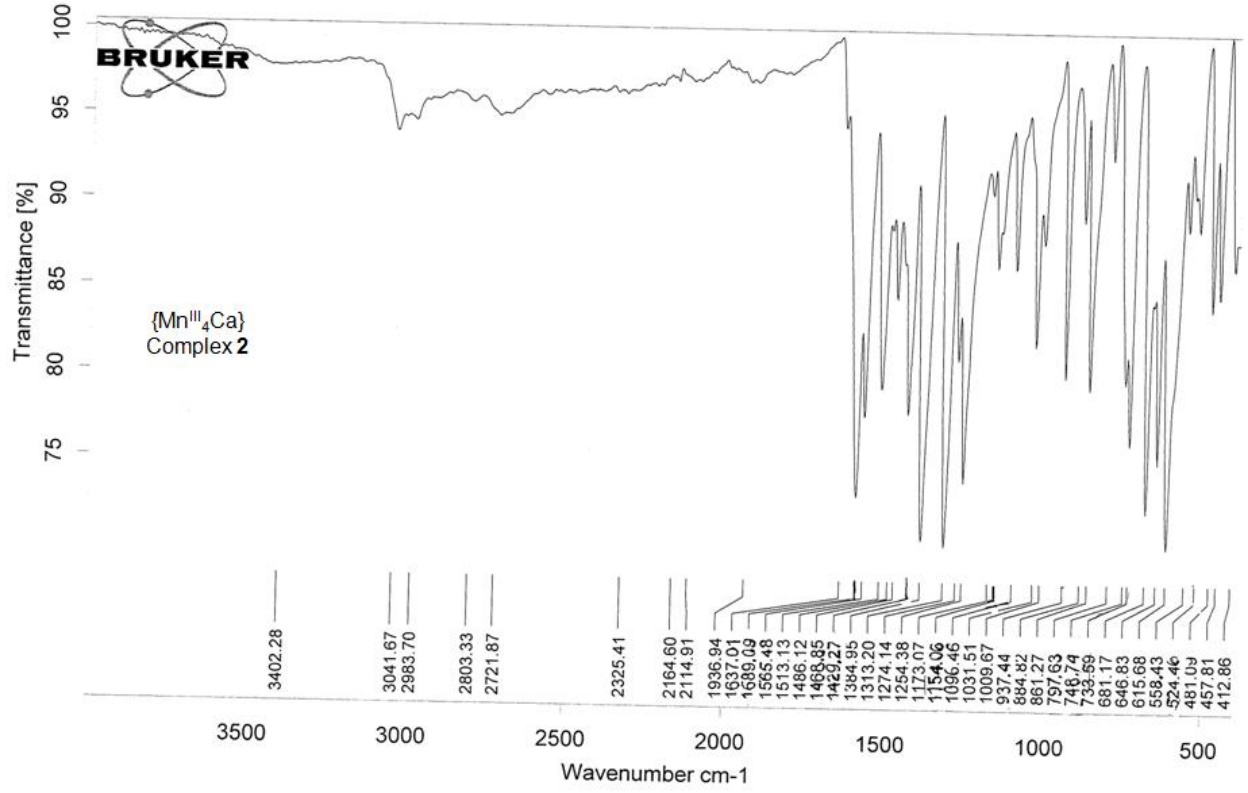
BRUKER
{Mn$^{III}_4$Ca}
Complex **2**
Transmittance [%]
100
95
90
85
80
75
3402.28
3041.67
2983.70
2803.33
2721.87
2325.41
2164.60
2114.91
1936.94
1637.01
1689.09
1565.48
1513.13
1486.12
1468.85
1420.27
1384.95
1313.20
1274.14
1254.38
1173.07
1154.06
1096.46
1031.51
1009.67
937.44
884.82
861.27
797.63
746.74
733.69
681.17
646.83
615.68
558.43
524.46
481.09
457.81
412.86
3500
3000
2500
2000
1500
1000
500
Wavenumber cm-1

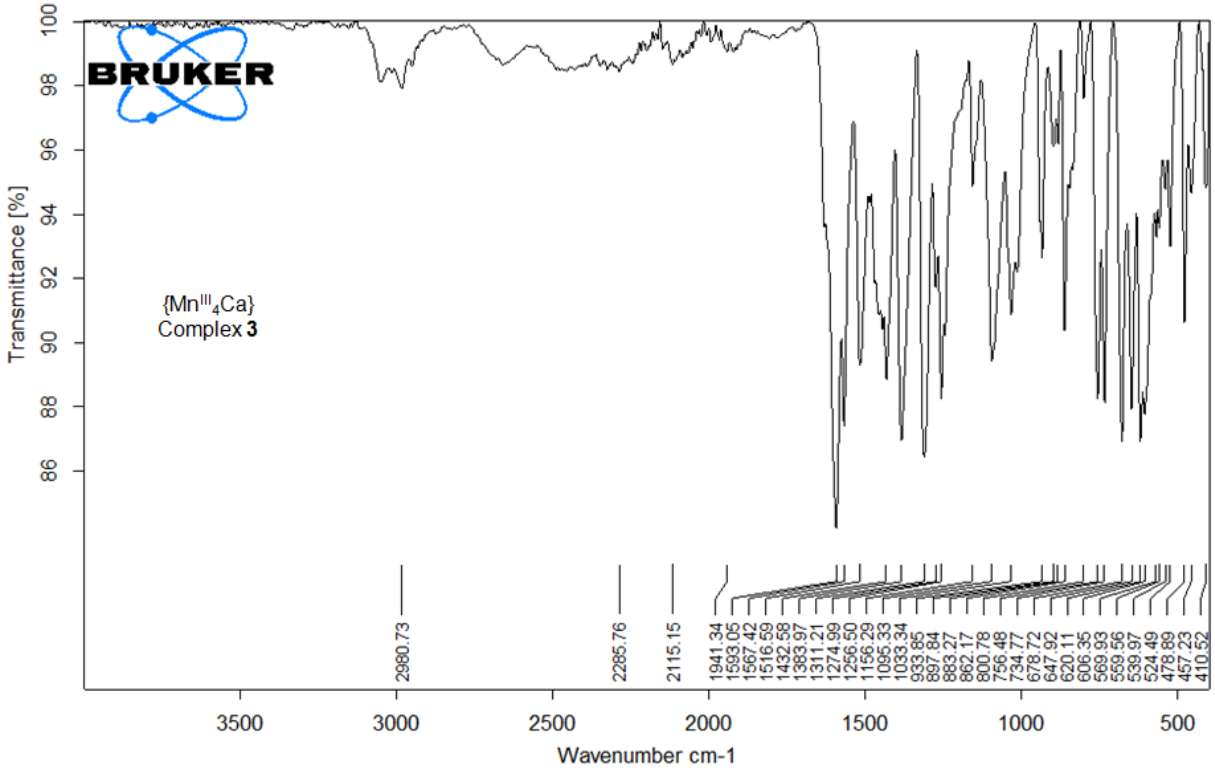
BRUKER
{Mn$^{III}_4$Ca}
Complex **3**
Transmittance [%]
100
98
96
94
92
90
88
86
2980.73
2285.76
2115.15
1941.34
1593.05
1567.42
1516.59
1432.58
1383.97
1311.21
1274.99
1256.50
1156.29
1095.33
1033.34
933.85
897.84
883.27
862.17
800.78
756.48
734.77
678.72
647.92
620.11
606.35
569.93
559.56
539.97
524.49
478.89
457.23
410.52
3500
3000
2500
2000
1500
1000
500
Wavenumber cm-1

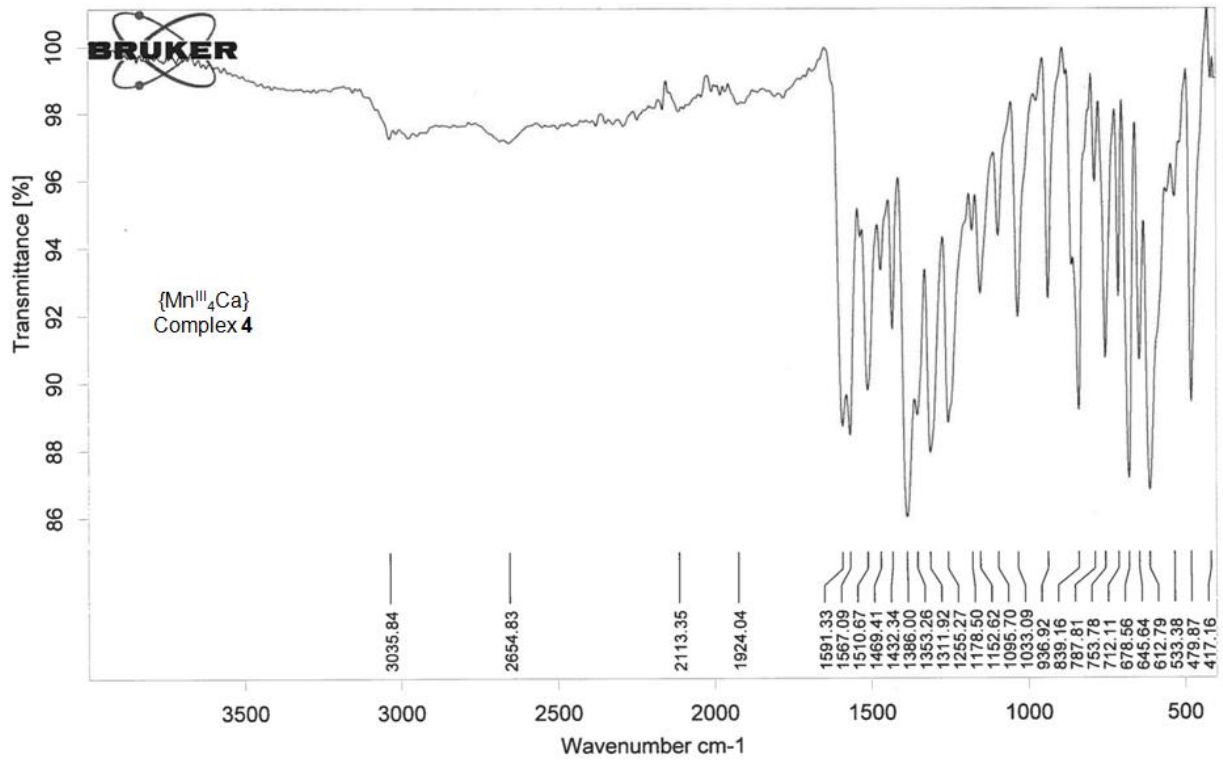
BRUKER
Transmittance [%]
100
98
96
94
92
90
88
86
{Mn$^{III}_4$Ca}
Complex **4**
3035.84
2654.83
2113.35
1924.04
1591.33
1567.09
1510.67
1469.41
1432.34
1386.00
1353.26
1311.92
1255.27
1178.50
1152.62
1095.70
1033.09
936.92
839.16
787.81
753.78
712.11
678.56
645.64
612.79
533.38
479.87
417.16
3500
3000
2500
2000
1500
1000
500
Wavenumber cm-1

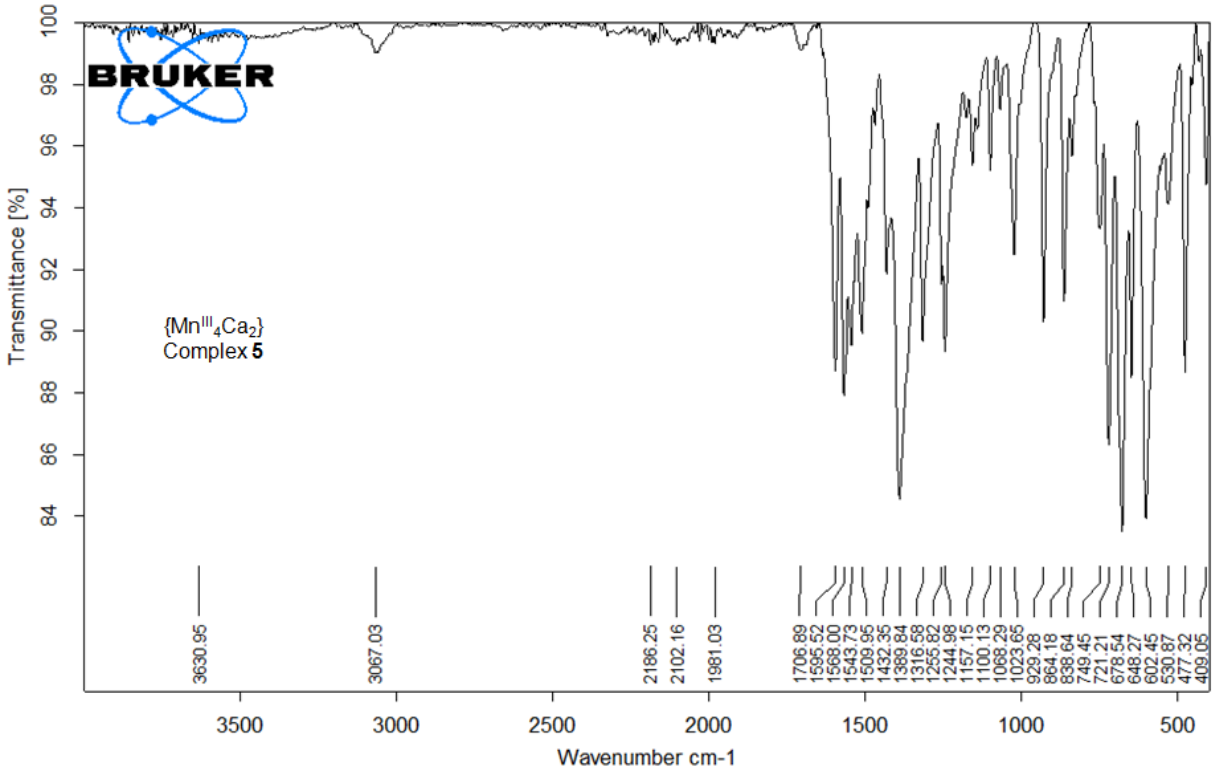
BRUKER
Transmittance [%]
100
98
96
94
92
90
88
86
84
{Mn$^{III}_4$Ca$_2$}
Complex **5**
3630.95
3067.03
2186.25
2102.16
1981.03
1706.89
1595.52
1568.00
1543.73
1509.95
1432.35
1389.84
1316.58
1255.82
1244.98
1157.15
1100.13
1068.29
1023.65
929.28
864.18
838.64
749.45
721.21
678.54
648.27
602.45
530.87
477.32
409.05
3500
3000
2500
2000
1500
1000
500
Wavenumber cm-1

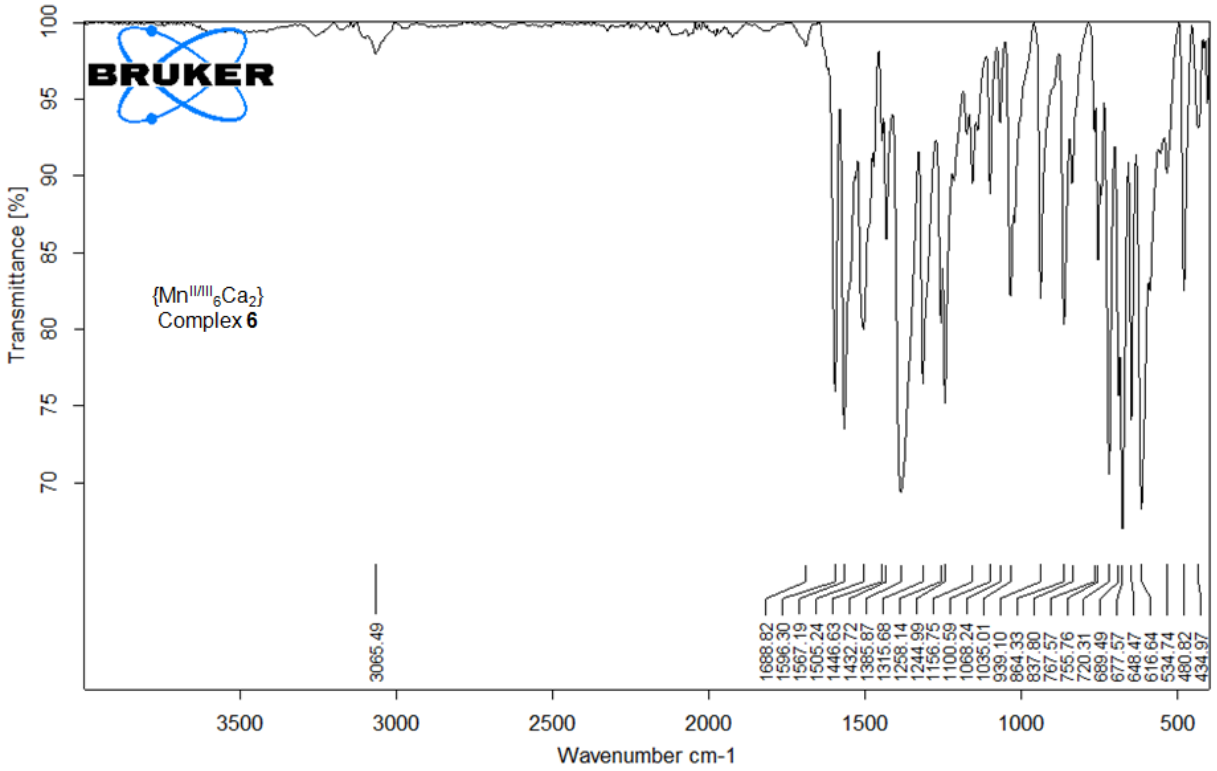
BRUKER
{Mn$^{II/III}_6$Ca$_2$}
Complex **6**
Transmittance [%]
100
95
90
85
80
75
70
3065.49
1688.82
1596.30
1567.19
1505.24
1446.63
1432.72
1385.87
1315.68
1258.14
1244.99
1156.75
1100.59
1068.24
1035.01
939.10
864.33
837.80
767.57
755.76
720.31
689.49
677.57
648.47
616.64
534.74
480.82
434.97
3500
3000
2500
2000
1500
1000
500
Wavenumber cm-1

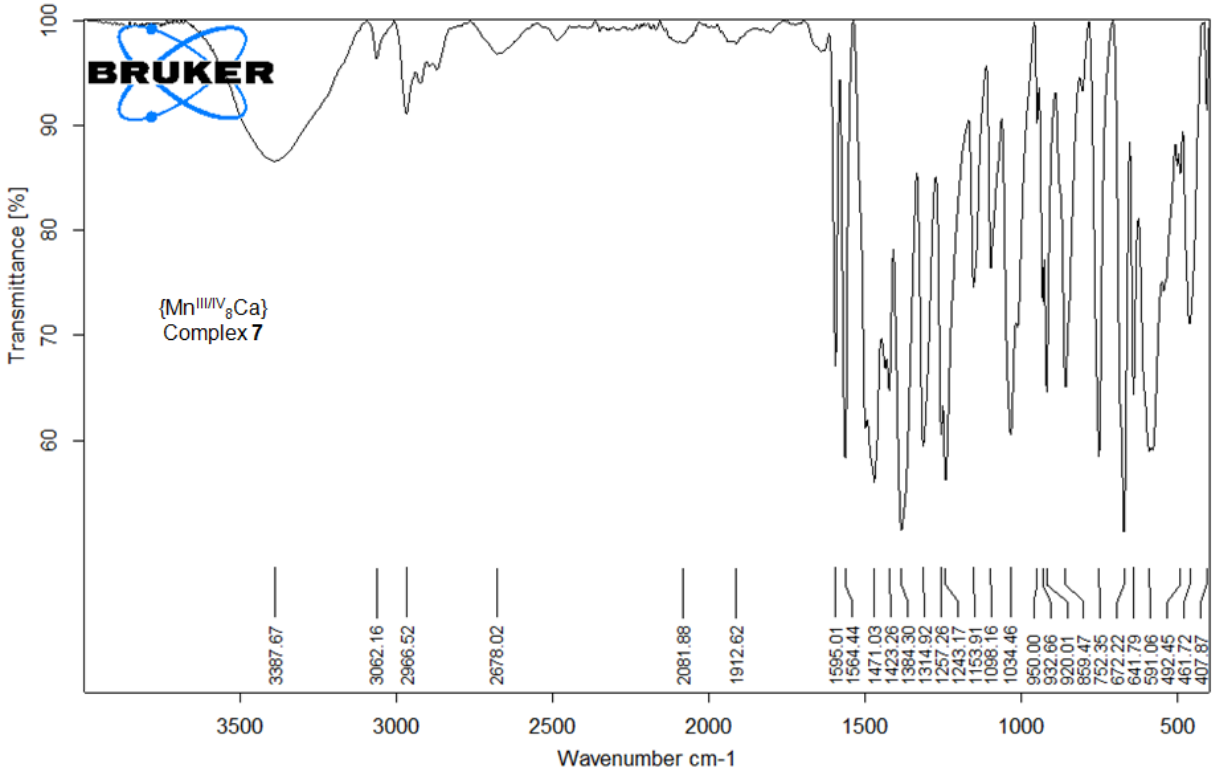
BRUKER
{Mn$^{III/IV}_8$Ca}
Complex **7**
Transmittance [%]
100
90
80
70
60
3387.67
3062.16
2966.52
2678.02
2081.88
1912.62
1595.01
1564.44
1471.03
1423.26
1384.30
1314.92
1257.26
1243.17
1153.91
1098.16
1034.46
950.00
932.66
920.01
859.47
752.35
672.22
641.79
591.06
492.45
461.72
407.87
3500
3000
2500
2000
1500
1000
500
Wavenumber cm-1

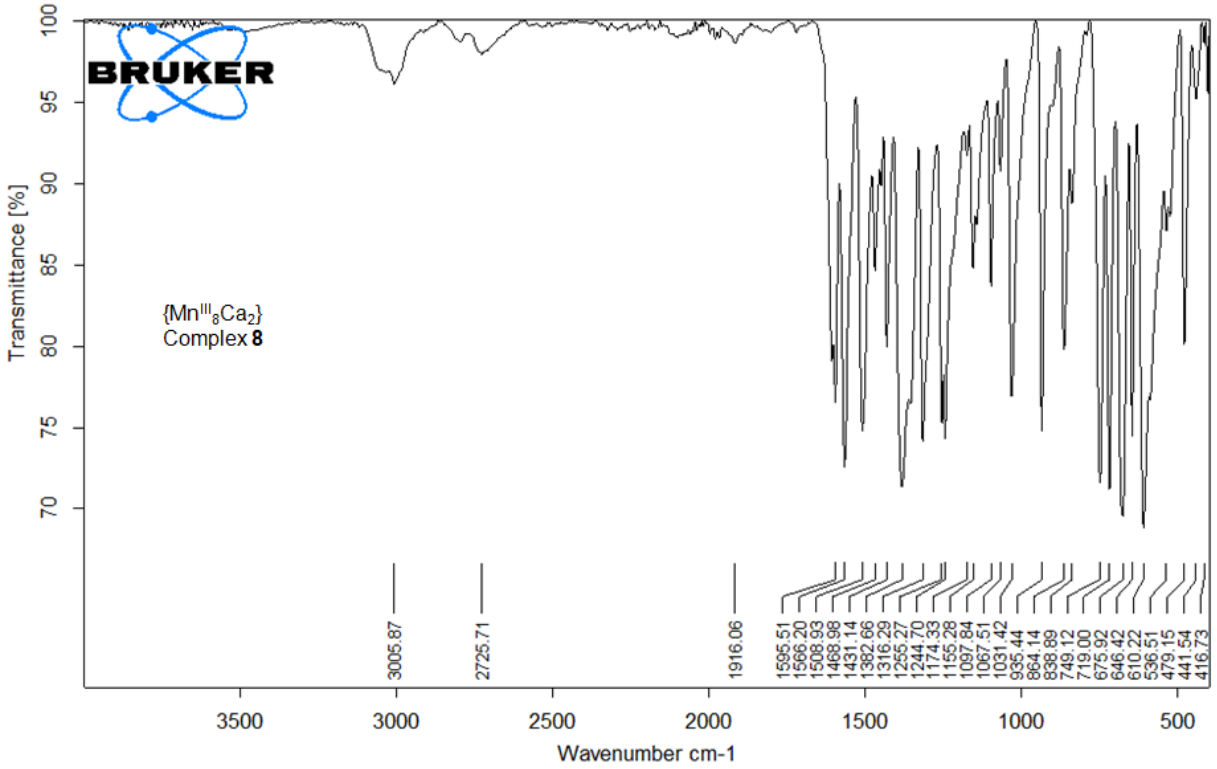
BRUKER
{Mn$^{III}_8$Ca$_2$}
Complex **8**
Transmittance [%]
Wavenumber cm-1
3005.87
2725.71
1916.06
1595.51
1566.20
1508.93
1468.98
1431.14
1382.66
1316.29
1255.27
1244.70
1174.33
1155.28
1097.84
1067.51
1031.42
935.44
864.14
838.89
749.12
719.00
675.92
646.42
610.22
536.51
479.15
441.54
416.73

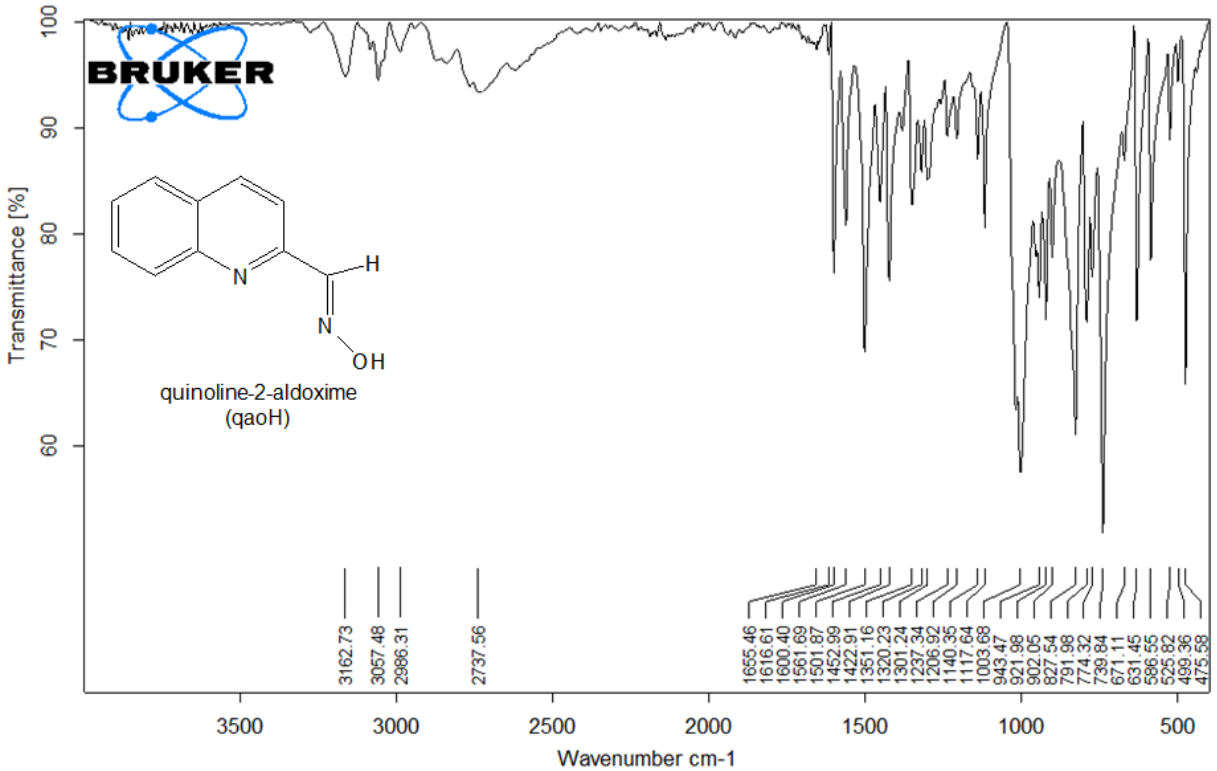
BRUKER
quinoline-2-aldoxime
(qaoH)
Transmittance [%]
Wavenumber cm-1
3162.73
3057.48
2986.31
2737.56
1655.46
1616.61
1600.40
1561.69
1501.87
1452.99
1422.91
1351.16
1320.23
1301.24
1237.34
1206.92
1140.35
1117.64
1003.68
943.47
921.98
902.05
827.54
791.98
774.32
739.84
671.11
631.45
586.55
525.82
499.36
475.58

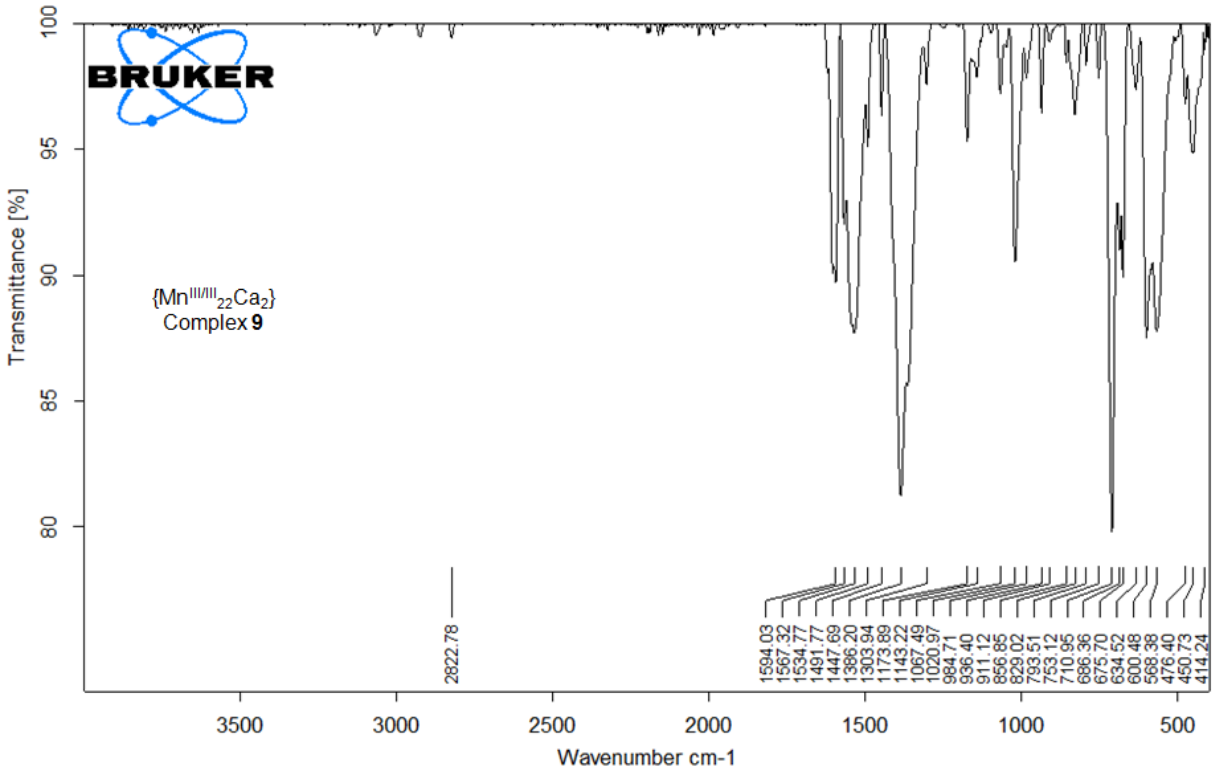
BRUKER
{Mn$^{III/III}_{22}$Ca$_2$}
Complex **9**
Transmittance [%]
Wavenumber cm-1
2822.78
1594.03
1567.32
1534.77
1491.77
1447.69
1386.20
1303.94
1173.89
1143.22
1067.49
1020.97
984.71
936.40
911.12
856.85
829.02
793.51
753.12
710.95
686.36
675.70
634.52
600.48
568.38
476.40
450.73
414.24

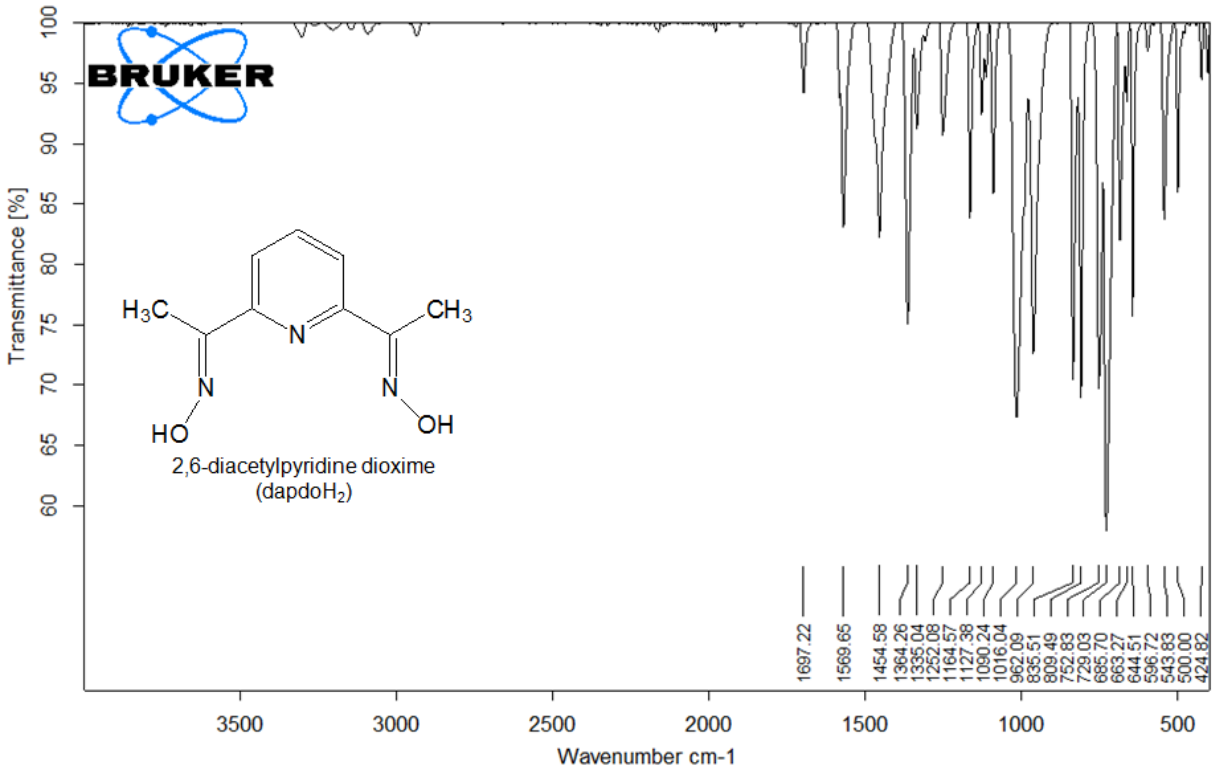
BRUKER
Transmittance [%]
Wavenumber cm-1
2,6-diacetylpyridine dioxime
(dapdoH$_2$)
1697.22
1569.65
1454.58
1364.26
1335.04
1252.08
1164.57
1127.38
1090.24
1016.04
962.09
835.51
809.49
752.83
729.03
685.70
663.27
644.51
596.72
543.83
500.00
424.82

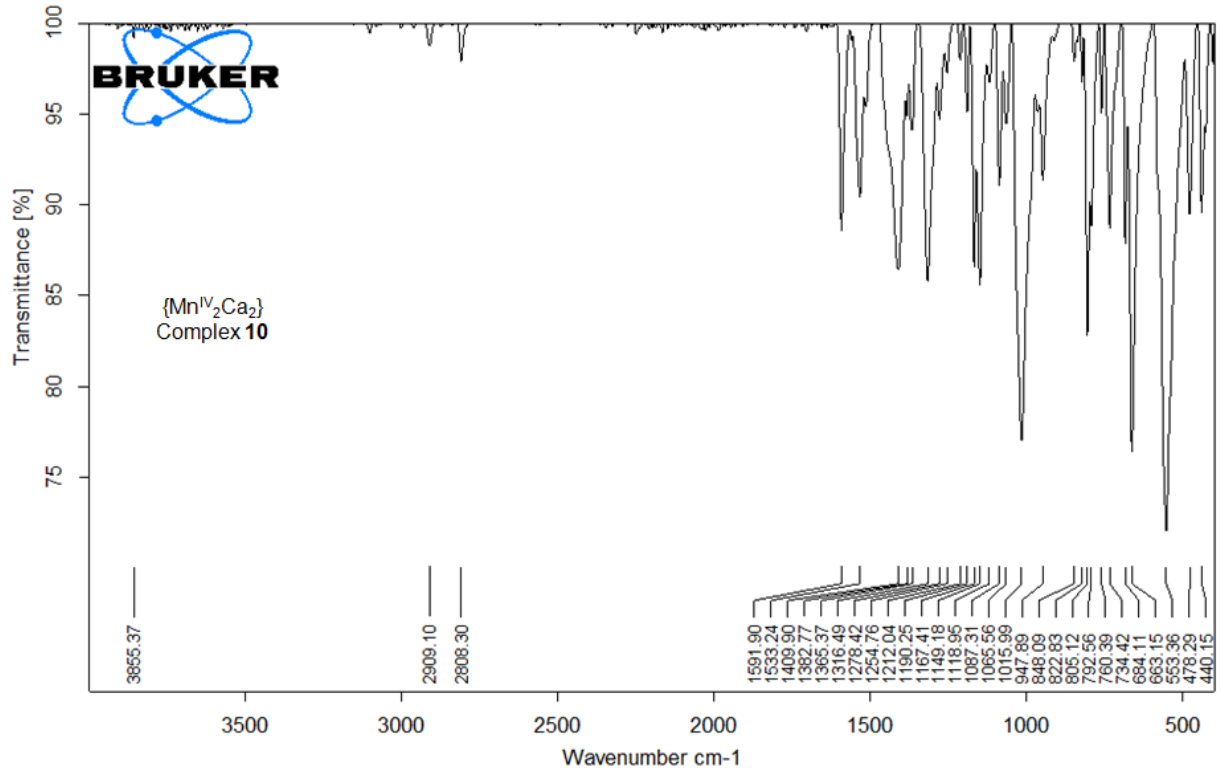
BRUKER
{Mn$^{IV}_2$Ca$_2$}
Complex **10**
Transmittance [%]
100
95
90
85
80
75
3855.37
2909.10
2808.30
1591.90
1533.24
1409.90
1382.77
1365.37
1316.49
1278.42
1254.76
1212.04
1190.25
1167.41
1149.18
1118.95
1087.31
1065.56
1015.99
947.89
848.09
822.83
805.12
792.56
760.39
734.42
684.11
663.15
553.36
478.29
440.15
3500
3000
2500
2000
1500
1000
500
Wavenumber cm-1